Résonateurs nano-optomécaniques à mode de galerie sur puce

Christopher Baker

HAL Id: tel-00923404
https://tel.archives-ouvertes.fr/tel-00923404

Submitted on 2 Jan 2014

UNIVERSITÉ PARIS DIDEROT

LABORATOIRE MATÉRIAUX ET PHÉNOMÈNES QUANTIQUES

UFR DE PHYSIQUE

THÈSE

présentée par

Christopher BAKER

pour obtenir le grade de
Docteur en Sciences de l'Université Paris Diderot

On-chip nano-optomechanical whispering gallery resonators

Membres du jury: Soutenue le 10 / 10 / 2013 devant la commission d'examen composée de:

M.	Philippe BOUCAUD,	Rapporteur
M.	Sylvain COMBRIÉ,	Examinateur
M.	Ivan FAVERO,	Directeur de thèse
M.	Antoine HEIDMANN,	Rapporteur
M.	Bernard JUSSERAND,	Examinateur
M.	Aristide LEMAÎTRE,	Invité
M.	Giuseppe LEO,	Directeur de thèse
Mme	Eva WEIG,	Invitée

Résumé

Ces travaux de thèse portent sur la conception, la fabrication et la caractérisation de résonateurs nano-optomécaniques sous forme de disques en arséniure de Gallium (GaAs). Ces disques sont à la fois des résonateurs mécaniques oscillant au GHz, et des résonateurs optiques à mode de galerie à haut facteur de qualité ($> 10^5$). En confinant l'énergie mécanique et optique sur un volume sub-μm^3, ils permettent d'atteindre un couplage optomécanique extrêmement large ($g_0 >1$ MHz). Nous présentons les développements technologiques ayant permis l'intégration de ces résonateurs avec des guides de couplage optique directement sur échantillon semi-conducteur, tout en maintenant des performances à l'état de l'art. Nous discutons les différents mécanismes de couplage optomécanique (pression de radiation, photoélasticité) dans les disques GaAs, ainsi que les sources de dissipation optique et mécanique dans ces résonateurs. Nous présentons également des expériences d'optoméca-nique à l'air libre et en cryostat à basse température, allant de la mesure du mouvement brownien et l'observation de rétroaction dynamique, jusqu'à des premières tentatives d'approche du régime quantique du mouvement. Enfin, nous présentons un développement nano-optomécanique complémentaire mené sur le matériau nitrure de silicium (SiN), aboutissant à la fabrication de résonateurs à mode de galerie sur puce à haut facteur de qualité. Après l'étude des instabilités optiques et de la dynamique d'auto-pulsation de ces résonateurs, nous présentons des premières signatures de couplage optomécanique dissipatif dans ces systèmes.

Mots-clefs: Optomécanique, mode de galerie, résonateur optique, mode de respiration, couplage evanescent, couplage critique, guide d'onde, optique guidée, photonique intégrée, haut facteur de qualité, pression de radiation, photoélasticité, GaAs, AlGaAs, SiN, nanofabrication, lithographie électronique, cryogénie, pertes optiques, auto-oscillation.

Abstract

This thesis work focuses on the design, fabrication and measurement of Gallium Arsenide (GaAs) nano-optomechanical disk resonators. These disks are both GHz frequency mechanical resonators, and high Q ($> 10^5$) optical whispering gallery mode resonators. By confining optical and mechanical energy on a sub-μm^3 volume, they enable extremely large optomechanical coupling strengths ($g_0 > 1$ MHz). We present the technological developments which enabled the integration of these resonators with optical coupling waveguides directly on a semiconductor chip, while maintaining state of the art performance. We discuss the different optomechanical coupling mechanisms (radiation pressure, photoelasticity) in GaAs disks, as well as the sources of optical and mechanical dissipation in these resonators. We present as well optomechanical experiments in air and in a cryostat at low temperature, which go from the measurement of Brownian motion and the observation of dynamical back-action, to the first attempts to approach the quantum regime of mechanical displacement. Finally, we present an additional nano-optomechanical development carried out on the silicon nitride (SiN) platform, which lead to the fabrication of high Q on-chip whispering gallery mode resonators. After the study of the optical instability and self-pulsing dynamics of these resonators, we present the first signatures of dissipative optomechanical coupling in these systems.

Keywords: Optomechanics, whispering gallery modes, optical resonator, radial breathing modes, evanescent coupling, critical coupling, waveguide, integrated photonics, high Q, Gallium Arsenide, GaAs, AlGaAs, silicon nitride, high stress, radiation pressure, photoelasticity, nanofabrication, e-beam lithography, cryogenics, optical losses, self-pulsing.

Remerciements

Je souhaite remercier tous ceux qui ont contribué à ce que cette thèse, effectuée au sein de l'équipe DON du Laboratoire Matériaux et Phénomènes Quantiques, se déroule dans les meilleures conditions.

Je tiens d'abord à remercier tous les membres de mon jury pour l'intért qu'ils ont porté à mon travail : un grand merci donc à Philippe Boucaud et Antoine Heidmann qui ont bien voulu prendre le temps de faire le travail de rapporteur, ainsi qu'à Sylvain Combrié, Aristide Lemaître, Eva Weig et au président du jury Bernard Jusserand.

Je voudrais bien sûr également remercier mes deux directeurs de thèse Ivan Favero et Giuseppe Leo. Ivan, j'ai beaucoup apprécié pouvoir travailler avec toi, et j'ai beaucoup profité de ta grande culture scientifique. Merci d'avoir été toujours aussi disponible, depuis le début de ma thèse jusqu'à ta relecture assidue du manuscrit ! Merci beaucoup à Giuseppe pour tes bons conseils ainsi que ton dynamisme et enthousiasme communicatifs. Merci aussi à Sara Ducci de l'équipe, dont le Master DQ(N) m'a donné envie de faire une thèse dans cette voie.

Je voudrais aussi remercier Pascale Senellart et Aristide Lemaître du Laboratoire de Photonique et de Nanostructures; Pascale pour son aide précieuse et son expertise sur la nano-fabrication de microdisques, et Aristide qui a toujours répondu à nos harcèlements pour toujours plus de wafers épitaxiés! Merci également à Cherif Belacel, avec qui j'ai travaillé au début de ma thèse.

Un grand merci encore à Eva Weig qui m'a gentiment accueilli dans son équipe à la LMÜ de Munich, et nous a fait profiter de sa grande expérience sur les nanoresonateurs en nitrure de silicium. Merci aussi à Sebastian Stapfner qui m'a montré tous les procédés de salle blanche et avec qui cela a toujours été un plaisir de travailler, à Munich et à Paris.

Un grand merci aussi à tous ceux avec qui j'ai travaillé au sein de l'équipe DON. Les optomécaniciens d'abord: Lu Ding, William Hease - qui reprend maintenant le flambeau avec un cryostat flambant neuf -, David Parrain - pour avoir su placer toujours plus haut la barre de la bogossité -, Dac-Trung Nguyen, Eduardo Gil Santos et Biswarup Guha. Merci aussi à tous les autres camarades du thésarium : Marc Savanier - à qui on ne la fait pas, sauf à Florence -, Alexandre Delga - pour son éclectisme invétéré -, Adeline Orieux, Alessio Andronico pour son aide précieuse pour les simulations numériques. Merci à Laëtitia, Filippo, Alberto, Fabien, Silvia, Andreas,

Contents

Contents

Contents

Glossary

AlGaAs Aluminum Gallium Arsenide.

BOE Buffered Oxyde Etch (7:1 NH_4F/HF).

BPM Beam Propagation Method.

CMT Coupled Mode Theory.

EIM Effective Index Method.

FBMS Fixed Beam Moving Stage.

FDTD Finite Difference Time Domain.

FEM Finite Element Method.

FSR Free Spectral Range.

FWHM Full Width at Half Maximum.

GaAs Gallium Arsenide.

HCl Hydrochloric acid.

HF Hydrofluoric Acid.

ICP-RIE Inductively Coupled Plasma Reactive-Ion Etching.

KOH Potassium Hydroxide.

LPCVD Low Pressure Chemical Vapor Deposition.

MBE Molecular Beam Epitaxy.

Glossary

MIBK Methyl IsoButyl Ketone.

MST Maxwell Stress Tensor.

NA numerical aperture.

PML Perfectly Matched Layer.

PMMA poly(methyl methacrylate).

PP-RIE Parallel Plate Reactive-Ion Etching.

Q Quality factor.

RBM Radial Breathing Mode.

RMS root mean square.

SEM Scanning Electron Microscope.

SiN Silicon Nitride.

SiO$_2$ Silicon dioxide.

TE Transverse Electric.

TED Thermoelastic Damping.

TEM Transmission Electron Microscope.

TM Transverse Magnetic.

TPA Two Photon Absorption.

WGM Whispering Gallery Mode.

Introduction

Brief history

The field of optomechanics deals with the interaction between light and a mechanical degree of freedom. This interaction is mediated via various types of forces, such as the *radiation pressure* force. Radiation pressure refers to the pressure exerted on any surface exposed to electromagnetic radiation. As far back as 1619, Kepler hypothesized that it was the *pressure* of light which was responsible for bending comets' tails away from the sun[1] [1] (see Figure 1, a). Radiation pressure was then theoretically predicted by Maxwell in the late 19th century and later experimentally verified by Lebedew [4] and Nichols and Hull [5] at the turn of the 20th century. In the 1960's Braginski et al. [6] noted that an "additional mechanical friction, ..., arises during mechanical vibrations of a body absorbing or reflecting electromagnetic radiation". An equivalent effect also occurs in a cavity, termed *dynamical back-action*, and can result in either adding or removing energy out of the mechanical mode, depending on the experimental parameters. Historically, the influence of radiation pressure has been much investigated in the context of gravitational wave detectors (such as LIGO or VIRGO, see Fig. 1 b), whose ultimate sensitivity is limited by quantum radiation pressure noise [7]. Further information can be found in the following review articles: [8, 9, 10].

Present status of experimental optomechanics

The reason one braces oneself for strong gusts of wind, or before stepping under a waterfall, but not before switching on the light, is because radiation pressure is generally very weak[2]. As a consequence, in order to feel the effects

---

[1]Radiation pressure is indeed responsible, along with solar winds, for pushing comets' tails (composed of dust particles and gas) away from the sun. The second mechanism, solar wind, consists of a stream of charged particles emitted by the sun.

[2]The radiation pressure due to sunlight striking the earth's surface is only ~ 4.5 μPa, assuming total light absorption and 1.3 kW·m^{-2} irradiance.

Figure 1: Three large scale systems sensitive to radiation pressure. (a) Comet's tail bending away from the sun. (b) VIRGO, a kilometer-sized Michelson interferometer located in Italy [2]. (c) NASA's NanoSail-D spacecraft (artist rendering) makes use of radiation pressure, in this case for space travel. Even though the acceleration provided by the solar radiation is feeble, it accrues over long periods of time, potentially allowing for fast and fuel-free space travel [3].

of radiation pressure, systems must be either extremely sensitive, very light, exposed to high light intensities, or a combination of the above. The past few years have witnessed a surge of interest in the field optomechanics, accompanied by the development of a huge variety of devices aiming to exploit optomechanical coupling. Figure 2 shows -a by no means comprehensive- overview of some of these different optomechanical coupling schemes.

Presentation of our devices

Here we provide a very brief presentation of the system we choose to study optomechanical effects: GaAs disk resonators [42, 43]. (See Figure 3 for a schematic). The GaAs disks described in this work are both *optical* and *mechanical* resonators. On the optical front, the optical energy is contained in *whispering gallery modes*[3] located on the periphery of the disk. The disks are very good optical resonators, and thus provide both large optical field enhancement and high sensitivity. Furthermore, with their extremely small size[4] and picogram mass, we see that GaAs disks meet all three of the previously mentioned criteria, and are therefore well suited to observe the effects of radiation pressure.

In the context of a collaboration with Eva Weig's team at the LMU in Munich, we also studied silicon nitride nanobeam resonators positioned in the evanescent field of a silicon nitride whispering gallery resonator (see section

---

[3]These are named in this fashion as the theoretical framework was initially developed by Rayleigh to describe traveling acoustic waves in the whispering gallery of St Paul's Cathedral in London [44].

[4]They are typically smaller than a red blood cell.
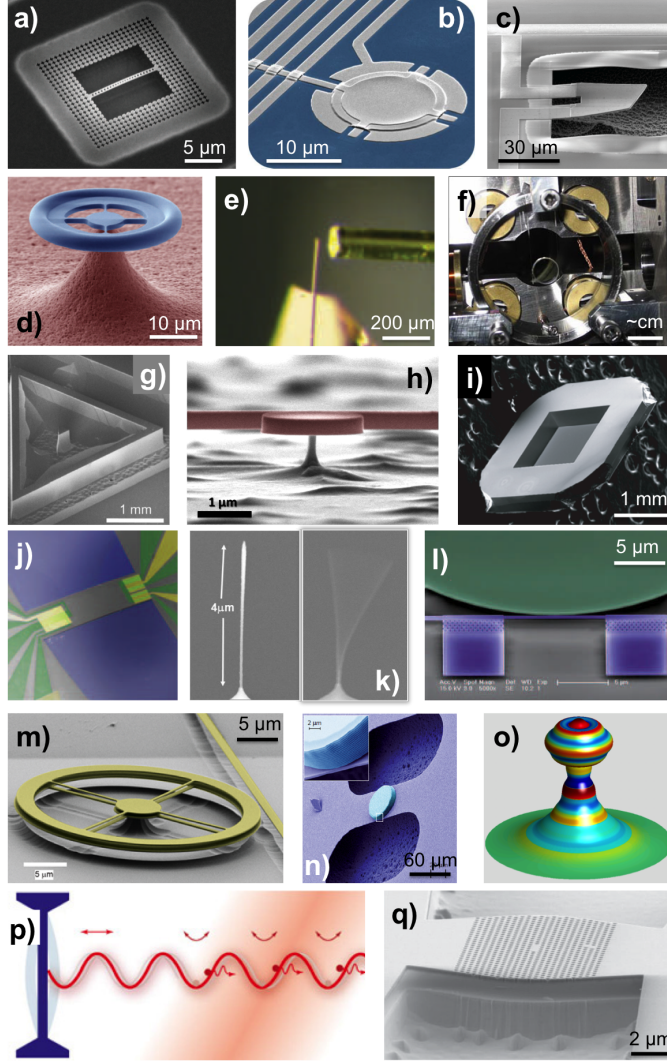
Figure 2: Non exhaustive overview of a few different optomechanical devices (arranged in no particular order). (a) Silicon optomechanical nanobeam resonator, Caltech [11]. (b) Aluminum drum membrane in superconducting microwave circuit, Boulder [12]. (c) Aluminum nitride mechanical resonator coupled to a superconducting Qubit, UCSB [13]. (d) Silica microtoroid resonator, EPFL, Caltech, U. of Queensland, . . . [14, 15, 16]. (e) Gold platted AFM cantilever, LMU Munich [17]. (f) Gram scale mirror, MIT [18]. (g) Suspended micro-pillar resonator, LKB [19]. (h) GaAs or Silicon WGM microdisk resonator, MPQ Paris, Yale, Rochester [20, 21, 22, 23]. (i) Suspended membrane resonator, Yale, Boulder, Copenhagen, . . . [24, 25, 26]. (j) GaAs electromechanical resonator, NTT [27, 28]. (k) Nanorod or carbon nanotube inside a fiber cavity, LMU [29, 30]. (l) Suspended waveguide nanoresonator, Yale [31]. (m) Double disk resonator, Cornell [32]. (n) Micro-mirror, U. of Vienna, LKB, LMU, . . . [33, 34, 35]. (o) Silica microspheres, Caltech, U. of Oregon, U. of Michigan [36, 37]. (p) Optomechanics with ultracold atoms, Berkeley, Uni. Basel [38, 39]. (q) 2D photonic crystal defect cavity, NTT, EPFL, LPN [40, 41].

3
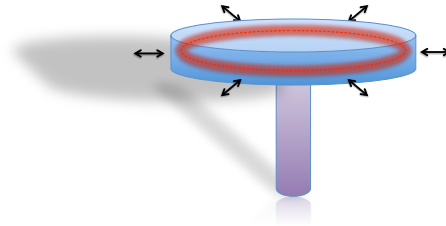
Figure 3: GaAs disk optomechanical resonator schematic. The GaAs disk (blue) is both an optical resonator supporting WGMs (red) and a mechanical resonator sustaining a variety of mechanical modes such as radial breathing modes of the entire disk (black arrows). The disk is isolated from the sample substrate (not shown here) on an AlGaAs pedestal (purple).

6.3).

The motivation of this thesis work was to develop a conceptual and experimental knowledge of the optical and mechanical properties of GaAs disk resonators, and study their potential for optomechanics. An important aspect of the work consisted in developing on-chip GaAs optomechanical disk resonators with integrated coupling waveguides. Such a chip can be used in vaccum at cryogenic temperatures and is part of our goal of optomechanically cooling a disk mechanical mode to the quantum ground state [13, 12, 11]. Beyond this aspect, these chips represent a multi-purpose platform with many potential applications such as mass and force sensing or biosensing.

The disk resonators are fabricated from the III-V semiconductor GaAs. While not as widely used as the n°1 semiconductor Silicon, GaAs is nonetheless a mature platform, with many uses ranging from high frequency electronics to LEDs and photovoltaics. Among its advantages are a high refractive index[5] which provides high optical confinement of the resonant optical modes (see section 1.2), allowing in turn for strong optomechanical coupling (section 3.8). GaAs is furthermore almost perfectly lattice-matched to the lower refractive index AlGaAs. This allows for the design of custom wafers with very precise thicknesses by Molecular Beam Epitaxy (MBE) for optically guiding structures. The MBE growth also provides a high purity crystal which is required for good optical and mechanical properties. Moreover, and perhaps most importantly, the GaAs/AlGaAs platform allows for the inclusion of quantum dots [45, 46] or quantum wells in the disk resonator, as well as the inclusion of electrically driven optically active elements directly on the chip. During this thesis we benefited from the expertise of Pascale Senellart and Aristide Lemaitre of the LPN on GaAs disks and GaAs/AlGaAs MBE.

---

[5]$n \geq 3.37$ in the near infrared.

As for the material SiN, it is chosen for its exceptional mechanical properties[6] (see section 2.8), but is also a platform of unique potential for integrated photonics and compatible with visible light applications.

Outline of the thesis

The first two chapters focus in turn on GaAs disk resonator's optical and mechanical properties. In chapter 1, the electromagnetic design of on-chip optomechanical resonators is presented. This includes a description of the optical coupling waveguide, of the disk's WGMs as well as of the coupled mode theory describing the waveguide to disk evanescent coupling. Next, in chapter 2, we provide an analytical description of both the out-of-plane and in-plane mechanical modes of the GaAs disks, and give some estimation of the magnitude of various mechanical loss sources. The mechanical properties of SiN beams under tensile stress are also briefly discussed. After this, in chapter 3, both a classical and a quantum formulation of optomechanics are presented. The magnitude of the different optical forces acting upon GaAs optomechanical disk resonators is calculated. Chapter 4 goes into much detail about the fabrication of on-chip GaAs and SiN nano-optomechanical resonators. Integrated optics experiments are then presented in chapter 5. A study of the origin of optical losses in GaAs disks and the observation and analysis of optical instabilities and self-pulsing in SiN WGM resonators are provided. Finally chapter 6 discusses our results on GaAs and SiN optomechanics.

---

[6]Under its high tensile stress form.

Chapter 1

Electromagnetic design of on-chip optomechanical resonators

In this chapter we discuss the design of an integrated on-chip nano-optomechanical device from an electromagnetic point of view. First we analytically describe the electromagnetic field inside the coupling waveguide and consider how the various experimental requirements influence the design specifications. Second we describe the electromagnetic field inside the WGM disk resonator. Finally we give a detailed description of the coupling between waveguide and disk resonator fields and offer ways to optimize it.

1.1   Waveguide design

1.1.1   Introduction

At the start of this doctoral work, the experimental technique used in our team to couple light in and out of a GaAs disk resonator relied on the use of pulled optical fiber tapers. (A *tapered* fiber is an optical fiber which has been thinned down in a localized section to allow for evanescent coupling). This very efficient technique has been used in a wide variety of experiments ranging from optics [47] to optomechanics [48] and sensing [49].

We also wished to develop a device where both the optomechanical resonator and the coupling waveguide would be monolithically integrated on a single chip of mm^3 dimensions. The use of an entirely on-chip sample facilitates among others operation in harsh environments (vacuum, cryogenics, liquids ...) and opens the potential for a variety of developments such as
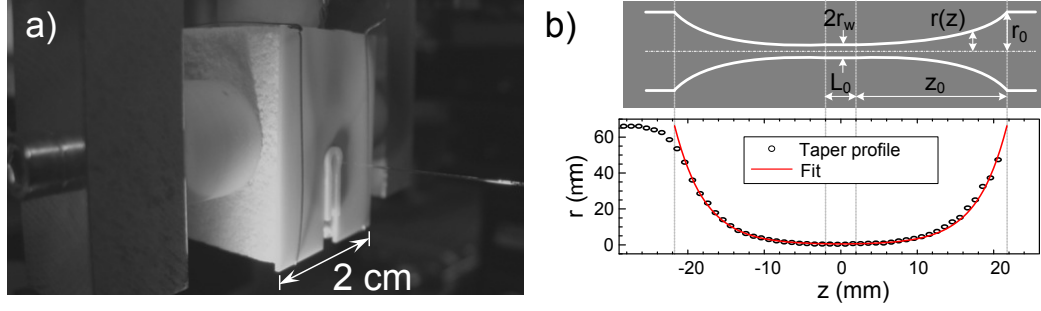
Figure 1.1: (a) Ceramic micro-oven used to heat the fiber up to its softening temperature. (b) Obtained fiber taper profile, with exponential fit (red line).

coupled resonator arrays [50], integration with active sources on the III-V platform, all integrated optomechanical sensing...

The optical fiber taper coupling scheme is very briefly described now before discussing the integrated coupling scheme, so as to be able to better highlight the similarities and differences between these two approaches. Both approaches (fiber coupling and integrated waveguide) are complementary and now used in parallel in the team.

Optical evanescent coupling via pulled fiber tapers

The fabrication procedes as follows [51]: a standard (SMF-28) optical fiber is stripped of its protective coating and placed inside a ceramic electric micro-heater (Fig. 1.1, a). The fiber is heated to its softening temperature while being gradually pulled on both ends by precision translation stages. The fiber's diameter is thus reduced from $\sim$130 μm to slightly under 1 μm over a length of several mm, following an exponential profile (Fig. 1.1, b). Finally the fiber can be looped to increase spatial selectivity [51] or kept straight when coupling to disk resonators raised above the sample surface on mesa-like structures (not shown here).

Coupling via a pulled fiber taper combines very high transmission powers with the possibility to adjust the coupling strength in real time' by varying the gap distance between fiber and disk resonator with piezo stages. Some drawbacks include a bulky setup, the fragility of the silica taper (whose transmission degrades in presence water molecules in the air for example [51]) and drifts in the coupling due to the taper's mechanical fluctuations.

Integrated coupling waveguide requirements

The fabrication of GaAs resonators with on-chip integrated waveguides should fulfill a number of requirements; the electromagnetic design proceeded with these in mind. They are listed below. Waveguides must:

- Have low optical transmission losses over their entire length.

- Provide efficient light in- and out- coupling.

- Offer broadband optical wavelength operation.

- Provide efficient and 'tunable' coupling between integrated waveguide and disk resonator.

Furthermore:

- The presence of the waveguide should not degrade the disk resonator's optical properties. Indeed the goal is to keep the very high ($\sim 5 \cdot 10^5$) optical quality factors that have been achieved on free standing GaAs disk resonators [20].

- The waveguide dimensions and fabrication process must be compatible with the desired disk resonator properties as this is a monolithic waveguide and disk design.

Designing on chip resonators with efficient waveguide to disk coupling requires a description of the electromagnetic field in the coupling waveguide (**1**), in the disk resonator (**2**) as well as an accurate estimate of the interaction between these two fields (**3**). These three points will be successively addressed in the following. Optimized designs are proposed and the limits of the coupled mode perturbation theory approach employed to describe the coupling are underlined. For clarity, Fig. 1.2 shows an illustration and schematic of a disk resonator next to its integrated coupling waveguide, along with the coordinate system and terminology used in the following.

1.1.2 Description of the Field in the coupling waveguide.

In this chapter, the electromagnetic field in the coupling waveguide is mostly described using the Effective Index Method (EIM) [52]. The EIM begins with the description of an electromagnetic wave propagating in a semi-infinite slab of material (see Figure 1.3). The effective optical properties of the guided
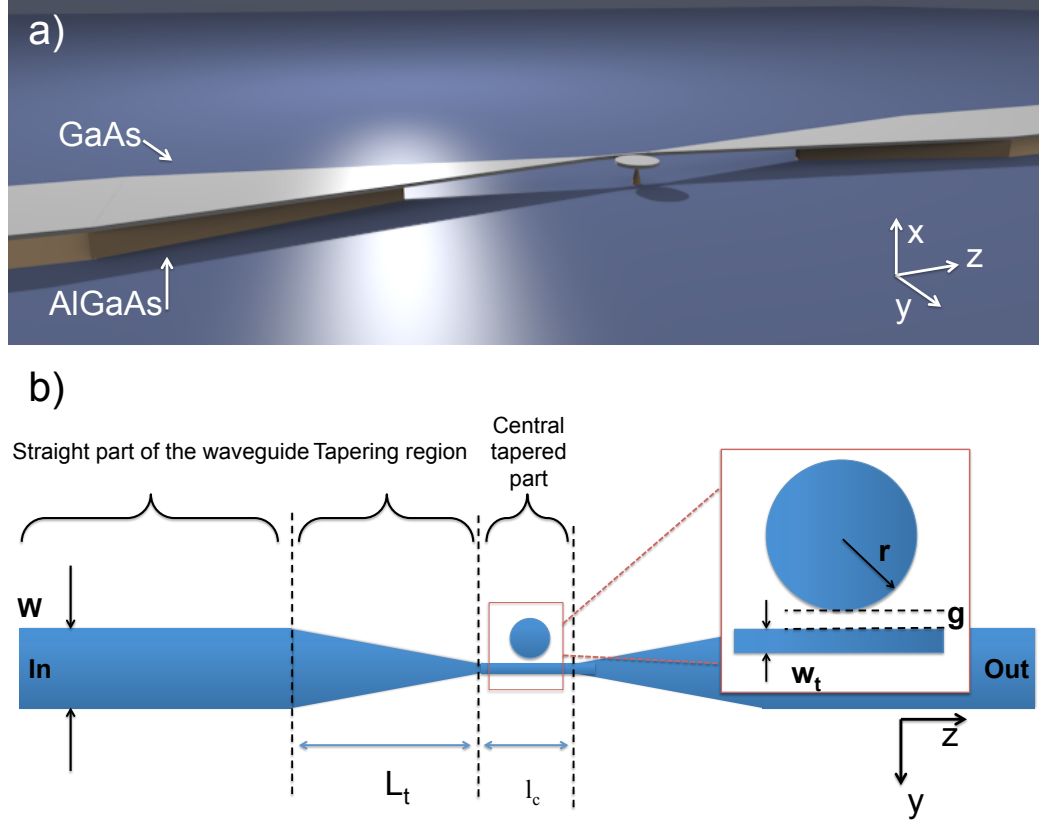
Figure 1.2: (a) Side-view illustration of a coupling waveguide positioned next to a disk resonator, along with the chosen coordinate system and the position of the distinct GaAs and AlGaAs layers. (b) Top-view schematic showing the disk and coupling waveguide. The straight portion of the waveguide of width W connects to the sample edge on one side and to a tapering region of length L_t on the other. This tapering region in turn connects to a central tapered region of length l_c and reduced width w_t in the vicinity of the disk resonator. The inset shows a blow up of the coupling region, with the disk resonator of radius r, positioned at a gap distance g from the taper of width w_t. Light is coupled into the waveguide by focusing a laser beam onto one extremity (In) and the outgoing light is collected at the other end (Out).

mode (e.g. its effective refractive index, see 1.1.2) induced by this one dimensional confinement are calculated. This procedure is then performed a second time, now using the previously obtained effective properties as the slab properties, so as to describe the two dimensional confinement by the waveguide lateral boundaries. The EIM approach thus decouples the in plane- from the out of plane confinement. Even though this approach is approximate it nonetheless offers pertinent design strategies.

Light propagation in a slab waveguide

We follow a standard description that can be found in many textbooks, see for example [53]. An electromagnetic wave propagating in a neutral medium is solution to the following wave equation derived from Maxwells equations.

$$\nabla^2 \mathbf{E}\left(\mathbf{r}, t\right) - \mu_0 \epsilon_0 n^2(\mathbf{r}) \frac{\partial^2}{\partial t^2} \mathbf{E}(\mathbf{r}, t) = 0 \tag{1.1}$$

We suppose the wave has an angular frequency ω. Therefore the electric field $\mathbf{E}$ is given by:

$$\mathbf{E}(\mathbf{r}, t) = \Re\left[\mathbf{E}(\mathbf{r}) e^{i\omega t}\right] \tag{1.2}$$

Combining equations (1.1) and (1.2) leads to (1.3):

$$\nabla^2 \mathbf{E}(\mathbf{r}) + k^2 n^2(\mathbf{r}) \mathbf{E}(\mathbf{r}) = 0 \tag{1.3}$$

Here k is the norm of the wave vector $\mathbf{k}$ and is given by k=ω/c , with ω the angular frequency and c the speed of light in vacuum. Finally we consider the case where the wave propagates along the z axis. The electric field $\mathbf{E}(r)$ can thus be written $\mathbf{E}(x, y) \, e^{-i\beta z}$ and equation (1.3) becomes:

$$\left(\frac{\partial^2}{\partial x^2} + \frac{\partial^2}{\partial y^2}\right) \mathbf{E}(x, y) + \left(k^2 n^2(\mathbf{r}) - \beta^2\right) \mathbf{E}(x, y) = 0 \tag{1.4}$$

The guiding slab is infinite along the y axis. We therefore assume the electric field does not vary along the y coordinate. In this case equation (1.4) takes the form of Eq.(1.5) in the slab and Eq.(1.6) in the upper and lower cladding layers:

$$\frac{\partial^2}{\partial x^2} E(x) + \left(k^2 n_1^2 - \beta^2\right) E(x) = 0 \ \text{ for } 0 \leq \text{x} \leq \text{h} \tag{1.5}$$

$$\frac{\partial^2}{\partial x^2} E(x) + \left(k^2 n_2^2 - \beta^2\right) E(x) = 0 \ \text{ for x} < 0 \text{ and x} > \text{h} \tag{1.6}$$

The guided modes in the slab waveguide correspond to the case kn$_2$ $< \beta <$ kn$_1$. When β respects this condition the electric field E(x) is sinusoidal inside the

1.1 Waveguide design
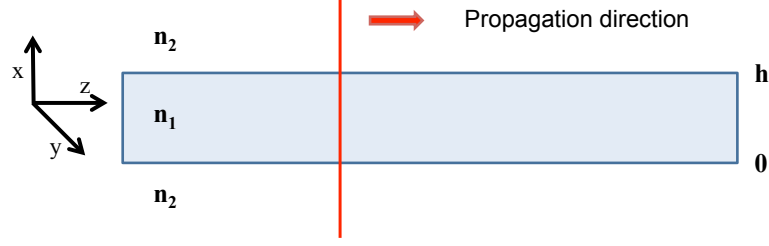
Figure 1.3: Schematic description of an electro-magnetic wave guided by a slab waveguide. The slab has an index of refraction n_1 and the upper and lower cladding layers have a refractive index n_2. The slab has a thickness h and is otherwise infinite along the y and z axes. We therefore refer to the yz plane as the slab plane. The electromagnetic wave propagates along the z direction.

slab and decays exponentially outside the slab. Note that this exponential decay of the field outside the slab is not associated with any power loss. In theory a guided mode in a slab waveguide can have the majority of its energy outside the waveguide and yet have zero propagation losses. In practice though strongly deconfining the mode will tendencially make it more sensitive to surface roughness and increase propagation losses.

In the following we consider two particular cases of the electric field polarization: The Transverse Electric (TE) polarization in which the electric field is oriented in parallel to the slab plane and the Transverse Magnetic (TM) polarization in which the magnetic field is oriented in parallel to the slab plane. In this thesis we will only consider TE modes of the waveguide (with the electric field parallel to y) which have lower optical transmission losses. The effect of the vertical (x) confinement on these modes is calculated with the TE formalism. On the contrary, when considering the lateral (y) confinement of these modes the electric field is orthogonal to the boundary. This lateral confinement is therefore treated with the TM formalism.

Transverse Electric (TE) waves

First we consider the in-plane polarization for the electric field (TE). The electric field takes the form $E(x,z) = \Re\left[E_y(x)e^{i(\omega t - \beta z)}\right]$. The fields E_y and B_z are parallel to the slab plane and therefore continuous at the slab interfaces in x=0 and x=h. Using $\nabla \times \mathbf{E} = -\frac{d\mathbf{B}}{dt}$ we get:

$$B_x(x) = -\frac{\beta}{\omega}E_y(x)$$
$$B_z(x) = \frac{i}{\omega}\frac{\partial}{\partial x}E_y(x)$$

(1.7)

Therefore the continuity conditions for E_y and B_z imply the electric field and its first derivative must be continuous at top and bottom interfaces (at x=h and x=0). Since we are interested in guided modes we write the following dependency for the electric field E_y:

$$E_y\left(x\right) = \begin{cases} De^{-\kappa(x-h)} \text{ for x} \geq \text{h} \\ B\cos(\alpha x) + C\sin(\alpha x) \text{ for } 0 <\text{x} <\text{h} \\ Ae^{\kappa x} \text{ for x} \leq 0 \end{cases} \qquad (1.8)$$

Solving the continuity conditions at the interfaces and having Eq. (1.8) verify Eqs. (1.5) and (1.6) leads to a specific set of conditions that must be respected by TE guided waves. These are summarized in (1.9).

$$\begin{aligned} \tan(\alpha d) &= \frac{2\kappa\alpha}{\alpha^2 - \kappa^2} \\ \beta^2 + \alpha^2 &= n_1^2 k^2 \\ \beta^2 - \alpha^2 &= n_2^2 k^2 \\ k &= \omega/c \end{aligned} \qquad (1.9)$$

This set of conditions leads to discrete solutions for the propagation constant β (and the associated parameters α and κ which respectively determine the oscillations of E_y inside the slab and the exponential decay of E_y outside the slab). If the slab is sufficiently thin only one guided mode is supported (the slab is called *single-mode*); thicker slabs support many modes. Even though there is no analytical solution to the set of conditions (1.9), propagation constants can be calculated to an arbitrary precision using a root finding routine. In Figure 1.4 we show the fundamental guided mode and the first higher order TE mode of a 320 nm thick GaAs slab waveguide, at a free-space wavelength λ=1.55 μm. In the following we will call the first higher order mode an order 2 mode to be consistent with the WGM notations in which an order 2 radial mode has two maxima of the squared electric field along the radial direction. This is in contrast to what is oftentimes used in the optical waveguide literature where the fundamental mode is numbered 0. Note that the fraction of the electric field outside the waveguide is much higher in the case of the order 2 mode than the fundamental mode. (Both modes are here normalized so that $\int_{-\infty}^{\infty} E_y^2 \, dx = 1$).

Effective refractive index and mode confinement

Here we introduce the effective refractive index (n_{eff}) of the guided mode, which is related to the phase velocity v_p of the propagating wave and the

1.1 Waveguide design
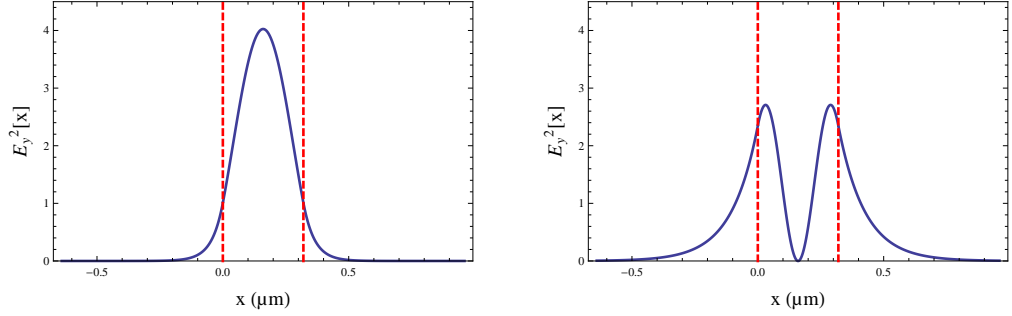
Figure 1.4: Left: Square of the electric field for the fundamental TE guided mode of a 320 nm thick GaAs slab (bulk refractive index n=3.374 at $\lambda = 1.55$ μm). The slab extends from x=0 to x=320 nm (dashed red lines) and is surrounded on either side by air (n=1). Right: first higher order TE guided mode of the same GaAs slab. The squared electric field has two maxima along the x direction. For the fundamental mode $\beta = 12.01$ and n_{eff}= 2.96 while for the order 2 mode $\beta = 6.27$ and n_{eff}=1.55.

speed of light in vacuum c by the relation $v_p = c/n_{\text{eff}}$. The effective refractive index n_{eff} is related to β by Eq. 1.10.

$$n_{\text{eff}} = \beta \frac{\lambda}{2\pi} \tag{1.10}$$

In Fig. 1.4 it is clear a large fraction of the order 2 guided mode's energy is no longer in the GaAs slab but in the surrounding air: this translates into the order 2 mode's n_{eff} being much smaller (closer to air's refractive index) than the n_{eff} of the fundamental mode, which is closer to the refractive index of bulk GaAs. Changing the slab thickness will also modify the confinement of a guided mode inside the slab and change this mode's n_{eff}. Figure 1.5 displays a systematic calculation of the effective refractive index of the fundamental TE guided mode as a function of the slab thickness as well as the fraction of the total electromagnetic energy which is inside the slab. For very thin slabs the energy is mostly outside the slab and n_{eff} is close to 1. For large slabs nearly 100 % of the energy is in the GaAs and n_{eff} is close to the index of bulk GaAs (3.374 at λ= 1.55 m). Here n_{eff} and the power fraction in the slab are monotonous functions of the slab thickness h. However, if we now look at the value of the electric field at the GaAs/Air interface ($E_y(0)=E_y(h)$) this no longer holds true. Figure 1.6 plots the value of the electric field square module $E_y^2(h)$ as a function of the slab thickness (we keep the normalization $\int_{-\infty}^{\infty} E_y^2\,dx = 1$). For thick slabs the electromagnetic (EM) energy is totally confined inside the GaAs and does not 'feel' the interface (Figure 1.7 right panel) . Likewise for very thin slabs : the electromagnetic energy is mostly in the surrounding air and the field at the GaAs/Air interface is small (Figure

14
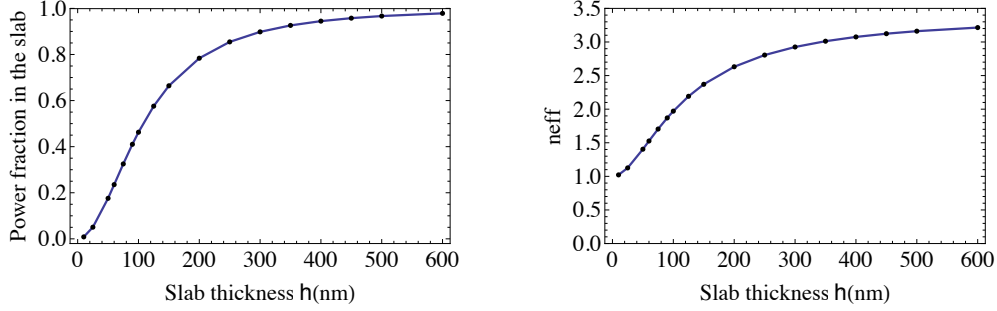
Figure 1.5: Left, fraction of the total electromagnetic power confined inside the GaAs slab for the fundamental TE guided mode at λ=1.55 μm as a function of the slab thickness h. Right, effective refractive index n_{eff} for the fundamental TE guided mode at λ=1.55 μm as a function of the slab thickness h.
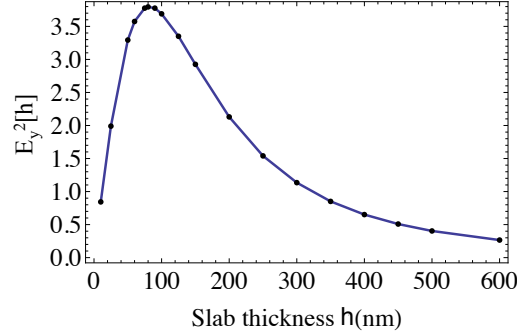
Figure 1.6: Electric field square module E_y^2(h) of the fundamental mode at the GaAs/air interface as a function of the slab thickness h. Field at the interface is maximal for h$\simeq$100 nm.

1.7 left panel). On the contrary for thicknesses around 100 nm the value of E_y^2 at the interface is strongly enhanced (Figure 1.7 center panel). If - as we believe is the case in our disk resonators - most optical losses occur at the interface (by scattering due to surface roughness or absorption for example) it is best to avoid strong fields at the interface and not make 100 nm thick disk resonators. As we will see in the following, the parameter β plays an important role in the coupling of the integrated waveguide to a disk resonator (see section 1.3.1).

Transverse Magnetic (TM) waves

The influence of the the lateral (y axis) confinement on the guided electric field $E_y(y)$ is then computed using the TM formalism described by Eq. 1.11, in a similar fashion to the TE section 1.1.2. Figure 1.8 shows the lateral
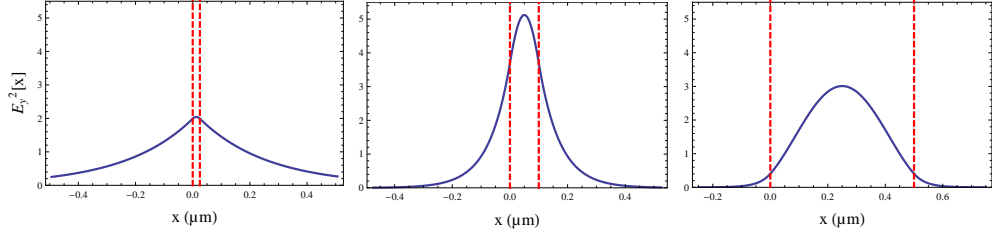
Figure 1.7: Plot of the transverse electric field squared (E_y^2) for the fundamental guided mode of a GaAs slab for three distinct slab thicknesses : from left to right h=25 nm, h=100 nm and h=500 nm.
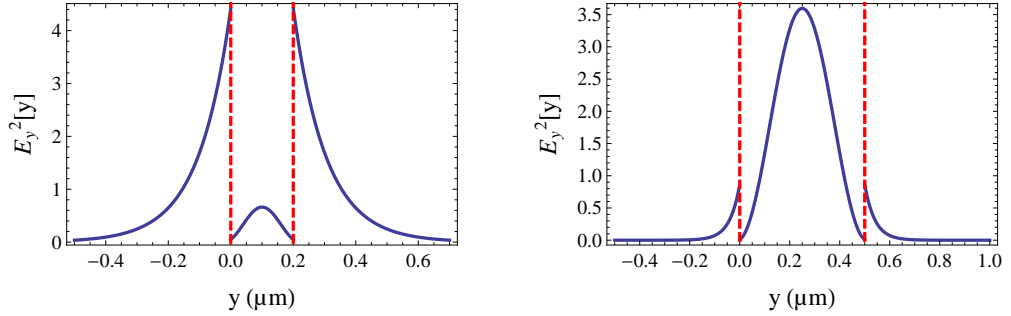
Figure 1.8: Square of the electric field for the TM case with λ=1.32 μm and width = 200 nm (left case) and 500 nm (right case). The position of the waveguide interface is materialized by the dashed red line. The plot window extends 500 nm on either side of the waveguide in both cases. Note how the field extends much more outside the waveguide in the case of the 200 nm wide taper, facilitating evanescent coupling to the disk.

profile of the electric field in the tapered section of the coupling waveguide, and the pronounced influence of the waveguide width on the field extension outside the waveguide.

$$
\begin{aligned}
\tan(\alpha d) &= \frac{2\,\epsilon_{12}\,\kappa\,\alpha}{\alpha^2 - \kappa^2} \\
\beta^2 + \alpha^2 &= n_1^2\,k^2 \\
\beta^2 - \alpha^2 &= n_2^2\,k^2 \\
\epsilon_{12} &= \left(\frac{n_1}{n_2}\right)^2
\end{aligned}
\tag{1.11}
$$
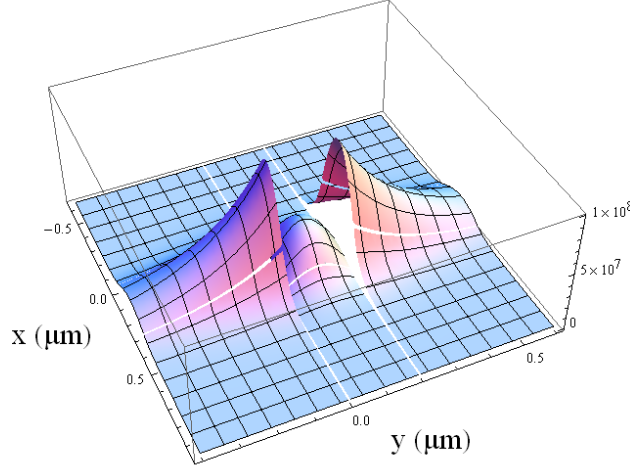
Figure 1.9: 3D Plot showing the TE fundamental guided mode's profile in the 320 nm thick and 200 nm wide suspended section of the coupling waveguide. This XY plane cross-section was calculated using the effective index method with λ=1.32 μm. The field extends much further in the direction of the disk resonator (**y** direction) than towards the substrate (**x** direction).

Waveguide mode profile

Finally the results of both vertical and lateral confinements described previously are combined to create the two dimensional cross section of the guided wave shown in Figure 1.9. This description will be used to estimate the coupling between the waveguide and the disk resonator in section 1.3. The following three sections (1.1.3, 1.1.4 and 1.1.5) deal with aspects of the guide that do not directly influence the coupling efficiency to the disk. Instead they aim to increase the overall optical transmission levels of the on-chip device. This is doubly important: first relatively large optical powers are required in order to reach certain optomechanical regimes such as dynamical backaction (see chapter 3). Second lost optical power can negatively impact the resonator's thermal environment in the case of cryogenic operation. With the improvements described in these sections very high total transmission efficiencies of $\sim$30% can be reached. (This percentage is defined as the ratio of power exiting the chip to power in the incident focused laser beam striking the waveguide facet).

1.1.3 Choice of straight waveguide width W

The on-chip GaAs resonator samples are notably developed for easy operation in vacuum and cryogenic environments. In this case light is coupled into

the integrated waveguides through cryostat windows using a long working distance microscope objective (see section C.0.1). Such an objective typically produces a focused spot size of $\varnothing$= 2 to 3 μm. A 3 μm waveguide width W (see Fig. 1.2) at the input/output facets was therefore initially chosen so as to roughly match this spot size. However this choice introduces large optical transmission losses which are not apparent in numerical simulations. Indeed, since the lateral underetch dimension (along y) is fixed by geometrical constraints coming from the disk diameter, a small width W of the straight part of the waveguide will translate into a strong optical field at the AlGaAs/air interface under the GaAs guiding layer (see arrows in Figure 1.10, a). This interface is quite rough due to the nature of the under-etching
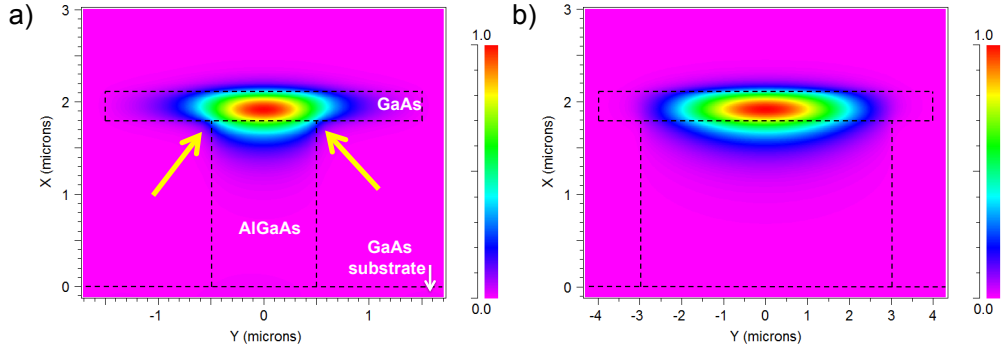
Figure 1.10: XY cross-section of the optical energy distribution for the fundamental guided mode of a 3 μm wide (a) and 8 μm wide (b) waveguide, both with a 1 μm under-etch of the AlGaAs sacrificial layer. The outline of the GaAs guiding layer, AlGaAs sacrificial layer and GaAs substrate are indicated by the superimposed dashed black lines. These simulations *do not* take roughness induced losses into account.

procedure (see fabrication chapter) and scatters the optical guided energy. Systematic experimental measurement of transmission levels as a function of waveguide width between 3 μm and 15 μm consistently show best transmission for waveguides 8 to 10 μm wide. For these widths the optical field is well shielded from the rough interface, as visible in Figure 1.10 b. This is the optimal width we adopted. Such a width makes this straight waveguide part TE multimode at our near infrared wavelengths - selection of the fundamental mode is obtained in experiments by central optical alignment of the injection spot.

1.1.4 Tapering of the coupling waveguide

Whereas the coupling waveguide is $\sim$8 μm wide in the input/output straight sections (1.1.3), it is only $\sim$200 nm wide in the disk vicinity to allow for
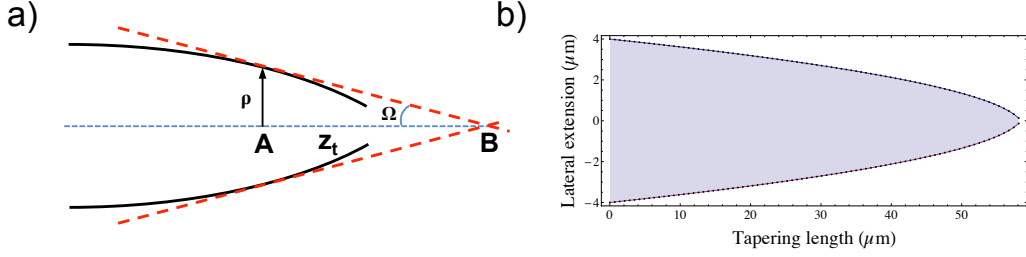
Figure 1.11: **Tapering of the coupling waveguide**. (a) Schematic illustrating the local tapering length scale z_t. At point A the waveguide has a half width ρ and the tangents to the tapering profile are represented by the dashed red lines. These lines meet at point B and define z_t as the length AB. The local tapering angle at point A is $\Omega \approx \rho/z_t$. (b) Calculated optimal adiabatic profile for a 320 nm thick GaAs waveguide with a wavelength λ used for the calculation of 1.3 μm. The tapering takes $\sim$60 μm.

evanescent coupling. The region over which the waveguide transitions between these two different widths is called the *tapering* region (see Fig. 1.2). This transition should be as short as possible to maintain good mechanical robustness while remaining gradual enough to introduce minimal optical loss to the fundamental guided mode[1].

The optimal tapering profile is calculated from the *adiabaticity criterion* described by Love et al. [54] which minimizes the optical power coupling from the fundamental mode to the second order guided mode. We verify that these analytical results are in good agreement with Beam Propagation Method (BPM) and Finite Difference Time Domain (FDTD) simulations. According to [54], power loss from the fundamental mode to the second order mode is minimized provided the local tapering length scale z_t (see Figure 1.11 (a) and Eq. 1.12) is larger than the local coupling length (beat length) between these two modes z_b (Eq. 1.13).

$$z_t \simeq \rho/\Omega \tag{1.12}$$

$$z_b = \frac{2\pi}{\beta_1 - \beta_2} \tag{1.13}$$

(Here β_1 and β_2 are the propagation constants of the fundamental and second order guided modes). Setting these two lengths z_t and z_b equal provides the adiabatic delineation criterion which indicates the maximum tapering angle

---

[1]When the tapering is too abrupt energy is coupled from the fundamental guided mode into higher order modes. These higher order modes are then filtered out by the taper if it is monomode (see section 1.1.6) resulting in power loss. Even if the taper supports these higher order modes, they are still undesirable as they do not couple ideally to the disk resonator WGMs (see section 1.3).
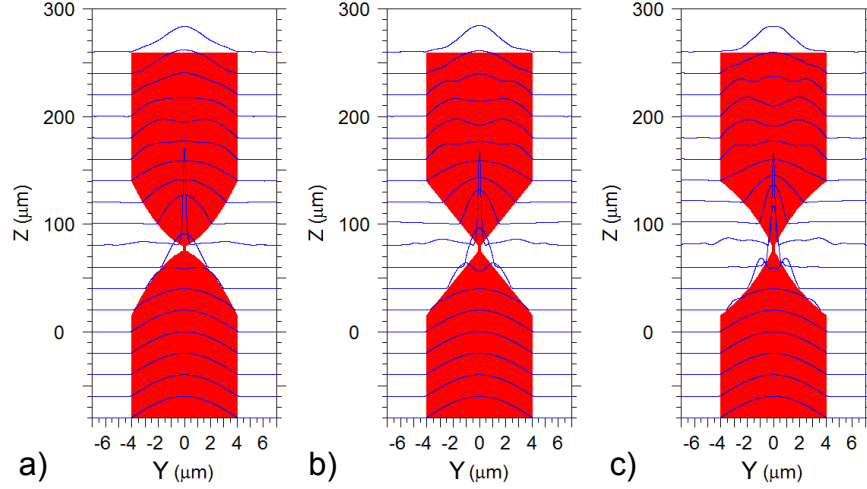
Figure 1.12: BPM comparison between the optical transmission of 3 different taper profiles: (a) calculated 'optimal' adiabatic (b) linear and (c) exponential. In red is the waveguide seen from the top, in blue the optical energy profile at different positions z along the guide. In all three cases λ=1.32 μm and the waveguide width is reduced from 8 μm to 200 nm over a 60 μm tapering length. The power transmission is 96% for (a), 91% for (b) and only 86.6% for the exponential profile (c). Evidence of coupling to the second order mode is well visible in (b) and (c) at Z$\simeq$40 μm.

Ω not to be exceeded at any point (Eq. 1.14).

$$\Omega = \frac{\rho\,(\beta_1 - \beta_2)}{2\pi} \tag{1.14}$$

From this criterion the optimal tapering profile is calculated in iterative fashion. Starting from the initial waveguide half width ρ_0 the values of β_1 and β_2 are calculated and provide Ω through Eq. 1.14. This allows to know ρ at the next point and so on until the complete profile has been obtained. Figure 1.11 (b) shows the calculated optimal tapering profile for a 8 μm wide GaAs waveguide reduced to a width of 200 nm. This profile is different from the typical exponential profile of pulled optical fiber tapers (see [47, 51] and Fig. 1.1 b) and presents a discontinuity in its first derivative at the end of the tapering. BPM simulations confirm the superiority of this optimal adiabatic profile over linear and exponential tapering profiles. The adiabatic profile transmits more power and is best at maintaining the fundamental mode spatial intensity distribution (see Figure 1.12). This approach also sheds light on the somewhat 'counter-intuitive' observation that while a high refractive index disk resonator can be 'bent' more (have a smaller radius of curvature) than a low refractive index resonator before incurring large bending losses (see section 1.2.1), a high refractive index waveguide must be 'bent' more

20

gradually than a low refractive index guide if no coupling to higher order modes (and transmission losses) are to occur. Indeed the spacing β_1-β_2 between the fundamental and second order guided modes is smaller in the case of a high refractive index guide, leading to a reduced tapering angle Ω (Eq. 1.14).

As a side note: the optical fiber tapers discussed in section 1.1.1 provide transmissions above 99% even with a 'sub-optimal' exponential tapering profile. This does not matter in that case due to the extremely reduced tapering angles involved (the fiber is tapered over tens of mm). Such extremely long tapering lengths are not compatible with integrated samples for reasons of device size, transmission losses and collapsing of the suspended portion (see fabrication chapter).

1.1.5   Power loss at the suspended section - choice of guiding layer thickness

In the vicinity of the disk resonator the tapered GaAs guiding layer is narrow enough ($\sim$200 nm) for the AlGaAs sacrificial layer below it to be completely under-etched in our standard fabrication, leaving the waveguide suspended. At this point, the majority of the guided optical energy in the AlGaAs will be lost. Indeed unlike for the horizontal tapering discussed previously (1.1.4) the fabrication process precludes a vertical tapering of the guide. The aim is therefore to confine most of the energy in the top GaAs guiding layer in order to avoid these 'vertical' transition losses as the optical wave enters the tapered region. Figure 1.13 shows an initial waveguide design (left) using a 200 nm thickness for the top guiding GaAs layer [20, 55, 21], as well as an optimized design which offers far superior transmission (right). The chosen 320 nm thickness for the GaAs guiding layer constitutes a good compromise between good optical transmission of the guide and optimized disk resonator thickness. A failed approach we attempted to solve this 'vertical' power loss problem at the suspended transition of the guide consisted in trying to 'force' the energy up into the GaAs guiding layer. This was done by working with a narrower waveguide which was laterally almost completely underetched so as to rest over its entire length upon a couple hundred nm wide AlGaAs 'rail', effectively confining the energy in the GaAs by air cladding. This technique failed for two reasons: first the optical energy was not well shielded from the rough AlGaAs surface (as discussed in section 1.1.3). Second, - and unsurprisingly in retrospect - waveguides supported over mm lengths on sub-micron wide rails proved to be incredibly fragile.

21
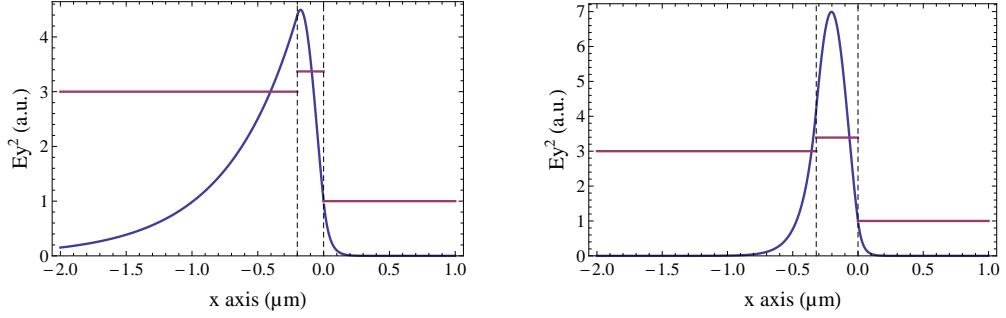
Figure 1.13: Comparison between the energy distribution (solid blue line) in the case of a 200 nm thick GaAs layer upon an AlGaAs layer operating at λ=1550 nm (left), and a modified waveguide design with a 320 nm thick GaAs layer operating at λ=1320 nm (right). The position of the GaAs guiding layer is materialized by the dashed black lines and each layer's bulk refractive index by the horizontal purple lines. In the first case the fraction of the energy in the GaAs guiding layer is only 21 % while in the second case it is slightly above 77 %. Note also how the field extends further into the AlGaAs in the left case. This gives rise to power loss into the substrate. (In both cases the top confinement is provided by air).

1.1.6 Single mode behavior of the tapered waveguide

The wide portions of the coupling waveguide support many guided modes. The tapered suspended section on the other hand can be either multimode or single-mode depending on its width. The switch between these two regimes occurs for a width w_t given by Eq. 1.15 [53].

$$w_t \simeq \frac{\lambda}{2\sqrt{n_{\text{eff}}^2 - n_{\text{cladding}}^2}} \qquad (1.15)$$

(For a 320 nm thick GaAs guiding layer with n_{eff}=3.06 at λ=1.32 μm cladded by air $w_t \simeq$225 nm). There is no need for the tapered waveguide to be single mode to reach high coupling efficiencies to the disk[56]. However device operation is more straightforward with a single mode taper. Indeed different guided modes of the waveguide will be excited by the focused laser beam depending on the sample's tilt and positioning and these modes do not couple identically to a given WGM. With a single mode taper all higher order modes of the guide are filtered out. Therefore maximizing the output power from the guide in an experiment automatically optimizes light injection into the fundamental guided mode for which the coupling to the disk is optimized in our design. On the contrary, with a multimode taper different powers can be dropped in the resonator for identical output powers, depending on the injection parameters. Furthermore, the use of a narrow single mode coupling
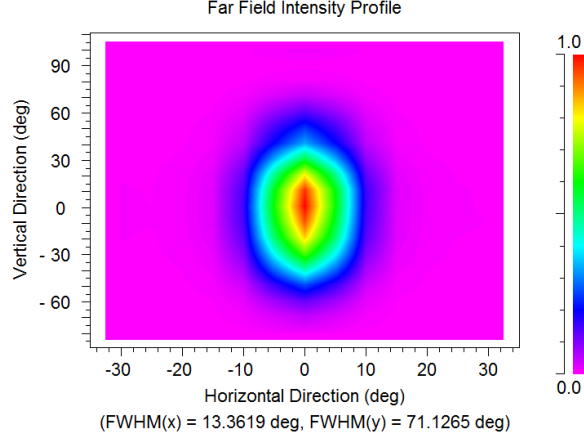
Figure 1.14: Far field intensity profile of the light exiting the waveguide at the cleaved output facet. Because of the elliptic guided mode shape visible in Fig. 1.10 b, the output divergence is larger along the vertical (x) direction than the horizontal (y) direction. For more see section C.0.1.

waveguide tends to bring about a lesser degradation the disk resonator's optical properties (see section 1.3.1).

1.1.7 Light injection and collection

We choose to inject light into the waveguide (and collect outgoing light) via the waveguide's cleaved input and output facets[2]. Such an approach has two main advantages over using a grating coupler [57, 58] scheme: first this allows for broadband operation, as the input laser wavelength can be tuned over several hundred nanometers while maintaining good coupling efficiency. (Grating couplers typically only provide efficient coupling over a wavelength range of a few tens of nanometers). Second our choice allows in principle for greater overall optical transmission efficiency. In our current design however, light exiting the waveguide has a large divergence along the vertical (x) direction (see Fig. 1.14). This can be problematic when using the sample in the cryostat, as discussed in section C.0.1. The output divergence can be reduced by terminating the waveguide extremities with an inverse taper [59, 60, 61]. This would have the added advantage of removing the Fabry-Perot fringes of the waveguide in the optical transmission spectra (see 5.2).

---

[2]See Fig. 1.2, or Fig. 4.22 for the Scanning Electron Microscope (SEM) picture of a cleaved waveguide facet in a fabricated device.

1.2 Description of the whispering gallery modes of the disk resonator

1.2.1 Whispering gallery mode properties

Classification

This section provides a very rapid overview of WGM properties and explains the terminology used in the following sections. Much more detailed information is available, among others, in the PhD theses [62] & [52], the review articles [63] & [64] and appendix A.0.1.

Optical WGMs are resonant modes of circular shaped dielectric cavities in which light is confined by total internal reflection at the curved outer boundary. The confinement only gives rises to resonant modes provided the confined electromagnetic wave closes upon itself in phase after a round trip, allowing the intensity to build up due to constructive interference. This resonance condition means the optical path length should be an integer times the free space wavelength λ (Eq. 1.16):

$$2\pi\, n_{\text{eff}}\, r \simeq m\, \lambda \qquad (1.16)$$

Here n_{eff} and r are respectively the disk's effective refractive index (see 1.1.2) and radius while the integer m is the WGM's *azimuthal* number and appears in the $e^{im\theta}$ dependency of the electric field. Solving Maxwell's equations with the resonators boundary conditions (see appendix A.0.1) can provide multiple solutions with identical azimuthal number m. These different solutions are labeled by the integer p which is the WGM's *radial* number and corresponds to the number of maxima in the electric field along the radial direction. Figure 1.15 offers a clearer visual depiction of this classification. For a p=1 mode, the optical energy is localized close to the disk's circular boundary, such that the geometric optics picture of a photon bouncing at total internal reflection angles becomes valid.

Quality factor and loss sources

Optical confinement inside WGM resonators is not perfect : the stored electromagnetic energy W is eventually dissipated (via various loss channels) at a rate given by $W(t) = W_0\, e^{-\gamma_{\text{tot}} t}$. Here γ_{tot} corresponds to the effective decay rate of the energy stored in the WGM and is equal to the sum of the decay rates γ_i through each individual loss channel. To each decay rate γ_i can be associated a related quality factor Q_i through $Q_i = \omega_0/\gamma_i$, where ω_0 is the optical angular frequency of the considered WGM (Eq. 1.17). The Quality
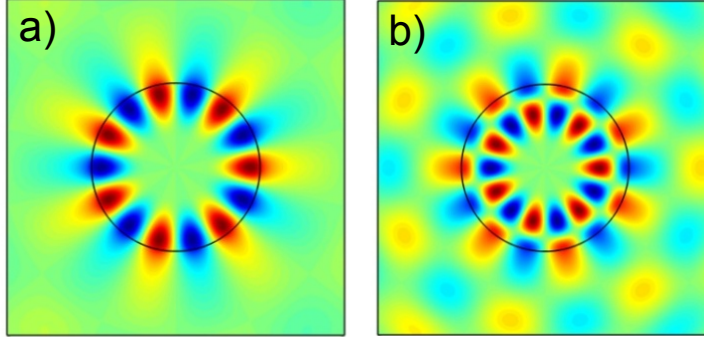
Figure 1.15: Example of WGMs sustained by a dielectric disk illustrating the WGM classification. (a) A WGM with m = 7 and p = 1. (b) WGM with m = 7 and p = 2. The black line represents the disk boundary. (Plotted in (a) and (b) is the out of plane magnetic field H_x).

factor (Q) thus indicates the degree of temporal confinement of energy inside the resonator.

$$\gamma_{\text{tot}} = \sum_i \gamma_i = \sum_i \frac{\omega_0}{Q_i} \qquad (1.17)$$

We have identified five main loss mechanisms. First due to the disk's finite radius of curvature some amount of energy can always leak out of the resonator. While these *bending losses* (or radiative losses - identified by a *rad* subscript) constitute a fundamentally inescapable lower bound on energy dissipation, they can be kept extremely low provided the resonator's dimensions and refractive index are large enough. For instance radiation losses for λ=600 nm light confined in a 50 μm radius water droplet only limit the Q_{rad} to a gigantic 10^{73} [63]. Even in our case with smaller $\varnothing$=2 μm disks operating at a larger wavelength of 1.3 μm the bending loss Q_{rad} is still $\geq 10^7$. This can be different in the case of higher order p WGMs, see section 1.2.1.

Second nanometer sized roughness on the disk sidewalls can scatter light out of the WGM into radiative modes or different modes of the resonator. Since this *surface scattering* (also called Rayleigh scattering -*ss* subscript) depends on the amount of roughness on finished devices, particular care must be taken to ensure as smooth as possible resonator sidewalls (see fabrication chapter). Since γ_{ss} is proportional to the energy density at the surface and hence 'sensing' the roughness, the smaller the disk the larger the effect will be (see section 1.2.2).

Third the GaAs crystal forming the disk resonator has a non-zero density of defects resulting in some optical *bulk absorption* (subscript *bulk*).

1.2 Description of the whispering gallery modes of the disk resonator

Fourth *surface absorption* (subscript *sa*) can occur in the native oxide at the interface between GaAs and air. The typically 2 nm native oxide layer (see fabrication chapter) is known to posses mid-gap electronic states which are responsible for optical absorption [65]. These losses will also be proportionally more pronounced for small diameter disks that possess a larger energy density at the surface (see section 1.2.2).

Finally fifth the presence of the coupling waveguide in the vicinity of the disk results in external *coupling losses* (subscript *ext*), which are necessary for efficient energy exchange between disk and waveguide. Thus one can write $\gamma_{\text{tot}} = \gamma_{\text{rad}} + \gamma_{\text{ss}} + \gamma_{\text{bulk}} + \gamma_{\text{sa}} + \gamma_{\text{ext}}$ and the effective quality factor Q_{tot} can be expressed as a function of all individual quality factors by Eq. 1.18.

$$1/Q_{\text{tot}} = \underbrace{1/Q_{\text{rad}} + 1/Q_{\text{ss}} + 1/Q_{\text{bulk}} + 1/Q_{\text{sa}}}_{1/Q_{\text{int}}} + \underbrace{1/Q_{\text{ext}}}_{1/Q_{\text{ext}}} \qquad (1.18)$$

Here we distinguished the *intrinsic* quality factor Q_{int} which relates to the physical properties of the resonator itself, from the *extrinsic* quality factor Q_{ext} which describes the coupling of the resonator to its outside environment. The quality factor measured through an optical experiment is therefore not Q_{int} but Q_{tot} (also called Q_{loaded}), as it includes the losses due to the coupling probe. Optimal energy transfer from waveguide to resonator occurs when the two quality factors Q_{ext} and Q_{int} are identical (see section 1.3.1).

Finesse and field enhancement

The finesse $\mathcal{F}$ of a resonance is proportional to the average number of round trips made by a photon confined in the resonator before exiting. In the case of a WGM resonance, the finesse can be simply expressed as:

$$\mathcal{F} = Q/m \qquad (1.19)$$

with m the WGM azimuthal number. The finesse is an important parameter as it is linked to an enhancement in the power circulating in the resonator P_{circ} with respect to the power given to the resonator by the waveguide (or *dropped* power, P_{dropped}) by the relation:

$$\frac{P_{\text{circ}}}{P_{\text{dropped}}} = \frac{\mathcal{F}}{2\pi} \qquad (1.20)$$

As indicated by Eq. 1.19, in the case of two WGM resonators of similar Q but different radius, the smallest resonator will support modes of larger finesse and therefore larger field enhancement. This enhancement can be

quite substantial. For instance for a $\varnothing=2$ μm GaAs disk resonator supporting a WGM with Q=10^5 and m=10, $\mathcal{F}$ is 10 000 and the circulating power enhancement 1600. This means the circulating power in the disk is 16 mW for dropped powers as low as 10μW and reaches 0.1 W for 62 μW dropped power. Large circulating powers are desirable for strong optomechanical actuation (section 3.2) and non linear optics [66], but can also give rise to significant Two Photon Absorption (TPA) (see section 5.3.2) and thermal effects. The latter are especially pronounced with very narrow AlGaAs pedestals (see chapters 2 and 4).

Higher order radial modes

A few words about WGMs with higher radial number p. For these modes the 'center of mass' of the energy distribution is pushed towards the inside of the disk (see Fig. 1.15, b) while the field intensity at the resonator boundary at $r = R$ becomes larger (not shown here). These two features generally negatively impact the WGM's Q_{int}. First since the field is pushed inside, the effective bending radius becomes quite small and these modes can incur large bending losses : for instance for a $\varnothing=7\mu$m disk, Q_{rad} is typically below 10^4 for WGMs with p$\geq$5 around $\lambda = 1.5$ μm. Second since the field is no longer confined to the disk's periphery, it can sense the rough AlGaAs pedestal below, bringing on substantial additional losses (as described in the case of the waveguide in section 1.1.3). Finally the larger field at the interface makes these modes generally more lossy due to heightened interaction with the sidewall imperfections (as discussed in section 1.2.2). For all these reasons we opt in our design to optimize coupling of the waveguide to the p=1 WGMs.

Simulating WGMs

In our group WGMs are simulated either with a homemade EIM approach [52], or using a 2D axisymmetric Finite Element Method (FEM) commercial approach (Comsol). The EIM technique gives satisfactory results for the determination of resonance wavelengths, but offers a poor estimate of the radiation loss Q_{rad} . The FEM approach on the other hand provides the most accurate estimates of resonance wavelengths and Q_{rad} but is also more time consuming and less convenient to automatize. It combines a weak formulation code [67] with Perfectly Matched Layer (PML) support (to mimic an infinite space around the resonator) [68]. Much more detailed information is available in (*cite book chapter*). An example of a WGM computed with this method is given in Figure 1.16. The resonance frequencies and optical Qs obtained with this method are in good agreement with results from a

1.2 Description of the whispering gallery modes of the disk resonator
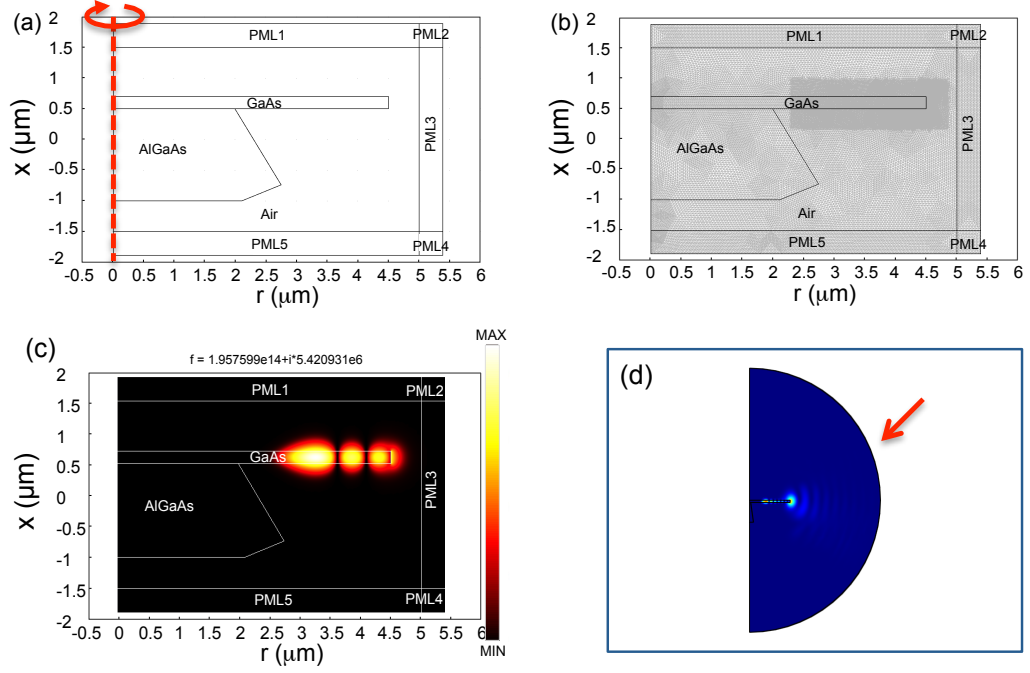
Figure 1.16: 2D axi-symmetric FEM modeling of a GaAs disk resonator WGM. The three figures show (a): the computational domain with the surrounding perfectly matched layers, (b) : the meshing of the various regions and (c): the radial intensity profile of a solved WGM (TE, p=3, m=33, $Q_{rad} \simeq 2 \cdot 10^7$). (d) Estimating an upper and lower bound for Q_{rad}. Setting the outer boundary conditions (red arrow) to perfect electric wall allows for calculating an lower bound for Q_{rad}, while setting the outer boundary conditions to impedance matching provides an upper bound for Q_{rad} [67]. In all four cases only an axi-symmetric cross section is shown. The full disk is obtained by revolving around the x axis (red dashed line in (a)).

homemade FDFD code developed in the team by A. Andronico [52] and with upper- and lower bound Q_{rad} estimates obtained by the method described in [67] (see Fig. 1.16 d).

1.2.2 Specific challenges associated with the realization of small diameter resonators

The very small 1μm radius disk resonators in this work have been fabricated with two goals in mind: obtain high frequency mechanical resonances and provide extremely large optomechanical coupling. Working with such small radii is particularly challenging however, as this makes the WGMs dramatically more sensitive to the disk boundary [69]. Figure 1.17 (a) shows how the profile of a p=1 TE WGM is transformed as the disk radius is reduced

a)

b)
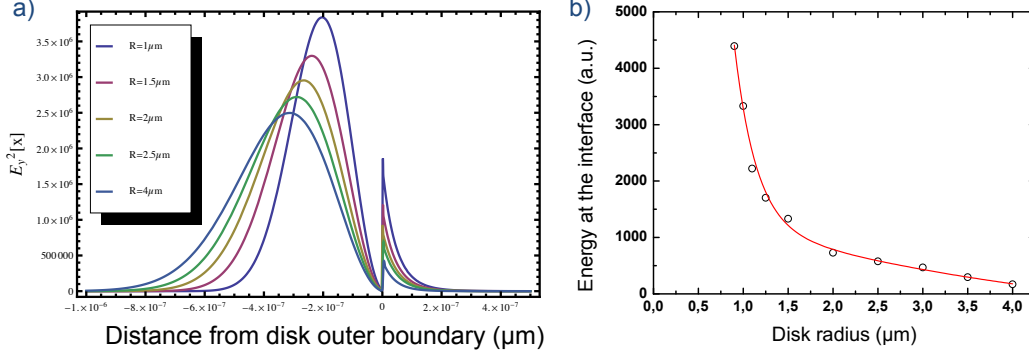
Figure 1.17: Influence of the disk radius on the WGM energy distribution. a) FEM computations showing the WGM field profile with respect to the disk outer boundary for 5 different disk radii. For easier comparison the disk outer boundary position is set to 0 in all cases. (b) WGM energy density at the disk boundary as a function of disk radius. The red line serving as a guide to the eye is a fit of the form $a_0 \, e^{-\alpha_0 \, r} + b_0 \, e^{-\alpha_0 \, r}$.

from 4 μm to 1 μm. The optical field's 'center of mass' is pushed towards the outer boundary and the value of the field at the vertical interface greatly increases.

Figure 1.17 (b) provides a more quantitative illustration of the latter effect. Here the value of $H_x^2(r)$ (which is proportional to the energy density at the disk's outer boundary) is plotted versus the resonator's radius r. Individual data points come from FEM simulations of individual p=1 WGMs with resonant wavelength close to λ=1.4 μm. The small jitter in the data points comes from the fact that all WGMs don't have exactly the same resonance frequency. The energy at the interface gradually increases as the disk's radius is reduced from 4 to 1.5 μm, then grows abruptly beyond that point as the disk's radius is further reduced from 1.5 to 0.9 μm.

Note how the energy density at the boundary is ∼**20 times** larger for r=1 μm than r=4 μm, which makes these devices that much more sensitive to sidewall roughness coming from the fabrication (see fabrication chapter) and to surface state absorption (see absorption section).

1.3 Waveguide to disk coupling

Now the guided modes of the waveguide and the disk are described, remains the critical aspect of actually being able to efficiently couple optical energy from one to another, *without degrading* the disk resonator's properties. A correct understanding of the coupling is crucial in the case of monolithic in-

tegrated samples as, unlike with the fiber taper coupling scheme ([20, 55], section 1.1.1) the coupling strength cannot be modified after fabrication simply by varying the fiber taper position.

1.3.1 Coupled mode theory

Principles

Coupled Mode Theory (CMT) is a formalism developed to describe the interaction between the modes of one or many waveguiding structures. To represent the field of a compound structure, the eigenmodes of each individual waveguiding element are first calculated in isolation. The field of the compound structure is then treated as a linear combination of these individual eigenmodes, which are perturbed by the presence of the other modes. This perturbation leads to coupling and power exchange between the guided modes [70, 71]. CMT is for instance used in nonlinear optics to describe energy transfer between different modes or different waveguides [72]. In the case of a disk coupled to a waveguide this approach therefore relies upon the assumption that the disk's WGMs are not too strongly modified by the presence of waveguide. We will see that CMT can provide valuable insight into the coupling mechanism and best design parameters as long as the waveguide dimensions are small enough compared to those of the disk.

To describe the coupling of the GaAs disk resonator to its coupling waveguide we follow the approach proposed by Haus [73, 74]. Figure 1.18 illustrates the relevant parameters used in the CMT description. s_+ and s_- are respectively the amplitudes of the input and output waves in the coupling waveguide, normalized so that their squared magnitudes are equal to the power in the waveguide mode. $a(t)$ is the cavity field amplitude, normalized so that $|a(t)|^2$ is the stored cavity energy.

Using energy conservation arguments the time dependent amplitudes of the resonator mode $a(t)$ and waveguide mode at output s_- can be expressed as (Eq 1.21) [73]:

$$
\begin{aligned}
\frac{da(t)}{dt} &= -i\omega_0\, a(t) + \left(\frac{\gamma_{\text{int}}}{2} + \frac{\gamma_{\text{ext}}}{2}\right) a(t) + \kappa s_+ \\
s_- &= s_+ - \kappa^*\, a(t)
\end{aligned}
\tag{1.21}
$$

with κ the coupling term between resonator and waveguide. If the input source s_+ has a $e^{i\omega t}$ time dependence, then the steady state WGM and waveg-
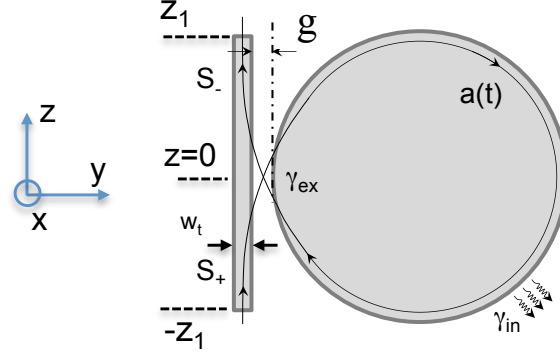
Figure 1.18: Schematic of a disk resonator and coupling waveguide showing the parameters used for the coupled mode theory description.

uide output amplitudes are given by Eq. 1.22:

$$a = \frac{i\sqrt{\gamma_{\text{ext}}}}{-i\Delta\omega + \left(\dfrac{\gamma_{\text{int}}}{2} + \dfrac{\gamma_{\text{ext}}}{2}\right)} s_+ \ , \ \ s_- = \frac{-i\Delta\omega + \left(\dfrac{\gamma_{\text{int}}}{2} - \dfrac{\gamma_{\text{ext}}}{2}\right)}{-i\Delta\omega + \left(\dfrac{\gamma_{\text{int}}}{2} + \dfrac{\gamma_{\text{ext}}}{2}\right)} s_+ \quad (1.22)$$

with $\Delta\omega$ the detuning from resonance equal to ω (the input wave angular frequency) minus the WGM resonance frequency ω_0. The intracavity stored energy divided by the input power is given by:

$$\frac{|a|^2}{|s_+|^2} = \frac{\gamma_{\text{ext}}}{\Delta\omega^2 + \left(\dfrac{\gamma_{\text{int}}}{2} + \dfrac{\gamma_{\text{ext}}}{2}\right)^2} \quad (1.23)$$

and the normalized transmission reads:

$$\frac{|s_-|^2}{|s_+|^2} = \frac{\Delta\omega^2 + \left(\dfrac{\gamma_{\text{int}}}{2} - \dfrac{\gamma_{\text{ext}}}{2}\right)^2}{\Delta\omega^2 + \left(\dfrac{\gamma_{\text{int}}}{2} + \dfrac{\gamma_{\text{ext}}}{2}\right)^2} \quad (1.24)$$

Equation 1.24 provides two important characteristics of the WGM resonance, the on resonance ($\Delta\omega = 0$) transmission T_{on} as well as the resonance Full Width at Half Maximum (FWHM) $\delta\omega$. These are written in Eqs. 1.25 and 1.26 and are simply expressed as a function of the parameter $K = \gamma_{\text{ext}}/\gamma_{\text{int}}$ which represents the relative strength of the coupling losses to the intrinsic losses of the WGM.

$$T_{\text{on}} = \left(\frac{1 - \gamma_{\text{ext}}/\gamma_{\text{int}}}{1 + \gamma_{\text{ext}}/\gamma_{\text{int}}}\right)^2 = \left(\frac{1 - K}{1 + K}\right)^2 \quad (1.25)$$

$$\delta\omega = \gamma_{\text{int}} + \gamma_{\text{ext}} = \gamma_{\text{int}}(1 + K) \tag{1.26}$$

This defines three distinct coupling regimes depending on the value taken by the parameter K which are commented in the following.

Under-, over- and critically coupled regime

- $K < 1$: *under-coupled* regime. The coupling losses are smaller than the intrinsic losses and power injection into the disk is sub-optimal. The resonance transmission contrast (equal to 1-T_{on}) is less than 1, and the measured Q_{loaded} lies between Q_{int} and $Q_{int}/2$.

- As the coupling strength increases the *critically coupled* regime is reached for K=1. At resonance power loss in the resonator equals the the waveguide input power, hence the output power drops to zero. The measured Q_{loaded} is equal to 1/2 Q_{int}. Stored energy in the resonator is maximal (Eq. 1.23).

- Further increasing the coupling ($K > 1$), the resonance enter the *over-coupled* regime. The resonator does not dissipate the input power fast enough and the on-resonance transmission increases anew. Due to the increased coupling losses the resonance's FWHM becomes very large.

Figure 1.19 plots the appearance of a WGM resonance in these three regimes. For optomechanics working at or near the critical coupling point is the best operating regime. Indeed the number of photons in the cavity at resonance is thus maximized, enhancing optomechanical coupling. The over-coupled regime is often not desirable on account of both low contrast and low Q_{loaded} and avoided. (Note this is not the case for ring resonator add-drop filters, for which a large K is beneficial for low loss power switching [74]).

The coupling term κ

The expression of the coupling term κ appearing in Eq. 1.21 was derived based on heuristic arguments in [74] and obtained more rigorously in the resonant approximation by Kamalakis et al. [75]. It is given in Eq. 1.27:

$$\kappa = i\frac{\omega\varepsilon_0}{4} \int_{-z_1}^{z_1} \mathrm{d}z \iint_{[\text{resonator}]} \mathrm{d}x\,\mathrm{d}y\,(n^2 - 1)\,\vec{e_r}^*\,\vec{e_+}\,e^{-i\beta z} \tag{1.27}$$

Here $\vec{e}_r\,(x, y, z)$ is the uncoupled resonator mode field normalized to unit energy (such that the electric field distribution in the resonator is $a\,(t)\,\vec{e}_r\,(x, y, z)$)
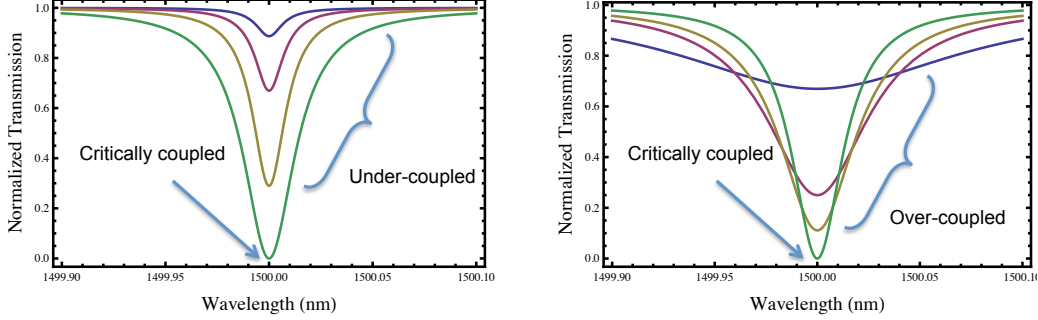
Figure 1.19: Numerical plots illustrating the under-coupled (left) and over-coupled (right) regimes. The WGM resonance has a lorentzian profile with on resonance transmission T_{on} given by Eq. 1.25 and FWHM given by Eq. 1.26. The ratio $\gamma_{\text{ext}}/\gamma_{\text{int}}$ successively takes the values 1/30 (blue), 1/10 (purple), 1/3 (yellow) and 1 (green) on the left and 1 (green), 2 (yellow), 3 (purple) and 10 (blue) on the right.

and $\vec{e}_+(x, y)$ is the unperturbed waveguide mode profile normalized to unit power (see Fig. 1.9). β is the unperturbed waveguide's propagation constant (see section 1.1.2) and the integration boundaries $-z_1$ and z_1 are defined in Fig. 1.18. They are chosen to be sufficiently far apart to encompass the entire disk resonator. κ is commonly described as proportional to the overlap integral between the resonator WGM and waveguide mode fields. Note however that the integral is only performed on the resonator volume. Indeed, from a physical perspective the two fields only interact with each other through their simultaneous excitation of the dipoles of a same portion of matter. (The fields do not couple to each other in vacuum). The term κ is linked to the coupling quality factor Q_{ext} by [73]:

$$-\frac{d|a(t)|^2}{dt} = \gamma_{\text{ext}}|a(t)|^2 = |\kappa\, a(t)|^2 \;\Rightarrow\; |\kappa|^2 = \gamma_{\text{ext}} \tag{1.28}$$

$$Q_{\text{ext}} = \frac{\omega_0}{\gamma_{\text{ext}}} = \frac{\omega_0}{|\kappa|^2} \tag{1.29}$$

Phase matching conditions

From Eq. 1.27 it appears that the value of κ and hence the strength of the waveguide to disk coupling is dependent upon the relative spatial dependencies of both the WGM and waveguide mode. (The WGM has a $e^{im\theta}$ phase dependency contained in $\vec{e}_r$, while the guided waveguide mode has a $e^{-i\beta z}$ spatial dependency.) For evanescent coupling to be efficient, the phase of the waveguide field must match the phase of the resonator field so that the induced fields in the disk coming from each portion of the waveguide add

up constructively. When this condition is met both fields are said to be *phase matched.* This is illustrated in Figures 1.21 (a) and (b), which respectively depict the poor and proper phase matching cases. Phase matching can simply be thought of in terms of a gear and chain analogy (see Fig. 1.20).

In order for efficient coupling to occur, the number of teeth in the gear must match the amount of links in the chain. In terms of coupling a WGM to a waveguide, there are two independent levers which can be adjusted in order to tune the phase matching: the width of the waveguide and the gap distance between disk and waveguide. This is illustrated in Fig. 1.21 (a) and (b). Phase matching considerations provide some insight into the optimal waveguide width for evanescent coupling, but do not give quantitative information on the optimal gap distance for fabrication, and how that optimal gap distance may vary with different WGMs or with changes in quality factor of the disk

Figure 1.20: Gear and chain phase matching analogy.

resonator. This is discussed in the following section. Note that the phase matching conditions vary with the WGM radial order p (for a similar resonance frequency λ, a higher p WGM will have lower azimuthal number m) so different modes couple with different efficiencies. Using a 'pulley' coupling scheme [76] (where the coupling waveguide wraps around the disk resonator) extends the interaction length between disk and waveguide in the integral of Eq. 1.27, thereby increasing the penalty for poor phase matching and therefore allowing to precisely select the desired excited mode. Such a coupling scheme seems however difficult to implement with a small 1 μm radius disk, due to the very important bending of the waveguide implied.

Tuning the guide to disk evanescent coupling

Figure 1.22 shows the systematic calculation of Q_{ext} via Eqs. 1.27 and 1.29 over the entire waveguide parameter space, for the p=1, m=10, $\lambda \simeq 1340$ nm WGM of a $\varnothing=2\mu$m disk, using the EIM. 900 discrete values of κ are calculated for 30 different values of taper width $w_t \times 30$ different values of gap distance g. In the following a discrete combination of these two values will be expressed as $\{w_t, g\}$. In order to reach the important critical coupling regime Q_{ext} should match the expected intrinsic quality factor Q_{int} of the fabricated disk. For typical small disks in our experiments $Q_{int} \simeq 10^5$, hence the target
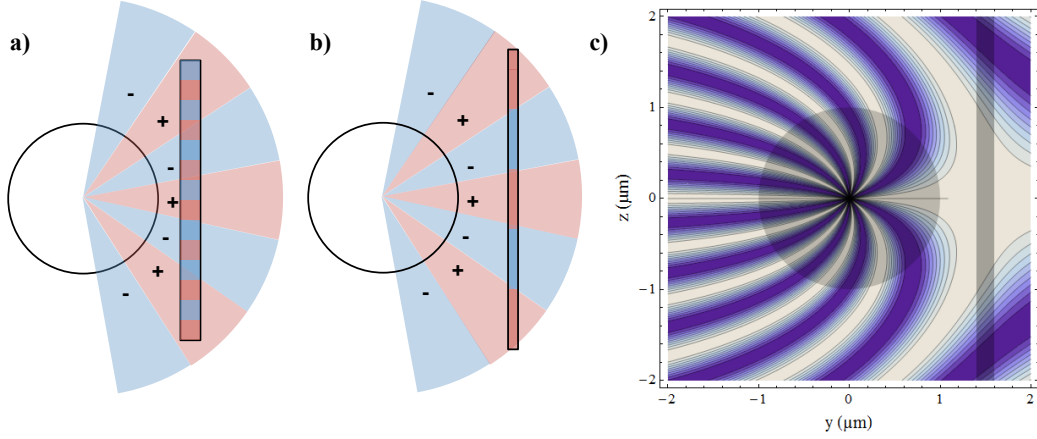
Figure 1.21: Different representations of the phase matching phenomenon. (a) and (b): Schematic illustration of poor/proper phase matching. In (a) a large GaAs waveguide with high n_{eff} ($\Rightarrow$ high β) is positioned close to a disk resonator with the m=8 WGM shown. The electric field is plotted red for $\Re(E)\geq 0$ and blue for $\Re(E)\leq 0$, for both WGM and waveguide. These regions do not match in case (a) (poor phase matching) leading to a small overlap integral (Eq. 1.27). (b) A narrower waveguide ($\Rightarrow$ low β) is positioned further from the disk. Here the spatial periodicity of WGM and waveguide E fields are similar and add up constructively in Eq. 1.27. These figures illustrate the two available levers to optimize phase-matching: taper width and gap distance between disk and taper. (c) A surface plot showing the spatial dependency $\Re(e^{im\theta} \times e^{-i\beta z})$ of the integrand in Eq. 1.27, for a m=10 WGM and a 200 nm wide waveguide. (The color code is white for 1 and blue for -1). The outline of the disk and waveguide are superposed over the plot for vizualisation purposes. From this it appears phase matching is satisfactory for gap distances ranging from 0 to ~ 1 μm. More precise optimal gap distance estimates are provided in section 1.3.1.
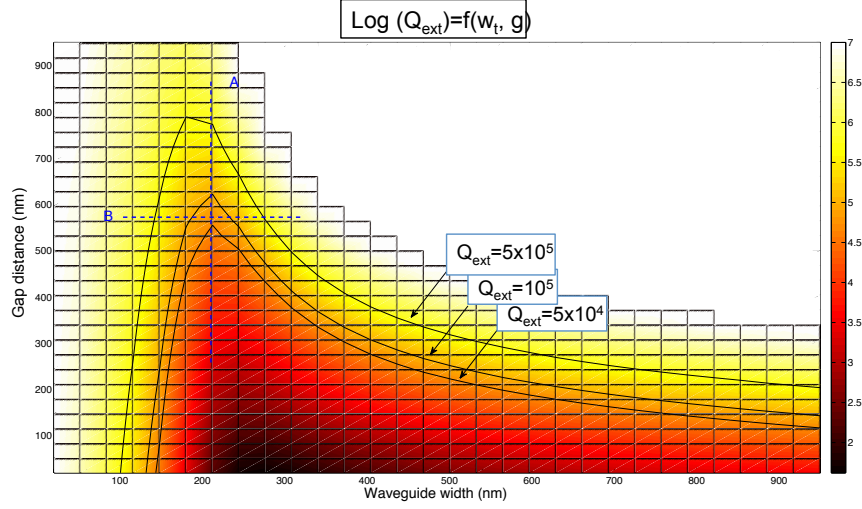
Figure 1.22: Surface plot displaying the calculated coupling quality factor Q_{ext} as a function of the waveguide width w_t and the disk to waveguide gap distance g. The space between the two outer solid black lines marks the target design region for best coupling to the $\varnothing$=2 μm disk's p=1 m=10 WGM (with estimated $5 \cdot 10^4 \leq Q_{int} \leq 5 \cdot 10^5$)

fabrication region (marked by the black lines in Figure 1.22) comprises the region of the parameter space with $5 \cdot 10^4 \leq Q_{ext} \leq 5 \cdot 10^5$. This aims to guarantee a WGM contrast of at least $1 - ((1-5)/(1+5))^2 \simeq 55\%$ (see Eq. 1.25). Several observations can be made from this calculation. First there exists an infinite combination of $\{w_t, g\}$ which produce the desired Q_{ext}. Even for a given gap distance two different waveguide widths can produce an identical Q_{ext}. Extreme values of waveguide widths (below 100 nm and above 900 nm) make for very inefficient coupling (high Q_{ext}) due to poor phase matching. For instance for widths ≤ 50 nm efficient coupling is impossible because the phase matching only occurs at very large gap distances for which the evanescent field has decayed too much. Such a plot is easy to compute (taking under one hour on a laptop computer) and provides an accurate starting point for the optimizing procedure of gap distance and waveguide width with real samples (see section 1.3.1). This method can further be used to estimate the extent to which the coupling is modified by operation in a liquid (see section 5.3.1), or how the optimal gap distance would be modified by Q_{int} altering surface treatments. It has been verified to provide results accurate within $\sim$150 nm for what concerns the optimal coupling gap distance on a variety of resonators of different sizes, thickness and refractive indices. The tendency is to somewhat overestimate the optimal coupling gap, in all likelihood due to the limitations of the effective index method for small

dimension waveguides and the fact that the coupling is assumed to be ideal (lossless).

Limits of the perturbation theory and optimal coupling parameters

According to the results shown in Figure 1.22, all combinations of $\{w_t, g\}$ along an iso-Q_{ext} curve (such as one of the black lines) should produce the same experimental results. In practice though this is not the case. We find for instance that approaching a large 900 nm wide waveguide near the disk resonator significantly degrades its measured (loaded) Q factor, even in the absence of additional fabrication induced sidewall roughness. This degradation goes far beyond what is predicted by the ideal coupled mode theory detailed above, where the loaded Q at critical coupling is 1/2 Q_{int} (Eq. 1.26). Indeed in this situation the loaded Q near critical coupling is one to two orders of magnitude lower than the intrinsic Q measured at large gap distances.

   This non ideal behavior is due to the coupling no longer being lossless, contrary to what is assumed in Eq. 1.28. When the coupling waveguide is 'approached', the WGM couples to the waveguide's fundamental mode (which is the desired outcome), but the WGM can also couple to some degree to the waveguide's radiation modes and higher order guided modes (if present). These additional loss channels -unlike the coupling to the fundamental mode- only serve to remove energy from the resonator, since incoming energy only arrives through the waveguide in the fundamental mode. This *parasitic* coupling therefore decreases the loaded Q more than expected by idealized CMT.

   The ideality I of the coupling junction [77] is defined as the ratio of power coupled into the fundamental mode to power coupled into all modes (Eq. 1.30).

$$I = \frac{\kappa_0^2}{\kappa_0^2 + \sum_{i \neq 0} \kappa_i^2 + \kappa_{rad}^2} \tag{1.30}$$

with $\sum_{i \neq 0} \kappa_i^2$ and κ_{rad}^2 respectively the coupling terms to the waveguide's higher order modes and radiation modes. For silica toroids coupled to pulled silica fiber tapers values of I above 99.9% are reported, but these rapidly decrease with increasing taper width [77]. Parasitic losses have also been reported in the case of a GaAs disk resonator coupled to a silica fiber taper [46]. This departure from ideality shouldn't actually be too surprising when one considers the relative scale of a $\varnothing = 2\mu$m disk to a 900 nm wide waveguide (see Figure 1.23), but should nevertheless not be neglected especially for small disk resonators with high refractive index coupling waveguides for which this becomes increasingly significant.
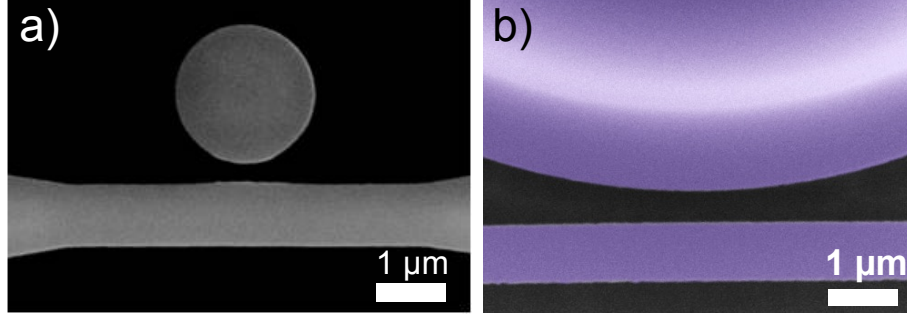
Figure 1.23: (a) SEM top view image of a 1 μm radius GaAs disk resonator positioned next to a 900 nm wide coupling waveguide at $\sim$250 nm gap distance, illustrating a resonator operating far from the weakly perturbed regime. (b) For scale comparison: artificially colored SEM image of a 10 μm radius silicon nitride disk resonator positioned next to a waveguide of identical width as the one in (a) [56].

From a purely pragmatic standpoint, one cannot do without a coupling waveguide near the disk. The question then becomes "what combination of $\{w_t, g\}$ provokes the least degradation in the WGM properties at critical coupling ?". We hypothesize this would occur with a single mode waveguide ($\sum_{i \neq 0} \kappa_i^2 = 0$) at the largest possible gap distance where the WGM is the least perturbed by the coupling waveguide (i.e. where $\iiint_{[\text{waveguide}]} E_{\text{disk}}^2 \, dv$ is minimal in order to minimize κ_{rad}^2). Figure 1.22 shows this occurs for a waveguide width of $\sim$200 nm. This turns out to be the optimally phase matched width for which coupling is strong even at large distances. Such an operating point is also advantageous as it is located around an area where $\partial Q_{\text{ext}} / \partial w_t \simeq 0$, making the coupling less sensitive to fabrication-dependent width variations. Working with a larger resonator for which κ_{rad}^2 is smaller in proportion to γ_{int} could naturally also help to mitigate these detrimental effects (see Figure 1.23).

Experimental optimization

Once the general optimal position has been determined (see previous section and position marked by an arrow in Figure 1.22), a fine tuning of the coupling is performed in experimental samples. This optimization is done by varying the gap distance for a fixed waveguide width in a series of waveguides and by varying the taper width for a fixed gap distance in a different series. This procedure corresponds to traveling respectively along the vertical and horizontal lines A and B shown in Figure 1.22 and allows to accurately determine the best coupling parameters (see chapter 5). The initial estimate provided by the numerical approach detailed in this chapter therefore narrows the search

and allows to gain time in both fabrication and device characterization steps.

FDTD simulations

Two dimensional FDTD simulations of the waveguide/disk resonator system confirm the Q_{loaded} degradation due to a 900 nm wide waveguide (not shown here). FDTD simulations are a powerful tool to characterize WGM resonances. However, in order to be accurate, the simulation time must be of the order of the photon lifetime in the resonator ($\equiv Q/\omega_0$) which is long for high Q resonators. Calculation times typically take many hours, and the computation of a complete map such as Figure 1.22 with FDTD tools, while more accurate, would be prohibitively long with a standard computer, as of 2013.

1.4 Conclusions

In this chapter we discussed the electromagnetic design of on-chip GaAs disk optomechanical resonators coupled to integrated coupling waveguides. The techniques described here allow to fulfill all the desired requirements : high optical power transmission with low optical losses, broadband operation, precise control and adjustment of the coupling strength between disk and waveguide without degradation of the high optical Q of the GaAs disk resonators, all the while using techniques compatible with the disk fabrication process[3]. Thanks to these developments optical transmission efficiencies above 30 %, critical coupling and WGMs with optical Qs $\geq 5 \cdot 10^5$ (the state of the art for free standing GaAs disk resonators [46, 20]) were eventually obtained in this PhD work with on-chip devices with monolithic integrated coupling waveguides.

---

[3]The design framework detailed in this chapter is also used to fabricate critically coupled on-chip high Q SiN WGM resonators, which are discussed in section 5.4. These resonators are conceptually identical to the GaAs resonators presented here, the main differences being their ten times larger size ($\varnothing$=20 μm) and lower refractive index (n$\simeq$2).

Chapter 2

Mechanics of optomechanical resonators

2.1 Introduction

The GaAs disks described in this thesis are both *optical* and *mechanical* resonators. In the previous chapter we described the disks from an optical standpoint and discussed the characteristics of the sustained whispering gallery modes. In this chapter we now look at the GaAs disk resonators from a mechanical point of view and consider the variety of vibrational modes of the disk itself.

We begin with a static analysis of the bending of the GaAs suspended coupling waveguide introduced in the previous chapter. Then an analytical description of the mechanical modes of the disk is given, treating successively the case of out-of-plane and in-plane modes. Second numerical simulations of the mechanics are detailed. Third the different loss mechanisms which limit the mechanical quality factor are discussed and some orders of magnitude of the mechanical deformations of the disk are given. Finally a description of the mechanical behavior of a stressed silicon nitride beam is provided.

2.2 Bending of the suspended waveguide

We use the beginning of this chapter to make a brief aside and address the static deformation of the tapered section of the integrated GaAs waveguide, which is suspended over tens of microns in the vicinity of the disk resonator. Here we discuss whether or not this leads to a significant amount of vertical sag, which would modify the coupling discussed in the previous chapter. In order to do so, the suspended waveguide is modeled as a doubly clamped

2.2 Bending of the suspended waveguide
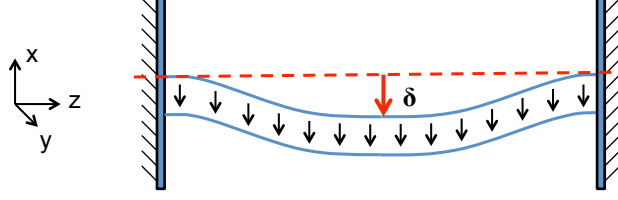
Figure 2.1: Schematic of a doubly clamped beam with distributed load, taken as a model of the suspended GaAs waveguide. The beam's sag is represented by δ.

beam supporting a distributed load (see Figure 2.1). In the limit of small deflections, the maximum sag δ_{max} for such a beam is (see appendix B.1):

$$\delta_{\mathrm{max}} = \frac{q\,L^4}{384\,E\,I} \tag{2.1}$$

L and E are respectively the beam's length and the beam material's Young's modulus. q is the distributed load (in Newtons per meter) due to the beam's own weight equal to $\rho g w_t h$, with w_t and h respectively the tapered waveguide's width and thickness, ρ the material's density and $g = 9.8$ m·s^{-2}. I is the second moment of area of the beam's cross section[1]. Thus for a beam of rectangular cross section only subject to its own weight, the maximal sag is given by Eq. 2.2:

$$\delta_{\mathrm{max}} = \frac{\rho\,g\,L^4}{32\,E\,h^2} \tag{2.2}$$

The sag does not depend upon the beam width so the choice of tapered waveguide width is of no consequence. Calculating Eq. 2.2 for a 320 nm thick GaAs beam suspended over 50 μm yields δ_{max} barely above 1 picometer[2]. The sag of the suspended waveguide is only $\sim$3 millionths of its thickness and can therefore safely be neglected.

Interestingly the sag scales with $\left(\frac{L}{h}\right)^2 L^2$, so simply maintaining a constant aspect ratio is not sufficient to keep the relative sag constant. As a consequence, structures with an aspect ratio such as the one described in this work are only feasible in the micro-scale. Indeed a hypothetical 50 m long and 32 cm thick GaAs beam would have a sag δ_{max} greater than 3 times its thickness and collapse upon the substrate.

Finally even though we showed that the beam's bending under its own weight is negligible, the surface tension of liquids can nevertheless be strong enough to stick the suspended waveguide onto the substrate (see fabrication chapter).

---

[1]The second moment of area with respect to the x axis (bending axis) is defined as $I_x = \iint_{\mathrm{cross-section}} x^2 \mathrm{d}x\,\mathrm{d}y = w_t \int_{-h/2}^{h/2} x^2\,\mathrm{d}x = w_t \frac{h^3}{12}$

[2]With $\rho_{\mathrm{GaAs}} = 5317$ kg·m^{-3} and $E_{\mathrm{GaAs}} = 85.9$ GPa
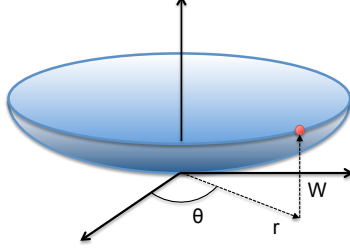
Figure 2.2: Deformation amplitude W of a point of the disk of coordinates r and θ.

2.3 Analytical description of disk mechanical modes

In this section we give an analytical description of the mechanical modes of the disk resonator, successively treating the out of plane and in plane cases. The analytical approach relies on certain simplifications such as idealized boundary conditions at the junction between the disk (GaAs) and the supporting pedestal (AlGaAs). As such, FEM simulations (such as described in section 2.4) generally give more accurate results. Nevertheless analytical descriptions are quite reliable in most cases and provide a useful 'feel' for the role of each physical parameter. This knowledge is valuable when designing a structure to meet specific mechanical properties. Throughout this thesis we make the important simplification of treating GaAs as a material with isotropic mechanical properties, which can therefore be described only through its Young's modulus E and Poisson ratio σ. While this is not the case, we nevertheless find this approach provides results in very good agreement with experimental measurements.

2.3.1 Out of plane modes of the disk

In order to describe the out of plane vibrations of our disk resonators we use the work *Vibration of Plates* by Arthur W. Leissa [78], which provides solutions to a wide variety of problems involving plate vibrations.

The general solution to the problem of the free out-of-plane (transverse) vibrations of a plate is given by Eq.2.3. The deformation amplitude W as a function of the polar coordinates r and θ reads (see Fig. 2.2 and appendix

2.3 Analytical description of disk mechanical modes

B.2 for derivation):

$$W\left(r,\theta\right) = \sum_{M=0}^{\infty} \left[A_M J_M\left(kr\right) + B_M Y_M\left(kr\right) + C_M I_M\left(kr\right) + D_M K_M\left(kr\right)\right] \cos M\theta$$

$$+ \sum_{M=1}^{\infty} \left[A_M^* J_M\left(kr\right) + B_M^* Y_M\left(kr\right) + C_M^* I_M\left(kr\right) + D_M^* K_M\left(kr\right)\right] \sin M\theta$$

$$= \sum_{M=0}^{\infty} W_M\left(r,\theta\right)$$

$$(2.3)$$

Here J_M and Y_M are respectively the Bessel functions of first and second kind, while I_M and K_M are the modified Bessel functions of first and second kind respectively. $W(r,\theta)$ is expressed as the sum of eigenmodes of order M, W_M. In the case of a plate with rotationally invariant boundary conditions, the $\sin M\theta$ terms can be discarded [78]. Furthermore if the plate does not have a hole in the center (e.g. a simple circular plate) the coefficients B_M and D_M must be zero, as the terms $Y_M(kr)$ and $K_M(kr)$ diverge for r=0. The deformation amplitude of the M_{th} mode then takes the more familiar form:

$$W_M(r,\theta) = [A_M\, J_M\left(kr\right) + C_M\, I_M\left(kr\right)] \cos\left(M\theta\right) \qquad (2.4)$$

The number M is called the mechanical mode's *azimuthal* number, and gives the number of nodal diameters in the deformation profile. For instance for M=1 all points situated on the line going through the points (r=1; $\theta = \pi/2$) and (r=1; $\theta = -\pi/2$) have zero displacement amplitude.

Modeling the disk as an annular plate

While equation 2.4 accurately describes the out of plane displacement of a non-supported plate (i.e. a disk resonator with an infinitely narrow pedestal), it fails to account for the effect of larger pedestals which significantly modify the mode profile. This is the case for the 200 nm thick disks studied in [20]. For disks with large pedestals best results are obtained when the disk is modeled as an annular plate of outer radius a equal to the disk radius R, and inner radius b equal to pedestal radius r_p (see Figure 2.3). The annular plate is considered fixed at the point of contact with the pedestal. We find this hypothesis works well for the first modes of vibrations of the disk. The function $W_M\left(r,\theta\right)$ which gives the displacement amplitude of the M*th* azimuthal mode in polar coordinates thus reads:

$$W_M\left(r,\theta\right) = [A_M\, J_M\left(kr\right) + B_M\, Y_M\left(kr\right) + C_M\, I_M\left(kr\right) + D_M\, K_M\left(kr\right)] \cos M\theta$$

$$(2.5)$$
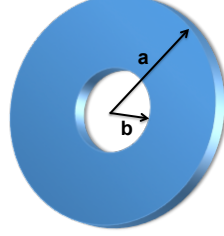
Figure 2.3: Annular plate of internal radius b and outer radius a. The plate is clamped at $r = b$ and free at $r = a$.

There are three simple possible boundary conditions for each boundary of the annular plate:

- *Free.* At a free boundary the exerted force $\dfrac{\partial^2 W}{\partial r^2}$ and moment $\dfrac{\partial^3 W}{\partial r^3}$ are zero.

- *Clamped.* At a clamped boundary, the displacement W as well as the slope $\dfrac{\partial W}{\partial r}$ are zero.

- *Simply supported.* At a simply supported boundary the plate displacement W as well as the moment $\dfrac{\partial^3 W}{\partial r^3}$ are zero.

We tested two different configurations: free at r=a and simply supported at r=b, or free at r=a and clamped at r=b. In the following we will detail the latter configuration, which provided more accurate results when compared to COMSOL 3D FEM modeling of the structure. Considering the beam as clamped at r=b and free at r=a, thus yields a set of four equations that must be verified by W_M:

$$
\begin{cases}
W_M(b) & = 0 \\
\left(\frac{\partial W_M}{\partial r}\right)_b & = 0 \\
\left(\frac{\partial^2 W_M}{\partial r^2}\right)_a & = 0 \\
\left(\frac{\partial^3 W_M}{\partial r^3}\right)_a & = 0
\end{cases}
\tag{2.6}
$$

2.3 Analytical description of disk mechanical modes
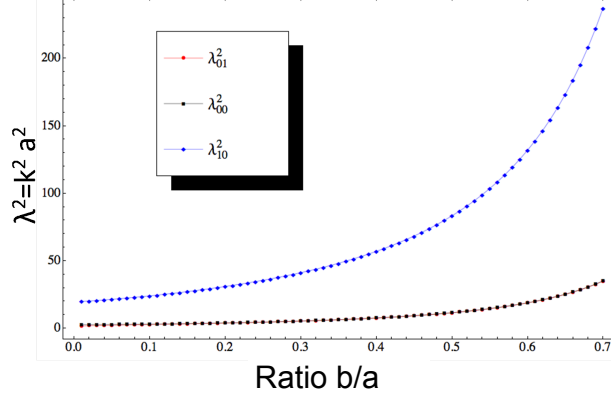
Figure 2.4: Dependency of the dimensionless frequency parameter $\lambda_{P,M}^2 = k_{P,M}^2 a^2$ with the ratio b/a, for the mechanical modes (P=0, M=0), (P=0, M=1) and (P=1, M=0). The curves for λ_{00} and λ_{01} are almost superposed, as the frequencies of the (P=0, M=0) and (P=0, M=1) modes are nearly identical (see Fig. 2.5).

In order for the set of equations (2.6) to give a non trivial solution for W_M, the following (4×4) determinant must be zero:

$$
\begin{vmatrix}
J_M(kb) & Y_M(kb) & I_M(kb) & K_M(kb) \\
\left(\frac{\partial J_M(kr)}{\partial r}\right)_b & \left(\frac{\partial Y_M(kr)}{\partial r}\right)_b & \left(\frac{\partial I_M(kr)}{\partial r}\right)_b & \left(\frac{\partial K_M(kr)}{\partial r}\right)_b \\
\left(\frac{\partial^2 J_M(kr)}{\partial r^2}\right)_a & \left(\frac{\partial^2 Y_M(kr)}{\partial r^2}\right)_a & \left(\frac{\partial^2 I_M(kr)}{\partial r^2}\right)_a & \left(\frac{\partial^2 K_M(kr)}{\partial r^2}\right)_a \\
\left(\frac{\partial^3 J_M(kr)}{\partial r^3}\right)_a & \left(\frac{\partial^3 Y_M(kr)}{\partial r^3}\right)_a & \left(\frac{\partial^3 I_M(kr)}{\partial r^3}\right)_a & \left(\frac{\partial^3 K_M(kr)}{\partial r^3}\right)_a
\end{vmatrix} = 0 \qquad (2.7)
$$

For a given M, this fixes a condition on the parameter k, which can no longer take all possible values, but only successive discrete values of k_M. We call the order of these successive solutions the *radial* number P, starting with 0 for the first order, hence the notation $k_{P,M}$. The radial order P corresponds to the number of times $W_M(r)$ cancels as r goes through the interval $]b, a]$. As such, P indicates the number of nodal circles in the deformation profile of a vibrational mode. Tabulated solutions to Eq. 2.7 are provided in [78] for certain values of the ratio b/a. Solutions can also be calculated numerically. In Figure 2.4 we provide solutions to this equation under the form of the dimensionless parameter $\lambda_{P,M}^2 \equiv k_{P,M}^2 \times a^2$ for three out of plane modes. The parameter $\lambda_{P,M}$ only depends on the disk's inner and outer radius through their ratio b/a, so it can be used to describe the mechanical modes of disks of any size. Once a solution to (2.7) is found, the coefficients A_M, B_M, C_M et D_M are obtained by solving for the boundary conditions (2.6). Thus a mechanical mode's profile is entirely determined by the knowledge of its

azimuthal and radial numbers[3] M and P. Figure 2.5 illustrates the first nine different deformation profiles of an annular plate, with P and M both taking the values {0,1,2}.

Resonance frequency

The frequency $f_{P,M}$ of the (P,M) mechanical mode is given by :

$$f_{P,M} = \frac{\lambda_{P,M}^2}{2\pi a^2} \times \sqrt{\frac{D}{\rho_s}} = \frac{\lambda_{P,M}^2 h}{2\pi a^2} \times \sqrt{\frac{E}{12\,\rho\,(1-\sigma^2)}} \qquad (2.8)$$

where ρ is the disk's density. Let us note that the quantity $\lambda_{P,M}^2\,(a-b)^2\,/a^2$, which only depends on the parameter b/a, varies little when b/a varies from 0 to 0.8 for the first flexural modes such as $\lambda_{0,0}$, $\lambda_{1,0}$, $\lambda0,1$ (not shown here). This implies that at a first level of description, the dependence of $f_{P,M}$ is well captured by a simple dependence in $1/(a-b)^2$, reminiscent of the usual $1/l^2$ dependence for the flexural motion of an elastic lever of length l [79].

---

[3]We use the capital letters M and P to distinguish the mechanical azimuthal and radial numbers from the WGM azimuthal and radial numbers m and p.
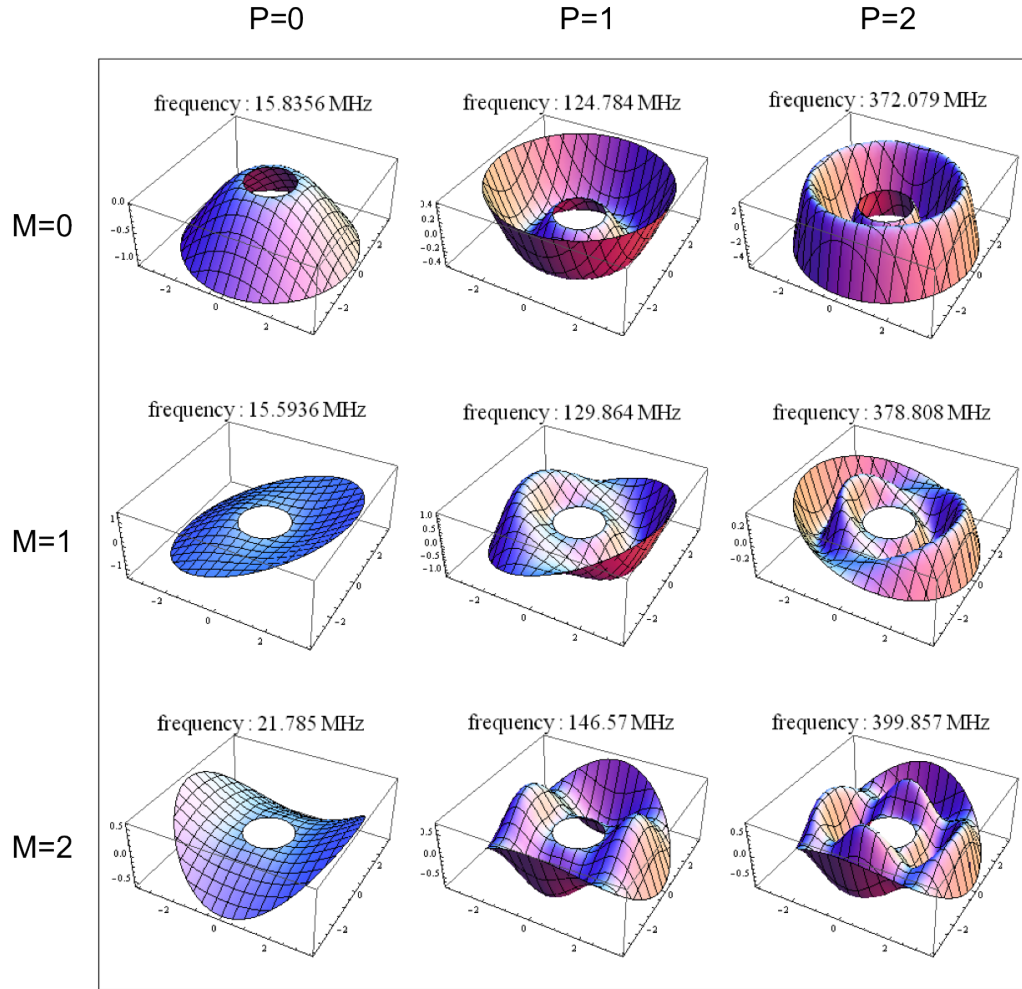
Figure 2.5: Deformation profiles for 9 out of plane modes of a 200 nm thick GaAs disk resonator with outer radius a=3.5 μm and inner radius b=1 μm, arranged by azimuthal and radial number M and P. The top left mode is a (P=0, M=0). From there going to the next column increases the radial order P by one, while going to the next row increases M by one. The deformation amplitude is strongly exaggerated for visibility. Note how the displayed resonance frequencies increase much faster with rising P than rising M.
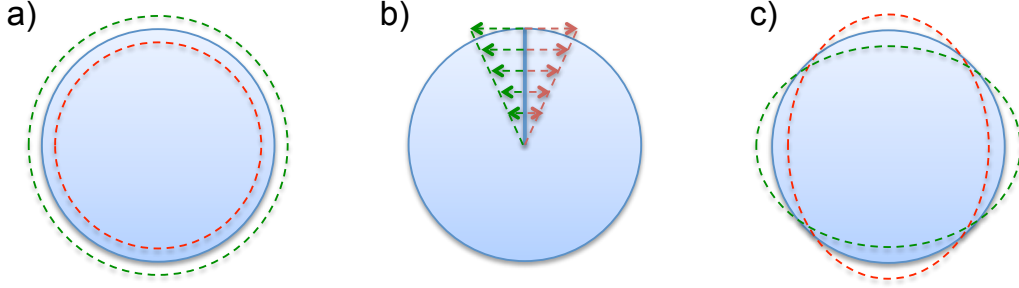
Figure 2.6: The three different families of in-plane mechanical modes. (a) Radial breathing modes. (b) Purely tangential modes. (c) Wineglass modes. The dashed lines represent the extremal displacements, while the solid disk shows the resonator at rest.

2.3.2 In plane modes of the disk

We now look at in-plane modes of vibration of disk resonators. The in-plane modes can be separated into three main categories [80], which are illustrated in Figure 2.6. The first contains modes with purely *radial* displacement, often called Radial Breathing Modes (RBMs) (Fig. 2.6, a). The second category comprises modes with purely *tangential* motion as shown in Fig. 2.6 (b). Finally the third category contains *compound* modes which are a combination of radial and tangential motion. These modes have a $\cos(M\theta)$ with $M \neq 0$ dependency of the radial displacement along the angular coordinate θ. They therefore exhibit nodal points with no displacement on the boundary (see Fig 2.6, c). These are often referred to as *wineglass modes* [81]. Unlike radial breathing modes, tangential and wineglass modes do not significantly change the disk's boundary length. As a consequence they do not couple much to optical WGMs and are therefore of less interest for optomechanics. For this reason we will only describe RBMs in the following.

Radial breathing modes

The RBM radial displacement amplitude $U(r, \theta)$ for any point of a circular plate of radius R with free boundary conditions is given by Eq. 2.9 [80, 82], assuming the radial displacement does not depend upon the vertical coordinate:

$$U(r, \theta) = U(r) = A \, \alpha_{\mathrm{P}} J_1 \left(\alpha_{\mathrm{P}} r \right) \tag{2.9}$$

where r is the distance to the center of the disk, J_n is the Bessel function of the first kind of order n, A a normalization constant and α_{P} a constant

2.3 Analytical description of disk mechanical modes

Frequency parameter λ_P			Effective mass ratio		
λ_1	λ_2	λ_3	m_{eff1}/m	m_{eff2}/m	m_{eff3}/m
2.055	5.391	8.573	0.786	0.969	0.988

Table 2.1: First three values of the frequency parameter λ_P and effective mass ratios for GaAs disk RBMs.

defined as:

$$\alpha_{\mathrm{P}} = \omega_0 \sqrt{\frac{\rho}{\left(\frac{E}{1+\sigma}\right) + \left(\frac{E\sigma}{1-\sigma^2}\right)}} \tag{2.10}$$

Here ρ, E, σ and ω_0 are respectively the density, Young's modulus, Poisson ratio and RBM resonance frequency. As is the case for out of plane modes, there are different order RBMs. The successive resonance frequencies (labeled by the integer P) are found by solving Eq. 2.11 for ω_0:

$$\frac{\zeta}{\xi} \frac{J_0(\zeta/\xi)}{J_1(\zeta/\xi)} = 1 - \sigma$$

$$\text{with} \quad \xi = \sqrt{\frac{2}{1-\sigma}} \quad \text{and} \quad \zeta = \omega_0 R \sqrt{\frac{\rho(2+2\sigma)}{E}} \tag{2.11}$$

The solution to Eq. 2.11 can be put in the following more intuitive form, which gives the resonance frequency w_P of the P*th* RBM:

$$\omega_P = \frac{\lambda_P}{R} \sqrt{\frac{E}{\rho(1-\sigma^2)}} \tag{2.12}$$

Here λ_P is a parameter dependent only on the Poisson ratio of the disk material and the RBM order. The first three values for GaAs are listed in Table 2.1. Eq. 2.12 is reminiscent of the $\frac{1}{l}\sqrt{\frac{E}{\rho}}$ frequency dependency for the longitudinal vibrations of a free beam of length l. Note how the frequency varies as $\frac{1}{R}$ in the case of RBMs, versus as $\frac{1}{R^2}$ for out-of plane modes (see section 2.3.1) . This translates into a reduced frequency penalty for large disks in the case of RBMs. The displacement amplitude (Eq. 2.9) can also simply be expressed as function of λ_P:

$$U_P(r) = A_P J_1(\lambda_P \frac{r}{R}) \tag{2.13}$$

effective mass

The maximal stored kinetic energy in the disk resonator E_c is given by [82]:

$$E_c = \frac{1}{2}\,\rho\,h \int_{\theta=0}^{\theta=2\pi} \int_{r=0}^{r=R} V_0^2(r)\,r\,\mathrm{d}r\,\mathrm{d}\theta \tag{2.14}$$

with V_0 the velocity at any point on the disk. From this, the effective mass m_{eff} *of a point on the disk boundary*[4] is expressed as:

$$m_{\mathrm{eff}} = \frac{2E_c}{V_0^2(R)} = \frac{2\pi\rho h \int_0^R r\, J_1\!\left(\lambda_P \dfrac{r}{R}\right)^2 \mathrm{d}r}{J_1(\lambda_P)^2} = \underbrace{\pi\,\rho\,hR^2}_{\text{mass}} \overbrace{\left(1 - \frac{J_0(\lambda_P)\,J_2(\lambda_P)}{J_1(\lambda_P)^2}\right)}^{m_{\mathrm{eff}}/mass} \tag{2.15}$$

In the case of a GaAs disk's first RBM, the ratio of effective mass to total mass m equals 0.786. This value is also only dependent upon the Poisson ratio (see Eq. 2.15). The values for the first three RBMs are listed in Table 2.1.

The above analytical formulas describe the behavior of completely free circular plates, and therefore do not take into account the effect of the supporting pedestal under the disk resonator. However for the large disk undercut ratios we now aim to fabricate the discrepancy is small. Reference [83] provides an analytical description for the in-plane modes of annular plates, which more accurately represent the RBMs of disk resonators with larger pedestals.

2.4 Numerical modeling of mechanical modes

FEM simulations are a complementary way to gather information on GaAs disks' mechanical properties. We perform these with the commercial FEM modeling software COMSOL. This method has the advantage of allowing for more complex boundary conditions and geometries. It can also provide accurate estimates of power loss to the substrate (see section 2.5.2) and measures of intrinsic damping mechanisms (section 2.5.4). The simulations can be performed with a 2D axi-symmetric layout for mechanical modes with rotational invariance (RBMs and M=0 out of plane modes) but must be fully 3D to account for the other modes (See Figure 2.7). Going to full 3D

---

[4]The choice of the reduction point for the effective mass is somewhat arbitrary. Here we choose for simplicity a point on the disk's outer boundary. This is however not quite the position of maximum radial displacement (see Fig. 3.15 for a RBM's displacement profile).

2.4 Numerical modeling of mechanical modes

	Analytical formula	Numerical without pedestal	Numerical with pedestal
RBM resonance frequency	1.38 GHz	1.376 GHz	1.377 GHz
Effective mass ratio	0.79	0.88	0.83

Table 2.2: Comparison between the results of the analytical formulation of section 2.3.2 and 3D FEM numerical simulations, for the resonance frequency and the effective mass ratio of a point on the disk's boundary. Here we consider the fundamental RBM of a 320 nm thick, 1 μm radius GaAs disk resonator with either no AlGaAs pedestal or a 100 nm radius pedestal (last column).

simulations one can also account for GaAs' anisotropic mechanical properties, however this goes beyond the scope of this thesis. Computations are quite fast, generally taking under one minute.

We find very good agreement between the RBM resonance frequency given by the analytical formula provided in section 2.3.2 and the frequency found through 3D FEM simulations, with the error being under 1% (see Table 2.2). Furthermore we verify the RBM resonance frequency is barely affected by the presence of a small diameter AlGaAs pedestal supporting the disk (see Table 2.2), as the RBM mechanical displacement is negligible near the center of the disk. Similarly good agreement is found regarding the radial deformation profile obtained through these two different methods (see Fig. 3.15). On the contrary the analytical approach tends to underestimate the effective mass, as it does not take into account the out of plane movement associated with the RBM.

For small disk resonators few mechanical modes are visible experimentally and these are widely spaced (> hundreds of MHz). In the case of larger disks with large pedestals, many mechanical modes can appear close together on a mechanical spectrum. This makes exact identification more challenging. One efficient way to do so is to look at the mechanical modes' experimental frequency dispersion with a parameter such as the disk size. This dispersion curve can then be compared with a simulated dispersion curve in order to resolve the uncertainty between different families of modes (see [20] and section 6.2.1). Different mechanical modes also couple differently to the optical field, which can help with their identification. This will be discussed in more detail in section 3.8. All relevant physical parameters used in the simulations are available in appendix D.
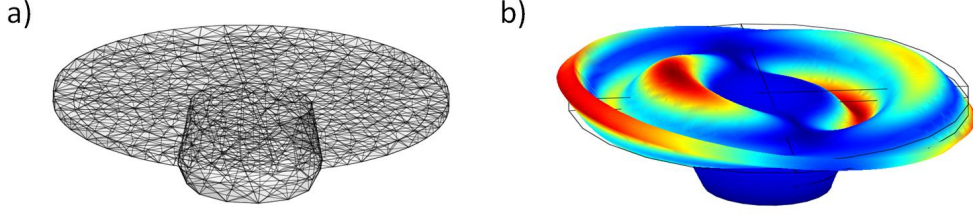
Figure 2.7: FEM simulation of the mechanical modes of a GaAs disk resonator. (a) Meshing of the computational domain. (b) Image of the simulated (P=2 M=1) out of plane mechanical mode, with exaggerated boundary deformation. The color code is blue for no displacement and red for maximum displacement amplitude.

2.5 Loss sources and Q factor estimation

2.5.1 Mechanical quality factor

The mechanical quality factor Q_M can be defined similarly to the optical quality factor, through equation 2.16:

$$Q_M = 2\pi \frac{\text{Energy stored}}{\text{Energy dissipated per cycle}} = \frac{\omega_0}{\delta\omega} \qquad (2.16)$$

with ω_0 and $\delta\omega$ respectively the mechanical resonance's frequency and FWHM of the associated lorentzian resonance. The mechanical quality factor is therefore a measure of the temporal confinement of the mechanical energy inside the disk resonator. There are many reasons why it is interesting to make Q_M as high as possible. The mechanical Q is a measure of the degree to which the resonator is isolated from its environment. Optomechanical cooling and actuation rely on this isolation in order to create a gradient between the amount of energy in the mechanical mode and in the environment. A high Q is also useful for sensing applications. If the mechanical resonator is subjected to a force gradient, the resonance frequency will be shifted by a certain amount. The resolution for this detection is determined by the mechanical resonance linewidth. Finally with a high Q resonator the mechanical energy will be concentrated over a smaller frequency bandwidth, facilitating detection above experimental noise sources.

Loss sources

We identify four main loss sources that can potentially limit the mechanical quality factor: clamping losses (or support losses), air damping, Thermoelastic Damping (TED) and surface losses (see sections 2.5.3, 2.5.2, 2.5.4 and

2.5.5). These dissipation mechanisms will be successively addressed and estimates of their magnitude for GaAs disk resonators will be provided.

2.5.2   Clamping losses

Clamping losses occur due to the *structural* connection between the mechanical resonator and its supporting environment. In the case of GaAs disks, the resonator is anchored to the environment (the sample chip) via its AlGaAs pedestal. When the resonator oscillates, it produces acoustical waves[5] which then radiate out of the resonator via the anchoring points, resulting in energy loss. Clamping losses are essentially set by the structure's physical design and the material's acoustic properties, and do not change much over the operating parameters (temperature between 300 K and 4 K, pressure between atmospheric pressure and 10^{-6} mbar) [84].

Estimating the clamping loss related quality factor Q_{clamping} for a disk resonator requires knowing the dissipated energy per mechanical oscillation. Reference [85] proposes a method to do so, by calculating the coupling between the in-plane RBM and the out of plane acoustic radiation in the pedestal via the disk's Poisson ratio.

We choose to estimate the clamping losses via FEM numerical simulations, which allow to simulate more complex pedestal geometries. With this method the computational domain consists of the disk resonator and a small chunk of the sample substrate, which is bounded by PMLs in order to emulate a semi-infinite medium (see Figure 2.8, a). These PMLs introduce loss in the simulation and are necessary to extract a quality factor. The disk resonator is then subjected to a time dependent driving force, of the form F(t)=F$_0$ × cos(ωt). The resonator's amplitude response is then computed, while sweeping the driving frequency ω across the resonance bandwidth. Q_{clamping} is then simply obtained by $\frac{\omega_0}{\delta\omega}$ (Eq. 2.16). Due to the larger computational area involved, these simulations take upwards of 10 minutes. The clamping losses can be mitigated by reducing the dimensions of the anchoring point, tethering the resonator to nodal points of displacement [81] or engineering the anchoring structure to have a phononic bandgap around the desired mechanical resonance frequency [86, 87]. In our case, we focused on reducing the anchoring losses by reducing the pedestal's lateral dimensions.

Figure 2.8 (b) plots Q_{clamping} for the first RBM of a 320 nm thick, 1 μm radius GaAs disk as a function of the AlGaAs pedestal radius r_p, obtained with FEM simulations, after systematic optimization of mesh, geometry and

---

[5]The acoustical wavelength is given by $\lambda = c/\nu$ with c the speed of sound in the infinite material and ν the mechanical frequency. For GaAs , c$\simeq$4700 m·s^{-1} and $\lambda_m \simeq 3.4$ μm for a 1.3 GHz mechanical mode.
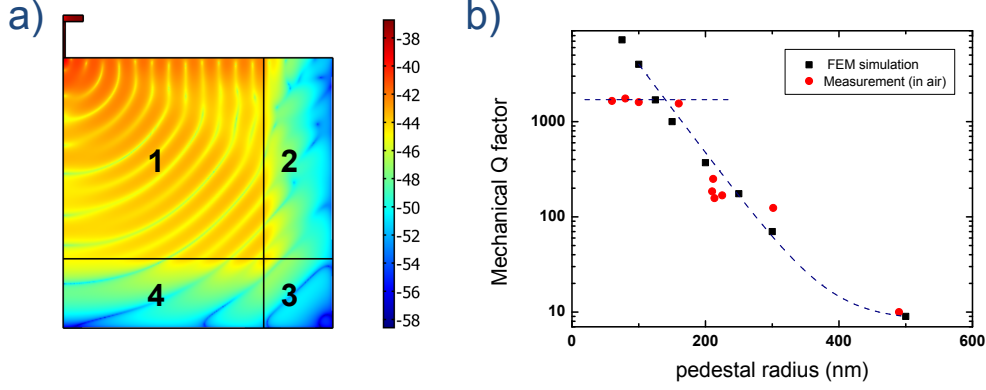
Figure 2.8: (a) View of the 2D axi-symmetric computational domain containing the disk resonator (top left) the substrate (region **1**) and the PMLs (**2**, **3**, and **4**). Acoustic waves can be seen radiating out of the pedestal into the substrate and being absorbed by the PMLs. The scale bar represents the log of the displacement amplitude, in arbitrary units. (b) FEM simulated Q_{clamping} as a function of AlGaAs pedestal radius (black squares) and experimentally measured values of Q_M (red circles). The dashed navy lines serve as guides to the eyes, distinguishing between two different damping mechanisms. Below a pedestal radius of $\sim$150 nm (corresponding to a 85 % undercut ratio), clamping losses cease to be the dominant loss source in favor of air damping.

PML parameters. Q_{clamping} depends strongly on r_p, increasing by more than two orders of magnitude as r_p is reduced from 500 nm to 100 nm. Red dots show experimental values for Q_M measured in air, which are in satisfactory agreement with the FEM values for Q_{clamping} for $r_p \geq 150$ nm. For r_p below $\sim$150 nm, the measured Q plateaus out around 1600, due to the contribution of air damping, which we discuss in the following section.

2.5.3 Air damping

The GaAs disk resonator's vibrations can also be damped by the interaction with the surrounding fluid (air or liquid). While there is no exact formula describing this damping, it can be satisfactorily estimated by adapting a method used to describe the damping of oscillating cantilevers [88, 89]. The method consists in covering the surface of the resonator with virtual Stokes spheres and summing their damping contributions[6]. In our case, the spheres have a displacement amplitude described by the analytical displacement profiles given in sections 2.3.1 and 2.3.2. We find that applying this method to GaAs disk resonators [91] satisfactorily explains the damping of out of plane

---

[6]'Stokes' spheres and cylinders are two geometries for which the equation of motion of linear oscillations in a viscous fluid can be analytically described [90].

modes, for which Q_M is typically limited in the hundreds by air damping [20].

We expect RBMs to display higher mechanical Q factors in air, due to the reduced interaction surface with the fluid compared to out-of plane flexural modes ($2\pi Rh$ vs πR^2). This is indeed the case: as the pedestal dimensions and clamping losses are reduced, Q_M saturates between 1500 and 1700 in air (see Figure 2.8). These higher values underline the reduced contribution of air damping for RBMs. These results are very similar to the reported Q=1600 in air for the first RBM of high frequency silicon resonators [22]. We are reasonably confident this upper bound comes from air damping. Indeed, even for larger $\varnothing = 10$ μm disk resonators with > 95 % undercut ratios and $Q_{clamping} \sim 10^5$ measured by D. Parrain in the team the Q in air is approximately 1550. This however warrants some further investigation as a simple kinetic theory of gases model[7] which compares the work done by the resonator against the surrounding gas during expansion and contraction would lead us to expect lower air damping and associated mechanical Qs in the 10^4 range. This discrepancy might be due to the neglected contribution of kinetic energy dissipation under the form of acoustic wave radiation, which can be important for high frequency nanoresonators [92].

Squeeze film damping

Squeeze film damping [93] is a special case of air damping, occurring when the resonator vibrates in close proximity to a static surface. Air caught between the resonator and the surface will either circulate in and out (*viscous* regime) or be compressed as in a piston (*elastic* regime) between the two, depending on the squeeze number σ_s [8]. As a rule of thumb, squeeze film damping becomes important when the ratio between film length and height is ≥ 3 (i.e. in our case when disk undercut/pedestal height ≥ 3) [94]. Indeed, we find squeeze film damping to be significant for the (P=0 M=1) *out-of-plane* mode of large GaAs disks ($\varnothing > 10$ μm) probed by a fiber interferometer [91]. For these resonators the disk undercut to pedestal height ratio was ~ 4.3. On the other hand, squeeze film damping is typically not a problem for smaller disk resonators ($\varnothing < 5$ μm) for which the ratio is generally below 1 and for

---

[7]Whether the disk's interaction with the surrounding gas should be treated according to continuum mechanics or statistical mechanics is determined by the Knudsen number $K_n = \frac{\lambda}{L}$. Here λ is the mean free path of the gas molecules ($\simeq 70$ nm in air at 300 K, 1 atm) and L the characteristic length of the problem (the 320 nm disk thickness). Since $K_n \simeq 0.2$, a continuum mechanics description of the gas is appropriate.

[8]$\sigma_s = \frac{12\,\mu\,\omega\,l^2}{P_a\,h_0^2}$ with μ, ω, l, P_a and h_0 respectively the air viscosity, the mechanical frequency, the resonator length, the atmospheric pressure and the distance between the two surfaces. The damping is viscous for $\sigma_s \leq\sim 10$ and elastic above [93].

RBMs which have essentially pure in-plane motion.

2.5.4   Thermo-elastic damping

Thermoelastic damping occurs any time a material is subjected to cyclic stress. During deformation, regions of the material under compressive stress heat up, while regions under tensile stress cool. Heat flow occurs between these hot and cool regions, raising the systems total entropy. This irreversible heat transfer converts mechanical energy into thermal energy, resulting in mechanical dissipation. This dissipation depends on the material's thermal conductivity κ , heat capacity c_p and thermal expansion coefficient α_{th}, as well as on the resonator's geometry and resonance frequency.

Approached analytical expressions for the thermoelastic damping quality factor Q_{td} are available for certain systems, such as the flexural modes of cantilevers [95] or the in-plane modes of beams [96] and thin circular plate resonators [97]. However, we choose to estimate Q_{td} using a 2D axisymmetric multi-physics FEM simulation as this allows us to take into account the influence of the supporting pedestal. This numerical approach contains two separate steps. In a first simulation the mechanical mode's deformation profile and associated thermal stress profile are calculated. These results are then imported into a second thermal conduction simulation which calculates the heat transfer between the hot and cool areas. This then allows to obtain the Q_{td}.

The results of these FEM simulations for GaAs disk resonators with no pedestal are presented in Figure 2.9. Figure 2.9(a) plots Q_{td} at room temperature for the fundamental (P=0) RBM of a GaAs disk as a function of the disk radius R. There is a relatively large variability for Q_{td} depending on the GaAs physical parameters used for the simulation (blue and red squares). However Q_{td} is typically close to or above 10^5. The presence of the pedestal under the disk facilitates the irreversible heat flow to and from the cooler and hotter regions under mechanical stress by adding a supplementary temperature conduction channel (see inset of Fig. 2.9, b). As a consequence adding a 150 nm radius cylindrical AlGaAs pedestal somewhat degrades Q_{td} as expected (circles vs squares). The Q factor decrease is most pronounced for small disks, for which the pedestal is proportionally larger, and is virtually non existent for R$\geq$3 μm (see Figure 2.9, a). Further increasing the pedestal radius can significantly degrade Q_{td}. For instance for a 1 μm radius disk, a 500 nm radius pedestal degrades Q_{td} more than five fold to the 10^4 range compared to the no pedestal case. However the clamping losses (section 2.5.2) increase much faster with r_p, effectively experimentally overshadowing the contribution of the thermoelastic damping.
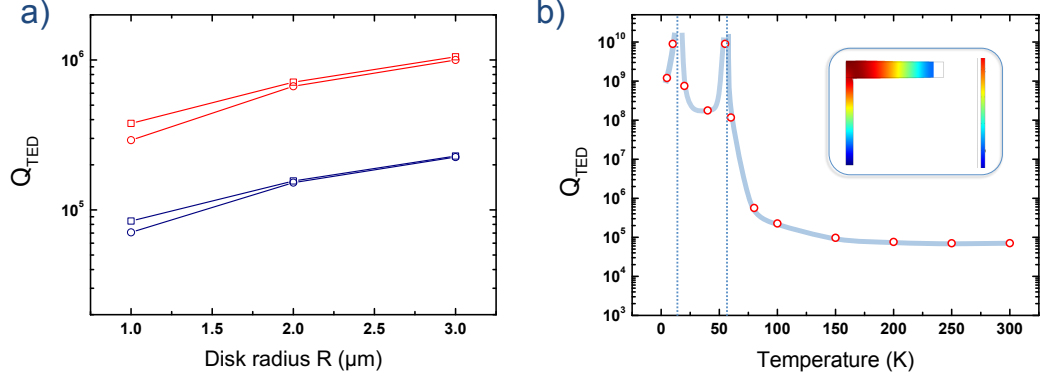
Figure 2.9: **Thermoelastic damping**. (a) FEM simulated values of Q_{td} for a 320 nm thick GaAs disk resonator with no AlGaAs pedestal (squares) and with a 150 nm radius pedestal (circles) as a function of the disk radius R, at room temperature. The red points are obtained using for GaAs the values $\kappa = 33$ W/(m·K), $c_p = 550$ J/(kg·K) from [98]. The blue points use $\kappa = 55$ W/(m·K), $c_p = 327$ J/(kg·K) from [84]. In both cases $\alpha_{th}=5.7 \cdot 10^{-6}$K^{-1}. (b) Dependence of Q_{td} with temperature (T) using the temperature dependent values $\kappa(T)$, $c_p(T)$ and $\alpha_{th}(T)$ from [84], illustrating the rise in Q_{td} at low temperature. The vertical dashed lines indicate the temperatures for which $\alpha_{th}(T)$ changes sign: 56 K and 12 K [84]. The blue curve serves as a guide to the eye. The inset serves to illustrate the strain temperature (a.u.) during contraction of the breathing mode, red=hotter, blue=cooler.

Figure 2.9 (b) investigates the dependency of Q_{td} with temperature, for the fundamental RBM of a 1 μm radius disk with a 150 nm radius pedestal. Indeed the parameters $\kappa(T)$, $c_p(T)$ and $\alpha_{th}(T)$ are strongly temperature dependent. Their values are taken from [84], corresponding to the worst case scenario (blue curves) of Fig. 2.9 (a). The simulations show Q_{td} strongly increases at low temperature (remaining above 10^8 for T$\leq$ 60 K), and diverges at two values of T for which α_{th} is zero : 12 K and 56 K. Thus by operating at cryogenic temperatures the thermoelastic damping can be kept extremely low. Indeed, reference [99] reports a marked increase in the mechanical Q of GaAs cantilevers around 50 K. Finally we verified the FEM simulations provide similar results to the analytical estimates discussed above.

2.5.5   Influence of the surface state

Small thickness resonators oftentimes operate in a regime where the total losses cannot be explained by the summed contributions of clamping losses, air damping and TED alone [100]. Additional loss mechanisms could be surface and/or bulk related. Work by Rugar et al. on silicon nitride and silicon cantilevers show a strong dependence of the mechanical quality factor

with resonator thickness, with the thinnest resonators typically having the worst Q [95]. Such a dependence is indicative of surface loss mechanisms.

Various surface and bulk treatments have been shown to increase mechanical quality factors, such as high temperature annealing of the resonators under ultra-high vacuum conditions [101] or in nitrogen atmosphere [95]. Silicon resonators with hydrogen- and methyl- terminated surfaces have also been shown to exhibit enhanced mechanical properties versus non-treated resonators with native oxide [102, 103].

Surface related mechanical dissipation is the least well known loss mechanism for our system. However we can expect this mechanism to be likely non-negligible for our very small GaAs disk resonators, which have a large surface to volume ratio and optical dissipation dominated by surface properties (see section 5.3). As such, surface dissipation and the influence of surface treatments will need to be investigated in future work.

2.6 Orders of magnitude

Using the formulas provided in section 2.3.2 , one can estimate some orders of magnitude of the mechanical displacement of small GaAs disk resonators (see Table 2.3). One micrometer radius disks have a picogram motional mass for their RBM at GHz frequency. It is interesting to see that the mechanical Brownian motion, which is readily measurable via optical means, is well below 1 picometer at 300 K. The Brownian motion amplitude of the disk boundary for the order P=2 (resp. P=3) RBM at 3.63 GHz (resp. 5.77 GHz) is $\sim$3 (resp. 4.7) times smaller than that of the first order RBM. Finally the disk's boundary can be considered almost static with respect to the surrounding gas molecules at room temperature. Indeed the disk boundary's root mean square (RMS) speed is more than five orders of magnitude lower than that of the molecules[9]. The Reynolds number of the problem is very low[10] and the air flow around the resonator can safely be considered laminar.

---

[9]The RMS speed of gas molecules is given by $v_{RMS} = \sqrt{\frac{3kT}{m}}$, with k and m respectively the Boltzmann constant and mass of one molecule. $v_{RMS} \simeq 500$ m·s^{-1} for 0_2 and N_2 at 300 K.

[10]The Reynolds number Re is defined as $Re = \frac{vL}{\nu}$ with v, L and ν respectively the disk's velocity with respect to the fluid, L the disk's thickness and $\nu \simeq 1.6 \cdot 10^{-5}$ m^{2}s^{-1} air's kinematic viscosity. Here $Re = 2 \cdot 10^{-5}$.

Parameter	Unit	Value
Mechanical frequency	GHz	$\sim$1.38
Disk mass	pg	5.3
m_{eff}/m	-	0.786
Brownian motion amplitude - 300 K	m	$1.6 \cdot 10^{-13}$
RMS boundary speed - 300 K	m·s^{-1}	$0.99 \cdot 10^{-3}$
Brownian motion amplitude - 5 K	m	$2.1 \cdot 10^{-14}$

Table 2.3: Some approximate values of the mechanical properties of the fundamental RBM of a 320 nm thick $\varnothing$=2 μm GaAs disk resonator.

2.7 Conclusion

In this chapter we discussed an analytical description of both the out-of-plane and in-plane mechanical modes of GaAs disk resonators. This description was found to be in good agreement with the results of FEM simulations. Finally we investigated the main loss mechanisms potentially limiting the mechanical Q of the disk resonators. This understanding will be useful in further developments aiming to boost the mechanical properties.

2.8 Mechanics of a stressed SiN beam

Here we briefly describe the mechanical behavior of our SiN on-chip optomechanical WGM resonators. These devices are conceptually identical to the GaAs devices introduced in Fig. 1.2. However in this case the mechanical element we are interested in is no longer the disk resonator itself but the suspended SiN coupling waveguide which acts as a beam nanomechanical resonator (see Fig. 2.10). The disk and resonator are fabricated from Low Pressure Chemical Vapor Deposition (LPCVD) SiN, which exhibits high *tensile* stress (like a drum membrane) in the GPa range (see chapter 4.1). Its is this tensile stress that is responsible for SiN's interesting mechanical properties. The resonance frequency f_i of the ith mechanical mode of a mechanical beam resonator with simply supported extremities[11] is given by : [104, 105]

$$f_i = \frac{i_{\text{th}}^2 \pi}{2L^2} \sqrt{\frac{E\,I}{\rho A}} \sqrt{1 + \frac{\sigma\,A\,L^2}{i_{\text{th}}^2\,E\,I\,\pi^2}} \qquad (2.17)$$

---

[11]There is no analytical solution to describe the doubly clamped extremities case, which is closer to what we have in fabricated devices.
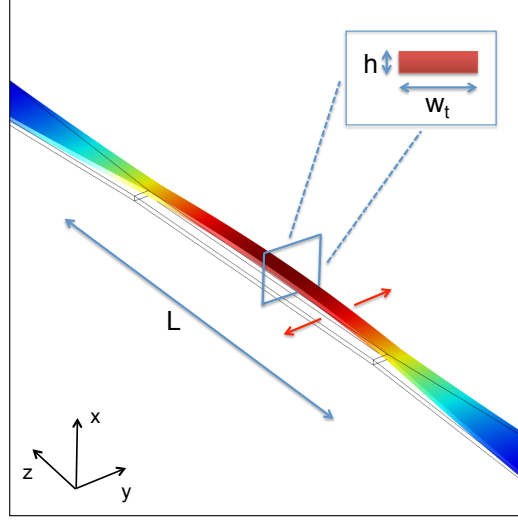
Figure 2.10: In plane movement (red arrows) of a suspended SiN beam of length L, and cross section $w_t \times h$. The color code represents the displacement amplitude with blue for zero and red for max.

Here L, A and I are respectively the beam's length, cross-section area (=h× w_t) and the second moment of area of the beam cross section (see section 2.2). These are shown in Fig. 2.10. Additionally E, ρ and σ are respectively the beam material's Young's modulus, density and tensile stress. i_{th} is the integer mode index (=1 for the fundamental mode, . . .). In the case of large tensile stress σ, the following holds true:

$$\frac{\sigma\, A\, L^2}{i_{\text{th}}^2 E\, I\, \pi^2} \gg 1 \tag{2.18}$$

In this high stress limit, Eq. 2.17 takes the simple form:

$$f_i = \frac{i_{\text{th}}}{2L} \sqrt{\frac{\sigma}{\rho}} \tag{2.19}$$

Here we see the mechanical behavior is entirely determined by the elongation energy of the beam which is proportional to σ; the contribution of the beam bending energy which is proportional to the terms E and I no longer appears in Eq. 2.19. Furthermore the resonance frequency f_i no longer scales with $1/L^2$ as in a relaxed beam, but with 1/L (like a guitar string). This explains the commonly used terminology of SiN *string* resonators for these suspended beam structures [105] under tensile stress.

Mechanism behind the high mechanical Q

High tensile stress LPCVD SiN is a material which has garnered a lot of interest for its ability to provide very high mechanical Qs. An explanation for this property is discussed in detail in [106]. Very simply put, the high tensile stress in the material substantially increases the stored energy inside the mechanical nanoresonator, while adding only a minor contribution to the mechanical energy dissipated per oscillation. From Eq. 2.16, we see this results in a mechanical Q boost.

More information on these SiN nanoresonators, including FEM simulations and experimental results, is available in section 6.3.

Chapter 3

Optomechanics

3.1 Introduction

In the last two chapters we discussed respectively the optical WGMs and the mechanical modes of GaAs disks. This chapter introduces optomechanical models describing how an optical and mechanical mode can couple to each other and exchange energy. We then investigate the various physical mechanisms through which light circulating inside a GaAs disk resonator and mechanical displacement can mutually influence each other and provide some estimates of the magnitude of these coupling mechanisms.

An illustration of the archetypal optomechanical setup is shown in Figure 3.1. It consists in a Fabry-Perot cavity with one fixed and one free end-mirror. Under laser illumination the confined optical field exerts a force on the mechanical boundary through radiation pressure (see section 3.5) and - in the case of a disk resonator - electrostriction and photothermal effects (see sections 3.6 and 3.7). In return, deformation of the mechanical boundary modifies the intracavity circulating power via a shift in the cavity resonance frequency ω_0. The change in ω_0 can be due to a change in the cavity dimensions (see section 3.8.1) and - in the case of a disk resonator - changes in the cavity's refractive index induced by the displacement (see 3.8.2).

Because of this coupling, when the drive laser is tuned to the flank of an optical resonance, a small mechanical displacement dx of the mirror is translated into a change in the transmitted optical intensity I (see Figure 3.2). The magnitude of this shift is given by Eq. 3.1:
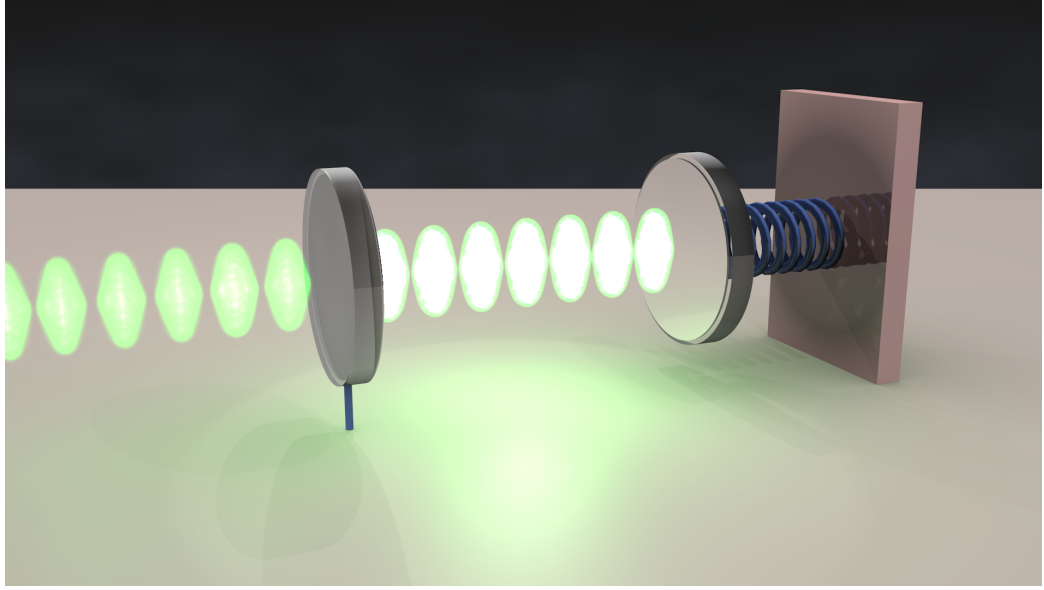
Figure 3.1: Archetypal illustration of an optomechanical resonator consisting of a laser-driven Fabry-Perot cavity with a fixed mirror (left) and a spring-mounted movable end mirror (right).

$$\frac{dI}{dx} = \overbrace{\frac{dI}{d\omega_0}}^{\propto Q_{\mathrm{opt}}} \underbrace{\frac{d\omega_o}{dx}}_{=g_{om}} \tag{3.1}$$

Here we identify the optomechanical coupling term g_{om} times the slope of the optical resonance at the operating point. In systems with high g_{om} and optical Q_{opt} such as GaAs disks very small displacements can be resolved, such as the Brownian motion of a 1.4 GHz RBM with RMS amplitude below 10^{-14} m. The optical field however not only measures the mechanical resonator but can also modify its properties. This is discussed in the following section.

3.2 Classical formulation of optomechanics

We wish to describe the ways in which the mechanical oscillator is modified by the presence of the optical field. To this end we will successively look at the results provided by two classical models. The first looks at the changes in properties of a mechanical oscillator subject to a time-delayed optical force (subsection 3.2.1). It is valid for different kinds of delayed optical forces,
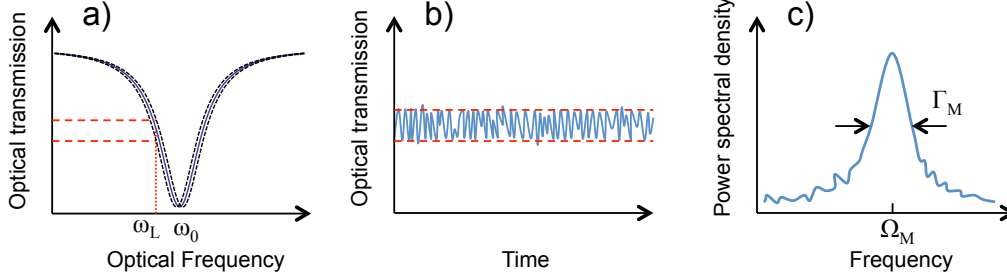
Figure 3.2: Reading out the mechanical Brownian motion of a GaAs disk resonator. (a) Lorentzian transmission profile of a disk's WGM (solid blue curve). Due to the disk's mechanical fluctuations which change the cavity length, the optical resonance frequency continuously fluctuates around its equilibrium position at ω_0 (dashed black lines). As a consequence, even with fixed a laser frequency ω_L the optical transmission varies as a function of time (dashed red lines). (b) Optical transmission as a function of time, with the laser positioned on the WGM resonance flank. Looking at the power spectral density of this signal reveals the presence of a mechanical mode at frequency Ω_M (c).

including photothermal or optoelectronic forces. The second model is based upon coupled mode analysis. It is restricted to radiation pressure effects but is able to correctly describe what happens in the special case when the mechanical frequency exceeds the optical linewidth (subsection 3.2.2).

3.2.1 Time-delayed optical force model

Optical forces do not respond instantly to a mechanical displacement dx of the resonator. This can be because of the finite lifetime of the photons in the cavity in the case of radiation pressure or electrostrictive forces, or because of an intrinsic thermal response time in the case of photothermal forces (see sections 3.5 to 3.7 for more details). Work done by Metzger et al. [107] shows how a mechanical oscillator subject to a time delayed optical force F can be described by an effective harmonic oscillator, with a modified effective damping rate Γ_{eff} and effective resonance frequency Ω_{eff}. In order to describe the time delayed response of the optical force F at time t to a sudden mechanical displacement x(t') at time t', we write:

$$F\left(x\left(t\right)\right) = F(x_0) + \int_0^t dt' \frac{dF\left(x\left(t'\right)\right)}{dt'} h(t - t') \tag{3.2}$$

where h is the delay function of the force F. We consider an exponential type delay function $h(t) = 1 - \exp\left(-t/\tau\right)$, where τ is the time it takes F to reach equilibrium after a sudden displacement. This type of delay function is a reasonable assumption, as it both adequately represents the delay in

3.2 Classical formulation of optomechanics
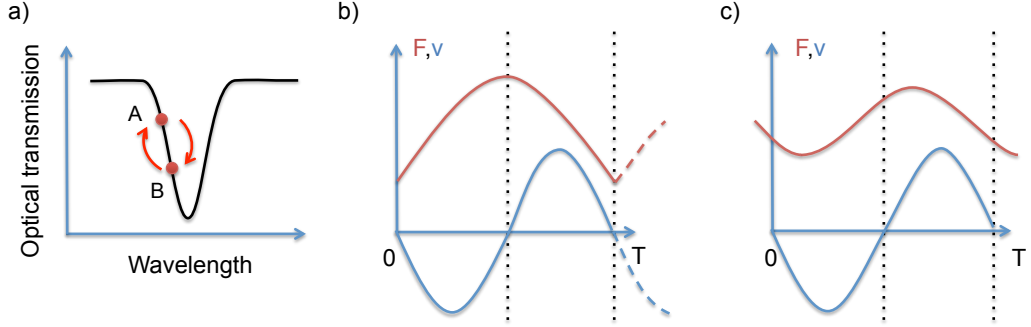
Figure 3.3: Work produced by a time delayed optical force. (a) The pump laser is tuned to the blue side of a WGM resonance. During a mechanical oscillation the optical transmission varies between a maximum at point A and a minimum at B. (b) & (c): Plot of the mechanical resonator velocity v (blue) and the optical force F (red) during a mechanical oscillation (of period T) from A to B and back to A. (b) The optical force is proportional to the intracavity energy, with no time delay. No work W is done by F during an oscillation, as $W = \int_0^T F\,v\,dt = 0$. (c) The optical force responds to changes in cavity length with a exponential time delay (see Eq. 3.2). Due to the time delay F's temporal variations are smoother and F's amplitude changes are reduced. F 'lags' behind v, so that $W = \int_0^T F\,v\,dt > 0$ (heating). If the time delay is too large, F becomes almost flat and $\int_0^T F\,v\,dt \to 0$. The work W is maximal for $\Omega_M \tau = 1$ (see Eq. 3.3). Similarly cooling happens on the other flank of the WGM resonance.

the radiation pressure and electrostriction due to the finite lifetime of the confined photons in the cavity, and the thermal response time of the resonator after photon absorption. With this kind of delay function, the new effective damping rate of the resonator Γ_{eff} can be written as a function of the original damping rate Γ as [107]:

$$\Gamma_{\text{eff}} = \Gamma \left(1 + Q_M \frac{\Omega_M \tau}{1 + \Omega_M^2 \tau^2} \frac{\nabla F}{K} \right) \tag{3.3}$$

where Ω_M, Q_M, $\Gamma_M = \Omega_M/Q_M$ and K are respectively the unperturbed mechanical mode frequency, quality factor, damping and stiffness, while $\nabla F = \partial F/\partial x$ represents the steady-state change in optical force for a small displacement dx of the mechanical resonator. Likewise, the modified resonance frequency Ω_{eff} is given by Eq. 3.4, [107].

$$\Omega_{\text{eff}}^2 = \Omega_M^2 \left(1 - \frac{1}{1 + \Omega_M^2 \tau^2} \frac{\nabla F}{K} \right) \tag{3.4}$$

The ∇F term in Eq. 3.4 can be seen as the contribution of an additional restoring force with positive or negative stiffness, modifying the resonance frequency Ω_M. This is called the *optical spring* effect. The modified mechan-

ical resonator still follows the equipartition theorem[1], however it behaves as if it were no longer at the bath temperature T but at a modified effective temperature T_{eff} defined by Eq. 3.5, [107]:

$$\frac{T_{\text{eff}}}{T} = \frac{\Gamma}{\Gamma_{\text{eff}}} \tag{3.5}$$

Figure 3.3 illustrates how the time-delayed optical force adds or removes vibrational energy from the mechanical mode, modifying its effective temperature. Using the results of this first model, we can calculate the necessary power threshold for the onset of self-oscillation (or self-sustained oscillations). Self sustained oscillations occur when the effective damping rate Γ_{eff} (Eq. 3.3) reaches zero. At this stage the movement is strongly amplified and reaches a maximal amplitude for which the energy fed into the resonator by the optical field per mechanical oscillation is equal to the dissipated mechanical energy during this same cycle. In order to compute this threshold in experimental terms, ∇F needs to be expressed a function of the pump laser power P_L. In the case of pure radiation pressure coupling and taking the approximation $g_{om} = -\omega_0/R$ with R the disk radius, we have:

$$F = \overbrace{N_{ph} \hbar \omega_0}^{stored\,energy} \frac{1}{R} = \frac{P_L Q_{\text{opt}}}{\omega_0 R} \Lambda\left(\omega_0\left(x\right)\right) \tag{3.6}$$

where N_{ph} is the number of intracavity photons of frequency ω. The derivation of the first equality of Eq. 3.6 is done in section 3.5. Here we write the stored energy in the resonator as P_L times the cavity storage time Q_{opt}/ω_0 times a lorentzian function $\Lambda\left(\omega_0\left(x\right)\right)$ describing the WGM resonance. The force gradient is then:

$$\nabla F = -\frac{P_L Q_{\text{opt}}}{\omega_0 R^2} \Lambda\left(\omega_0\left(x\right)\right) + \frac{P_L Q_{\text{opt}}}{\omega_0 R} \overbrace{\frac{\partial \Lambda}{\partial \omega_0}}^{\propto Q_{\text{opt}}} \underbrace{\frac{\partial \omega_0}{\partial x}}_{g_{om}} \simeq -\frac{P_L Q_{\text{opt}}^2}{R^2 \omega_0} \tag{3.7}$$

The first term in Eq.3.7 represents the change in radiation pressure with cavity radius at constant photon number and can safely be neglected as it is negligible compared to the second term proportional to g_{om} times the slope of the lorentzian curve. Therefore setting Eq. 3.3 equal to zero and writing $K = m_{\text{eff}}\Omega_M^2$, we get the self-oscillation threshold optical power P_{thresh}:

$$P_{\text{thresh}} \simeq \frac{m_{\text{eff}} R^2 \omega_0^2 \Omega_M}{Q_{\text{m}} Q_{\text{opt}}^3} \left(1 + \Omega_M^2 \tau^2\right) \tag{3.8}$$

---

[1]Which states $\frac{1}{2}K < x^2 >= \frac{1}{2}k_B T$, with k_B Boltzmann's constant.

From Eq. 3.8, we can see that in the case of $\Omega_M \tau$ smaller than 1, P_{thresh} exhibits a $1/Q_{\text{m}}$ and $1/Q_{\text{opt}}^3$ dependency. The case $\Omega_M \tau < 1$ is called the *bad cavity* or *unresolved sideband* limit (see Figure 3.5). This inverse cube dependency on optical quality factor can be traced back to its three distinct origins. Indeed the threshold power P_{thresh} is inversely dependent upon the force's time delay ($\propto Q_{\text{opt}}$), upon the intracavity circulating power ($\propto Q_{\text{opt}}$) and upon the slope of the optical resonance ($\propto Q_{\text{opt}}$). As a side note, in the case of the RBMs of a disk resonator, Ω_M scales with $\sim 1/\text{R}$, while m_{eff} scales with R^2. Therefore P_{thresh} scales with R^3 in the unresolved sideband regime, underscoring the merit of miniaturizing resonator dimensions (if the self-oscillation regime is desired).

According to this model, for $\Omega_M \tau \gg 1$, the power threshold keeps decreasing with increasing Q_{opt} but at a slower rate ($\propto 1/Q_{\text{opt}}$), illustrating how a too large time delay for the optical force is less effective at producing work. However this model does not take into account the effect of detuning on the optical cavity dynamics which is important if focusing on radiation pressure effects. When $\Omega_M \tau$ becomes larger than 1 (*good cavity* or *resolved sideband* limit) the discrepancy becomes significant and this model is no longer accurate, as shown in the following section.

3.2.2 Coupled mode analysis model

This model developed in the team of Kerry Vahala [48, 108] is based upon coupled-mode theory (see Chapter 1). The model aims to describe the optomechanical dynamics of a silica WGM toroid coupled to a fiber taper, hence it includes the coupling effects associated with the waveguide resonator junction. The model describes the mechanical oscillator interacting with the light field as a set of linked differential equation describing the time evolution of the pump, stokes, antistokes and mechanical mode amplitudes (see Fig. 3.5). Solving these equations in the steady state gives the following threshold for the onset of self-oscillation, using the notation of [23]:

$$P_{\text{thresh}} = \frac{m_{\text{eff}} \omega_0}{2g_{om}^2} \frac{\Gamma_0 \Gamma_M}{\Gamma_t \, \Delta} \left[(\Delta - \Omega_M)^2 + (\Gamma_t/2)^2 \right] \left[(\Delta + \Omega_M)^2 + (\Gamma_t/2)^2 \right] \quad (3.9)$$

Where Γ_0 and Γ_t are respectively the photon decay rates for the unloaded and loaded optical cavity (see chapter 1 for details), while Γ_M and $\Delta = \omega_L - \omega_0$ are respectively the mechanical energy decay rate and the laser-cavity detuning. Note that in the bad cavity limit and for $g_{om} = -\omega_0/R$, Eq. 3.9 reduces to:

$$P_{\text{thresh}} \propto \frac{m_{\text{eff}} R^2 \omega_0^2 \Omega_M}{Q_{\text{m}} Q_{\text{opt}}^3} \quad (3.10)$$
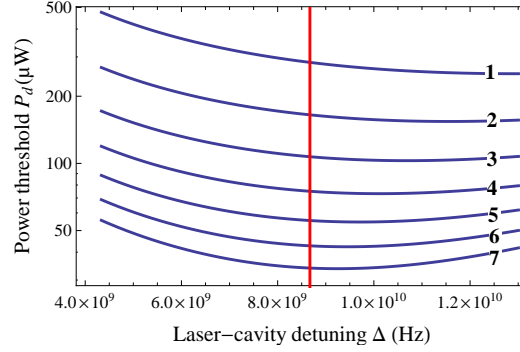
Figure 3.4: Self oscillation threshold power P_{thresh} as a function of laser-cavity detuning Δ, for different intrinsic cavity quality factors Q_{int}. Curves 1 through 7 correspond to Q_{int} taking the values $5 \cdot 10^4$ through $1.1 \cdot 10^5$ by 10^4 increments. The vertical red line corresponds to a cavity detuning $\Delta = \Omega_m$. As Q_{int} increases and the system nears the resolved sideband regime, the optimal detuning tends to $\Delta = \Omega_M$.

which is identical to the result from the time-delayed model (Eq. 3.8) with the same $1/Q_m \times 1/Q_{\text{opt}}^3$ dependency. In the good cavity limit ($\Omega_M \tau > 1$), two competing effects occur. The heating efficiency in terms of circulating power is maximal when the stokes sideband is resonant with the optical cavity. However in the good cavity limit this only occurs with the pump laser laser lying outside the WGM resonance and therefore unable to adequately buildup circulating power. This imposes an asymptotic minimal threshold power, which can be shown to occur in the overcoupled regime ($\Gamma_t > 2\Gamma_0$) where the $\Omega_M \tau < 1$ condition is again met.

Figure 3.4 plots an estimate of P_{thresh} as a function of the laser-cavity detuning Δ, for different values of the optical quality factor for a GaAs disk. This calculation is done for the first RBM of a $\varnothing = 2 \ \mu$m disk with a mechanical quality factor of 1500 in air and the WGM at critical coupling ($\Gamma_t = 2\Gamma_0$). Because of the $1/Q_{\text{opt}}^3$ dependency, small gains in Q_{opt} lead to dramatic decreases in P_{thresh}.

3.3 Quantum formulation of optomechanics

Optomechanical Hamiltonian

Equation 3.11 shows the optomechanical Hamiltonian describing an optical field coupled to a mechanical resonator [109]:

$$\hat{H} = \hbar \omega(\hat{x}) \hat{a}^\dagger \hat{a} + \hbar \Omega_M \hat{b}^\dagger \hat{b} + ... \tag{3.11}$$

$\hat{a}^\dagger$ ($\hat{b}^\dagger$) and $\hat{a}$ ($\hat{b}$) are respectively the photon (phonon) creation and annihilation operators. Left out are terms relating to the pump laser and coupling to

the environment. The photon frequency is dependent upon the mechanical displacement $\hat{x} = x_{\text{ZPF}} \left(\hat{b} + \hat{b}^\dagger \right)$. x_{ZPF} corresponds to the amplitude of the mechanical zero point fluctuations[2] and is given by:

$$x_{\text{ZPF}} = \sqrt{\frac{\hbar}{2\, m_{\text{eff}}\, \Omega_M}} \tag{3.12}$$

writing $\omega(\hat{x})$ as $\omega_0 - g_{om}\, \hat{x}$ in the linear approximation with ω_0 the resonance frequency at zero displacement makes a $-F\hat{x}$ term appear in Eq. 3.11. F is the radiation pressure force:

$$\hat{F} = -\hbar g_{om} \hat{a}^\dagger \hat{a} \tag{3.13}$$

The standard optomechanical Hamiltonian is therefore:

$$\hat{H} = \hbar\omega_0 \hat{a}^\dagger \hat{a} + \hbar\Omega_M \hat{b}^\dagger \hat{b} - \hbar g_0 \hat{a}^\dagger \hat{a} \left(\hat{b}^\dagger + \hat{b} \right) + ... \tag{3.14}$$

where g_0 is the optomechanical single photon coupling strength. It represents the frequency shift due to a displacement equal to x_{ZPF} with $g_0 = g_{om} x_{\text{ZPF}}$. For a strong laser drive, $\hat{a}$ can be written $\hat{a} = (\alpha + \delta\hat{a}) \exp(-i\omega_0 t)$ with $\alpha = \sqrt{N_{ph}}$ the average optical field amplitude and $\delta\hat{a}$ the field fluctuations. Then:

$$\hat{a}^\dagger \hat{a} = \alpha^2 + \alpha \left(\delta\hat{a}^\dagger + \delta\hat{a} \right) + \delta\hat{a}^\dagger \delta\hat{a} \tag{3.15}$$

Neglecting the first term responsible for a static force and the last which is smaller than the other two provides the Hamiltonian of linearized optomechanics:

$$\hat{H} \approx \underbrace{-\hbar \overbrace{g_0\alpha}^{\text{g}} \left(\delta\hat{a}^\dagger + \delta\hat{a} \right) \left(\hat{b}^\dagger + \hat{b} \right)}_{\text{linearized optomechanical interaction}} + \hbar\Omega_M \bar{b}^\dagger \hat{b} - \hbar\Delta\delta\hat{a}^\dagger \delta\hat{a} + ... \tag{3.16}$$

This introduces the optomechanical coupling strength g which scales with $\sqrt{N_{ph}}$. While the optical and mechanical frequencies are vastly different, in this picture we see the mechanical mode effectively couples to fluctuations in the optical field which are of comparable frequency.

Quantum limit of optomechanical cooling

According to the classical models presented in section 3.2, the optical damping can in theory be increased to arbitrarily high values simply by increasing

---

[2]In the case of the first RBM of a 320 nm thick and $\varnothing = 2\ \mu$m GaAs disk, $x_{\text{ZPF}} = 1.2 \cdot 10^{-15}$ m.

the laser power. The minimal effective temperature attainable for the mechanical vibration mode would thus tend to zero (via Eq. 3.5). In a quantum picture this does not happen as increasing the laser power increases the shot noise fluctuations of the photon field in the resonator, resulting in increased fluctuations of the optical force δF. This added noise prevents the mechanical mode temperature from becoming arbitrarily small with increasing laser power.

Quantum theory of cavity-assisted cooling of a mechanical resonator developed by Marquardt et al. [110] shows that it is the asymmetry between the stokes and antistokes noises (that leads to cooling or heating) which is ultimately responsible for the minimal attainable temperature/phonon occupancy[3]. The model assumes a high mechanical quality factor ($Q_M \gg 1$) and an optically induced damping rate Γ_{opt} and mechanical damping rate Γ_M much weaker than the cavity's intrinsic decay rate κ ($\Gamma_{\mathrm{opt}}+\Gamma_M \ll \kappa$), both of which are verified in our devices. The mean steady-state number $\bar{n}_M^O$ of resonator phonons in the absence of mechanical damping (oscillator only coupled to the light field and no thermal environment) is determined by the ratio between the strength of the antistokes (cooling) and stokes (heating) mechanisms and given by Eq. 3.17 [110].

$$\bar{n}_M^O = -\frac{(\Omega_M + \Delta)^2 + (\kappa/2)^2}{4\Omega_M \Delta} \tag{3.17}$$

In the case of a detuning $\Delta = -\Omega_M$ (optimal for $\Omega_M > \kappa$), $\bar{n}_M^O$ becomes: [110]

$$\bar{n}_M^O = \left(\frac{\kappa}{4\,\Omega_M}\right)^2 \tag{3.18}$$

This number is only well below unity in the resolved sideband regime ($\Omega_M > \kappa$). For the same $\Delta = -\Omega_M$ detuning, the optical damping is worth: [110]

$$\Gamma_{\mathrm{opt}} = 4\left(\frac{x_{\mathrm{ZPF}}}{L}\right)^2 \frac{\omega_0^2 N_{\mathrm{ph}}}{\kappa} \frac{1}{1 + \left(\frac{\kappa}{4\Omega_M}\right)^2} \tag{3.19}$$

With L the cavity length (R for a disk) and N_{ph} the mean photon number in the resonator. Adding the contribution of the mechanical damping Γ_M yields the mean steady state phonon number $\bar{n}_M$: [110]

$$\bar{n}_M = \frac{\Gamma_{opt}\, \bar{n}_M^O + \Gamma_M\, \bar{n}_M^T}{\Gamma_{opt} + \Gamma_M} \tag{3.20}$$

---

[3]The mechanical mode's effective temperature T_{eff} is linked to the mode's mean phonon number $\bar{n}_M$ through $\hbar\Omega_M \left(\bar{n}_M + 1/2\right) = k_B T_{\mathrm{eff}}$.

Figure 3.5: Bad cavity (a) versus good cavity (b) limits. The schematics show the optical resonance, of linewidth κ, plotted in the frequency domain. The interaction between the optical field oscillating at the laser frequency ω_L and the mechanical oscillator at Ω_M results in two sidebands, called the stokes (S) and antistokes (AS) sidebands at $\omega_L \pm \Omega_M$. In the bad cavity limit, Ω_M is smaller than the cavity linewidth κ, so both sidebands can simultaneously lie within the cavity resonance. This is no longer the case in the good cavity limit where $\Omega_M > \kappa$. In both (a) and (b) the antistokes sideband is resonant with the optical cavity, favoring the process of pump photons leaving the resonator at higher frequencies (higher energy), resulting in net cooling of the mechanical mode. In (b) however the asymmetry between the two sidebands is larger, leading to a smaller minimum phonon occupation (see section 3.3).

Here $\bar{n}_M^T$ is the mean mechanical mode phonon occupation at equilibrium with the bath at T. Equation 3.20 represents the competition between mechanical energy removal from the resonator by the optical field and replenishment by the surrounding thermal bath. It emphasizes the benefits of high mechanical quality factors and low bath temperatures (cryogenics) to reach the quantum regime.

For a GaAs resonator oscillating at 1.4 GHz, the optical Q needs to be above $1.6 \cdot 10^5$ to be in the good cavity limit and be able to approach the quantum ground state.

3.4 Optomechanical forces in GaAs disks

In the following three sections we will investigate the three main optical forces through which the confined light field can act upon the GaAs disk resonator. These are the radiation pressure force (section 3.5), the electrostrictive force (section 3.6) and the photothermal or bolometric force (3.7). The magnitude and pertinence of each of these forces for optomechanical experiments will be examined.

3.5 Radiation pressure in a disk resonator

In this section we describe the particular case of radiation pressure exerted by photons confined by total internal reflection inside a circular disk resonator. The radiation pressure will be calculated both through simple analytical energy and momentum conservation arguments (see section 3.5.1) and by 3D FEM computations of the Maxwell Stress Tensor (MST) (see section 3.5.2). While both approaches fittingly yield consistent results, each provides specific insights into the radiation pressure mechanism.

3.5.1 Analytical estimation

Energy conservation arguments

In this section, we will consider that the cavity resonance frequency is only dependent on the geometrical dimensions of the resonator and that the disk's refractive index is not modified by the mechanical displacement. The influence of the mechanical displacement on the local refractive index is investigated separately in sections 3.6 and 3.8.2. In the general case, the stored electromagnetic energy in the resonator is given by Eq. 3.21:

$$E = N_{ph}\hbar\omega \tag{3.21}$$

with N_{ph} the number of stored photons in the resonator, ω the photon's frequency and $\hbar$ Planck's constant. A small mechanical displacement of the disk δx leads to a change in the photon frequency $\Delta\omega$ and stored energy ΔE such that $\Delta E = N_{ph}\hbar\Delta\omega$. Therefore the force associated to this work can be written as Eq. 3.22:

$$F = -\frac{\Delta E}{\Delta x} = -N_{ph}\hbar\frac{\Delta\omega}{\Delta x} = -N_{ph}\hbar g_{om} \tag{3.22}$$

Momentum conservation arguments

Let us consider the radiation pressure exerted on the outer boundary of a disk resonator by a confined photon, through momentum conservation arguments. In free space, the momentum associated with a photon of wavelength λ_0 is $\hbar k_0$, with $\hbar$ = Planck's constant and $k_0 = 2\pi/\lambda_0$ the free space wavenumber. When this photon impinges on a mirror with orthogonal incidence, and is perfectly reflected, conservation of momentum dictates that the mirror receives $2\hbar k_0$ momentum (see Fig. 3.6 , a). We now wish to describe how much momentum is transferred to a circular resonator by a photon confined by total internal reflection, as this photon performs a round-trip. Using ray

3.5 Radiation pressure in a disk resonator
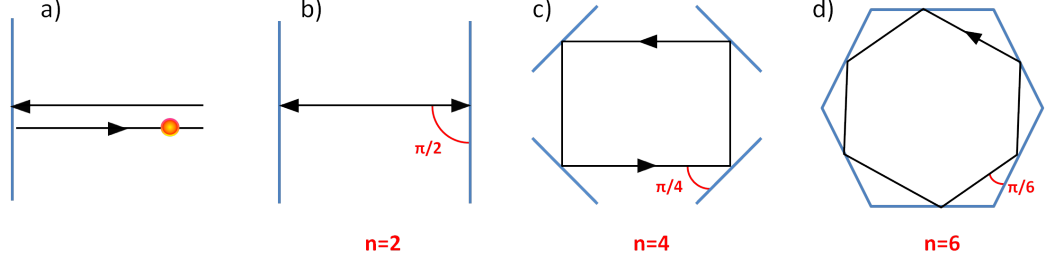
Figure 3.6: (a) Momentum transfer as a photon strikes a reflective surface. (b), (c) and (d) : schematic view of an optical cavity composed of n=2; 4 or 6 mirrors and the associated grazing angles.

optics considerations, a photon confined inside a regular cavity with n side-walls will strike the sidewalls n times per round-trip at an angle of π/n, each time transferring a momentum $2\hbar k \sin(\pi/n)$ (see Fig. 3.6 b, c, d). The momentum transfer as one photon completes one round trip inside a circular disk resonator can be therefore seen as the limit :

$$2\hbar k \lim_{n\to\infty} n \sin(\pi/n) = 2\pi\hbar k \tag{3.23}$$

Note how we now use k instead of k_0 for the wavenumber of the photon, as we now consider the case of a photon confined inside a dielectric medium. The value of k in the dielectric will be defined as a function of k_0 in the following. The associated force per photon is therefore the momentum transfer per round-trip (Eq. 3.23) divided by the round-trip time τ_{rt} and can be written for a disk of radius R and thickness h:

$$F = m \times a = \frac{dP}{dt} = \underbrace{\frac{2\pi\hbar k}{2\pi R n_{\text{eff}}/c}}_{\tau_{rt}} = \frac{\hbar k c}{n_{\text{eff}} R} \tag{3.24}$$

Here c is the speed of light in vacuum, and n_{eff} is the effective index of refraction 'felt' by the photon. Provided we write the photon momentum $\hbar k$ in a material of refractive index n_{eff} as $\hbar k = \hbar k_0 \, n_{\text{eff}}$ [4] and use the geometrical approximation $g_{om} = -\omega_0/R$, for a purely radial displacement of the disk, we can write the radial force F_{rp} exerted by a number N$_{ph}$ photons confined in a disk resonator under the simple form:

$$F_{rp} = N_{ph} \frac{\hbar \, k_0 \, c}{R} \simeq -N_{ph} \, \hbar \, g_{om} \tag{3.25}$$

Here we see the expression of the radiation pressure force obtained through momentum conservation (Eq. 3.25) is consistent with that obtained through

---

[4] This is the Minkowski formulation for the momentum of a photon in a dielectric [111].

Radiation pressure in GaAs disks				
Parameter	Name	Unit	*System 1*	*System 2*
Disk radius	R	μm	1	3.5
Disk weight	P_{disk}	N	$5.2 \cdot 10^{-14}$	$4 \cdot 10^{-13}$
Resonance wavelength	λ_0	μm	1.32	1.55
Intrinsic optical Q	Q_{int}	-	10^5	10^5
Finesse	$\mathcal{F}$	-	$5 \cdot 10^3$	1560
Round trip time	τ_{rt}	s	$6.4 \cdot 10^{-14}$	$1.9 \cdot 10^{-13}$
Dropped power	P_d	μW	200	10^3
Circulating power	P_{circ}	mW	159	249
Stored photons	N_{ph}	-	$\sim 68\ 000$	$\sim 372\ 000$
Photon energy $\hbar\omega_{opt}$	E_{ph}	J	$1.5 \cdot 10^{-19}$	$1.28 \cdot 10^{-19}$
Radiation pressure force per photon	F_{rp}/N_{ph}	N	$1.5 \cdot 10^{-13}$	$3.6 \cdot 10^{-14}$
Radiation pressure force	F_{rp}	N	$\sim 1 \cdot 10^{-8}$	$1.36 \cdot 10^{-8}$
Radiation pressure per photon	P_{rp}/N_{ph}	Pa	$7.5 \cdot 10^{-2}$	$8.3 \cdot 10^{-3}$
Radiation pressure	P_{rp}	Pa	5100	3100

Table 3.1: Optical parameters and related radiation pressure orders of magnitude for two typical GaAs disk resonator systems. *System 1* corresponds to a typical on chip $\varnothing = 2$ μm and 320 nm thick GaAs disk resonator with integrated coupling waveguide, while *system 2* is a typical freestanding 200 nm thick $\varnothing = 7$ μm GaAs disk resonator coupled to via a pulled silica fiber (as the ones in [20]). (The two different coupling schemes explain the distinct typical dropped powers).

energy conservation (Eq. 3.22). As a result of Eq. 3.25, the radiation pressure P_{rp} exerted by N_{ph} photons on the disk resonator's vertical outer boundary of surface $S = 2\pi R\, h$ is given by Eq.3.26:

$$P_{rp} = F_{rp}/S = N_{ph} * \frac{\hbar k_0 c}{2\pi R^2 h} = N_{ph} * \frac{\hbar c}{\lambda_0 R^2 h} \qquad (3.26)$$

From Eqs. 3.25 and 3.26 we can see that the exerted force and pressure depend on the number of stored photons inside the cavity. This underlines the importance of working with a resonator of high optical quality factor Q_{opt}, as the number of stored photons for a fixed pumping optical power scales with Q_{opt}. Furthermore, the $\frac{1}{R^2}$ pressure dependency illustrates the benefit of using small diameter disk resonators. Finally we can see both force and pressure exerted by the stored photons are independent of the refractive index of the resonator material. The benefit of using high refractive index materials appears only indirectly, through the reduced disk radii fea-

sible before incurring significant radiation losses. Equations 3.25 and 3.26 are expressed in terms of the stored cavity photon number N_{ph} which is proportional to the stored energy. This energy can be expressed in terms of the more experimentally accessible parameter P_{drop}, which is the dropped power in the disk resonator :

$$E = N_{ph}\hbar\omega = P_{\text{circ}}\,\tau_{rt} \propto \frac{P_{\text{drop}}}{R}R \qquad (3.27)$$

Equation 3.27 shows the number of photons in the resonator N_{ph} is proportional to the dropped power P_{drop}. As a consequence, the same $\frac{1}{R}$ dependency for the force and $\frac{1}{R^2}$ dependency for radiation pressure hold when expressing these as a function of the dropped power, in the limit where the optical Q does not depend on the disk radius.

A numerical estimate of Eq. 3.26 for a *single* photon of wavelength λ_0=1.32 μm confined inside a disk resonator of radius 1 μm and thickness 320 nm yields a relatively high P_{rp}=0.075 Pa. Table 3.1 provides detailed estimates of the radiation pressure magnitude for two typical GaAs disk resonator systems.

Due to the strong optical confinement and optical quality factor they provide, GaAs disk resonators are subject to significant levels of radiation pressure in realistic experimental conditions. Indeed, notice the high value of the radiation pressure P_{rp} - in the several 10^3 Pascal range - exerted on the outer vertical boundary of the small resonators of *System 1*. For comparison, the atmospheric pressure at sea level is roughly 10^5 Pa, while the radiation pressure due to sunlight striking the earth's surface, assuming perfect reflection is only $\sim 9 \cdot 10^{-6}$ Pa (considering a 1.3 kW/m^2 irradiance). Furthermore, the very large magnitude of the radiation force F_{rp} exerted on these small resonators relative to their size is also highlighted by the fact that F_{rp} can be more than a hundred thousand times larger than the disk's own weight (see Table 3.1).

3.5.2   Numerical simulation: Maxwell stress tensor

In this section we estimate the magnitude of the radial radiation pressure per confined photon by computing the spatially dependent Maxwell stress tensor (MST) in a GaAs disk resonator. The MST formalism stems from momentum conservation arguments applied to the charges in the material and the confined electromagnetic field [112]. It can be used to describe the optically induced stress distribution inside a dielectric medium [113].

In a dielectric medium of relative permittivity $\varepsilon_r(x, y)$ and permeability
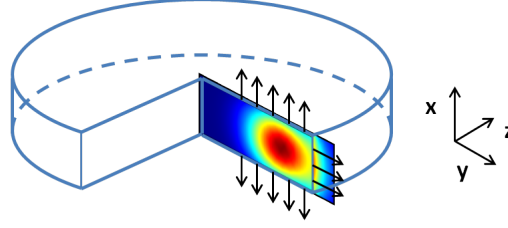
Figure 3.7: Illustration of the radiation pressure due to confined electromagnetic energy inside a GaAs WGM resonator. The schematic shows the coordinate system, along with the xy cross-section over which the stress distribution is computed (see Fig. 3.8). The radiation pressure due to confined photons is directed outwards (black arrows).

μ_r, the ij components of the MST are given by Eq. 3.28:

$$T_{ij} = \varepsilon_0\,\varepsilon_r(x,y)\left[E_i E_j - \frac{1}{2}\delta_{ij}\,|E|^2\right] + \mu_0\,\mu_r\left[H_i H_j - \frac{1}{2}\delta_{ij}\,|H|^2\right] \qquad (3.28)$$

Here $\varepsilon_0 = 8.85 \cdot 10^{-12}$ F·m^{-1} and $\mu_0 = 4\pi \cdot 10^{-7}$ H·m^{-1} are respectively the vacuum permittivity and permeability, δ_{ij} is Kronecker's delta and $E_i\,(H_i)$ is the ith electric (magnetic) field component. In the following we will take $\varepsilon_r(x,y) = n^2 \in \mathbf{R}$ and $\mu_r{=}1$ inside the GaAs, and $\varepsilon_r{=}\mu_r{=}1$ in the surrounding air. With the choice of notations of Eq. 3.28 (same as [113]), the radiation pressure induced stress σ_{ij}^{rp} (applied on the face normal to the i direction along the j direction) is expressed as a function of the MST element T_{ij} as $\sigma_{ij}^{rp} = -T_{ij}$. This approach not only allows for computing the normal stresses in the structure (for which the stress is normal to the applied face, i.e. σ_{ii}), but also the shear stresses ($\sigma_{ij}, i \neq j$) due to the presence of the photon. In the following however, we will only focus on the normal radial stress, as it is the main stress that actually produces work when coupled to the radial displacement of a mechanical RBM. Since the disk material cannot respond to rapidly varying forces at optical frequencies (10^{14} Hz range), we will compute the time averaged value of the radial stress over an optical cycle.

Figure 3.7 provides an illustration of the confined electric field inside a GaAs disk resonator, along with the choice of coordinate system. For consistency we employ the same x, y, z coordinate system as in Chapter 1. The electromagnetic distribution and stress distribution are computed and plotted in the illustrated xy cross-section starting at the center of the disk. Due to the problem's rotational invariance around the x axis, the x, y and z components of the electromagnetic and stress distributions can be thought of as respectively the radial, azimuthal and axial components.

In order to calculate the radial radiation pressure due to a photon con-

fined in the resonator in a specific WGM, we first perform a FEM simulation of the desired WGM (in this case a p=1, m=10 at $\lambda_0 \simeq 1320$ nm). This simulation provides all the main electric and magnetic field components needed to compute Eq. 3.28. These main field components are plotted in Figure 3.8 a, b, c, d, and e. With the knowledge of these, the value of the time-averaged normal radial stress $\sigma_{yy}^{rp} = -T_{yy}$ is calculated at every point in space along the xy cross-section (see Fig. 3.8, f). From this we can see that the normal radial stress is largest near the outer edge of the disk, where the light is confined. To a local stress can be associated a local volume force (force per unit volume) $\mathcal{F}$, by the relation:

$$\mathcal{F}_j^{rp} = -\partial_i \sigma_{ij}^{rp} = \partial_i T_{ij} \tag{3.29}$$

The spatial distribution of the radiation volume force $\mathcal{F}_y^{rp}$ is maximal right at the discontinuous dielectric interface (at y=1 μm), lending some degree of support to the previously used image of the photon as a particle exerting a force as it bounces off the resonator sidewalls (not shown here).

In order to compare the results of the MST method to the previous momentum conservation method (section 3.5.1), we define a volume averaged normal radial stress $\overline{\sigma}_{rr}^{rp}$ in Eq. 3.30:

$$\overline{\sigma}_{rr}^{rp} = \frac{\iiint \sigma_{rr}^{rp} \, dV}{\pi \, R^2 \, h} \tag{3.30}$$

Here the integration in the numerator carries over the volume of the GaAs disk resonator, and r refers to the radial coordinate. In the case of a single confined photon of wavelength $\lambda \simeq 1.3$ μm, we find $\overline{\sigma}_{rr}^{rp}$=0.084 Pa. This value is quite close to the 0.075 Pa found using the analytical formalism. The small ($\sim$10%) difference between the two disappears when one uses an effective radius of ~ 0.85 μm in Eq 3.26, which represents the center of mass of the electromagnetic energy distribution in the example considered here.

Radiation pressure also exerts an outward pressure oriented along the x axis upon the horizontal disk boundaries (see vertical arrows in Fig. 3.7). The magnitude of this axial pressure is comparable to the radial pressure.

Steady state boundary displacement and resonance wavelength shift

In sections 3.5.1 and 3.5.2 we showed that under realistic experimental conditions, the steady-state radiation pressure applied on the disk's periphery could be quite large. Here we wish to rapidly discuss whether or not this pressure leads to a significant boundary displacement δr and associated resonance wavelength shift $\delta\lambda$. In the case of *System 1*, the $\sim$5$\cdot$10^3 Pa pressure
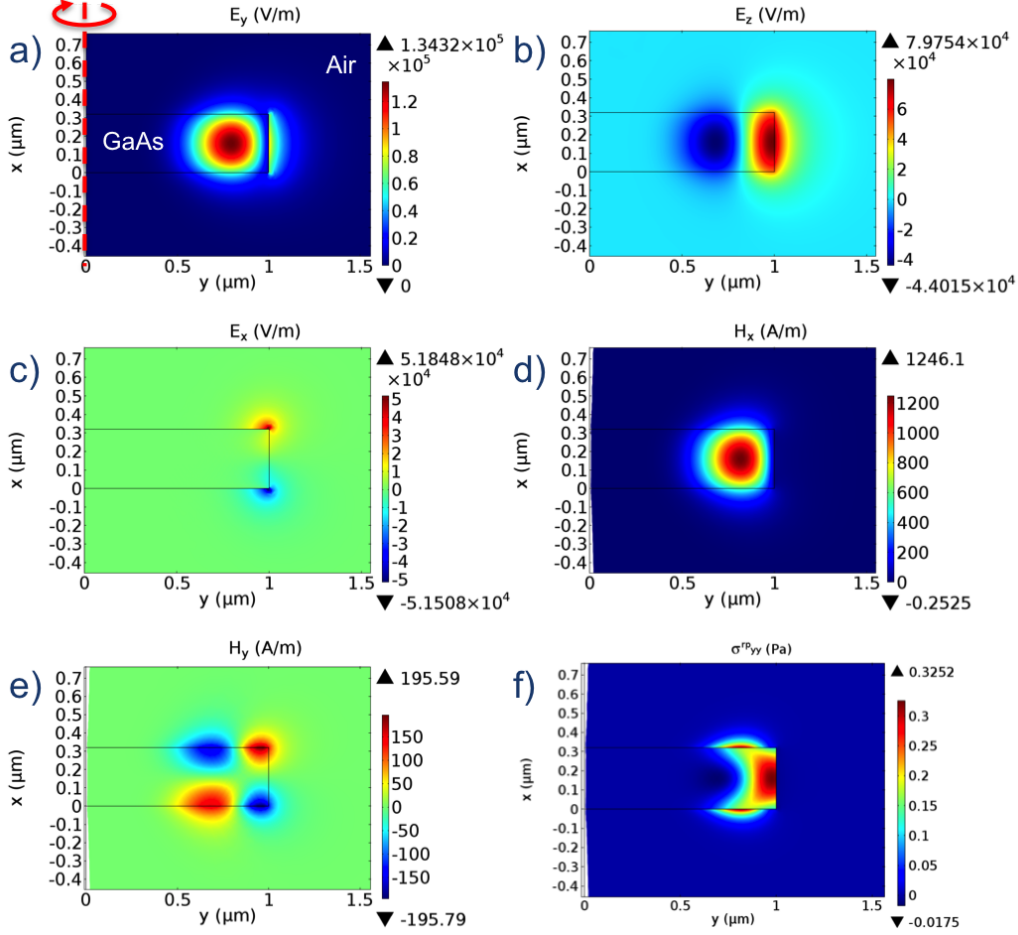
Figure 3.8: 2D axi-symmetric FEM modeling of the normal radial 'radiation pressure' stress σ_{yy}^{rp} in a 320 nm thick and 1 μm radius GaAs WGM disk resonator. The considered WGM is a (p=1, m=10) at $\lambda \simeq 1.3\mu$m. The black lines show the boundary of the two computational domains: the GaAs disk and the surrounding air. 2D axi-symmetric cross sections are shown here, the whole disk is obtained by revolving around the x axial symmetry axis (dashed red line). The AlGaAs pedestal, being sufficiently remote from the optical field, is therefore not included in the simulation. Images (a) through (e) show the computed time and space averaged electrical and magnetic field RMS amplitude cross-sections, normalized such that the total electromagnetic energy in the resonator is equal to the energy of one photon. (a) Radial electric field E_y. (b) Azimuthal electric field E_z. (c) Axial electric field E_x. (d) Axial magnetic field H_x. (e) Radial magnetic field H_y. Since the simulated WGM is TE, the in plane electric field and out of plane magnetic field components E_y, E_z and H_x are dominant. (f) Normal radial stress exerted by a confined photon σ_{yy}^{rp}. The optically induced stress is largest near the outer boundary of the disk resonator, where most of the electromagnetic energy is located.

leads to a steady state radial displacement $\delta r \simeq 6 \cdot 10^{-14}$ m and associated $\delta\lambda \simeq 0.08$ pm wavelength shift. Thus these steady state shifts are extremely small, particularly when compared to the important thermo-optic shift at these circulating powers (see section 5.3).

3.6 Electrostriction

After discussing radiation pressure, we now shift our focus to electrostriction. Electrostriction is a mechanism whereby electric fields can induce strain within a material. Electrostriction is different than piezoelectricity in that the induced strain is proportional to the square of the electric field, and not simply the electric field as for piezoelectricity. As such, reversal of the electric field's sign reverses the piezoelectric strain but leaves the electrostrictive strain unperturbed. Since the electric fields we consider are rapidly oscillating at optical frequencies, we can expect the time averaged piezoelectric strain to be zero, while the time averaged electrostrictive strain contribution should remain.

Electrostrictive stresses scale quadratically with the electromagnetic field, and scale with the fourth power of the dielectric refractive index, making them of significant importance for high refractive index materials such as silicon and gallium arsenide (for which n $\geq$ 3.3 at telecom wavelengths). Recently Rakich et al. showed that for certain geometries of straight silicon photonic waveguides the electrostrictive stress could be commensurate or even slightly larger than the more commonly studied radiation pressure stress [113, 114] .

In the following, we adapt their method to the specific case of light confined in a WGM of a GaAs disk resonator. As in the previous section, we start with a FEM simulation of the desired optical WGM, which provides the complete electromagnetic field distribution (see Fig. 3.8 a through e). Using these results we subsequently compute the electrostrictive stress distribution inside the disk resonator.

The electrostrictively induced stress can be expressed in terms of the material photoelastic tensor p_{ijkl} [115, 113]. Photoelasticity links a material strain S_{ij} to a change in the material's dielectric tensor ε_{ij}. The material strain is defined as a function of the material displacement v_i along the ith coordinate by Eq. 3.31:

$$S_{ij} = \frac{1}{2}\left(\partial_j v_i + \partial_i v_j\right) \tag{3.31}$$

The change in the inverse dielectric tensor associated to this strain is

expressed in terms of the photoelastic tensor[5] in Eq. 3.32:

$$\varepsilon_{ij}^{-1}\left(S_{kl}\right) = \varepsilon_{ij}^{-1} + \Delta\left(\varepsilon_{ij}^{-1}\right) = \varepsilon_{ij}^{-1} + p_{ijkl}S_{kl} \tag{3.32}$$

The photoelastic tensor in principle has $3^4 = 81$ different elements. However, these reduce to only 3 independent coefficients in the case of amorphous materials and cubic crystals such as GaAs and silicon [118]. These three parameters are p_{11}, p_{12} and p_{44}, written here in contracted notation, where $11 \rightarrow 1$; $22 \rightarrow 2$; $33 \rightarrow 3$; $23, 32 \rightarrow 4$; $31, 13 \rightarrow 5$; $12, 21 \rightarrow 6$. Using this definition, Eq. 3.33 links the electrostrictively induced stresses to the electric field components in the following way:

$$\begin{pmatrix} \sigma_{xx}^{es} \\ \sigma_{yy}^{es} \\ \sigma_{zz}^{es} \\ \sigma_{yz}^{es} = \sigma_{zy}^{es} \\ \sigma_{xz}^{es} = \sigma_{zx}^{es} \\ \sigma_{xy}^{es} = \sigma_{yx}^{es} \end{pmatrix} = -\frac{1}{2}\varepsilon_0\,n^4 \underbrace{\begin{pmatrix} p_{11} & p_{12} & p_{12} & 0 & 0 & 0 \\ p_{12} & p_{11} & p_{12} & 0 & 0 & 0 \\ p_{12} & p_{12} & p_{11} & 0 & 0 & 0 \\ 0 & 0 & 0 & p_{44} & 0 & 0 \\ 0 & 0 & 0 & 0 & p_{44} & 0 \\ 0 & 0 & 0 & 0 & 0 & p_{44} \end{pmatrix}}_{\text{photoelastic tensor}} \begin{pmatrix} E_x^2 \\ E_y^2 \\ E_z^2 \\ E_y\,E_z \\ E_x\,E_z \\ E_x\,E_y \end{pmatrix} \tag{3.33}$$

The value of the three photoelastic coefficients for silicon and GaAs are provided in Table 3.2. These three parameters entirely describe the material's properties, and are independent of the considered crystallographic axes. The link between electrostriction and photoelasticity may not be immediately intuitive. One simplified way of seeing it is considering a disk resonator suddenly subject to strain. This strain leads to a change in the materials permittivity $\Delta\varepsilon$, via the photoelastic properties. Provided some electric energy was stored in the disk at the time, this stored energy (proportional to $\varepsilon\,E^2$) to is going to change due to the change in permittivity $\Delta\varepsilon$. This change in energy ΔE can be seen as the work of the electrostrictive force during the displacement[6] (see Figure 3.9).

Since mechanical systems do no respond fast enough to forces at optical frequencies ($\sim 2\cdot10^{14}$ Hz in our case), we will again only be considering the time averaged stresses in response to time averaged electric fields (without using the bracket notation $\langle\sigma_{ij}\rangle$). Looking at Eq. 3.33 and the values of the photoelastic coefficients in Table 3.2, it appears in our case that the electrostrictively induced normal stresses are much larger than the shear

---

[5]One should take care as the photo-elastic (or elastooptic) coefficients are defined in many different manners in the literature, for instance as the strain induced change in the inverse dielectric tensor (as is the case here), or as the stress induced change in the dielectric tensor [116] or strain induced change in the dielectric tensor [117].

[6]A more rigorous version of this argument is developed in [115].

3.6 Electrostriction

Material	Wavelength (μm)	p_{11}	p_{12}	p_{44}	Reference
GaAs	1.15	-0.165	-0.140	-0.072	[119]
Si	3.39	-0.09	+0.017	-0.051	[120]

Table 3.2: Photo-elastic material parameters for GaAs and silicon (Si).

$$\text{Strain} \rightleftarrows \Delta\,\varepsilon_r \rightleftarrows \Delta\,E$$

Figure 3.9: Illustration of the link between photoelasticity and electrostriction. A strain leads to change in refractive index (photoelasticity) which itself leads to a change in the stored electric energy. Electrostriction is the converse mechanism (red arrows), whereby electric fields (stored energy) induce strain in the material.

stresses. We will focus here just on the radial σ_{yy}^{es} and axial σ_{xx}^{es} normal stress components:

$$
\begin{aligned}
\sigma_{yy}^{es} &= -\frac{1}{2}\varepsilon_0\, n^4 \left[p_{11}|E_y|^2 + p_{12}\left(|E_x|^2 + |E_z|^2\right) \right] \\
\sigma_{xx}^{es} &= -\frac{1}{2}\varepsilon_0\, n^4 \left[p_{11}|E_x|^2 + p_{12}\left(|E_y|^2 + |E_z|^2\right) \right]
\end{aligned}
\tag{3.34}
$$

Figure 3.11 (a) and (b) show the value of σ_{yy}^{es} and σ_{xx}^{es} due to a single $\lambda_0 \simeq$ 1.3 μm photon confined inside a 1 μm radius GaAs disk resonator. Figure 3.11 (c) and (d) represent the associated volume force for both these stresses where $\mathcal{F}_y^{es} = -\partial_y\sigma_{yy}^{es}$ and $\mathcal{F}_x^{es} = -\partial_x\sigma_{xx}^{es}$. The black arrows show the net direction these forces are pointing in. We can see here the electrostrictive force pushes outwards in both the radial and axial directions, adding constructively to the radiation pressure force discussed in the previous section (3.5.2).

The fact that electrostriction and radiation pressure add up constructively as they do here is not automatically guaranteed. As we can see from Eq. 3.34, the main difference between σ_{yy}^{es} and σ_{xx}^{es} is that in σ_{xx}^{es} the electric field component E_y is multiplied by p_{12} instead of p_{11} (E_x is nearly 0 since we consider a TE WGM). Since these two parameters are of same sign and
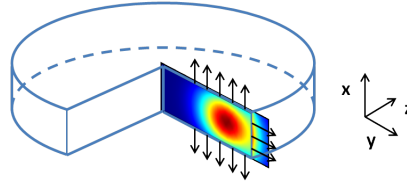
Figure 3.10: Schematic illustrating the overall direction of electrostrictive forces acting on a GaAs disk resonator due to photons confined in a WGM (black arrows), and representing the cross section over which the stress and volume force are plotted in Fig. 3.11.
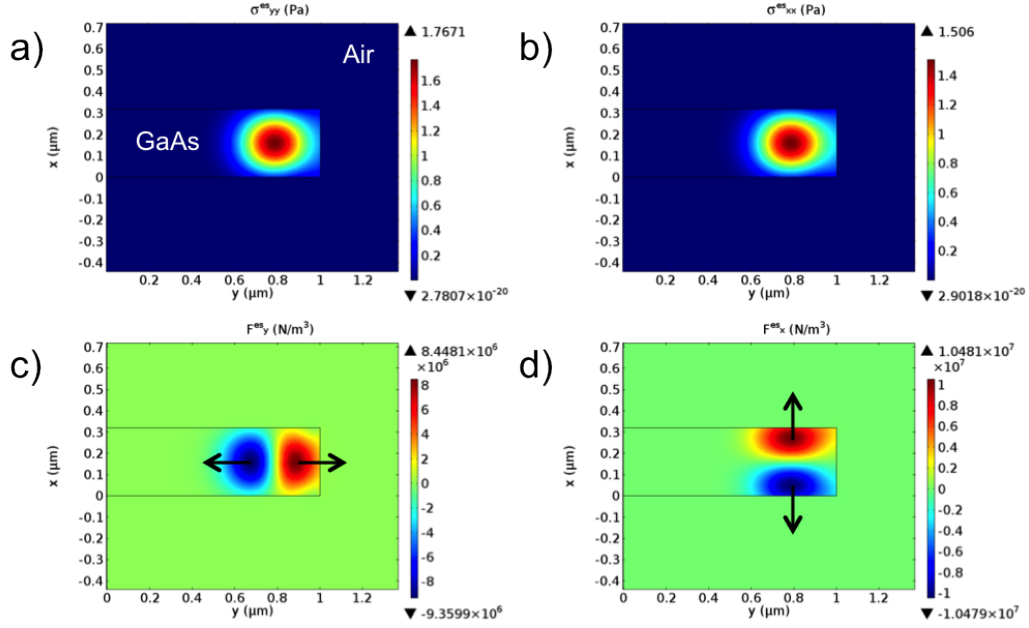
Figure 3.11: 2D axi-symmetric FEM modeling of the electrostrictive stress and volume force in a 320 nm thick and 1 μm radius GaAs WGM disk resonator. The considered WGM is a (p=1 m=10) at $\lambda \simeq 1.3\mu$m. The black lines show the boundary of the two computational domains: the GaAs disk and the surrounding air. Only half of the disk is represented in these cross sections, the whole disk is obtained by revolving around the x axial symmetry axis (as in Fig. 3.8). (a) and (b) show respectively the xy cross-section of the radial σ_{yy}^{es} and axial σ_{xx}^{es} electrostrictive stress distributions. (c) and (d) plot the associated radial and axial volume force distribution. The black arrows indicate the overall direction these forces point in.

magnitude for GaAs, there is no big difference between the radial and axial stress, as evidenced in Figure 3.11. However this would not be the case for silicon disk resonators or waveguides, as the coefficients p_{11} and p_{12} are of different sign and significantly different magnitude [113]. In order to compare the magnitude of the electrostriction acting upon the disk to the previously estimated radiation pressure, we again consider a volume averaged normal radial stress (Eq. 3.35):

$$\overline{\sigma}_{rr}^{es} = \frac{\iiint \sigma_{rr}^{es}dV}{\pi R^2 h} \tag{3.35}$$

Here, under the same single photon conditions, we find the volume averaged electrostrictive normal radial stress $\overline{\sigma}_{rr}^{es}$ to be 0.529 Pa. This value is roughly **6** times larger than the 0.084 Pa found for $\overline{\sigma}_{rr}^{rp}$. The high value of the electrostrictive force in GaAs resonators should not be too surprising, considering electrostriction and radiation pressure are already of comparable magnitude in the case of silicon waveguides, and the photoelastic coefficients for GaAs are several times larger than those of silicon (Table 3.2).

These calculations of the MST and electrostrictive forces were also verified using the effective index method discussed in Chapter 1, which produced similar results (not shown here).

We will see in the following sections 3.8.1 and 3.8.2 that while the electrostrictive stress may be significantly larger than the radiation pressure stress, they both couple differently to the strain resulting from the mechanical motion of a RBM, so that the work produced by both forces during a radial displacement is in fact similar.

3.7 Photothermal forces

Light can also interact with a mechanical system through photothermal (also called bolometric) forces. When light is absorbed in the material, it creates heat. This heat creation then leads to a time delayed displacement via the material's thermal expansion coefficient. This displacement can be used to drive a mechanical mode. The difference in thermal expansion coefficients between two materials in a bi-material device can also be exploited to obtain efficient deflection of a mechanical system. Using this property, photothermal forces have been used to efficiently cool or excite the motion of gold plated silicon cantilevers [17, 121, 107]. Furthermore, recent work has demonstrated the possibility of using photothermal forces to reach the quantum ground state [122].
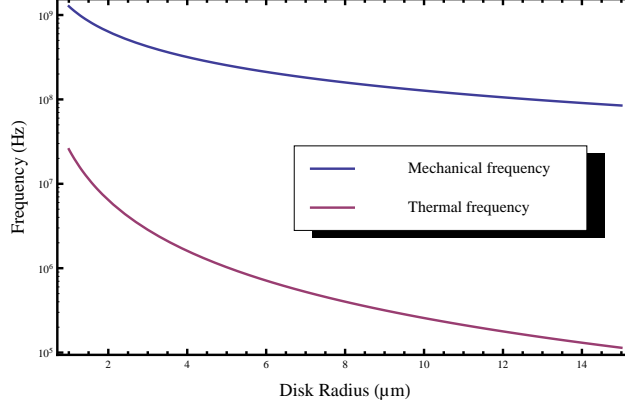
Figure 3.12: Thermal frequency $1/\tau$ (red) versus first mechanical RBM frequency $\Omega_M/(2\pi)$ (blue), as a function of GaAs disk radius. The mechanical mode frequency is calculated from the analytical expression given in chapter 2. The thermal frequency is calculated from the GaAs disk and AlGaAs pedestal geometries and thermal characteristics (conductivity, specific heat, etc) for a fixed pedestal radius. This calculation is detailed in the following chapter.

However, we do not believe photothermal forces can be usefully leveraged to amplify or damp the mechanical motion of RBMs in GaAs disk resonators. Indeed, in order to be able to do so efficiently the optical force F must respond to a change in the mechanical displacement x with a delay matching the mechanical frequency (see section 3.2.1 and Fig. 3.3). The effective damping due to the time-delayed optical force F is given by Eq. 3.3 [107]. As we saw in section 3.2.1 the ability of F to dynamically back-act on the motion appears under the form of the dimensionless parameter $\Omega_M\tau$, which is a ratio between the mechanical frequency and the thermal force's frequency $1/\tau$. In the silicon levers of [17], the value of $\Omega_M\tau$ is roughly $2\pi \times 4$, indicating the resonator can oscillate ∼4 times before F reaches equilibrium after a sudden change[7]. In the case of GaAs disk resonators, Figure 3.12 plots the mechanical frequency $\Omega_M/(2\pi)$ of the first RBM, versus the thermal force's frequency $1/\tau$, as a function of disk radius. We calculate τ as the time necessary for the GaAs disk to thermalize after a sudden temperature change[8]. The figure shows a difference of two to three orders of magnitude between mechanical and thermal frequencies depending on the disk radius. As a consequence a

---

[7]τ=0,56 ms; Ω_M=2$\pi\times$ 7.3 kHz.

[8]The cavity response time τ_{cav}=Q$_{\text{opt}}/\omega_{\text{opt}} \sim 10^{-10}$ s is instantaneous compared to the disk's thermal response time τ_{th}, so the response time τ of the thermal force F to a displacement is entirely dominated by τ_{th}.

photothermal force F would only react to a mechanical displacement after the system has had time to perform 100 to 1000 oscillations. The time delay is so large that F's contribution is essentially averaged out (this translates into a large penalty term in Eq. 3.3, with $\Omega_M\tau > 600$). Corroborating this conclusion, first experimental measurements of optomechanical dynamical back-action can be well explained explained through the contribution of radiation pressure and electrostriction alone. Furthermore, at cryogenic temperatures the thermal expansion coefficient of GaAs is significantly reduced [84], thereby strongly weakening the contribution of photothermal forces to the optomechanical coupling.

3.8 Estimating the optomechanical coupling

In this section we wish to discuss the optomechanical coupling between the light field in the disk's optical WGM and a given mechanical mode of the disk resonator. The optomechanical coupling term g_{om} quantifies how much the WGM resonance frequency ω_0 is shifted for a given mechanical displacement dx and represents the ability to efficiently transfer optical energy into mechanical energy and vice-versa. We will discuss two mechanisms contributing to optomechanical coupling in GaAs disk resonators, and offer numerical ways to compute their magnitude.

In Chapter 1, we saw a confined optical wave is only resonant provided it closes upon itself in phase after a round-trip, respecting the condition: $2\pi n_{\text{eff}}R \simeq m\lambda$. From this it appears that the resonance wavelength is modified by a small mechanical displacement dx which changes the cavity radius R. But this small displacement, by modifying the whole crystal lattice, also changes the refractive index (photoelasticity) and through this the resonance wavelength of the WGM. In terms of g_{om} this means the total g_{om} can be split into two independent contributions depending on each of these two mechanisms:

$$g_{om} = \frac{d\omega_0\left(R,\varepsilon\right)}{dx} = \underbrace{\frac{\partial\omega_0}{\partial R}\frac{\partial R}{\partial x}}_{geometric\ g_{om}^{geo}} + \underbrace{\frac{\partial\omega_0}{\partial\varepsilon}\frac{\partial\varepsilon}{\partial x}}_{photoelastic\ g_{om}^{pe}} \qquad (3.36)$$

Here ε is the material's permittivity, which is no longer necessarily isotropic nor equal everywhere inside the disk under stress. The photoelastic contribution to the g_{om}, g_{om}^{pe} is obviously unique to resonators where light is confined inside matter, like a disk, toroid or photonic crystal, and would not appear in an empty Fabry-Perot optomechanical cavity. For this reason, it has mostly

been disregarded in the optomechanics community. The geometric and photoelastic contributions to the g_{om} will be successively addressed in sections 3.8.1 and 3.8.2.

3.8.1 Geometric contribution $\mathbf{g}_{om}^{geo}$

Determining analytically how much a WGM resonance wavelength is modified by a certain mechanical displacement is challenging. Under the assumption that the in-plane and out-of-plane components of the electric field can be treated separately (effective index method) and considering a purely radial mechanical displacement the geometric optomechanical coupling in a disk resonator of radius R takes the simple form $g_{om}^{geo} = -\omega_0/R$ [20]. However a more accurate estimation method is needed, which could also be applied to all mechanical displacements, not just purely radial. Reference [123] provides a perturbation theory for Maxwell's equations in the case of shifting material boundaries. This theory can be applied to determine the frequency shift of an optical WGM to an arbitrary mechanical deformation of the confining dielectric disk. Following this method, the term g_{om}^{geo} can be calculated as a surface integral of the unperturbed optical fields over the perturbed dielectric interface, see Eq. 3.37:

$$g_{om}^{geo} = \frac{\omega_0}{4} \iint_{\text{disk}} (\vec{q} \cdot \vec{n}) \left[\Delta\varepsilon_{12} |\vec{e_{\parallel}}|^2 - \Delta\left(\varepsilon_{12}^{-1}\right) |\vec{d_{\perp}}|^2 \right] dA \qquad (3.37)$$

Here $\vec{q}$ and $\vec{n}$ are respectively the normalized mechanical displacement vector and surface normal vector. $\vec{e_{\parallel}}$ (resp. $\vec{d_{\perp}}$) is the parallel (orthogonal) component to the surface of the electric field (electric displacement field). $\vec{q}$ and $\vec{e}$ are normalized such that $\max|\vec{q}|=1$ and $\frac{1}{2} \int \varepsilon |e|^2 dV = 1$. $\Delta\varepsilon_{12} = \varepsilon_1 - \varepsilon_2$ is the difference in permittivity between the materials on either side of the boundary and $\Delta\left(\varepsilon_{12}^{-1}\right) = \varepsilon_1^{-1} - \varepsilon_2^{-1}$. In this calculation we are only interested in the geometric contribution to the g_{om}, so ε_1 is simply n^2 over the entire disk, while $\varepsilon_2 = 1$. From Eq. 3.37, g_{om}^{geo} is calculated in the following fashion. First the desired mechanical eigenmode is calculated using a FEM simulation software (Comsol Multiphysics), see Fig. 3.13, (a) to (d). The deformation profile of the mechanical mode is imported into a FEM simulation of the desired *unperturbed* WGM (Fig. 3.13, e). The optomechanical coupling g_{om}^{geo} is then calculated by computing the surface integral of Eq. 3.37 over the disk's three different boundaries (Fig. 3.13, f). The results for the four mechanical modes shown in Fig. 3.13 are summarized in Table 3.3.

For a given mechanical mode, the displacement of every point of the disk is not uniform, (e.g. the extremities move more than the center in the case

3.8 Estimating the optomechanical coupling
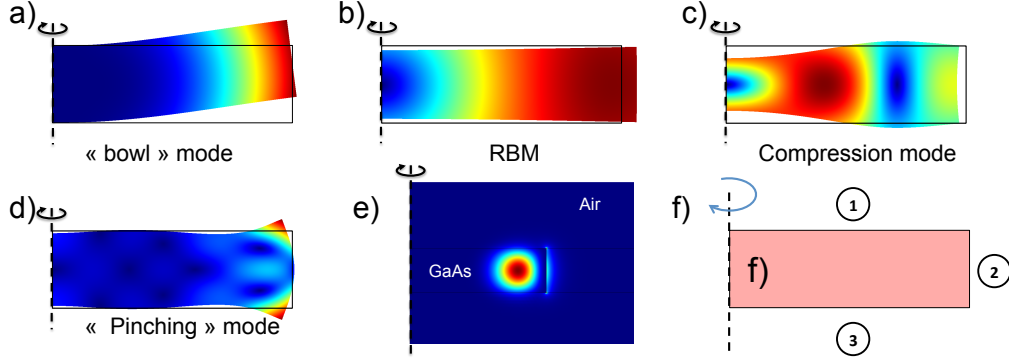
Figure 3.13: Calculating the optomechanical coupling term g_{om}^{geo}. (a) through (d): Axisymmetric cross section of the displacement profile for the four mechanical eigenmodes listed in Table 3.3. The black rectangle represents the outline of the non deformed disk's geometrical boundaries. The eigenmodes' deformation amplitude has been voluntarily exaggerated. The surface color code illustrates the total displacement, with red as maximum and blue as minimum. Full profile is obtained by revolving around the vertical axis (dashed black line). (a) P=0, M=0 out of plane mechanical mode ('bowl' mode). (b) First RBM. (c) 'Compressive' mode. (d) Extremity 'pinching' mode. (e) In-plane electric field for (p=1 m=10) WGM used in the calculation, $\lambda \simeq 1.3$ μm. (f) Schematic of the integration surfaces.

Mechanical mode	'bowl'	1st RBM	'compression'	'pinching'
Frequency	494 MHz	1.375 GHz	3.5 GHz	5.72 GHz
g_{om}^{geo} (GHz/nm)	0.11	1080	412	82

Table 3.3: Optomechanical coupling term g_{om}^{geo} for some mechanical modes of a 320 nm thick $\varnothing = 2$ μm GaAs disk, with a p=1 m=10, $\lambda \simeq 1.3$ μm WGM. The 'bowl' mode refers to the (M=0, P=0) out of plane mode. Deformation profiles for these mechanical modes are available in Fig 3.13. The optomechanical coupling is particularly large for the first RBM, reaching the THz/nm range.

of a RBM). As a result the value of g_{om}^{geo} is dependent on the somewhat arbitrary choice of the reduction point which experiences the displacement dx - just as in the calculation of an effective mass. We choose in all cases the point of maximal displacement as reduction point. As evidenced in Table 3.3, different mechanical modes have vastly different values of g_{om}^{geo}. Note for instance how the g_{om}^{geo} value for the RBM is roughly 10 000 times larger than for the out of plane 'bowl' mode. This difference illustrates how efficiently each mechanical mode modulates the total cavity length (the $\partial R/\partial x$ term in Eq. 3.36). Figure 3.14 clarifies this point. Incidentally this demonstrates that the first RBM is necessarily the mechanical mode with the highest g_{om}^{geo}, and explains why it is by far dominant in experimental mechanical spectra.

Due to their extremely miniaturized dimensions, $\varnothing=2$ μm GaAs disks exhibit remarkably large optomechanical coupling, reaching over 1 THz/nm in the case of the first RBM. (Here we see that the $\sim$1.1 THz/nm numerically computed value is roughly 20% below the value provided by the simplified expression $g_{om} = -\omega_0/R \simeq 1.4$ THz/nm). The zero point fluctuations x_{ZPF} are found by normalizing the potential deformation energy in the mechanical resonator to $\hbar\Omega_M/2$, yielding $x_{ZPF}=1.2\cdot10^{-15}$ m for the first RBM. The single photon optomechanical coupling strength g_0 for this mechanical mode is thus $g_0=g_{om}x_{ZPF} \simeq 1.3$ MHz. Note however that unlike g_{om}, g_0 is independent of the chosen reduction point[9] and is therefore a somewhat more reliable measure of optomechanical coupling.

These calculations are done without any AlGaAs pedestal and therefore only valid for small pedestal radii ($\geq$ 90 % undercut). For larger radii the stated mechanical frequencies and g_{om}^{geo} may differ significantly. While disk resonators support a wide variety of in- and out of plane modes, we have shown here just a few. Indeed many modes can be immediately ruled out through symmetry arguments. This is detailed the selection rules subsection.

Selection rules for optomechanical coupling

The integrand in Eq. 3.37 contains a $\cos(M\theta)$ term describing the azimuthal dependency of the mechanical mode. This implies only modes with perfect rotational symmetry (i.e. M=0) should have significant coupling to optical WGMs[10]. (see Figure 3.14 for an example).

In our early works on GaAs disk resonators [20] this selection rule was not perfectly verified, as evidenced by the variety of mechanical modes with M$\neq$0 visible in experimental spectra. We hypothesized this was due to rotational symmetry breaking caused by the presence of a rather large non circular pedestal. Indeed in more recent work involving smaller pedestals these M$\neq$0 mechanical modes are no longer visible, confirming the previous hypothesis and the pertinence of the selection rule.

Comparison with different optomechanical systems

GaAs disks confine both mechanical and optical energy on a very small $\sim \lambda^3$ interaction volume and thus provide very high optomechanical coupling, which compares favorably to other optomechanical systems. For example a -far from comprehensive- list of optomechanical resonators such as

---

[9]g_0 is solely dependent upon the mechanical deformation profile.
[10]Since the optical field is rotating inside the disk, the $\cos^2(m\theta + \phi)$ azimuthal dependency of the WGM can be neglected.
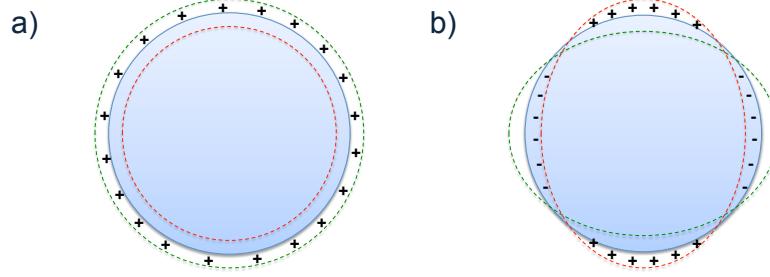
Figure 3.14: Schematic comparison between two mechanical modes with good (a) and poor (b) optomechanical coupling g_{om}^{geo}. Mechanical modes are: (a) the fundamental RBM and (b) a (M=2) wineglass mode (see chapter 2 for more details). The solid blue disk shows the outline of the disk resonator at rest, while the green and red dashed lines represent the extremal displacements of the mechanical mode. (a) In the case of the RBM all radial displacements add up constructively (+ signs), effectively efficiently modulating the total cavity length. This is not the case for the wineglass mode for which the cavity length remains essentially unchanged.

silica microtoroids [124], micro-mirrors [34, 125], a carbon nanotube [30] or a membrane inside an optical cavity [24] and a SiN string in the near field of a toroid resonator [126] provide an optomechanical coupling term g_0 well below the MHz range. The high g_{om} and g_0 provided by GaAs disks is comparable to the high values reached in optomechanical crystals [11]. Of course the g_{om} and g_0 terms are not the only relevant parameters: the optical and mechanical quality factors are also of great importance.

3.8.2   Photoelastic $\mathbf{g}_{om}^{pe}$

Initially we had only considered the influence of the geometrical boundary displacement on the resonance frequency shift: g_{om}^{geo}. Taking only this mechanism into account typically provides reasonable agreement with experimental data but discrepancies of up to factor $\sim$2 sometimes remain between the experimentally measured g_{om} and the simulated g_{om}^{geo} [20].

Can this discrepancy can be explained by the photoelastic contribution to the optomechanical coupling g_{om}^{pe} ? Here we compute this contribution in the case of the first mechanical RBM. First the unperturbed resonance frequency of the desired WGM is found through a FEM simulation (with uniform and isotropic ε). Second the desired mechanical eigenmode is solved for in another FEM simulation. The maximum displacement dx is normalized to be commensurate to the Brownian motion amplitude. The simulation provides the complete deformation profile and strain distributions inside the resonator. Figure 3.15 (a) and (b) display the radial displacement and normal
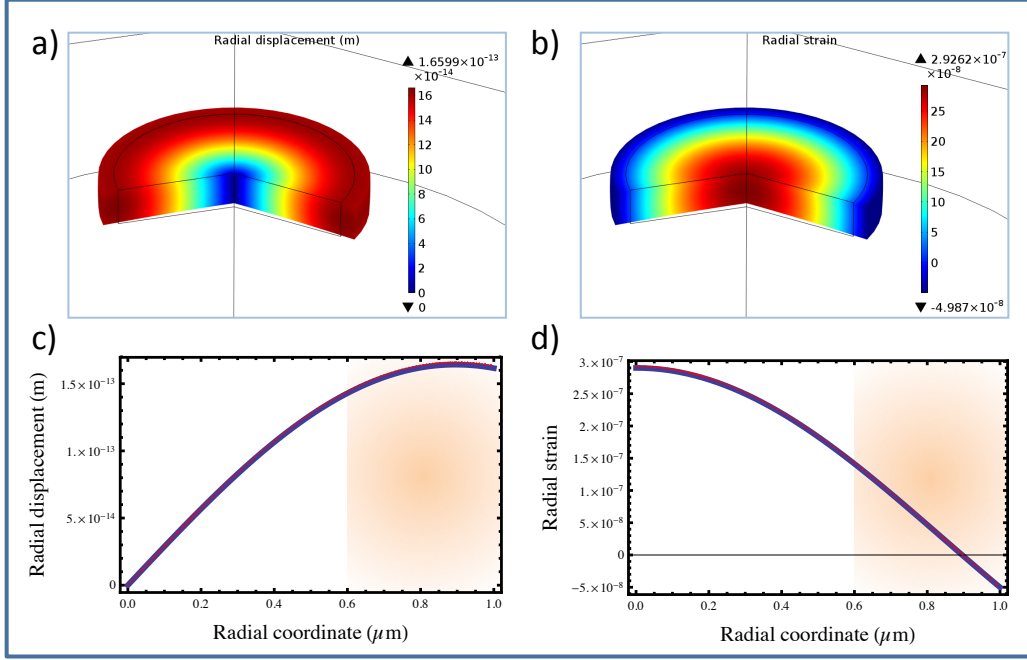
Figure 3.15: Displacement and strain for the first RBM of a 320 nm thick $\varnothing$=2 μm GaAs disk resonator, at $\sim$ 1.38 GHz. (a) and (b) show a 3D cross-section of the COMSOL FEM modeling of the mechanical mode with deformed boundary. The approximation of an isotropic Young's modulus for GaAs was used. (a) Magnitude of the radial displacement v_r. (b) Magnitude of the radial normal strain $S_1 = S_{rr} = \partial v_r / \partial r$. (c) and (d): value of the radial displacement (resp. radial strain) as a function of the radial coordinate, taken from COMSOL simulation (dashed red line) and analytical formula of Chapter 2 (solid blue line). The orange highlighted zone between r=0.6 μm and r=1μm marks the region of maximal electromagnetic energy density for a p=1 WGM.

radial strain S_{rr} (=S_1 in contracted notation[11]) distributions. While the radial displacement is zero at the center and maximum near the periphery, the behavior for the normal radial strain is reversed. S_1 is maximal at the center of the disk and changes sign right by the edge of the disk[12] (see Fig. 3.15, c and d). The behavior is similar for the normal azimuthal and axial strains S_2 and S_3, which are of similar magnitude and largest near the center of the disk. The S_4 and S_6 strain components are zero over the whole disk, while the S_5 strain component is roughly three orders of magnitude smaller than $S_{1,2,3}$. We now use Eq. 3.38 to see how the stress distribution inside

---

[11]11$\rightarrow$ 1; 22 $\rightarrow$ 2; 33 $\rightarrow$ 3; 23, 32 $\rightarrow$ 4; 31, 13 $\rightarrow$ 5; 12, 21 $\rightarrow$ 6. The 1st, 2nd and 3rd coordinate directions refer respectively to the radial, azimuthal and axial directions in cylindrical coordinates.

[12]This is a normal consequence of the circular geometry.

the disk due to the RBM displacement modifies the dielectric tensor:

$$\varepsilon_{ij}^{-1}(S_{kl}) = \varepsilon_{ij}^{-1} + \Delta\left(\varepsilon_{ij}^{-1}\right) = \varepsilon_{ij}^{-1} + p_{ijkl}S_{kl} \qquad (3.38)$$

(Here p_{ijkl} is the photoelastic tensor detailed in Eq. 3.33). Since S_4, S_5 and S_6 are negligible, the off-diagonal terms in the dielectric tensor can be neglected. The dielectric tensor modified by the RBM displacement therefore takes the form shown in Eq. 3.39:

$$\begin{pmatrix} \varepsilon_1 & & \\ & \varepsilon_2 & \\ & & \varepsilon_3 \end{pmatrix} \text{ with } \begin{cases} \varepsilon_1 = (1/n^2 + p_{11}S_1 + p_{12}S_2 + p_{12}S_3)^{-1} \\ \varepsilon_2 = (1/n^2 + p_{12}S_1 + p_{11}S_2 + p_{12}S_3)^{-1} \\ \varepsilon_3 = (1/n^2 + p_{12}S_1 + p_{12}S_2 + p_{11}S_3)^{-1} \end{cases} \qquad (3.39)$$

Note that the dielectric tensor is now both anisotropic and dependent upon the position inside the disk resonator. The difficult problem of finding the new WGM resonance frequency under these conditions can fortunately be solved through another FEM simulation (with unperturbed geometric boundaries). This provides the photoelastic frequency shift due to the known mechanical displacement dx. The photoelastic optomechanical coupling strength g_{om}^{pe} is 0.98 THz/nm for the first RBM and p=1 WGM at 1.3 μm, which is just slightly less than the $g_{om}^{geo}=\sim 1.1$ THz/nm. This value is remarkably high especially considering just how sub-optimal the refractive index modulation is through a RBM. Indeed in order to maximize the photoelastic frequency shift the optical mode should be localized in the region of highest strain. In the case of the RBM the strain is not only weak but also changes sign right around the area of highest optical energy density (see the highlighted area of Fig. 3.15). Recent work investigating the optomechanical coupling in distributed Bragg reflector GaAs/AlAs vertical cavities [127] shows these geometries are much better suited to take advantage of the photoelastic coupling mechanism. Indeed in those structures the strain and optical field maxima overlap more effectively, and thanks to this the photoelastic contribution to the g_{om} is roughly 20 times larger than the geometric displacement contribution, reaching several THz/nm.

Finally these considerations also shed light on two seemingly contradictory observations. On one hand the photoelastic coupling g_{om}^{pe} is slightly smaller than the geometric coupling g_{om}^{geo}. On the other hand the radial stress per photon is much larger for electrostriction than radiation pressure. This can be understood by looking at the actual work produced by the optical forces during a radial displacement. The stored mechanical energy density is proportional to the product of stress times the strain. For a small RBM displacement dx producing a strain δS, the work δU done by the optical force
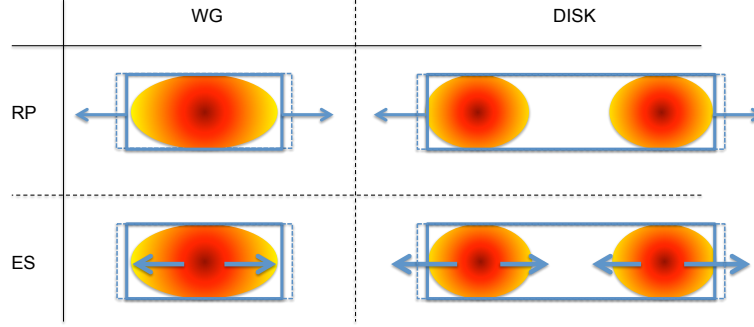
Figure 3.16: Schematic illustration of the horizontal radiation pressure (RP) and electrostrictive (ES) forces (blue arrows) exerted by the light confined in a waveguide (WG) or a disk resonator (DISK), the outline of which is represented by the solid blue boundary. As previously discussed radiation pressure is essentially exerted at the discontinuous dielectric boundary, while electrostrictive forces originate inside the material in the regions of highest electromagnetic energy density (red). From this schematic it is readily apparent in the case of the waveguide that both radiation pressure and electrostrictive forces similarly assist purely lateral expansion (dashed blue outline). On the contrary in the case of a lateral expansion of the disk resonator both regions of inward pointing electrostrictive volume force will oppose the movement and produce negative work. The total work done by the electrostrictive force during a lateral expansion of the disk is nonetheless still positive as the region with outward pointing force has a larger volume than the region with inward pointing force, because of the circular geometry.

is given by Eq. 3.40:

$$\delta U = \int \sigma \, \delta S \, dV \qquad (3.40)$$

Because of the non uniform strain distribution resulting from the RBM (see Fig. 3.15), both optical forces (radiation pressure and electrostriction) produce comparable work during a RBM compression or extension. An easy way of visualizing this is shown in Fig. 3.16.

3.9   Conclusion

We have seen how the properties of a mechanical resonator can be controlled through the optomechanical coupling with the optical field. Models for this coupling were presented and the quantum limit of optomechanical cooling was discussed. The various mechanisms responsible for the optomechanical interaction were presented and their relative magnitude calculated. This analysis underscored the strength of GaAs disk resonators for optomechanical applications, while pointing towards ways through which the coupling could be further enhanced.

Chapter 4

Fabrication of integrated nano-optomechanical resonators

4.1 GaAs Nano-fabrication

This chapter deals with the various steps and tools needed to fabricate 'on-chip' GaAs disk resonators coupled to monolithically integrated coupling waveguides, as well as simple free standing GaAs disk resonators [20, 21, 55]. Since the seemingly most mundane details, such as the way the sample is agitated in the etchant solution, can have drastic effects on the outcome of the fabrication process and the performance of the devices (see 4.1.10), this chapter will go into very minute details of the fabrication process. Therefore we will start with a simple overview of the main fabrication steps for the reader who does not wish to delve too deeply into the fabrication aspects. Many aspects of the fabrication were determined by trial and error; brief accounts of failed approaches will also be provided, so that they need not be reproduced. Since we did not have time to explore all the possible fabrication parameters, we will underline the areas where we believe there is still most room for improvement.

The GaAs nanofabrication developments discussed in the following started at the Laboratoire de Photonique et Nanostructures (LPN) in Marcoussis, in collaboration with Pascale Senellart. Later on, after the opening of the cleanroom at the Université Paris Diderot, we moved the fabrication of samples there, while the e-beam lithography was performed in the ENS cleanroom. Around the same time, we switched from a chemical wet etch- to a dry-etch technique which provides better fabrication control (see section 4.1.9).

I would like to thank here Pascale Senellart of the LPN who taught me the cleanroom fabrication techniques and performed the lithography at the beginning of my thesis and Michael Rosticher of the ENS for later teaching me how to perform e-beam lithography.

4.1.1 Main fabrication steps

This section provides a simple overview of the main fabrication steps. These steps are summarized in Figure 4.1. We employ a semi-insulating GaAs substrate, on which we grow epitaxially a 500 nm GaAs buffer layer, a 1.8 μm $Al_{0.8}Ga_{0.2}As$ sacrificial layer, and finally a 320 nm GaAs top layer (Figure 4.1 (a)). The growth by MBE of our wafers is carried out by Aristide Lemaitre and Elizabeth Galopin at the LPN laboratory in Marcoussis. Negative ebeam resist (Ma-N 2401 from Microresist Technology) is then spun on the wafer and exposed using a Raith e-Line ebeam lithography system (see Figure 4.1 (b) and section 4.1.2 for more details). After exposure the sample is developed in a chemical solution (AZ 726 MIF from MicroChemicals). Only the exposed resist remains after development (Figure 4.1 (c) and section 4.1.6). This resist pattern then serves as an etch mask for an Inductively Coupled Plasma Reactive-Ion Etching (ICP-RIE) etch step (or non-selective wet etch) which removes the top GaAs layer and AlGaAs sacrificial layer everywhere but under the features protected by the resist. This defines what will ultimately be the GaAs disk resonator positioned in the vicinity of an integrated coupling waveguide (Figure 4.1 (d) and sections 4.1.8 and 4.1.9). The sample is then dipped in a refrigerated dilute Hydrofluoric Acid (HF) solution. This solution only etches the $Al_{0.8}Ga_{0.2}As$ sacrificial layer while leaving the GaAs intact. This results in isolating the GaAs disk resonator on an AlGaAs pedestal, as well as locally suspending the narrowest part of the tapered coupling waveguide (Figure 4.1 (e) and section 4.1.10). At the end of the procedure the remaining resist is removed either with acetone and isopropanol (IPA) or with an O_2 plasma cleaning procedure (Figure 4.1 (f) and section 4.1.11).

4.1.2 Ebeam lithography

Ebeam resist choice

Ma-N 2400 series resist is chosen for fabrication. Depending on the desired thickness Ma-N 2403 or Ma-N 2401 is selected. This resist presents two main advantages. First of all it is a high-resolution resist which offers good resistance to acidic wet etches and HF as well as good dry-etch selectivity
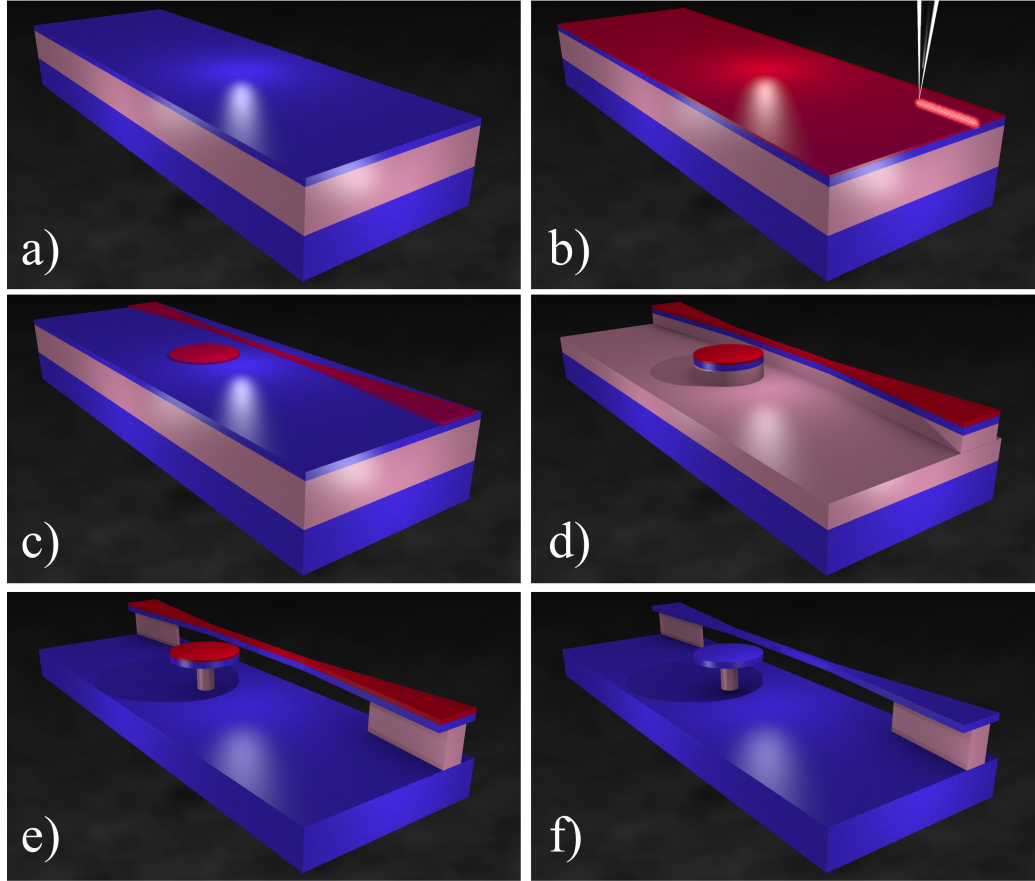
Figure 4.1: **Main nano-fabrication steps**. (a) The sample is composed from top to bottom of a 320 nm thick GaAs layer (blue) and a 1.8 μm thick $Al_{0.8}Ga_{0.2}As$ sacrificial layer (beige) both epitaxially grown on a GaAs substrate. (b) Negative ebeam resist is spun on the sample and exposed using a focused electron beam (top right). (c) After the development step only the exposed resist remains on the sample. (d) The resist serves as an etch mask, protecting the disk and waveguide features during a non selective etch step through the top GaAs layer. (e) A dilute HF solution selectively under-etches the sacrificial $Al_{0.8}Ga_{0.2}As$ layer. (f) The negative ebeam resist is removed yielding a finished device.

with GaAs/AlGaAs. Second the use of a dry-etch resistant *negative* tone resist removes the need for a pattern transfer from a positive resist to a hard etch mask. Removing this step simplifies the process and does away with an extra possible source of sidewall roughness. Ma-N 2400 series consists of two components: a phenolic resin (novolac) and a photo-active compound for cross-linking [128]. Cross-linking (hardening) of the resist occurs in the areas exposed to electron or UV exposure.

Substrate preparation

Starting from the epitaxially grown wafer small sample chips (roughly 1cm by 1cm) are cleaved using a diamond pen. The samples are then thoroughly cleaned and prepared for the ebeam lithography step using the following procedure:

- The sample is first sonicated for 10 minutes in an acetone ultrasound bath followed by another 10 minutes in an isopropanol (IPA) ultrasound bath in order to remove grease and dust contaminants. After taking the sample out the IPA it is blow-dried with an N_2 gun. The sample is inspected under the optical microscope to ensure a perfectly clean surface as any debris remaining on the sample surface can lead to broken waveguides in the subsequent fabrication steps.

- After the cleaning procedure and before spin coating the resist, the sample is dehydrated on a hotplate at 160 °C for 10 min to promote better resist adhesion (see following section).

Carbon tipped tweezers are used to manipulate the chip as metal tweezers can break off tiny bits of GaAs that dirty the sample surface.

4.1.3 Spin coating

Adhesion promotion

The very thin layer of negative e-beam resist we use is especially prone to delamination during the development step - in particular the small features such as the 1 μm radius disks or the 200 nm wide tapered part of the waveguide. Delamination is characterized by having the exposed patterns in the resist lose adherence and lift off in the developer, floating away and sometimes redepositing elsewhere on the sample. A dramatic example of this is shown in Figure 4.2. In some cases the delamination can be more subtle and simply result in a slight bend in the tapered region of the waveguide which skews the nominal gap distance between waveguide and disk. This phenomenon is
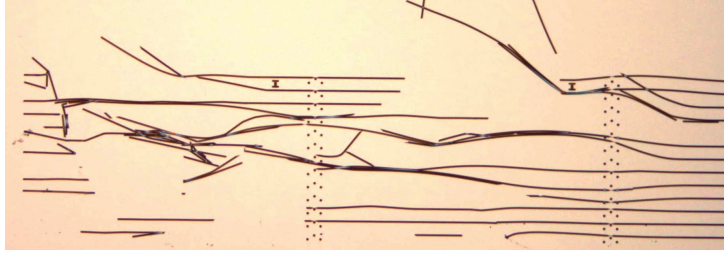
Figure 4.2: Optical microscope image showing the effect of resist delaminating during the development procedure. (For scale the displayed region is ~1.5 mm×0.5 mm).
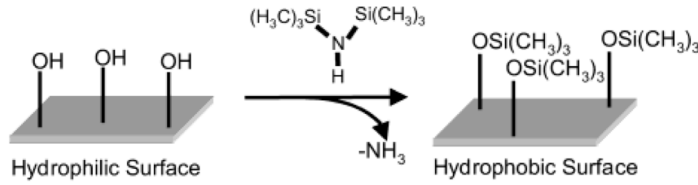
Figure 4.3: Reaction between the hydrophilic native surface oxide and HMDS leading to a hydrophobic surface with better adherence with the resist. Figure reproduced from [129].

due to poor adherence between the GaAs and the resist caused by a small layer of moisture remaining between the two. While this problem originates during the spin-coating step, it only becomes evident *after* the time consuming e-beam exposure step. Fortunately this problem can be solved by the use of an adhesion promoting layer to increase the adhesion of the ebeam resist to the GaAs substrate. First a thin layer of the adhesion promoter HexaMethylDiSilazane (HMDS) is coated on the surface (a procedure called priming). The HMDS reacts with the GaAs native oxide releasing ammonia and leaves a TMS (TriMethylSylil [-Si(CH$_3$)$_3$]) terminated surface which is hydrophobic and offers superior adherence for the resist, see Figure 4.3. This HMDS priming procedure is quite standard for silicon process flows and is generally conducted in the vapor phase at ~150°C. Few papers in the literature mention its applicability for III-V semiconductors. Reference [129] however shows HMDS reacts with GaAs native oxide even at room temperature and can be used to pattern organic structures onto GaAs. We find HMDS priming to greatly enhance resist adhesion to both GaAs and AlGaAs surfaces. Removal of the GaAs native oxide using an NH$_4$OH rinse has also been reported to improve adhesion [130].

The sample is taken off the hotplate (dehydration step) and put onto the spin coater chuck, a coat of HMDS is then rapidly applied before moisture

has time to settle on the sample surface. The parameters are:

$$\begin{cases} \text{Speed} & \text{6000 rpm} \\ \text{Acceleration} & \text{4000 rpm/s} \\ \text{Time} & \text{30 s} \end{cases}$$

The sample is then coated with Ma-N 2401 negative ebeam resist with the following parameters to produce a 100 nm thick layer:

$$\begin{cases} \text{Speed} & \text{3000 rpm} \\ \text{Acceleration} & \text{3000 rpm/s} \\ \text{Time} & \text{30 s} \end{cases}$$

Finally the sample is prebaked for 65 s at 95°C on a hotplate. Longer prebake times lead to longer development times after exposure. This can allow for more precise control of development for critically small structures. The development times given later are for 1 min 5 sec prebake times. Baking the sample for 1 minute at 100 °C between the HMDS coating and Ma-N 2401 coating steps or simply proceeding as described without bake were found to give similar results.

A small scratch is then made with the tweezers on the resist at the edge of the sample to provide a reference for the focusing of the electron beam in the following lithography step. Since the Ma-N 2401 resist is also sensitive to UV exposure the sample must not be exposed to direct light from the time is has been coated to the time it has been completely developed.

4.1.4   Mask design, alignment and exposure

Mask design

The mask for GaAs disk resonators coupled to integrated coupling waveguides contains two 'conflicting' design elements. On the one hand the central part of the chip contains micrometer sized disks and sub-micrometer wide tapered waveguides which must be exposed with extreme precision and therefore small beam currents. On the other hand the non-tapered parts of the coupling waveguides which connect the tapered region of the waveguide near the disk to the sample facets are several micrometers wide and several millimeters long. Such large areas would be prohibitively long to expose with a small electron beam current. Therefore the mask is exposed using two different beam currents and two different exposure techniques.

The small central part containing the tapering region and the disk (shown in red in Figure 4.4) is exposed with a small step size ($\Rightarrow$ high resolution)
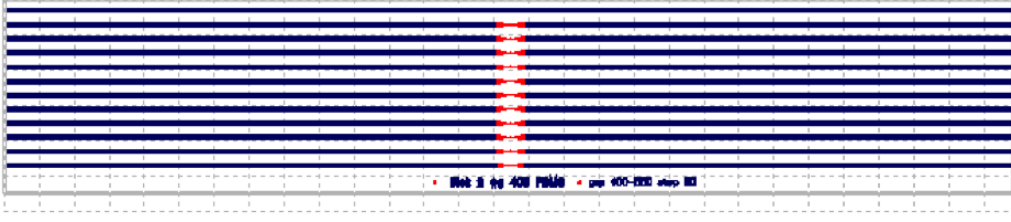
Figure 4.4: Screenshot of a mask file showing the two different exposure regions, exposed with small electron beam aperture (red) and large aperture (blue). The grey dashed lines delineate 100 μm x 100 μm squares which mark the boundaries of individual write-fields.

and small microscope aperture ($\Rightarrow$ low beam current). It is exposed in Write Field (WF) mode, in which the electron beam is deflected in order to expose regions 100 μm x 100 μm. In order to expose adjoining 100 μm by 100 μm regions (called write fields) the sample is moved by the translation stage. The stitching between two write fields (shown as grey dashed lines in Figure 4.4) is not perfect and can lead to small misalignments or gaps (not shown here). Therefore it is imperative not to have the disk resonator lying on the boundary between two different write fields.

The straight segments of the coupling waveguide (in blue in Figure 4.4) are exposed with a large microscope aperture ($\Rightarrow$ high beam current), lower resolution and a different exposure mode called Fixed Beam Moving Stage (FBMS). In FBMS mode, the electron beam stays 'fixed' (it has a small circular motion) while the sample is continuously translated underneath using a precision piezo translation stage [131]. This mode allows for rapid and stitching error-free exposure of long straight waveguides.

Column Alignment

The scratch in the resist made in step 4.1.3 serves as a first reference for rough focusing. The fine alignment of the ebeam column parameters (focus, stigmatism, ...) is done by visualizing the appearance of contamination dots (or burn dots) burned in the resist. These are produced by parking the beam for a few seconds on a single spot of resist. The appearance of these dots thus directly provides information on the focused beam shape. After proper column alignment these dots should be perfectly circular (indicative of good stigmatism) and have a diameter $\leq$25 nm (indicative of good focusing). These dots also serve as reference points for a write field alignment procedure in which the stitching between two adjacent write fields is optimized (as the tapered section of the waveguide can extend over two or more write fields). The column settings for both exposure modes must be optimized

101

independently. This optimization should be done near the region where the lithography is going to be performed on the sample. Indeed the sample never lies perfectly flat and the beam can therefore be slightly out of focus several mm away from the optimization point.

Finally when changing from the small (10 μm) to the large (60 μm) aperture column settings the beam does not stay perfectly in place. The beam position experiences a shift of a few microns and this shift, if not taken into account and corrected, leads to a misalignment between the exposures at different apertures (see Figure 4.5).

Exposure parameters

Exposure is done with the 'circular exposure mode' activated. Using this mode disks are exposed with the electron beam tracing concentric circles and therefore have very smooth sidewalls. This is important as in the default setting the disk is fractured into polygons which are consecutively exposed in raster mode. This leads to staircasing effects which are detrimental to the optical Q factor of the finished device.

- The tapered region and disk resonator (red region in Figure 4.4) are exposed with the following parameters: a 10 μm aperture (producing a current of roughly 25 pA), a 10 nm step size and 120 μA·s·cm^{-2} dose resulting in a beam speed of $\sim$2.5 mm/s

- The straight coupling waveguides (blue in Figure 4.4) are exposed with a 60 μm aperture (current $\sim$1.3 nA), a 150 nm step size, a 120 μA·s·cm^{-2} dose in FBMS mode with a FBMS stage speed of $\sim$0.09 mm/s.

The correct aperture size is chosen to give a beam speed between 1 and 5 mm/s in combination with the desired step size. Slower beam speeds just make the exposure unnecessarily slow while faster beam speeds lead to exposure problems (uneven doses, jagged edges ...). With these parameters the exposure time for a series of 20 disks + coupling waveguides is roughly 25 minutes.

The 120 μA·s·cm^{-2} dose is chosen as a compromise between smoothness and proximity effects: using a lower dose results in added resist sidewall roughness after development as the resist is not sufficiently exposed. On the other hand while a slightly over-exposed dose (> 150 μA·s·cm^{-2}) leads to even smoother sidewalls, it also generates increased proximity effects between disk and taper (see following section).
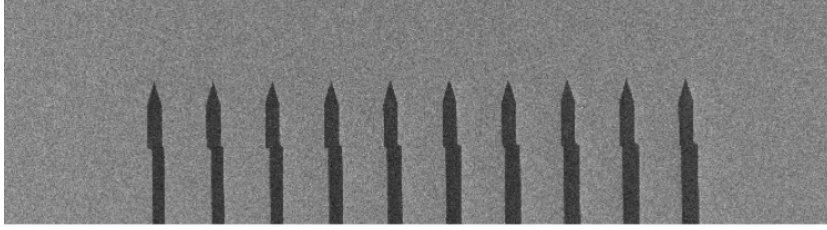
Figure 4.5: SEM micrograph displaying poor alignment between the tapered region of the waveguide (top) exposed in write-field mode with a 10 μm column aperture and the straight segment of the coupling waveguide written in FBMS mode with a 60 μm column aperture. Only half of the waveguides and no disks were exposed for this testing procedure. For scale each waveguide is ∼10 micrometers in width.

4.1.5 Proximity effect

The focused electron beam has a finite spot size. Once the electrons enter the resist, they can experience small angle scattering events through interactions with the resist electrons. This phenomenon leads to a widening of the electron beam as it goes through the resist and is called forward scattering. Electrons having gone through the resist can also be scattered back upwards (large angle scattering) through collisions with atom nuclei in the wafer and expose the resist on their second passage. This phenomenon is called backward scattering and also leads to an effective widening of the electron beam spot. Using a thinner layer of resist reduces the influence of forward scattering. Working with higher electron energies (obtained by increasing the acceleration voltage) also decreases forward scattering, but increases the width of backward scattering (see Figure 4.6). Both forward and backward scattering lead to proximity effects: the exposed resist pattern is greater than the scanned pattern. This means resist outside the scanned pattern also receives non-zero dose. When the design file only includes isolated disks, proximity effect is not much of an issue: the disks in the developed resist will just be slightly larger than the disks in the design file. However when the design file includes a coupling waveguide in close proximity to the disk the proximity effect becomes problematic. In this case the narrow region between the disk and the coupling waveguide can receive a sufficiently large dose to cross-link and remain partially in place after development. The result depends on the magnitude of the proximity effects. In the worse case the disk and waveguide can become fused together in the developed resist (not shown here). In a slightly less extreme albeit still problematic case, the disk and coupling waveguide sidewalls near the coupling region may exhibit larger surface roughness (see Figure 4.7), which is deleterious to the finished disk resonator's optical Q. The larger the disk and coupling waveguide and

103
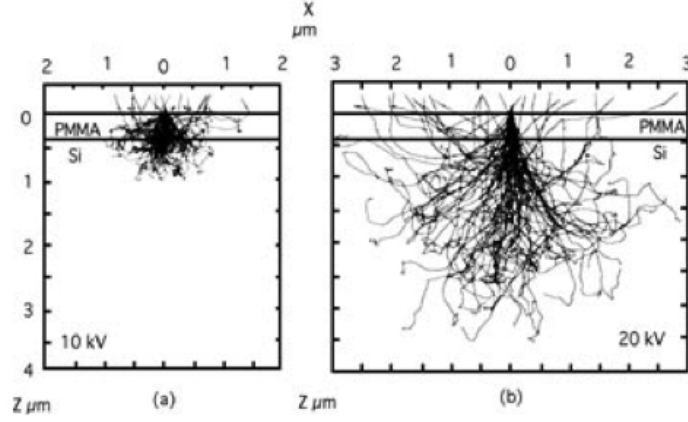
Figure 4.6: Monte Carlo simulation of electron scattering in resist on a silicon substrate at a) 10 kV and b) 20 kV. From [132].

the smaller the gap, the more problematic this proximity effect becomes. In practice, using 100 nm thick Ma-N 2401 and a 20 kV acceleration voltage, we find the smallest gap distance we can obtain -without adding significant sidewall roughness- between a 1 to 3.5 μm radius disk and a 200 nm to 700 nm wide coupling waveguide is slightly below 100 nm. Longer development times and strong agitation in the developer reduce the impact of proximity effects, but also start to reduce the size of the exposed patterns and increase the risk of delamination. The broadening of the electron beam spot's effective diameter due to forward scattering is given by the empirical formula [133]:

$$d_f = 0.9(R_t/V_b)^{1.5} \tag{4.1}$$

where d_f and R_t are respectively the effective e-beam spot diameter and the resist thickness, both in nanometers and V_b is the electron beam acceleration voltage in kilo volts. With our experimental parameters (R_t= 100 nm and V_b = 20 kV) this formula gives d_f = 10 nm. This value is close to the smallest burn dot diameters we can obtain which measure roughly 20 nm. This formula also explains the significantly more detrimental proximity effects we observed when using 300 nm thick resist (ma-N 2403). In this case the beam broadening due to forward scattering alone is above 50 nm which makes ~100 nm sized gaps in the resist impossible to obtain.

4.1.6 Development

Once the sample has been exposed in the ebeam writer, the resist must be developed. Crosslinking occurred in the resist where it was exposed to the
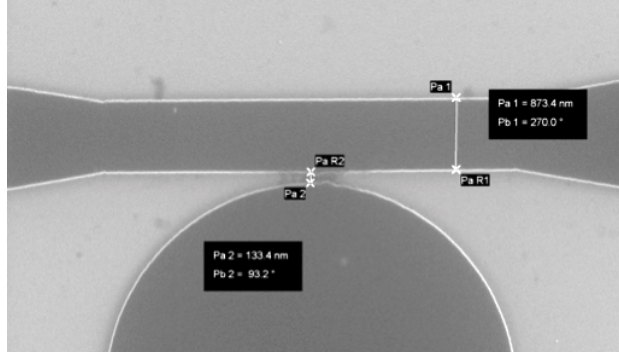
Figure 4.7: SEM micrograph of developed resist showing how non-optimal exposure parameters lead to proximity effects between disk and taper. The disk is 2.5 μm in radius, the waveguide is $\sim$900 nm wide at its thinnest and the gap between the two is roughly 100 nm. Remaining resist residue is visible between the disk and the waveguide lending a grayish color to the area. Notice also the increased sidewall roughness in the portion of the disk resonator closest to the waveguide.

electrons, elsewhere the resist remains in its initial state. The cross-linked resist dissolves significantly slower in the developer solvent than the unexposed resist, therefore only the exposed regions remain as a mask on the sample after development. The sample is developed in AZ 726 MIF. AZ 726 MIF is a metal ion free TMAH (tetra methyl ammonium hydroxide) based alkali developer with added surfactants which help with homogeneous resist removal. The development time is between 15 and 25 seconds, 20 seconds generally gives good results. To prevent the resist from delaminating it is better to do develop the resist in small steps (e.g. 3×8 s instead of 24 s at once). The sample should be slowly agitated in the developer solution. A bit of agitation helps to remove the remaining resist from the narrow region between disk and taper, but too strong agitation can lead to delamination. After each step in the developer the sample is rinsed for 1 min in deionized (DI) water and thoroughly dried with a N_2 gun to get rid of all remaining moisture. The development progress can be monitored with an optical microscope - making sure a UV filter is inserted, otherwise visualizing the resist will also expose it, rendering further development impossible. After a few seconds ($\sim$5 s) most of the unexposed resist on the sample is already removed. However the partially exposed resist between disk and coupling waveguide takes longer to remove, this is why the development time is longer than 5 s. It is not possible to resolve gaps on the order of a few hundred nanometers under the optical microscope. However when the development time is too short, and there is still some remaining resist between disk and tapered waveguide, the color in that region will be an intermediate between the resist color (dark blue) and

105
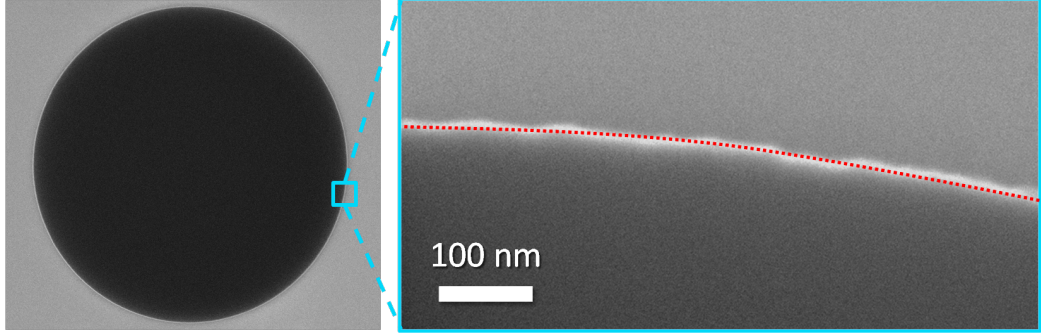
Figure 4.8: Left: SEM micrograph top view of a $\varnothing= 7$ μm disk patterned in Ma-N 2401 resist after development. Right: SEM micrograph top view displaying a close-up of the resist sidewall (image rotated 90 °counterclockwise). The dashed red line serves as a guide to the eye, defining what a perfectly smooth boundary would be. While the left image looks perfectly smooth, the zoomed view reveals non-periodic roughness with a $\sim$5 to 10 nm maximal amplitude.

the substrate color (beige under the microscope). After development the size of the features (disks, waveguides) in the resist are measured to be within 1% of their nominal size in the mask file.

4.1.7 Resist reflow

To achieve the highest possible optical Q factors the GaAs disk resonators sidewalls must be as smooth as possible. Since any roughness present in the resist mask will likely be transferred onto the finished device sidewalls during the ICP-RIE etch, it is crucial to start with a smooth resist mask. After the development step the resist smoothness is inspected under the SEM. Results are shown in Figure 4.8. The overall shape of the disk is perfectly round and shows no staircasing effects. Indeed the disk is exposed with the electron beam describing concentric circles instead of the 'common' method of polygon fracturing. A small level of seemingly randomly distributed roughness is however present over the whole boundary (Figure 4.8, right). To reduce this roughness we employ the *resist reflow* technique. After development the resist is briefly heated up to its softening temperature. At this temperature under the influence of surface tension the sidewalls reform and roughness is greatly reduced. Resist reflow has been successfully employed with ZEP resist to fabricate high optical Q silicon WGM disk resonators [134] and with Ma-N 2403 for silicon nitride resonators [135]. This approach of softening a material to reduce surface imperfections is also commonly used for the fabrication of silica microsphere [136] and toroid [15] WGM resonators.

After a successful reflow step the resist sidewalls become slopped : the
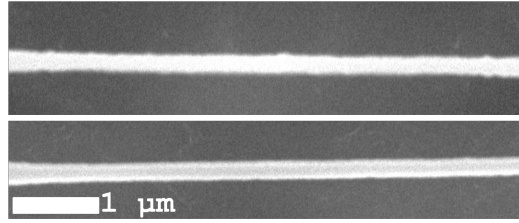
Figure 4.9: SEM micrographs of the 200 nm wide GaAs tapered section of the coupling waveguide taken at the end of the fabrication process. In the top case the fabrication process did not include resist reflow, while the bottom case included a resist reflow step.

top of the resist shrinks (∼5 to 10 %) while the bottom keeps the same dimensions. For Ma-N 2403 heating the resist for 5 minutes at 145 °C gives good results, while for the thinner Ma-N 2401 1.5 minutes at 145 °C is sufficient. The effect of reflowing the 2401 resist on a finished device is shown in Figure 4.9.

4.1.8   ICP dry etching

Principle

The 320 nm thick upper GaAs layer that will define the disk and the waveguide is etched with a dry Reactive Ion Etching (RIE) step. In a conventional Parallel Plate Reactive Ion Etching (PP-RIE) system a radio frequency (generally 13.56 MHz) alternating electric signal is applied between two metal plates. The oscillating electric field ionizes the gas molecules creating a plasma. In an transient initial stage the heavy ions are less displaced by the field than the lighter electrons. Electrons striking the upper plate or chamber sidewalls are led to the ground (see Figure 4.10, left). On the other hand electrons striking the DC-isolated lower plate give it a negative DC bias. This negative bias in turn accelerates the positive ions toward the bottom plate where they collide with the wafer. An equilibrium is rapidly reached between the number of electrons and ions striking the bottom plate for a given bottom plate bias called *self-bias*. This self-bias is an important parameter as it determines the kinetic energy of the ions striking the surface (high energy collisions tend to damage the sample). In the case of an Inductively Coupled Plasma RIE (ICP-RIE) two independent RF sources are used (see Figure 4.10, right). The top source (generally called ICP power) is inductively coupled to the gas via a coil, producing a high density plasma. The second source (called RF power) is contacted to the sample chuck in order to produce a bias to extract and accelerate the reactive species towards the sample (as in a PP-RIE). The separation of these two RF sources in ICP-
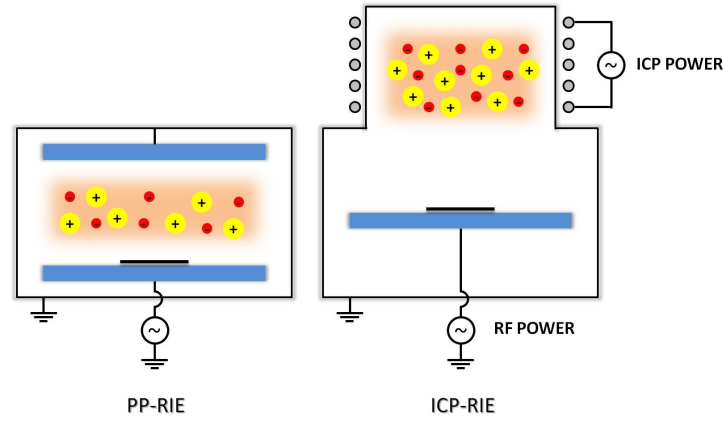
Figure 4.10: Schematic comparison between a conventional parallel plate reactive ionic etcher (PP-RIE) (left) and an ICP-RIE (right). The ICP-RIE design generally allows for smoother etch profiles.

RIE systems allows for low-bias operation which generally produce smoother etches.

Procedure and optimization

Before dry etching, the sample is hard-baked for 10 minutes at 100°C on a hot plate in order to increase the etch resistance of the resist. ICP-RIE etches are very sensitive to the chemical state of the reaction chamber side-walls. Therefore before each etch a SF_6-O_2 cleaning procedure followed by a conditioning run with the desired etch recipe but without the sample are performed to ensure reproducible chamber operation conditions.

The samples are then etched in the ICP-RIE system (Sentech SI500) with a $SiCl_4$-Argon gas mixture, using a Si wafer as a sample tray [137]. Even once the etch gases are selected the parameter space for optimization is still very large : gas flows for each gas, ICP Power, RF power, sample temperature and chamber pressure. In consequence we did not have time to study the influence of each separately. Below are some rudimentary observations from our various recipe trials. Very generally speaking the ICP power controls the density of the plasma; the RF power controls the directionality of the etching process. At high ICP power to RF power ratio the etching is rather isotropic (as evidenced by under-etching beneath the resist mask), whereas the opposite configuration (lower ICP to RF power ratio) leads to a more directional etching. Argon (Ar) is an inert gas, and Ar ions will therefore contribute to physical etching of the sample through high-energy collisions with the surface atoms (sputtering). $SiCl_4$ once ionized produces Cl- ions
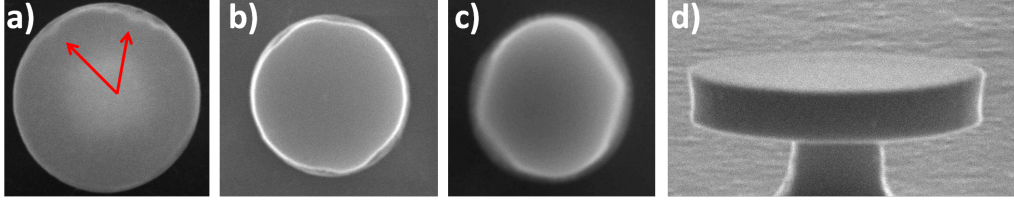
Figure 4.11: a,b and c: influence of the ICP to RF power ratio. a) Ratio = 2, some localized sidewall erosion is visible (red arrows). b) Ratio = 3. c) Ratio = 25, an octagonal shape is visible due to preferential etching along crystallographic axes. d) Slightly caved in disk resonator sidewalls with a Ar to SiCl$_4$ ratio of 1.

Ar (sccm)	SiCl$_4$ (sccm)	RF Power (W)	ICP Power (W)	Temperature (°C)	Pressure (Pa)
9	3	17	25	10	0.1

Table 4.1: Optimized ICP etch parameters used for the fabrication of the disk resonator shown in Figure 4.12.

that also chemically react with the GaAs. Therefore the ratio of Ar to SiCl$_4$ can control whether the etch is more physical or chemical in nature. Using a chamber pressure of 0.1 Pa gave smoother results than a pressure of 0.2 Pa, all further trials were carried out with 0.1 Pa pressure. Increasing the RF power increases the self-bias as opposed to increasing the ICP power which reduces self bias. We aimed to keep the self-bias absolute value below 100 V, as higher values tend to produce plasma damage and rough sidewalls. One way of keeping a low self-bias is with a high ICP power to RF power ratio. This approach however gave poor results with marked sidewall erosion (see Figure 4.11 a,b and c). Best results were obtained with a reduced ($\sim$1.5) ICP power to RF power ratio combined with low RF power to keep the self-bias low. Increasing the proportion of Ar to SiCl$_4$ (ratio=3) also produces more vertical sidewalls which otherwise tend to cave in (Figure 4.11 d). The influence of sample temperature was not investigated, although it has been reported to influence both smoothness and etch anisotropy [137]. (A sample temperature of 10 °Cwas kept throughout all this work).

Results and ICP etch parameters

The optimized recipe described in Table 4.1 produces very smooth vertical sidewalls (see Figure 4.12). The etch speed (measured in-situ with laser interferometry) is rather slow at $\sim$25 nm/min.
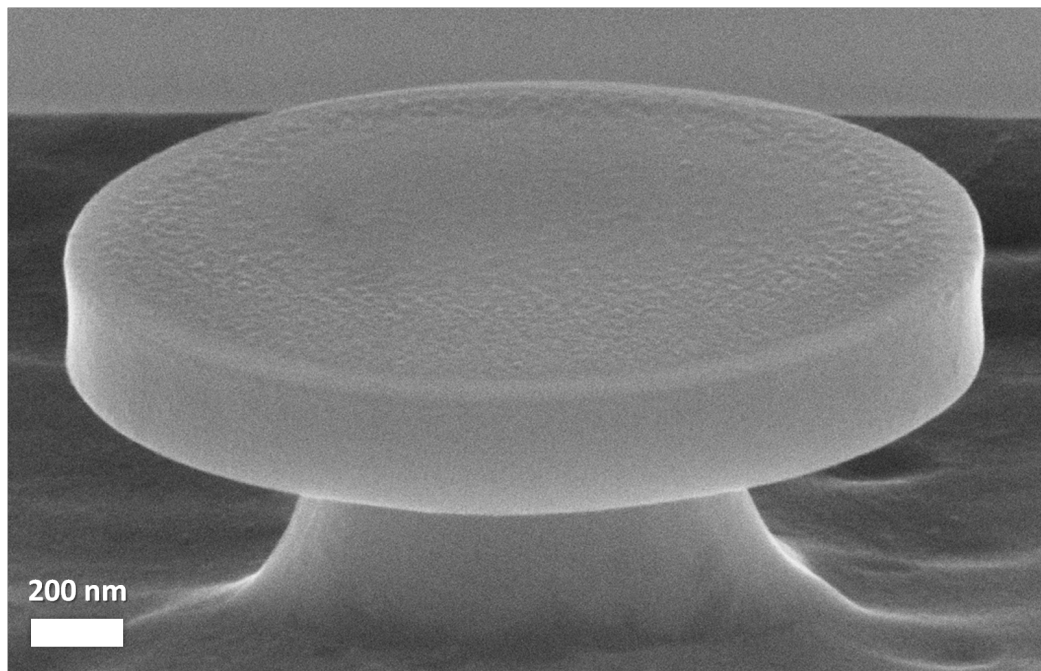
Figure 4.12: SEM micrograph displaying a very smooth sidewall on a 320 nm thick and $\varnothing = 2\ \mu$m disk resonator obtained the from the optimized ICP etch recipe of Table 4.1. The pedestal has a large diameter because of a short HF under-etch. Small amounts of resist residue are still visible on the top surface as the cleaning step has not been completed.

Etch selectivity

The selectivity of the resist (defined by the ratio between the etch speed of GaAs/AlGaAs and the etch speed of the resist) depends on the nature of the etching recipe. For the optimized recipe described in Table 4.1 the selectivity is quite good at ~35 meaning it is possible to etch 3.5 microns into the GaAs/AlGaAs before the resist is completely gone (with 100 nm thick resist). In practice, it is better not to etch too much of the resist away, as this can lead to extra roughness.

4.1.9   Non selective wet etching

The ICP-RIE dry etch step discussed in 4.1.8 can be replaced by a non-selective wet etching step of GaAs and AlGaAs which plays exactly the same role. This is the approach we initially employed. In this section we will discuss this non-selective wet etch which we used to form free-standing (i.e. with no coupling waveguide) GaAs optomechanical disk resonators with extremely smooth sidewalls [20, 55]. This wet etch step can even be used to form disk resonators with integrated coupling waveguides [21]. However for integrated structures we now favor using an ICP-RIE dry etch over a non-selective wet etch for reasons we will discuss in the following.

We use a solution consisting of equal parts of Hydrobromic acid (HBr), acetic acid (CH_3COOH) and a saturated solution of potassium dichromate ($K_2Cr_2O_7$) in DI water (14.7 g $K_2Cr_2O_7$: 100 mL DI). This etchant was first described by Adachi [138] in 1982 and dubbed **BCK** after its three main components H**Br**, **CH$_3$COOH** and **K$_2$Cr$_2$O$_7$**. This etchant was also used in subsequent works on GaAs disk resonators [45]. In [138] the fraction of potassium dichromate m was varied with regard to the two other components *i.e.* (1:1:m). Low $K_2Cr_2O_7$ fractions (m <0.1) led to pitted surfaces, whereas values of m >0.2 gave smooth pit-free results. In our work, we always kept the fractions equal at (1:1:1). Best and most reproducible results are obtained when the solution is kept at 4 °C in a thermostated bath.

The etch speed for this etchant is strongly dependent on agitation (e.g. agitating only in one direction during the etch produces oval shaped disks). Furthermore this etchant gives smooth rounded surfaces without any preference for crystallographic axes. These two properties are strongly indicative of the *diffusion controlled* etch regime (also called diffusion-limited) [139]. The diffusion controlled regime is very desirable to produce smooth disk resonator sidewalls - however this only works well when a stable etch regime is reached. This is the case for the fabrication of free-standing GaAs disk resonators where the sample is kept immobile for a time $\geq$ 75 s in the 4°C
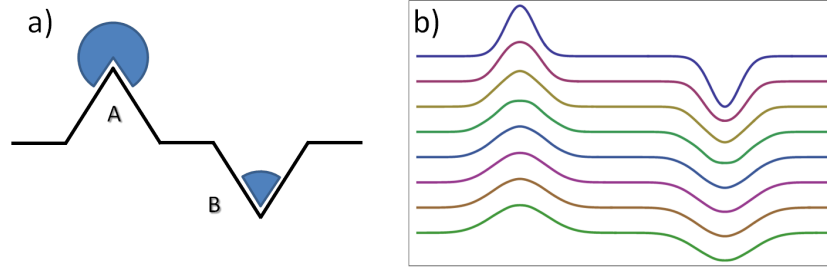
Figure 4.13: Schematic illustration of the smoothing mechanism of a diffusion limited etchant. a) More reactants (symbolized by the blue sector) are available to react with point A than point B. b) Very simple toy model showing the gradual smoothing of an interface. Successive curves from top to bottom are obtained by $f_{n+1}(x) = f_n(x) - \alpha + \beta \dfrac{\partial^2 f_n(x)}{\partial x^2}$ (available reactant quantity depends on the second derivative of the curve).

BCK etchant solution. This time is long enough to etch through the top GaAs layer as well as the sacrificial $Al_{0.8}Ga_{0.2}As$ layer (see Figure 4.15 for etch speeds). During this time a stable diffusion-limited etch regime is established and any irregularity on the disk boundary (coming for instance from the resist etch mask) will be gradually smoothed out as more reactants are available around sharp protruding features than recessed ones (see Figure 4.13). This mechanism leads to the remarkably smooth etch profiles shown in Figure 4.14 a.

For the fabrication of disk resonators with integrated coupling waveguides however the use of this wet etch presents 3 major drawbacks.

- Not all gap distances between disk and waveguide are accessible. Since the etchant is essentially isotropic and must etch through the top GaAs guiding layer of typically 200-300 nm thickness. Gap distances smaller than this thickness are inaccessible.

- For the short etch times used for this application (typically $\leq$ 12 s) a stable etch regime is never reached. Turbulence in the etchant flow around the resist during the dipping in & taking out phases of the etch and irregular diffusion of etchants around the disk due to the broken symmetry caused by the presence of the waveguide produce irregularities in the fabricated devices which are not present in the mask. (See Figure 4.14 b).

- Because of the short etch depth both the disk resonator and waveguide sidewalls are quite slopped (see Figure 4.14 b). This makes the accurate determination of the optimal gap distance through numerical modeling significantly more difficult.
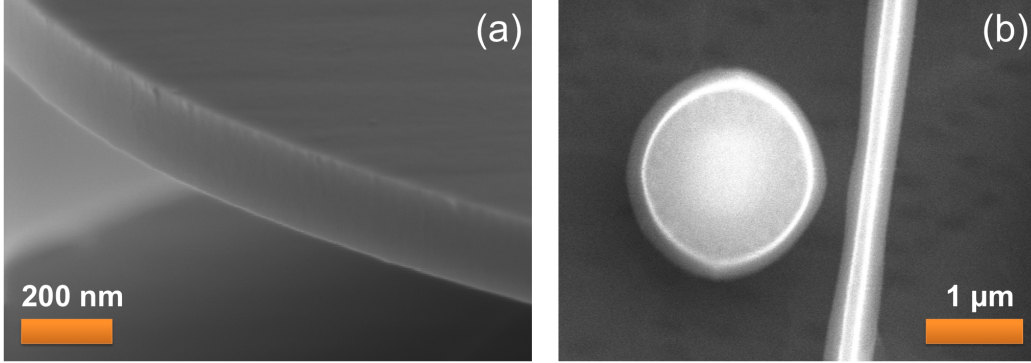
Figure 4.14: (a) SEM micrograph side view showing very smooth sidewalls on a finished 200 nm thick disk after a non-selective BCK wet etch followed by a selective HF under-etch. (b) SEM micrograph of a 1 μm radius GaAs disk resonator positioned next to its suspended coupling waveguide. The first non selective etch step was performed with a 12 s dip in the BCK wet etchant described in 4.1.9, at 4 °C. The sloped disk and waveguide sidewalls are typical of an isotropic etch. The coupling waveguide has a trapezoidal cross-section with the top being $\sim$ 100 nm wide and the bottom 400 nm. Notice the irregularities in waveguide width and in the overall circular shape of the disk. These are not due to defects in the resist mask but to variations in the etchant flow around the resist.

The fact that short etch times are strongly dominated by transient etch dynamics also explains why attempts to smooth disks post-fabrication by a short dip (1 to 2 s) in the BCK etchant did not succeed. On the contrary, such a 'flash wet etch' produces greatly increased roughness (not shown here).

4.1.10   Selective wet under-etching

Hydrofluoric acid (HF) is known to etch $Al_xGa_{1-x}As$ with an extremely high selectivity over GaAs. When the aluminum fraction x is greater than 0.5, HF etches $Al_xGa_{1-x}As$ over 10^6 times faster than GaAs [141]. Because of this HF is commonly used to remove sacrificial layers of AlGaAs. After the sample has been etched in the ICP or BCK, the $Al_{0.8}Ga_{0.2}As$ layer is selectively under-etched using HF. Concentrated HF (40 to 50%) reacts quite 'violently' with AlGaAs at room temperature. The reaction is very fast and releases large amounts of H_2 bubbles [142]. In our experience samples etched in such a fashion were almost entirely destroyed. The suspended waveguides were all broken, and most disks had fallen off their pedestal. In order to gain a slower and more reproducible underetching procedure, we work with very dilute HF (1.25 HF: 100 $H_2$0) at 4°C. In these conditions we find that the dilute HF etches with a slight preference for certain crystallographic axes, with a speed that does not depend on agitation and with a rate which strongly depends on temperature and etchant concentration. All these properties are indicative
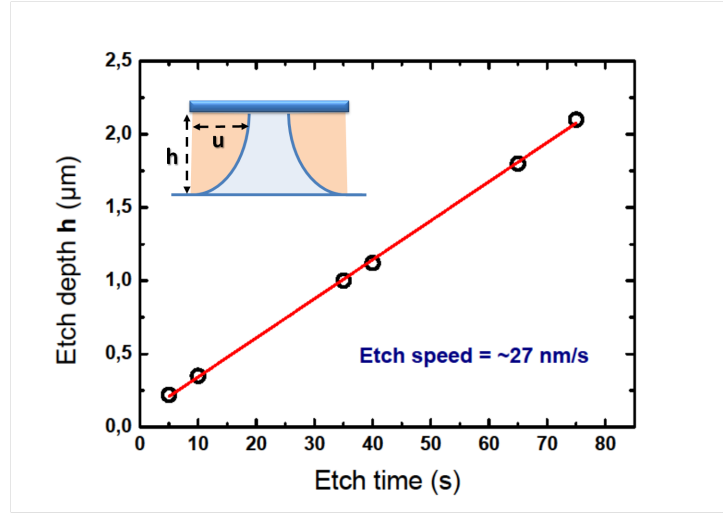
Figure 4.15: Determination the etch speed of the BCK etchant at 4 °C with no stirring. The etch depth **h** (see inset figure) is plotted as a function of time. We experimentally verify that the ratio of etch depth **h** to lateral undercut **u** is ~1.3, in excellent agreement with the quantitative model of an ideal diffusion controlled etch profile [140].

of a *reaction-rate limited* chemical reaction [65].

Influence of agitation

While the AlGaAs under-etch reaction occurs in the reaction-rate limited regime in which sensitivity to agitation is normally reduced, the final pedestal geometry is nevertheless found to be strongly dependent on agitation. Indeed, the reaction between HF and $Al_{0.8}Ga_{0.2}As$ seems to preferentially favor certain crystallographic axes. Moreover the reaction is both exothermic and strongly temperature dependent (higher temperatures lead to higher etch speeds). These last two characteristics constitute the basis of a positive feedback loop on the etch process, and lead to the irregular and jagged features in the pedestal of the disk shown in Figure 4.16 (a). Here the underetching was performed in (2 HF: 100 H_2O) at 4°C while maintaining the sample perfectly immobile. These rough and irreproducible pedestal geometries are undesirable. Furthermore the overall cone shape of the pedestal is detrimental to the mechanical quality factor of the disk resonator, as it provides a good conduit for mechanical energy to dissipate into the substrate. Fortunately, the pedestal geometries can be made smoother and more cylindrical by agitating the sample in the HF solution during the under-etch. Best results are obtained when the agitation is done rapidly and successively in different directions (e.g. left-right, top-bottom, forward-backward), see Figure 4.16
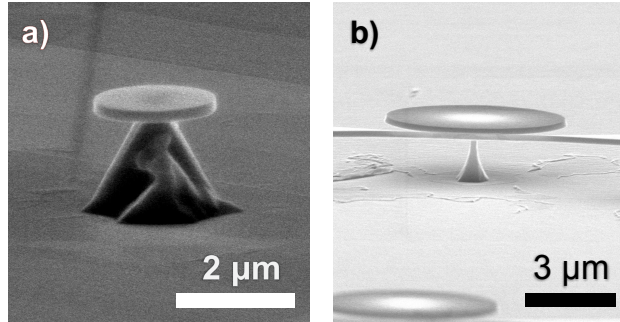
Figure 4.16: Two SEM images illustrating the effect of sample agitation during the HF under-etch step. a) Holding the sample immobile during the under-etch step leads to jagged and irregular pedestal geometries. b) Rather smooth and cylindrical AlGaAs pedestal obtained by agitation of the sample in the 4°C dilute HF solution. The pedestal has a diameter of approximately 200 nm at the junction with the GaAs disk. One can still recognize multiple distinct facets at the base of the pedestal, which are characteristic of a reaction-rate limited etch regime.

(b). Once the sample has been under-etched both suspended waveguides and disk resonators become slightly more fragile. Care should be taken not to blow too hard on the sample with the N_2 gun during the drying step to avoid damaging the free standing structures.

Potassium hydroxide cleaning

Trying to etch away large amounts of AlGaAs with HF, for instance when the ICP etch step does not reach the GaAs substrate, can be problematic. The reaction products of AlGaAs with HF are poorly soluble in the dilute HF solution. Indeed oxide removal is less efficient at higher pH [65] and some reaction products can redeposit on the sample, blocking further etching. In less extreme cases, flakes coming from -we presume- the HF under-etching can redeposit everywhere on the sample surface and on the disk resonators (see Figure 4.17 a). In [143] the authors used a pipette to create a HF flow to remove these debris. However, in [144] and [145] the authors speculate that these debris are hydroxides of aluminum coming from the HF wet etching of AlGaAs and show that they can be removed by a dip in a Potassium Hydroxide (KOH) solution. Indeed, in our experiments these debris can be removed by taking the sample out the HF, rinsing it thoroughly in DI water then dipping it in a KOH solution (e.g. 10 g KOH in 100 mL DI water) for 120 s. The sample is then rinsed anew in DI water and the HF etching can be resumed if necessary. Such a procedure leads to the clean looking results shown in Figure 4.16 (b) for instance.

115
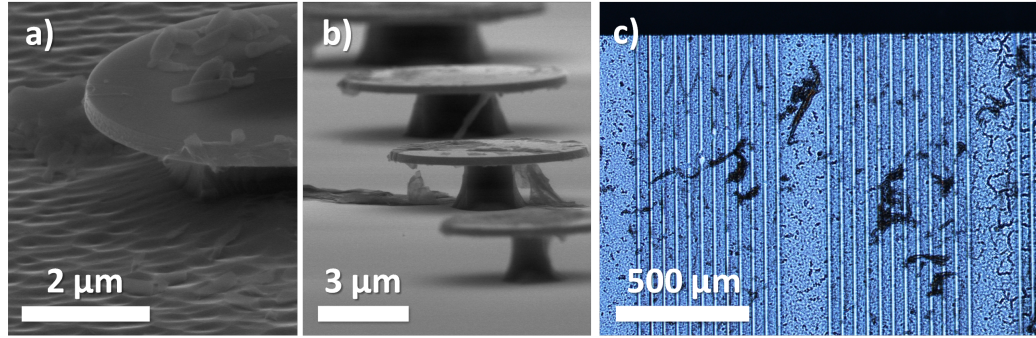
Figure 4.17: Examples of problematic HF under-etching. a) SEM image of etch debris redepositing on the surface. b) SEM micrograph and c) optical microscope top-view of oxide films occurring in samples where the AlGaAs was exposed to air. (HF and BOE give similar results).

AlGaAs oxidation

If the sample is exposed to air between the ICP etch (or the non-selective wet etch) and the HF under-etch for any length of time, a thin oxide layer will start to form on the exposed AlGaAs surface. This oxide 'sheet' will crack and be set free during the HF under-etch step and can then redeposit on the sample (see Figure 4.17 b). When this happens it cannot be removed neither by a concentrated KOH dip, nor by an IPA/acetone rinse, nor by an O_2 plasma cleaning procedure. Effects of air exposure start to manifest after only $\sim$1 minute and are particularly dramatic for samples exposed to air for weeks (Figure 4.17 c). To avoid this, samples are immediately put in isopropanol or acetone (not water) as soon as they are taken out of the ICP load-lock. This way of preventing oxidation gives good results and allows for a precise control of pedestal dimensions (see Figure 4.18 and next section).

Etch speed and pedestal dimension control

Fabrication of disks with high undercut ratio and small pedestal radius ($\sim$100 nm) requires very precise control of the under-etch speed. Initially in our process the HF under-etch speed was not reproducible as samples were exposed to air for varying durations between ICP and HF etching. The etch dynamics of the AlGaAs oxide layer being different from that of the bulk AlGaAs, identical etch times produced different sized pedestals. Preventing oxidation as described in section 4.1.10 allows for $\leq$50 nm precision in fabricated pedestal diameters (see Figure 4.19).
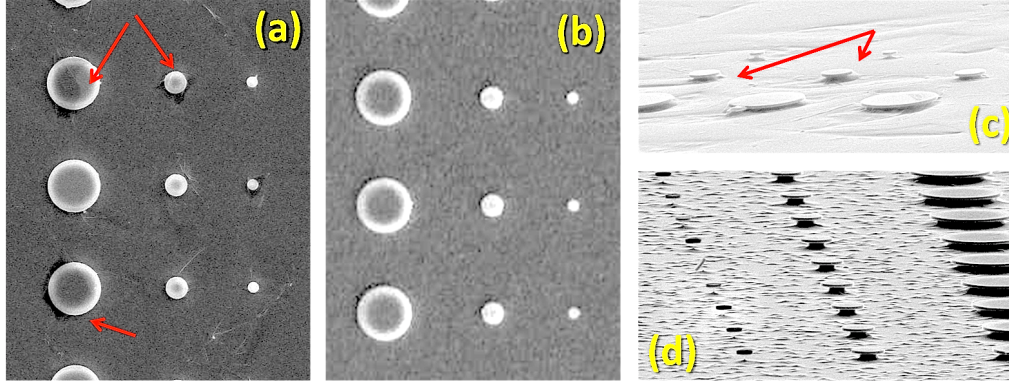
Figure 4.18: SEM micrographs showing the effect of oxidation of the AlGaAs layer on two different samples. Both samples were identically processed to the exception that sample 1 (a and c) was kept for 3 hours in water between the ICP etch and the HF undercut, while sample 2 (b and d) was kept in isopropanol for 3 hours. Notice the cracked oxide films on the sample kept in water (a and c) marked by the red arrows. Another important difference is the HF undercut speed which is significantly larger for sample 2. (Keeping the sample in water or air gives similar results). Interestingly the pedestal radius in the smaller disks of (d) is below 30 nm.
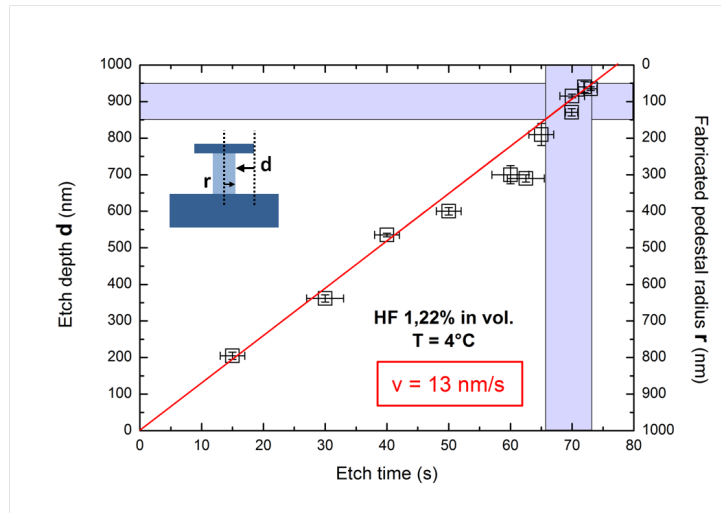
Figure 4.19: Derivation of the HF underetch speed at 4 °C. The solution consists of 2.5 mL of 50% concentration HF diluted in 100 mL DI water ($\Rightarrow$ 1.22 % HF in volume). The left axis represents the one-sided underetch depth **d** (see inset figure). The right axis gives the corresponding AlGaAs pedestal radius **r**, *for a 1 µm radius disk*. 70±3 s etch times reliably produce disk resonators with a pedestal radius of ∼100 nm (blue target region) such as the one shown in Fig. 4.23. These etch speeds were measured for AlGaAs *unexposed* to air. Data acquired in the team by Dac Trung Nguyen.

117
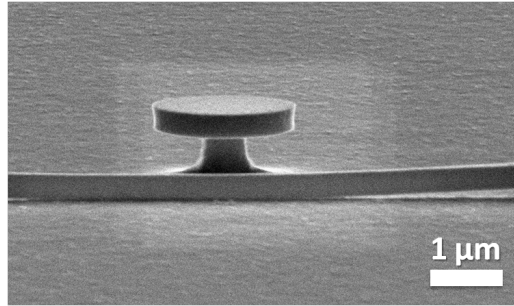
Figure 4.20: SEM micrograph showing a collapsed suspended waveguide after the HF under-etch step. The waveguide collapsed due to surface tension acting between it and the substrate.

Collapsing of the under-etched waveguide

While the bending of the suspended portion of the coupling waveguide under its own weight is negligible (as discussed in section 2.2), the very strong effects of surface tension at micrometer scales can cause the suspended portion of the beam to collapse. An example of this is given in Figure 4.20. This should be avoided as once the beam has collapsed stiction keeps it stuck to the substrate : it does not spontaneously 'pop back into position' after drying. The two main causes of collapsed beams are:

- Too strong agitation in the HF, KOH or DI water.

- Spending too much time in the DI water rinse. Indeed as the sample leaves the KOH it is highly hydrophobic (as evidenced by the high contact angle of water droplets on the sample). The longer the sample is kept in the DI the more hydrophilic it becomes, increasing the likelihood of the beam collapsing during drying. Keeping the time spent in the DI rinse under a minute prevents this problem. The sample can also be dipped in acetone or isopropanol (both of which offer lower surface tension) before the final drying step.

Provided the above recommendations are met virtually no beams collapse during the fabrication process without need for the use of a critical point drying system.

Under-etching with Hydrochloric acid (HCl)

HCl is also known to successfully selectively etch AlGaAs over GaAs [146, 147]. This approach was tried for the fabrication of GaAs disk resonators. However, while refrigerated (4°C) 36% (w/w) HCl offers well controlled etch
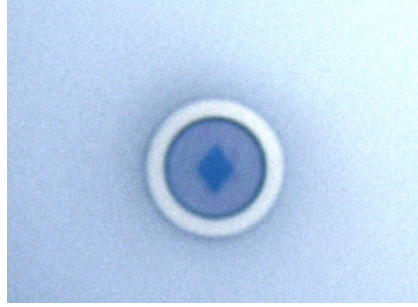
Figure 4.21: Optical microscope image of a ∅= 6 μm stand-alone GaAs disk resonator fabricated using a non-selective BCK wet etch followed by a selective HCl under-etch step of the AlGaAs sacrificial layer at 4 °C. The AlGaAs pedestal (deep blue) is visible by transparency through the purple GaAs disk resonator. Notice the diamond shape of the pedestal due to the strongly anisotropic under-etch.

speeds and very clean etches devoid of the problems reported in sections 4.1.10 and 4.1.10, it is also strongly anisotropic, producing diamond shaped AlGaAs pedestals which are problematic for the disk resonator's mechanical properties (see Figure 4.21). For this reason this etch method was not selected for fabrication.

4.1.11 Cleaving & cleaning

Cleaving

At the end of fabrication the sample is cleaved at both ends to produce the waveguide input/output facets. A example is shown in Figure 4.22. A small indent is made with a diamond onto the sample top surface at the desired cleave location. The sample is then turned upside down in a round bottomed wafer carrier box (so that the sample top surface does not come in contact with anything) and pressure is applied right above the indent position. This procedure is straightforward and very reproducible with no breakage.

Cleaning

At the end of fabrication samples are cleaned to remove any remaining resist residues (KOH is a strong base and already removes most of the resist in step 4.1.10). The long resist hard-baking and plasma etch tend to increase resist adhesion to the GaAs. Efficient removal can be done with an hour long bath in warm acetone or a short O_2 plasma treatment. Pictures of finished devices are shown in Figure 4.23.
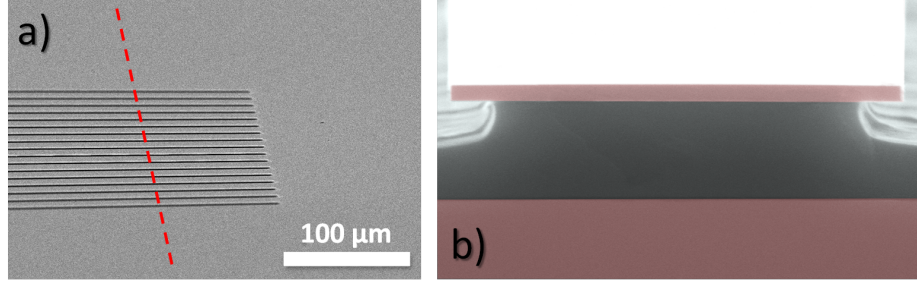
Figure 4.22: Cleaving procedure. a) SEM micrograph sideview of the edge of an array of waveguides at the end of fabrication. The dashed red line indicates the rough position of the ulterior crystalline cleave. b) SEM micrograph of a waveguide input/output facet after the cleave. From top to bottom : the 8 μm wide and 320 nm thick GaAs guiding layer, the 1.8 μm thick AlGaAs sacrificial layer and the GaAs substrate. For better contrast both GaAs layers are colored in red.
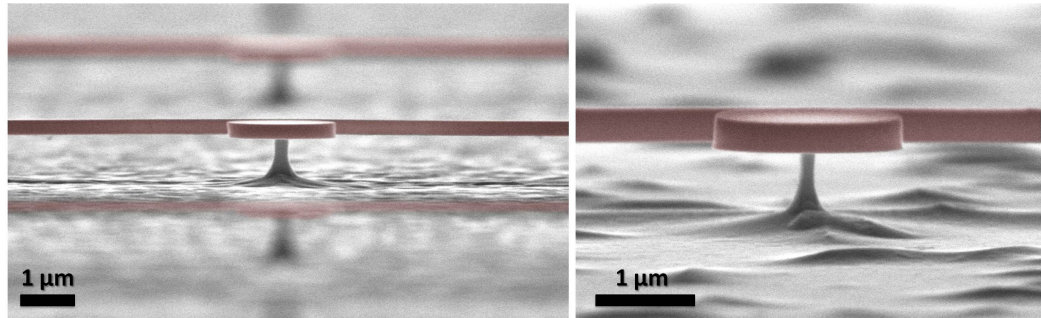
Figure 4.23: Left:SEM micrograph side-view of $\varnothing=2$ μm GaAs disk resonator positioned in front of its suspended coupling waveguide. The AlGaAs pedestal diameter is slightly above 200 nm at the junction with the GaAs disk. For better visibility the GaAs guiding layer is colored red and the AlGaAs remains gray. Here - as in Figure 4.22 - the HF under-etch did not reach the GaAs substrate leaving it invisible. Right: Close-up on a different disk resonator with slightly smaller 80 nm radius pedestal.

4.2 Silicon Nitride Nano-Fabrication

This section describes the different steps necessary for the fabrication of high optical Q SiN disk resonators with integrated suspended coupling waveguides [56]. This section is shorter than the previous one on GaAs disk resonators as many of the techniques involved have already been described. The fabrication is also slightly less challenging overall. Indeed the silicon nitride WGM disk resonators described here are 10 times larger than the $\varnothing$=2 μm GaAs disks - making them less sensitive to fabrication imperfections - and do not require a precise control of pedestal geometries. Finally the Silicon nitride/Silicon dioxide/Silicon platform has the advantage of being less prone to problematic oxidations than GaAs/AlGaAs (4.1.10) and therefore more straightforwardly offers clean fabrication results. Figure 4.24 summarizes the main fabrication steps. Special care was taken throughout to minimize disk resonator sidewall roughness at every step. These samples were fabricated in the cleanroom of the nanophysics group at the LMU in Munich with Sebastian Stapfner of Eva Weig's team. This team developed an important know-how in the fabrication of SiN nanomechanical beam resonators which we adapted here to the fabrication of integrated optical resonators. Over the course of four successive week-long stays at the LMU we acquired a better understanding of silicon nitride's optical properties and the fabrication requirements for high Q optical resonators. Here we present only the optimized fabrication steps for the on-chip WGM resonators; some additional details on our early study of optical losses in SiN with straight waveguides fabricated by photolithography and e-beam lithography can be found in section 5.4.

4.2.1 Sample preparation

The fabrication starts from a commercial (HSG-IMIT) wafer composed from top to bottom of a 300 nm thick layer of high tensile stress Low Pressure Chemical Vapor Deposition (LPCVD) SiN, a 3 μm thick SiO2 sacrificial layer and a Si substrate. Small (roughly 1 cm $\times$ 1 cm) wafer pieces are cleaved and then cleaned in successive acetone and isopropanol ultrasound baths. The sample chips are then coated with two different layers of PMMA resist. These two layers differ by their molecular weight (MW) which is indicative of the average length of the polymer chains. The bottom layer has shorter chains (MW = 150k) than the top layer (MW=500k) and will therefore dissolve faster in the developer than the top layer (see section 4.2.2). This leads to a undercut profile in the resist pattern (see Figure 4.24, b) which is desirable for the lift off step (see section 4.2.3). Each layer of PMMA resist is spun first 3 s at 800 rotations per minute (rpm) then 30 s at 5000 rpm followed
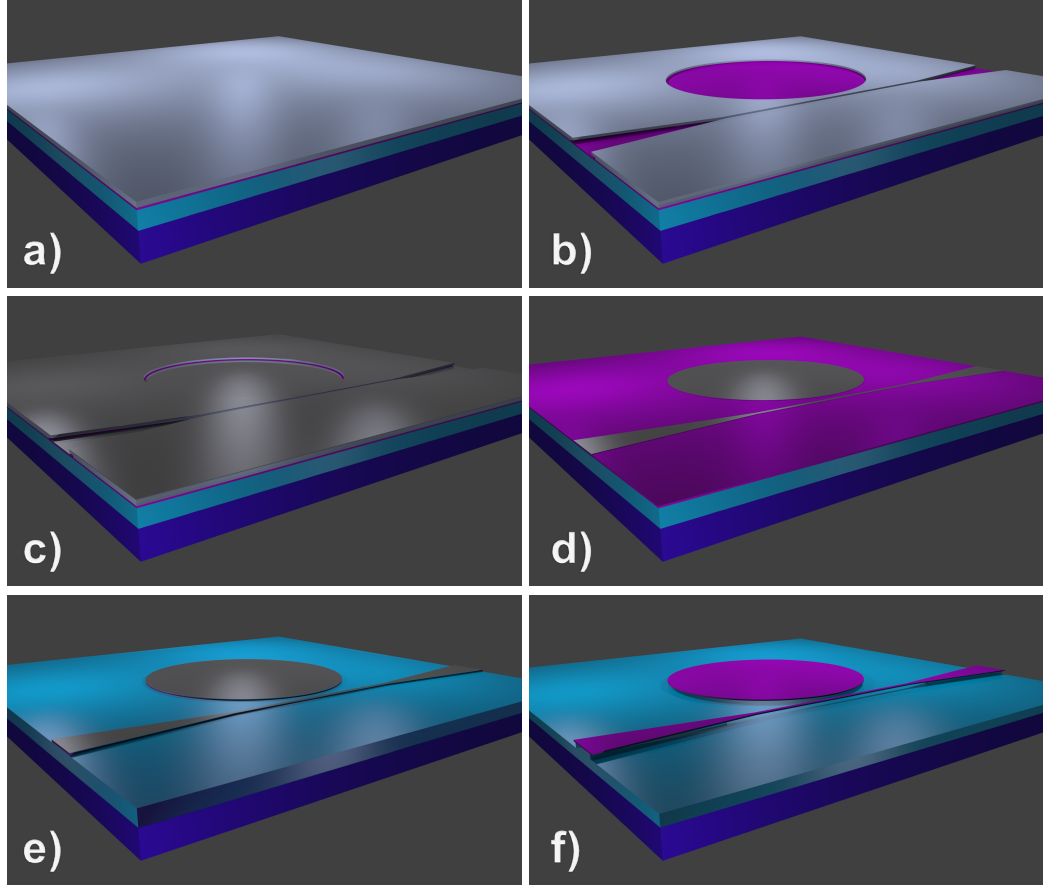
Figure 4.24: **Main nano-fabrication steps**. (a) The sample is composed from top to bottom of a 300 nm thick LPCVD silicon nitride layer (purple) over a 3 μm thick SiO_2 sacrificial layer (light blue) on top of a silicon substrate (deep blue). Two coats of PMMA (white) are spun and baked on the sample (see section 4.1.3). (b) The resist is exposed in the ebeam lithography system and developed : only the unexposed resist remains on the sample (see section 4.2.2). (c) A 40 nm thick cobalt layer is evaporated upon the entire sample. (d) A lift-off in warm acetone dissolves the PMMA and only leaves the cobalt etch mask in place (see 4.2.3). (e) The cobalt etch mask protects the disk and waveguide patterns during an ICP-RIE dry etch through the top SiN layer (see 4.2.4). (f) The cobalt is removed in Piranha etchant and the sacrificial SiO_2 layer is selectively under-etched using Buffered Oxide Etchant (BOE), isolating the SiN disk resonator on a SiO_2 pedestal and locally freeing the coupling waveguide (see 4.2.5).

by a 2 minute bake at 170 °C. Finally a scratch is added on the side of the sample with a diamond pen for ulterior focusing of the electron beam (see next section).

4.2.2 Ebeam exposure and development

The samples are exposed in a Raith eline ebeam lithography system[1] using two different column apertures and exposure modes: Write Field (WF) mode and FBMS mode (see section 4.1.4). The 3 μm thick SiO$_2$ layer beneath the SiN is a bad charge conductor : initially the double layer PMMA was covered with a 2 nm thick chrome layer in order to minimize charge buildup in the sample. However the removal after ebeam exposure of this 2 nm layer with a chrome etch solution is a significant source of added roughness in the patterned resist, as measured under the SEM (not shown here). For that reason the use of a chrome layer was removed from the process. Working without a chrome layer prevents the burning of contamination dots in the resist (see section 4.1.4) : the scratch in the sample done in step 4.2.1 serves as a reference for column settings optimization instead. The central part of the mask file containing the tapered waveguide and the disk resonator (see Figure 4.4) is exposed in write field mode with a 30 μm aperture, 20 kV acceleration voltage and a 150 μC·cm^{-2} dose. The straight portions of the waveguides are exposed in FBMS mode with 120 μm aperture, 20 kV acceleration voltage and a 150 μC·cm^{-2} dose. Disks are exposed with the electron beam tracing successively larger concentric circles in order to produce smooth boundaries (see section 4.1.4). Exposure dose was optimized to allow small gap distances between disk and waveguide with little added surface roughness. We find PMMA resist to be less prone to problematic proximity effects than Ma-N 2400 series resist (see section 4.1.5).

After exposure, the resist is developed for 50 s in a solution of 3:1 Isopropanol/Methyl IsoButyl Ketone (MIBK). The use of double layer PMMA produces an undercut in the resist profile observable under the optical microscope. The resit is inspected under the SEM and shows no signs of roughness $\geq$10 nanometers[2].

---

[1]The straight SiN waveguides discussed in section 5.4 were fabricated by photolithography with AZ-5214 image reversal resist, or with the e-beam lithography protocol described here.

[2]Roughness amplitude is defined here as the deviation from an ideal circular boundary.

Ar (sccm)	SF$_6$ (sccm)	ICP Power (W)	RF Power (W)	Temperature (°C)	Pressure (Pa)
4	2	70	35	12	0.24

Table 4.2: ICP etch parameters used for the fabrication of the disk resonators shown in Figure 4.25.

4.2.3 Metal evaporation and lift-off

After development the pattern in the positive resist is transferred to a hard metal etch mask. Cobalt is chosen as a mask material for its small grain size leading to reduced sidewall roughness. (Initial trials with aluminum masks gave poorer results because of larger grain size). A 40 nm layer of cobalt is evaporated over the whole sample (Figure 4.24, c). The sample is then dipped in a solution of warm acetone (40 °C) which dissolves the remaining PMMA and removes the cobalt layer deposited over it (lift-off). The cobalt evaporated onto the SiN remains firmly in place. The use of a resist with an undercut is crucial in this step as otherwise parts of the cobalt mask in contact with both the SiN and the PMMA can tear off, giving rise to greatly increased sidewall roughness. 100°C DMSO (dimethylsulfoxide) can also help remove remnants of stuck PMMA. After lift-off surface roughness in the cobalt mask is controlled under the SEM to be ≤10 nm.

4.2.4 ICP etch

The cobalt etch mask protects the disk and waveguide during a ~400 nm deep ICP etch (through the SiN layer and ~100 nm into the SiO$_2$) with a SF$_6$-Ar gas mixture (see 4.1.8 for more details). The process parameters are given in Table 4.2. This recipe produces smooth and vertical SiN sidewalls with maximal roughness amplitude still ≤10 nm, with an etch speed of ~20 nm/min. Initial trials with a standard Parallel Plate Reactive-Ion Etching (PP-RIE) (see Figure 4.10) lead to significant sidewall roughness in the finished devices and reduced optical Q (not shown here).

4.2.5 Selective under-etch

Before the under-etch the sample is coated in thick photoresist and cleaved (see 4.1.11). The cleaving must be done at this stage while the sample is still robust (not yet under-etched). Indeed cleaving SiO$_2$ and SiN which are not crystalline requires the application of a good amount of force which could damage the more fragile under-etched disks and suspended waveguides. A ~1
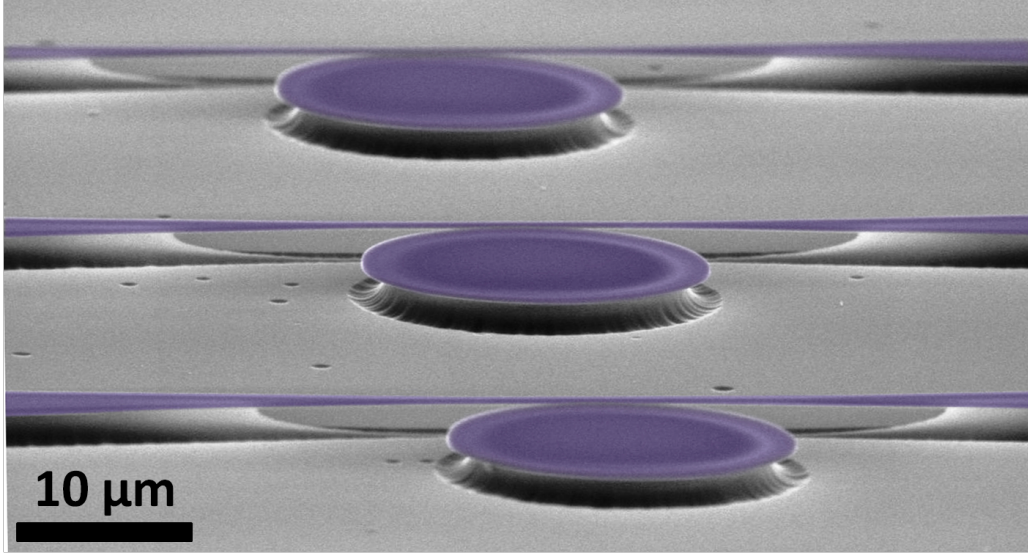
Figure 4.25: SEM micrograph side view showing three $\varnothing=20\mu$m silicon nitride disk resonators positioned in front of their integrated coupling waveguide. The SiN layer has been colored purple while the SiO$_2$ remains gray. Typical tapered waveguide widths and disk to waveguide gap distances are 500 to 900 nm and 0.2 to 1 μm respectively.

min dip in Piranha solution (3:1 H$_2$SO$_4$/H$_2$O$_2$) removes both the photoresist and the remaining cobalt mask. Complete removal of the cobalt is important, as it seems metal residue serves as a kind of catalyst for the attack of SiN by BOE in the following under-etch step, resulting in added surface roughness. Piranha solution is also believed to reduce the amount of surface optical absorption, see discussions in [56, 148]. Finally the SiO$_2$ layer is selectively under-etched in a pure BOE solution at room temperature for 15 minutes. This isolates the SiN disk resonator on a SiO$_2$ pedestal and locally frees the coupling waveguide (see Figure 4.25). The under-etch has a very reproducible speed of 110±3 nm/min and does not add any extra roughness to the SiN layer. A picture of a finished device is shown in Figure 4.25.

4.3   Conclusion

In this chapter we discussed in detail the fabrication of integrated GaAs and SiN nano-optomechanical resonators. The GaAs disk resonators presented here are miniaturized to the utmost so as to exhibit sub-λ^3 optical mode volumes. Because of these small dimensions, this made for a quite challenging fabrication and required time consuming developments. Great care was taken on both GaAs and SiN samples to keep deleterious fabrication induced

4.3 Conclusion
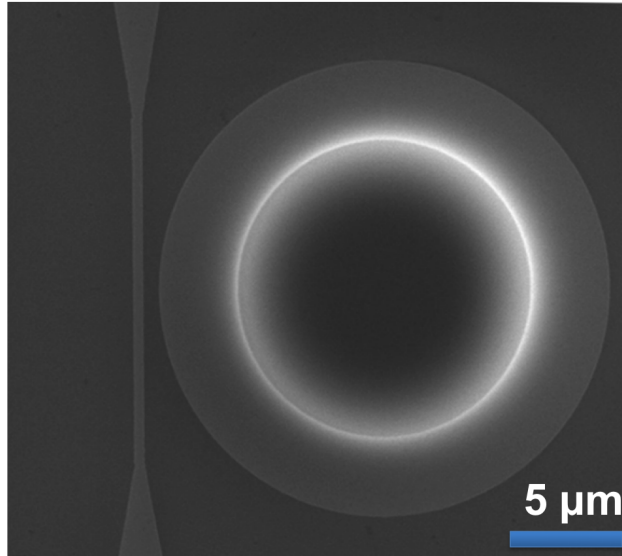
Figure 4.26: SEM micrograph top view showing one $\varnothing$=20μm silicon nitride disk resonator positioned right of its integrated coupling waveguide. The outline of the resonator's SiO$_2$ pedestal is visible by transparency as a bright white circle underneath the SiN disk.

sidewall roughness to a minimum. In the coming chapter we talk about these integrated samples' optical performance.

Chapter 5

Integrated optics experiments

5.1 Introduction

At the onset of this doctoral work, there was little experience in the team regarding the design and fabrication of on-chip optomechanical resonators with integrated coupling waveguides. We therefore went through several evolutions in the chip design which allowed for significant boosts to both optical quality factor and device optical transmission, while providing better control of evanescent coupling. The main changes leading to these improvements will be briefly summarized in section 5.2. Then an analysis of the various loss mechanisms which limit the optical Q in GaAs disks is presented (section 5.3). Preliminary results obtained while operating the integrated devices in a liquid environment will also be presented in section 5.3.1.

Next, results of work performed on high Q silicon nitride WGM disk resonators are detailed in section 5.4. The successive steps in the device development are presented. Finally optical instabilities and self-pulsing observed on these devices is reported.

5.2 Progress in on-chip GaAs resonators

Progress in GaAs optomechanical devices occurred on three main fronts, optical quality factor, optical transmission levels and evanescent coupling. During this optimization phase, samples were rapidly characterized using the setup shown in Figure 5.1.

The optical Q was mostly enhanced by two changes. The first consisted in reducing the lithographic proximity effects (see section 4.1.5) which were responsible for extra sidewall roughness and broke the disk circularity. After a first generation of devices realized by pure chemical etching, we switched to

Figure 5.1: Device characterization setup. (a) Light from a fine external cavity diode laser is injected in the chip by a micro-lensed optical fiber (left), and collected with a large numerical aperture microscope objective (right). Both are positioned on XYZ translation stages. Alignment is performed under an illuminated binocular magnifier. (b) Zoom displaying the stripped extremity of the micro-lensed fiber (left), a GaAs chip (center) and the microscope objective (right). One of our GaAs chips is typically 6 mm long by 1 to 2 mm wide and contains on the order of 60 coupling waveguides/disk resonators.

an ICP-RIE approach which enabled us to better control the evanescent coupling and to selectively couple to p=1 WGMs which have higher radiative Q. These two improvements, along with an optimized ICP-RIE dry-etch recipe allowed to boost the measured optical Qs in integrated devices roughly a hundredfold from the 10^3 to the 10^5 range and to reproducibly reach a situation of critical coupling even on miniature disks of radius 1 μm. On 1 μm radius disks, loaded optical Qs slightly above 10^5 are measured, comparable to the highest reported Qs for disk resonators of these dimensions [149]. On $\varnothing = 7$ μm disks, optical quality factors up to 700 000 are measured, equivalent to the highest optical Q ever reported in a GaAs optical resonator [150].

Optical transmission levels[1] were initially very poor for suspended waveguides, well below 1% of incident power. A large discrepancy existed between this poor transmission, and the better transmission of straight waveguides (with no tapering and suspended section) fabricated alongside, suggesting most of the losses occurred in the tapered region of the waveguide. This was confirmed by looking at the upwards scattered light intensity with an infrared camera [151], which was indeed maximal in that area. These losses were reduced by enhancing the taper's adiabadicity (see section 1.1.4) and better confining the optical field inside the guiding top GaAs layer (see section 1.1.5). Finally working with wider waveguides to shield the optical field from the rough waveguide sidewalls diminished distributed losses (see section 1.1.3). These combined improvements allowed to boost optical transmission

---

[1]Defined as the ratio between power exiting the chip and power in the incident laser beam focused on the waveguide input facet

typically a hundredfold as well up to ∼30%.

Article

The following article shows some our early devices featuring a GaAs disk resonator coupled to an integrated suspended waveguide. For the first time in such a system critical coupling was demonstrated. These resonators were fabricated using purely wet chemical etching steps (see section 4.1.9). Continued developments described above have since then allowed for further progression in transmission levels and optical Q.

Further progress

What needs to be done for progression beyond the current levels ? Optical transmission could still be marginally improved by further increasing the GaAs guiding layer thickness beyond 320 nm. Furthermore the ∼30% reflectivity occurring at the input/output facets due to effective index mismatch (∼3.3 in the guide versus 1 in air)[2] could be reduced by adopting an inverted taper design [59, 61]. As far as further improvements in the optical Q go, it is necessary to understand which loss mechanisms are currently responsible for limiting the Q and see whether they can be reduced. This will be discussed in the following section (5.3).

---

[2]Reflectivity$\simeq \left(\frac{3.3-1}{3.3+1}\right)^2$

Critical optical coupling between a GaAs disk and a nanowaveguide suspended on the chip

C. Baker,[1] C. Belacel,[2] A. Andronico,[1] P. Senellart,[2] A. Lemaitre,[2] E. Galopin,[2] S. Ducci,[1] G. Leo,[1] and I. Favero[1,a)]

[1]*Laboratoire Matériaux et Phénomènes Quantiques, Université Paris Diderot, Sorbonne Paris Cité, CNRS-UMR 7162, 10 rue Alice Domon et Léonie Duquet, 75013 Paris, France*
[2]*Laboratoire de Photonique et Nanostructures, CNRS, Route de Nozay, 91460 Marcoussis, France*

We report on an integrated GaAs disk/waveguide system. A millimeter-long waveguide is suspended and tapered on the chip over a length of 25 μm to evanescently couple to high Q optical whispering gallery modes of a GaAs disk. The critical coupling regime is obtained both by varying the disk/guide gap distance and the width of the suspended nanoscale taper. Experimental results are in good agreement with predictions from coupled mode theory. © *2011 American Institute of Physics*. [doi:10.1063/1.3651493]

Whispering gallery mode (WGM) gallium arsenide (GaAs) optical cavities combine the optical properties of GaAs with small mode volumes and high quality factors Q, enabling a boost of light-matter interaction in different contexts: in quantum electrodynamics experiments,[1–3] for the realization of lasers,[4] in non-linear optics,[5] and now in optomechanics experiments.[6–8] The best Q factors on GaAs WGM cavities are of a few 10^5, measured by evanescent coupling to an optical fiber taper.[6,8,9] However, fiber tapers suffer from a poor mechanical stability and are affected by a rapid degradation in standard humidity.[10] An integrated optics approach, with direct access to the cavity by an on-chip bus waveguide, can increase the range of operation of GaAs WGM cavities.[11] For example, a GaAs waveguide/disk structure was developed[12] and optically probed through a narrow-band grating coupler, allowing observing evanescent coupling in the under-coupled regime. However, for many applications, obtaining the critical coupling is crucial.[13] This applies in optomechanics[14–16] where maximal number of photons in the cavity is for example needed to reach optomechanical self-oscillation.[17–19]

Here, we investigate a GaAs waveguide/disk integrated structure but adopt direct injection at the cleaved facet of the guide, with a two-fold advantage: first, simple optics is used for waveguide coupling; second, the coupling is wavelength independent, allowing broadband (100 nm) spectroscopy of the system. We observe evanescent coupling and by varying the disk/guide gap distance or the guide taper width, the overlap between the disk and guide optical modes is adjusted and the important critical coupling regime is reached in a controlled manner. Our experimental results are in good agreement with coupled mode theory (CMT) expectations.[20,21]

We employ a semi-insulating GaAs substrate, on which we grow epitaxially a GaAs 500 nm buffer layer, a 1.8 μm Al$_{0.8}$Ga$_{0.2}$As sacrificial layer, and finally a 200 nm GaAs top layer. The guides and disks are defined by e-beam lithography with a negative resist. We draw straight optical waveguides 5 μm wide and 2 mm long, extending up to the sample facets (Fig. 1(a)). The central region of each guide is tapered in the vicinity of the target disk, to allow evanescent coupling (Inset of Fig. 1(a)). The nominal disk diameter is 7.4 μm. In a first non-selective wet-etch, we separate the guide from the disk and define the boundaries of the guiding structures, etching away the 200 nm of GaAs. In a second etch step, we use hydrofluoric acid to under-etch the AlGaAs layer. First, this results in locally suspending both the disk and the waveguide (see Fig. 1(b)) with a sub-micron gap between the two (see Fig. 1(c)). Second, the lateral edges of the 5-μm wide waveguide are under-etched on their whole length, resulting in a rail-like guiding structure (Fig. 1(d)). In this structure the transverse electric (TE), in-plane polarized, fundamental mode is confined in the 200 nm GaAs layer by semiconductor/air interfaces, with a small residual leaking into the substrate, which reduces the guide transmission when increasing the wavelength. Conversely, beam propagation method (BPM) simulations predict that the out-of-plane polarized (TM) fundamental mode leaks importantly into the substrate, leading to important optical losses of the rail-guide, which are confirmed experimentally. As a result, our waveguides efficiently select TE polarization. For the taper profile, we have chosen a 3-part linear profile, with lengths of 10, 5, and 10 μm. The width of the central taper part is chosen to generally ensure a single TE guided mode. For these profiles, BPM calculations predict a transmission of the TE fundamental mode through the taper over 90%.

Optical spectroscopy of the disk/waveguide is performed in the 1300-1400 nm band using a CW external cavity diode laser, whose beam is focused onto the guide input facet using a micro-lensed fiber. The TE polarization is selected. Output light is collected by a microscope objective and sent on a p-i-n-photodetector. Fig. 2 shows the normalized transmission of a guide evanescently coupled to a disk as a function of the laser wavelength. Several resonances appear in this spectrum: they correspond to WGMs of the disk, whose loaded Q factors can reach 55 000, as shown in the inset of Fig. 2. This corresponds to intrinsic optical Q in the high 10^4 range. We note pronounced Fano profiles involving broad and fine optical resonances. Similar profiles, observed on Silica WGM toroid cavities coupled to a fiber taper, were attributed to interference between different modes of the cavity.[22]

a)Electronic mail: ivan.favero@univ-paris-diderot.fr.
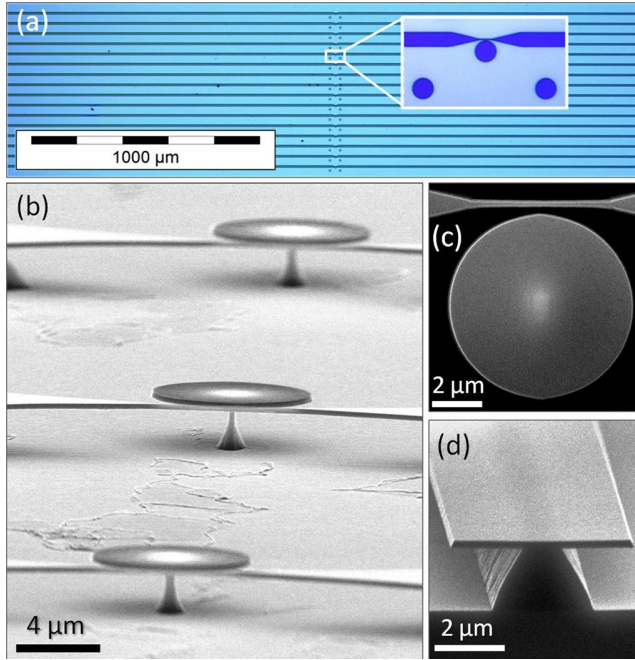
FIG. 1. (Color online) (a) Optical top view of the complete sample, containing 16 guide/disk lines. Inset: tapered part of the guide in the disk vicinity. The two other disks are fabrication witnesses. (b) SEM side-view of 3 disk/waveguide systems. (c) SEM top view of the central part of the tapered waveguide next to a disk. (d) SEM side view of the cleaved facet of the rail-guide.

Here, we focus on the fine control of the disk/waveguide evanescent coupling, in order to reach critical coupling where intrinsic and coupling losses of the cavity are equal. Our first strategy is to vary the gap distance g between disk and guide.[8,13,23] Fig. 3(a) shows transmission spectra obtained by varying g, keeping a constant taper width of 320 nm. From spectra 1–8, g is reduced in 25 nm steps from 350 to 190 nm. The gap distances are measured in a scanning electron microscope (SEM) with an uncertainty of ± 7 nm and agree within 5% with nominal values. In spectra 5–8 most notably, several resonances approach zero transmission, reflecting critical coupling.
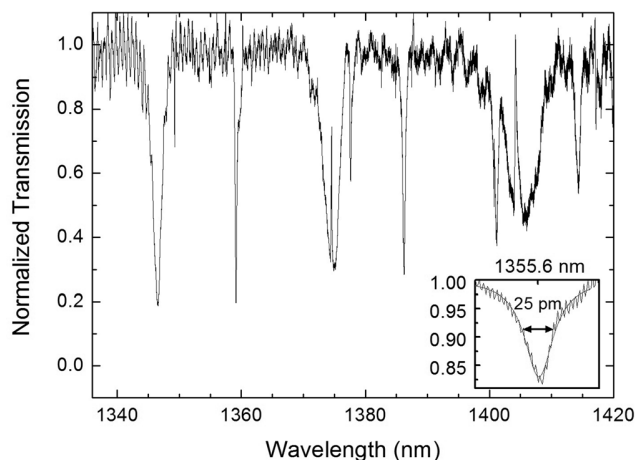
FIG. 2. Transmission spectrum of a suspended tapered waveguide coupled to a 7.4 μm diameter GaAs disk. Inset: a fine optical resonance at $\lambda = 1355$ nm, measured on another disk. The small amplitude oscillations in the base transmission correspond to Fabry-Perot fringes of the waveguide and are not noisy in nature.
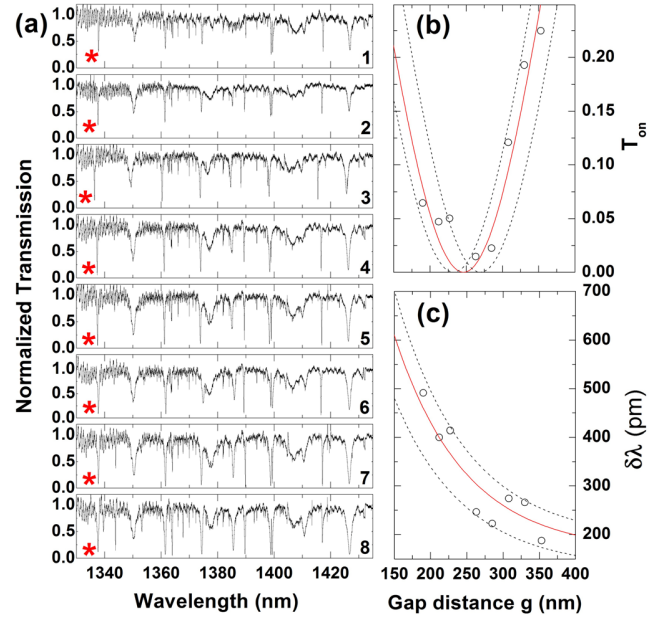
FIG. 3. (Color online) (a) Transmission spectra of suspended waveguides coupled to GaAs disks. From spectrum 1–8, g diminishes from 350 to 190 nm in steps of 25 nm. (b) T_{on} as a function of g, for the resonance marked with a star in (a). The open symbol size represents experimental uncertainties in g and T_{on}. (c) Width of the same resonance as a function of g.

Let us follow in detail the resonance marked with a star in Fig. 3(a). Figs. 3(b) and 3(c) show its on-resonance normalized transmission T_{on} and its linewidth $\delta\lambda$ as a function of g. As g decreases, the overlap between the WGM and the guide mode increases, increasing evanescent coupling. In Fig. 3(b), T_{on} decreases when g decreases, before reaching zero at critical coupling for g = 250 nm. Smaller g-values make the system enter the over-coupled regime, where coupling losses overcome intrinsic losses. In Fig. 3(c), $\delta\lambda$ is enlarged as g decreases, reflecting again losses of the WGM due to its coupling to the guide.

CMT can describe the disk/guide evanescent coupling and its transition from the under to over-coupled regime. A heuristic CMT (Ref. 20) approach leads to simple expressions $T_{on} = [(1 - \gamma_e/\gamma_i)/(1 + \gamma_e/\gamma_i)]^2$ and $\delta\lambda = (\lambda_0/Q_{int})(1 + \gamma_e/\gamma_i)$, where γ_e is the extrinsic WGM-to-guide coupling rate, $\gamma_i = (2\pi c/\lambda_0)/Q_{int}$ is the intrinsic WGM loss rate, λ_0 the WGM resonance wavelength, and Q_{int} the related intrinsic Q. These expressions were used to describe fiber taper evanescent coupling experiments with γ_e taken as a parameter varying exponentially with the gap distance g:[8,24,25] $\gamma_e(g) = \gamma_e(0) \exp(-\eta g)$, with η the inverse of the evanescent coupling decay length. In Fig. 3(b), the solid line is a fit using this exponential approximation and the above formula for T_{on}, taking $\gamma_e(0)/\gamma_i$ and η as adjustable parameters. The best agreement is obtained for $\gamma_e(0)/\gamma_i = 12.6$ and $\eta = 1/97$ nm^{-1}. In Fig. 3(c), the solid line corresponds to the above formula for $\delta\lambda$, for the same fit parameters as above and where we use $Q_{int} = 8100$. However, nanofabrication tolerances result in slightly different disk and waveguide for each targeted gap distance. Amongst others, Q_{int} cannot be considered as a constant when we vary g. In Fig. 3(c), we capture this variability by bounding the results with two dashed

curves, obtained with the same value of $\gamma_e(0)/\gamma_i$ and two bounding values of $Q_{int} = 7040$ and 10280. These bounding values are injected back in the formula for T_{on}, with the same value of η and with $\gamma_e(0)$ extracted from $\gamma_e(0)/\gamma_i = 12.6$ and from the average Q_{int} of 8100. This leads to the two dashed curves of Fig. 3(b), which correctly bound the experimental results. To summarize, our experimental data are explained by a variability of $\pm 20\%$ of Q_{int}. We note however that a full parameter-free modeling would necessitate to abandon the exponential approximation for γ_e and consider the exact evolution of $\gamma_e(g)$ for each disk-waveguide couple.

Finally, in our disk/guide device, we can modify the evanescent tail of the waveguide mode by changing the width of the central taper, circumventing the difficulty of bringing the disk and guide arbitrarily close to one another. We used this approach by varying the taper width in steps of 20 nm, from 380 to 280 nm, for constant $g = 220$ nm, and could also obtain under-coupling, critical coupling, and over-coupling regimes.

In summary, we developed an integrated GaAs disk/ waveguide system, where the nanoscale tapered part of the guide couples critically to WGMs. Our system offers integrated optical access to on-chip GaAs cavities of sub-micron mode volume and high Q. Perspectives include integrated quantum optomechanics experiments,[26–29] benefiting from the strong optomechanical coupling of GaAs disk resonators.[6,7] The GaAs platform would additionally allow for coupling active optical elements, possibly electrically pumped, to optomechanical functionalities.

[1]B. Gayral, J. M. Gerard, A. Lemaitre, C. Dupuis, L. Manin, and J. L. Pelouard, Appl. Phys. Lett. **75**, 1908 (1999).
[2]A. Kiraz, P. Michler, C. Becher, B. Gayral, A. Imamoglu, L. Zhang, E. Hu, W. V. Schoenfeld, and P. M. Petroff, Appl. Phys. Lett. **78**, 3932 (2001).
[3]E. Peter, P. Senellart, D. Martrou, A. Lemaître, J. Hours, J. M. Gérard, and J. Bloch, Phys. Rev. Lett. **95**, 067401 (2005).
[4]S. L. McCall, A. F. J. Levi, R. E. Slusher, S. J. Pearton, and R. A. Logan, Appl. Phys. Lett. **60**, 289 (1992).
[5]A. Andronico, I. Favero, and G. Leo, Opt. Lett. **33**, 2026 (2008).
[6]L. Ding, C. Baker, P. Senellart, A. Lemaitre, S. Ducci, G. Leo, and I. Favero, Phys. Rev. Lett. **105**, 263903 (2010).
[7]L. Ding, C. Baker, P. Senellart, A. Lemaitre, S. Ducci, G. Leo, and I. Favero, Appl. Phys. Lett. **98**, 113108 (2011).
[8]L. Ding, P. Senellart, A. Lemaitre, S. Ducci, G. Leo, and I. Favero, Proc. SPIE **7712**, 771211 (2010).
[9]C. P. Michael, K. Srinivasan, T. J. Johnson, O. Painter, K. H. Lee, K. Hennessy, H. Kim, and E. Hu, Appl. Phys. Lett. **90**, 051108 (2007).
[10]L. Ding, C. Belacel, S. Ducci, G. Leo, and I. Favero, Appl. Opt. **49**, 2441 (2010).
[11]D. Rafizadeh, J. P. Zhang, R. C. Tiberio, and S. T. Ho, J. Lightwave Technol. **16**, 1308 (1998).
[12]S. Koseki, B. Zhang, K. De Greve, and Y. Yamamoto, Appl. Phys. Lett. **94**, 051110 (2009).
[13]M. Cai, O. Painter, and K. J. Vahala, Phys. Rev. Lett. **85**, 74 (2000).
[14]I. Favero and K. Karrai, Nat. Photonics **3**(4), 201 (2009).
[15]F. Marquardt and S. Girvin, Physics **2**, 40 (2009).
[16]M. Aspelmeyer, S. Gröblacher, K. Hammerer, and N. Kiesel, J. Opt. Soc. Am. B **27**, 189 (2010).
[17]C. Hohberger and K. Karrai, in *Proceedings of 4th IEEE Conference on Nanotechnology* (IEEE, New York, 2004), pp. 419–421.
[18]T. Carmon, H. Rokhsari, L. Yang, T. J. Kippenberg, and K. J. Vahala, Phys. Rev. Lett. **94**, 223902 (2005).
[19]C. Metzger, M. Ludwig, C. Neuenhahn, A. Ortlieb, I. Favero, K. Karrai, and F. Marquardt, Phys. Rev. Lett. **101**, 133903 (2008).
[20]C. Manolatou, M. J. Khan, S. Fan, P. R. Villeneuve, and H. A. Haus, IEEE. J. Quantum Electron. **35**(9), 1322 (1999).
[21]T. Kamalakis and T. Sphicopoulos, IEEE. J. Quantum Electron. **42**(8), 827 (2006).
[22]Y. F. Xiao, L. He, J. Zhu, and L. Yang, Appl. Phys. Lett. **94**, 231115 (2009).
[23]A. Vörckel, M. Mönster, W. Henschel, P. H. Bolivar, and H. Kurz. IEEE Photon. Technol. Lett. **15**(7), 921 (2003).
[24]M. Eichenfield, C. P. Michael, R. Perahia, and O. Painter, Nat. Photonics **1**, 416 (2007).
[25]S. M. Spillane, T. J. Kippenberg, O. Painter, and K. J. Vahala, Phys. Rev. Lett. **91**(4), 043902 (2003).
[26]M. Eichenfield, R. Camacho, J. Chan, K. J. Vahala, and O. Painter, Nature **459**, 550 (2009).
[27]M. Li, W. H. P. Pernice, C. Xiong, T. Baehr-Jones, M. Hochberg, and H. X. Tang, Nature **456**, 480 (2008).
[28]I. Favero, S. Stapfner, D. Hunger, P. Paulitschke, J. Reichel, H. Lorenz, E. M. Weig, and K. Karrai, Opt. Express **15**, 12813 (2009).
[29]D. Van Thourhout and J. Roels, Nat. Photonics **4**, 211 (2010).

5.3 The origin of optical losses in GaAs disk resonators

As discussed in Chapter 1, we have identified five main sources of optical loss in GaAs WGM disk resonators:

1. Rayleigh scattering through surface roughness

2. Bending losses (radiative losses)

3. Coupling losses to the waveguide

4. Absorption through deep defects in the GaAs crystal lattice

5. Absorption through surface states in the oxide at the interface between GaAs and air

Bending losses can be accurately determined through FEM simulations and are quite small provided the disk is large enough[3]. Coupling losses to the waveguide are perfectly known by optical spectroscopy measurement of a WGM's resonance wavelength, contrast, FWHM and under- or overcoupled nature. However the contribution of loss mechanisms 1, 4 and 5 is much more difficult to estimate. Indeed the exact nature of the GaAs surface oxide and amount of deep defects in the crystal lattice are not well known, while the calculation of losses through surface roughness requires very high resolution images of the disk sidewalls over the whole boundary [134]. Nevertheless it can be noted that the first three loss mechanisms function by coupling light from the whispering gallery mode into different optical modes (inside or outside the resonator) and produce no light absorption hence no heat in the resonator. On the other hand loss mechanisms 4 and 5 involve heat generation through optical absorption.

Thus measuring the power dissipated as heat in the resonator provides an indication as to the dominating loss mechanisms. This can be done by measuring the magnitude of the thermo-optic shift of WGM resonances at high laser power.

Thermo-optic shift

As the refractive index of bulk GaAs is dependent on temperature, the effective index n_{eff} of a WGM also displays a temperature dependence, of the

---

[3]A (p=1, m=10) WGM of a R=1μm, 320 nm thick GaAs disk resonator at $\lambda_0 = 1338$ nm has a bending loss limited Q of 50 million.

5.3 The origin of optical losses in GaAs disk resonators
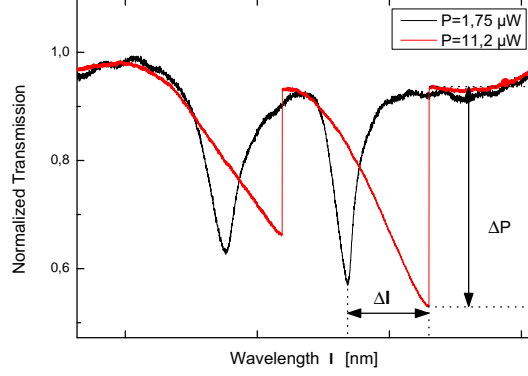
Figure 5.2: Optical resonance at low laser power (P=1.75 μW, black curve) and higher laser power (P=11.2 μW, red curve). Both curves have been normalized to display an off-resonance transmission of 1. The optical resonance position has been shifted by an amount $\Delta\lambda$, for an amount of dissipated optical power ΔP.

type:

$$\frac{dn_{\text{eff}}}{dT} = \frac{n_{\text{eff}}}{n}\frac{dn}{dT} \tag{5.1}$$

Here n is the refractive index of bulk GaAs and $\frac{dn}{dT}$ the related thermo-optic coefficient, worth $2.3 \cdot 10^{-4}$ K^{-1} at room temperature. The term $n_{\text{eff}}/n < 1$ accounts for the fact that only a certain fraction of the WGM's energy is inside the disk and therefore sensitive to changes in its index of refraction. Because of this temperature dependence, when slowly scanning over a WGM resonance at high laser power with the laser wavelength coming from the blue detuned side, the resonance wavelength is gradually red shifted as the power buildup leads to rising temperatures in the disk. This thermo-optic shift causes optical bistability [152], evidenced by the triangular optical resonance profile seen in Fig. 5.2, instead of the traditional lorentzian resonance profile seen at low laser power. The shift in resonance wavelength $\Delta\lambda$ can be related to a shift in effective refractive index[4] Δn_{eff} through Eq. 5.2.

$$\Delta\lambda = \frac{2\pi R}{m}\Delta n_{\text{eff}} \tag{5.2}$$

---

[4]The increase in radius with increasing temperature can safely be neglected, as the thermal expansion contribution is ~ 20 times smaller than the thermo-optic contribution in GaAs.
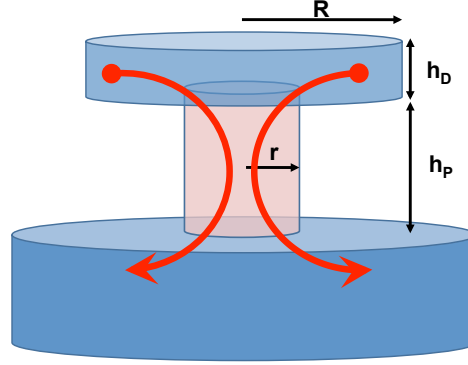
Figure 5.3: Thermal power flow (red arrows) out of the GaAs disk resonator of radius R, through the $Al_{0.8}Ga_{0.2}As$ pedestal of radius r and height h_P and into the GaAs substrate.

with m the azimuthal number of the WGM. The shift in refractive index can in turn be related to a temperature increase ΔT by Eq. 5.1:

$$\Delta T = \frac{n}{n_{\text{eff}}} \left(1/\frac{dn}{dT}\right) \frac{m\Delta\lambda}{2\pi R} = \frac{n}{\lambda}\Delta\lambda/\frac{dn}{dT} \tag{5.3}$$

Once the temperature increase has been determined by measuring $\Delta\lambda$, we can calculate the amount of thermal power generated in the disk necessary to maintain this steady state temperature increase ΔT. In the steady state, the thermal power generated in the disk through absorption is identical to the thermal power flow out of the disk. This flow occurs essentially through the disk and pedestal into the substrate, see Fig. 5.3. Indeed power loss through radiation and convection with the surrounding air is significantly smaller and can be safely neglected. We then compare the thermal power generated at resonance to the total dissipated (dropped) power at resonance ΔP, see Fig. 5.2. In this way one can estimate the fraction of dissipated optical energy that is lost as heat, and the fraction that is lost by surface roughness induced scattering to external radiation losses, or by bending losses. The thermal power flow P_{th} out of the disk and into the substrate is given by:

$$P_{th} = G\,\Delta T \tag{5.4}$$

Here G is the thermal conductance[5] of the disk with its pedestal. Its calculation is performed as follows by separately treating the disk and pedestal.

---

[5]The thermal conductance G determining the heat flow through an element of surface S, thickness l and conductivity κ is $G = \kappa\frac{S}{l}$

Calculating G

The thermal conductance of the AlGaAs pedestal G_P is defined as the product of the thermal conductivity of AlGaAs κ_{AlGaAs} times the ratio between the pedestal's cross section and height h_P:

$$G_P = \kappa_{\text{AlGaAs}} \frac{\pi r^2}{h_P} \tag{5.5}$$

The thermal conductance G_D of the GaAs annulus linking the disk periphery (where the WGM is located) to the edge of the pedestal is found by summing the thermal resistances of concentric rings with radius r to R:

$$R_D = G_D^{-1} = \int_r^R \frac{dx}{\kappa_{\text{GaAs}}\, 2\pi h_D\, x} = \frac{1}{\kappa_{\text{GaAs}}\, 2\pi h_D} \ln\left(\frac{R}{r}\right) \tag{5.6}$$

Here κ_{GaAs} and h_D are respectively the thermal conductivity of GaAs and the disk height. Finally the combined conductance of the disk with its pedestal G is obtained by Eq. 5.7:

$$G = \left(G_D^{-1} + G_P^{-1}\right)^{-1} \tag{5.7}$$

In practice the thermal conductance of the pedestal is generally much smaller than that of the disk, so that $G \simeq G_P$.[6] These expressions are in very good agreement with the results of thermal FEM simulations (not shown here).

Conclusion

The results of this analysis at two different dropped laser powers are summarized in Table 5.1, for the disk displaying the thermo-optic shift shown in Fig. 5.2. At both incident laser powers, the power loss through optical absorption P_{th} is almost equal to the total power loss ΔP. The uncertainties in the numerical parameters make it difficult to put a precise value on the non-absorptive losses. Nevertheless it is safe to say that the dominant source of optical loss involves absorption either in the surface oxide or in deep defects in the bulk. Such a situation has already been demonstrated in high Q silicon WGM resonators, shown to be no longer limited by Rayleigh scattering [134]. Additional observations point towards the fact that this optical absorption occurs mainly in the surface oxide and not in the GaAs

---

[6]The disk's thermal response time τ_{th} discussed in Chapter 3 is defined as $\tau_{th}=(m_D \cdot c_D)/G$, with m_D and c_D respectively the disk's mass and specific heat.

Pedestal radius r	460 nm	
Pedestal height h_P	1.8 μm	
Thermal conductivity of AlGaAs $\kappa_{Al_{0.8}Ga_{0.2}As}$	14 W/(m·K)	
Thermal conductance G	$5.17 \cdot 10^{-6}$ W/K	
Incident laser power	4.7 μW	11.2 μW
Resonance wavelength shift $\Delta\lambda$	31.2 pm	123 pm
Temperature increase ΔT	0.24 K	0.95 K
Thermal power flow P_{th}	1.47μW	4.9 μW
Total dissipated power at resonance ΔP	1.5 μW	5 μW

Table 5.1: Physical parameters & results summary.

bulk. Indeed Eq. 5.8 relates the optical Q to the linear loss coefficient α, the free-space wavelength λ_0 and the effective index of the WGM n_{eff}:

$$Q = 2\pi \frac{1}{1 - e^{-\alpha\lambda_0/n_{\text{eff}}}} \tag{5.8}$$

A dominant bulk absorption would result in an effective linear loss coefficient α_b, for which we would not expect a dependency of the optical Q with the disk radius. This is not what is observed, with the maximum measured optical Q increasing with increasing disk radius[7] and closely matching the electromagnetic energy density at the disk interface shown in Fig. 1.17. Surface absorption dominated losses would furthermore explain why higher order p>1 WGMs - which have higher field at the interface - generally have lower optical Qs. This conclusion seems to be corroborated by preliminary results obtained while operating the resonators in liquids, detailed in the following section.

5.3.1 Experiments in liquids

Protocol

With the integrated GaAs chip positioned in the setup of Fig. 5.1, a micro-liter droplet of liquid ($\sim$1 mm^3) is deposited on the sample surface with a micro-pipette. This droplet covers several adjacent disk resonators and waveguides, see Fig. 5.5. The overall optical transmission is relatively unchanged. The disk WGM resonances are shifted roughly 10-15 nm towards higher wavelengths, due to the higher refractive index of the liquid (n$\simeq$1.33) compared to air. The observed shift is in good agreement with FEM simulations. The optimal evanescent coupling conditions are shifted ($\sim$ 100

---

[7]Typically Q$\sim 10^5$ at R=1 μm and Q$> 5 \cdot 10^5$ for R>3 μm.
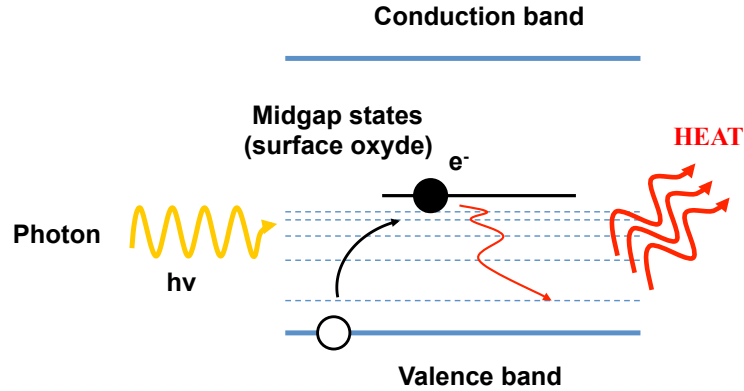
Figure 5.4: Optical absorption by the mid-gap states in the GaAs native surface oxide results in heat generation.

nm) towards greater gap distances between waveguide and disk. Indeed, the evanescent field extends further out of the disk and waveguide due to the decreased refractive index mismatch between GaAs and liquid. Measurements can be carried out for 5 to 10 minutes before the liquid droplet dries.

Results

Figure 5.6 shows the same WGM resonance of a GaAs disk measured at increasing laser powers with the disk in air (a), immersed in deionized (DI) water (b), or in a solution of ammonia (NH_4OH) (c). Ammonia is chosen because dilute acids or bases (such as dilute ammonia and hydrochloric acid) remove GaAs' native surface oxide [65]. Provided no oxidizer is present in the solution minimal etching occurs once the oxide is removed[8]. With the disk measured in air (a), we recognize the typical WGM distortion due GaAs' positive thermo-optic coefficient. When the measurement is done in water (b), one can identify two trends. The positive thermo-optic distortion of the resonance is still present, albeit a bit less pronounced. Additionally, the overall position of the resonance is blue shifted with increasing laser power. This phenomenon is caused by gradual heating over time of the water droplet combined with water's (and most liquids') negative thermo-optic coefficient [153]. Both positive and negative thermo-optic shifts are apparent because the laser sweep speed is slow compared to the disk's thermal response time,

---

[8]Etching solutions - such as the BCK described in Chapter 4.1 - function by combining an oxidizer with an acid or base. The oxidizer continually produces fresh oxide for the acid or base to dissolve.
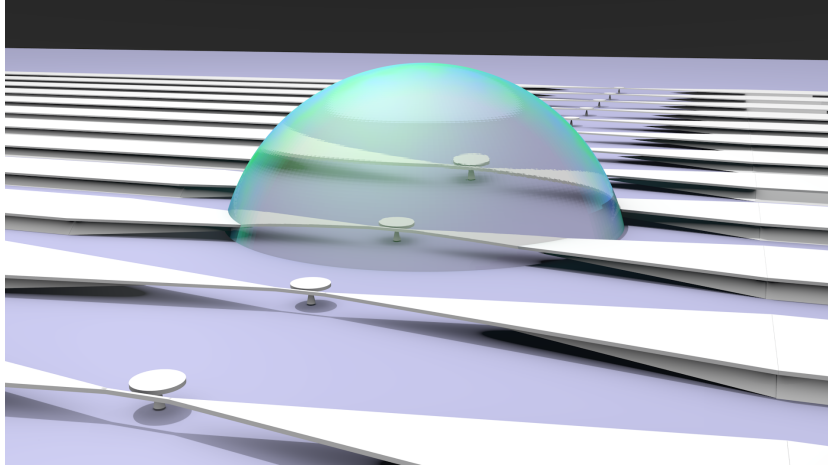
Figure 5.5: Measuring the disk's optical properties while immersed in a droplet of DI water, or ammonia (NH_4OH) in order to remove the surface oxide. (The droplet displayed is smaller than in reality for better visibility).

Thermal conductivity of water at 293 K	0.6 W/(m·K)
Thermal conductivity of saturated ammonia at 293 K	0.5 W/(m·K)
Water specific heat (at 293 K - 1 atm)	4.18 kJ/(kg·K)
Saturated ammonia specific heat (at 293 K - 1 atm)	4.7 kJ/(kg·K)
Thermo-optic coefficient for water (300 K - λ=1550 nm)	-8·10^{-5}

Table 5.2: Physical parameters for water and ammonia, see ref [154].

but fast compared to that of the droplet[9]. After drying of the droplet, the behavior reversibly returns to the case (a). The lower positive thermo-optic distortion in water can be ascribed to the added thermal conductance of the surrounding water, which reduces temperature rise in the disk. Finally the same WGM is measured in NH_4OH (c). The WGM resonance is irreversibly blue shifted by a few nanometers, consistent with the removal of 1-3 nanometers of native oxide over the entire disk. The overall blue shift due to heating of the droplet is still present. However, the positive thermo-optic distortion is no longer present, even though the injected laser power is comparable to the measurement in DI water. This is not due to different thermal properties of dilute NH_4OH, as these are similar to those of water, see Table 5.2. This experiment seems to indicate no more heating occurs inside the GaAs disk when the oxide layer is removed. Since we could not find the precise negative

---

[9]With our laser sweep speed of 100 nm/s, the laser wavelength is only tuned to the WGM resonance on the order of 10^{-4} to 10^3 seconds, which is slow compared to the disk's few microseconds thermal response time τ_{th} but fast compared to that of the droplet.
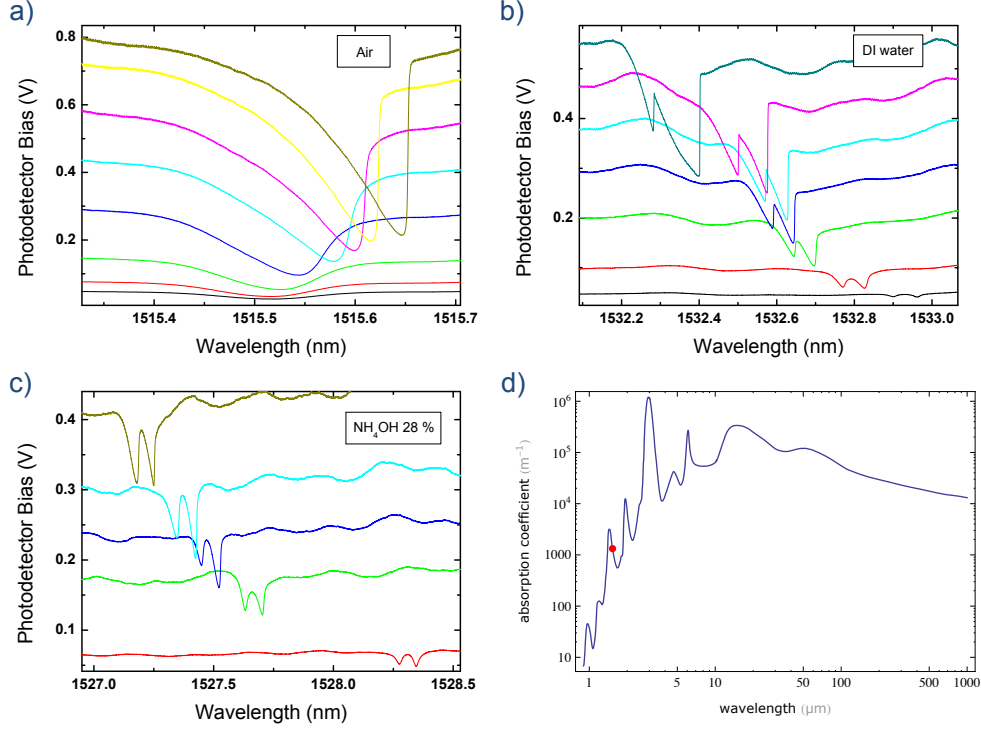
Figure 5.6: Optical transmission spectra measured at increasing laser powers, for a same WGM resonance of a GaAs disk in air (a), in DI water (b) and in ammonia (c). Optical power circulating in the waveguide is proportional to the photodetector bias. (d) Water optical absorption coefficient as a function of wavelength. The red dot marks the absorption $\sim$1330 m^{-1} at 1530 nm. Data from [155].

thermo-optic coefficient for ammonia solutions it is still not possible to rule out how this could counterbalance the positive thermo-optic shift of GaAs. Nevertheless we wish to stress that while these results are not yet completely conclusive, combined with the previous observations they strongly hint towards the role played by the interface in such miniature resonators. This is consistent with in depth analysis of sidewall roughness performed by means of high resolution Transmission Electron Microscope (TEM) imagery by David Parrain in the team which indicate that surface roughness is not responsible for clamping the optical Q below 10^6.

Quality factor in liquid

If surface absorption is removed by an acid or a base, shouldn't the optical quality factor be significantly increased ? In fact water has a large absorption coefficient in the near infrared (see Fig. 5.6, d) around 13.3 cm^{-1} at the
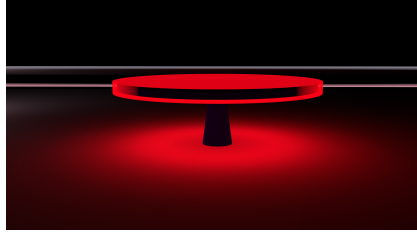
wavelength $\lambda = 1530$ nm used in the measurement. FEM simulations show 15.2% of the electromagnetic energy of the WGM is located in the liquid. Water absorption is therefore responsible for an effective loss of the WGM of $0.152 \times 13.3 \simeq 2$ cm^{-1}. Using Eq. 5.8, we find the maximal optical quality factor attainable in these conditions is $Q_{\mathrm{max}} = 6 \cdot 10^4$, which is precisely equal to the measured value. Following these observations, major gains in optical Q will require focused efforts on minimizing the surface absorption, for example through passivation (see section 5.3.3).

5.3.2 Two photon absorption

TPA describes the nonlinear process in which the simultaneous absorption of two photons excites an electron from the valence to the conduction band. The TPA cross-section β is defined as follows:

$$-\frac{dI}{dz} = \alpha I + \beta I^2 \tag{5.9}$$

Where I is the light intensity, α the linear absorption coefficient and dz the length of the optical path. β in GaAs is rather large, with $\beta \sim 20-30$ cm/GW at $\lambda = 1.3$ μm and $\beta \sim 10-15$ cm/GW at $\lambda = 1.5$ μm. [156, 157, 158] Because of the high finesse of GaAs resonators and resulting large circulating intensities, TPA losses become comparable to linear losses in $\varnothing = 2$ μm, Q=10^5 resonators for a dropped power as low as 50 μW. This is indeed experimentally verified by measuring how an undercoupled WGM's on resonance transmission T_{on} becomes higher at large dropped powers (see section 6.2.7), revealing increased intrinsic losses[10]. With Q=10^6, the contribution would be noticeable below 1 μW, limiting the range of attainable circulating powers. The carriers generated by TPA can in turn absorb photons (free carrier absorption) and change the refractive index of the material (free carrier dispersion). These non-linear phenomena can give rise to complex time-dependent dynamics. For instance optical instabilities and self-sustained oscillations resulting from the interplay between thermal and free carrier dynamics have

---

[10]$T_{\mathrm{on}} = \left(\frac{1-\gamma_{\mathrm{ext}}/\gamma_{\mathrm{int}}}{1+\gamma_{\mathrm{ext}}/\gamma_{\mathrm{int}}}\right)^2$.

been reported silicon microdisk resonators [159]. More recently GHz self-oscillations resulting from the interaction between free-carrier dispersion and TPA have been reported in silicon disk resonators [160] and photonic crystal cavities [161]. We have however not yet seen such instabilities and self-pulsing behavior in GaAs disk resonators.

5.3.3 Surface passivation

Unlike silicon, which has a native oxide (SiO_2) with a low density of interface states, GaAs suffers from a rather poor native oxide with a high density of interface states (10^{13} cm^{-2}) located within the bandgap [65]. These interface states are responsible for degrading the optical properties of GaAs resonators. Passivation aims to change the chemical properties of the surface in order to enhance the optical properties. (Simply removing the native oxide with a chemical treatment is not enough, since a new layer of oxide forms again within moments upon renewed exposure to oxygen). Photoluminescence experiments[11] are often used to monitor changes in surface state densities associated with passivation. Since mid-gap states increase non-radiative decay, increased photoluminescence intensity is associated with a more ideal surface. For GaAs, treatments with sulfur containing compounds such as sodium sulfide (Na_2S) or ammonium sulfide (($NH_4)_2S$) [162, 163, 164, 165] and photochemistry between GaAs and water [166] have been reported to significantly improve photoluminescence. Hydrogen is also known to be able to diffuse inside the material and passivate defects in the bulk. Even if many such treatments are reported to be temporary, lasting only hours or days and precluding their use in commercial applications, they could provide a boost for academic experiments which can be performed in vacuum for instance.

Attempted trials to boost the optical Q

We attempted a few experiments to boost the optical Q of GaAs disk resonators. These included sputtering the surface with an argon gun, repeatedly dipping the sample in acid and exposing it to air [167] and various oxygen plasma cleaning procedures. Since these treatments only address surface roughness and surface contamination, they provided little to no optical improvement. Furthermore thermal annealing of the disks for 15 min at 575°C under nitrogen atmosphere completely destroys the optical properties, as sublimation of arsenic from the GaAs crystal starts occurring at these tem-

---

[11]A laser is employed to generate carriers in the material and the intensity and/or wavelength of the light produced when these carriers radiatively recombine is then measured.

peratures. The influence of surface passivation on GaAs disk resonators' optical properties will need to be investigated in depth in future work.
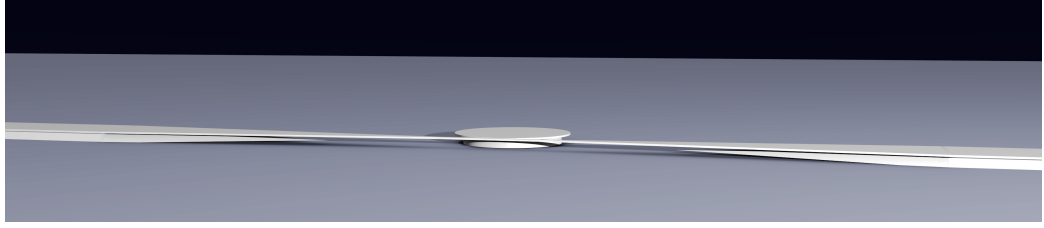
5.4 High Q Silicon Nitride WGM resonators

5.4.1 Development

Here we briefly summarize the work done on silicon nitride devices during this thesis in collaboration with Eva Weig's team at the LMU in Munich. Although our collaborators had extensive knowledge on SiN mechanical nanoresonators [126, 168], they had no experience in its use as an optical material. We therefore started this collaborative work by fabricating simple short waveguides to learn about the optical properties of SiN and its optical losses at various wavelengths. (Losses are measured through raw transmission levels, the top-view scattering method [151] and the Fabry-Perot interference technique [169]). After this, several centimeter long straight waveguides such as shown in Fig. 5.7 were made in order to more accurately measure optical losses. The influence on surface and bulk losses of the different chemistries used during the fabrication as well as post-fabrication treatments such as thermal annealing were investigated, for 6 different wavelengths ranging from green to 1.6 μm. The results of this investigation are recapitulated in the appendix of the article reproduced in the following.

This preliminary work served as the basis for the fabrication of high Q SiN WGM resonators with integrated coupling waveguides (see Fig. 5.8). These devices enable the optomechanical detection of the Brownian motion of the suspended waveguide. This will be detailed in the following chapter.

5.4.2 Optical instabilities

The high Q SiN resonators described in this work exhibit interesting optical instabilities and self-pulsing optical output under continuous laser excitation. This is explained by a novel coupling between the fast thermo-optic nonlinearity in the disk and a much slower thermo-mechanic nonlinearity of the structure. The self-pulsing regime has a periodicity spanning several orders of magnitude and ranging up to unprecedentedly long periods of above
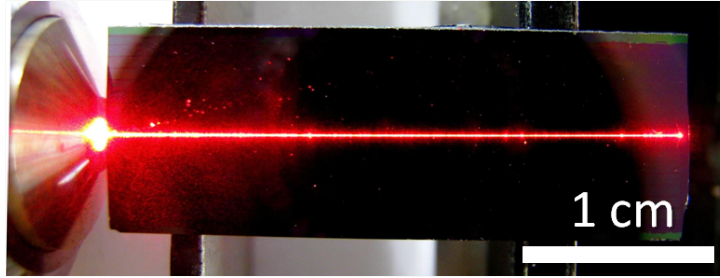
Figure 5.7: SiN sample with 3 cm long straight waveguides of various widths to accurately determine optical losses through the top-view scattering method [151] and the Fabry-Perot interference technique [169]. Here 633 nm light from a HeNe laser is injected in a guide with a microscope objective (left).
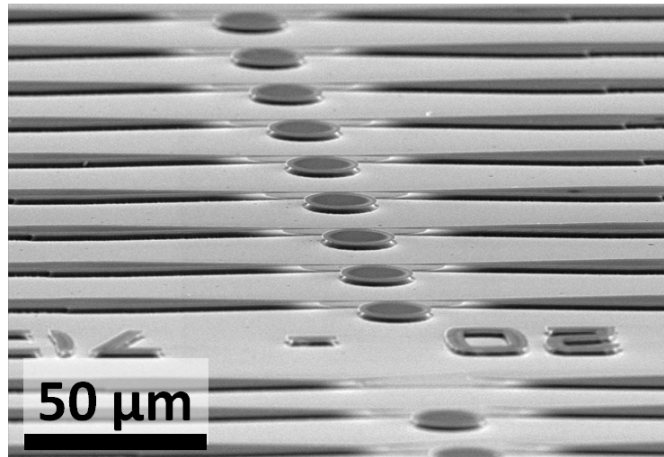
Figure 5.8: Array of 20 μm diameter SiN disk resonator with their integrated suspended coupling waveguide.

145

a minute. The following reproduced article details these results. Recently similar behavior has been reported in PMMA-coated silica toroids and the use of such an oscillator for sensing applications was demonstrated [170].

Optical instability and self-pulsing in silicon nitride whispering gallery resonators

Christophe Baker,[1,*] Sebastian Stapfner,[2] David Parrain, [1] Sara Ducci, [1] Giuseppe Leo, [1] Eva M. Weig,[2] Ivan Favero[1]

[1]Université Paris Diderot, Sorbonne Paris Cité, Laboratoire Matériaux et Phénomènes Quantiques, CNRS-UMR 7162, 10 rue Alice Domon et Léonie Duquet, 75013 Paris, France
[2]Fakultät für Physik and Center for NanoScience (CeNS), Ludwig-Maximilians-Universität, Geschwister-Scholl-Platz 1, 80539 München, Germany
[*]christophe.baker@univ-paris-diderot.fr

Abstract: We report time domain observations of optical instability in high Q silicon nitride whispering gallery disk resonators. At low laser power the transmitted optical power through the disk looks chaotic. At higher power, the optical output settles into a stable self-pulsing regime with periodicity ranging from hundreds of milliseconds to hundreds of seconds. This phenomenon is explained by the interplay between a fast thermo-optic nonlinearity within the disk and a slow thermo-mechanic nonlinearity of the structure. A model for this interplay is developed which provides good agreement with experimental data and points out routes to control this instability.

References and Links

1. C. Manolatou, M. J. Khan, S. Fan, P. R. Villeneuve, H. A. Haus, and J. D. Joannopoulos, "Coupling of modes analysis of resonant channel add-drop filters," IEEE J. Quantum Electron. **35**(9), 1322–1331 (1999).
2. S. T. Chu, B. E. Little, W. Pan, T. A. Kaneko, S. A. Sato, and Y. A. Kokubun, "An eight-channel add-drop filter using vertically coupled microring resonators over a cross grid," IEEE Photon. Technol. Lett. **11**(6), 691–693 (1999).
3. F. Vollmer, D. Braun, A. Libchaber, M. Khoshsima, I. Teraoka, and S. Arnold, "Protein detection by optical shift of a resonant microcavity," Appl. Phys. Lett. **80**(21), 4057 (2002), doi:10.1063/1.1482797.
4. J. Zhu, S. K. Ozdemir, Y. F. Xiao, L. Li, L. He, D. R. Chen, and L. Yang, "On-chip single nanoparticle detection and sizing by mode splitting in an ultrahigh-Q microresonator," Nat. Photonics **4**(1), 46–49 (2010).
5. Y. Okawachi, K. Saha, J. S. Levy, Y. H. Wen, M. Lipson, and A. L. Gaeta, "Octave-spanning frequency comb generation in a silicon nitride chip," Opt. Lett. **36**(17), 3398–3400 (2011).
6. E. Peter, P. Senellart, D. Martrou, A. Lemaître, J. Hours, J. M. Gérard, and J. Bloch, "Exciton-photon strong-coupling regime for a single quantum dot embedded in a microcavity," Phys. Rev. Lett. **95**(6), 067401 (2005).
7. T. Aoki, B. Dayan, E. Wilcut, W. P. Bowen, A. S. Parkins, T. J. Kippenberg, K. J. Vahala, and H. J. Kimble, "Observation of strong coupling between one atom and a monolithic microresonator," Nature **443**(7112), 671–674 (2006).
8. T. J. Kippenberg, H. Rokhsari, T. Carmon, A. Scherer, and K. J. Vahala, "Analysis of radiation-pressure induced mechanical oscillation of an optical microcavity," Phys. Rev. Lett. **95**(3), 033901 (2005).
9. L. Ding, C. Baker, P. Senellart, A. Lemaitre, S. Ducci, G. Leo, and I. Favero, "High frequency GaAs nano-optomechanical disk resonator," Phys. Rev. Lett. **105**(26), 263903 (2010).
10. L. Ding, C. Baker, P. Senellart, A. Lemaitre, S. Ducci, G. Leo, and I. Favero, "Wavelength-sized GaAs optomechanical resonators with gigahertz frequency," Appl. Phys. Lett. **98**, 113801 (2011).
11. K. H. Lee, T. G. McRae, G. I. Harris, J. Knittel, and W. P. Bowen, "Cooling and control of a cavity optoelectromechanical system," Phys. Rev. Lett. **104**(12), 123604 (2010).
12. A. Andronico, I. Favero, and G. Leo, "Difference frequency generation in GaAs microdisks," Opt. Lett. **33**(18), 2026–2028 (2008).
13. P. S. Kuo, W. Fang, and G. S. Solomon, "4-quasi-phase-matched interactions in GaAs microdisk cavities," Opt. Lett. **34**(22), 3580–3582 (2009).
14. A. E. Fomin, M. L. Gorodetsky, I. S. Grudinin, and V. S. Ilchenko, "Nonstationary nonlinear effects in optical microspheres," J. Opt. Soc. Am. B **22**(2), 459–465 (2005).

15. C. Schmidt, A. Chipouline, T. Pertsch, A. Tünnermann, O. Egorov, F. Lederer, and L. Deych, "Nonlinear thermal effects in optical microspheres at different wavelength sweeping speeds," Opt. Express **16**(9), 6285–6301 (2008), doi:10.1364/OE.16.006285.
16. T. J. Johnson, M. Borselli, and O. Painter, "Self-induced optical modulation of the transmission through a high-Q silicon microdisk resonator," Opt. Express **14**(2), 817–831 (2006).
17. W. H. P. Pernice, M. Li, and H. X. Tang, "Time-domain measurement of optical transport in silicon micro-ring resonators," Opt. Express **18**(17), 18438–18452 (2010), doi:10.1364/OE.18.018438.
18. S. Chen, L. Zhang, Y. Fei, and T. Cao, "Bistability and self-pulsation phenomena in silicon microring resonators based on nonlinear optical effects," Opt. Express **20**(7), 7454–7468 (2012).
19. A. Gondarenko, J. S. Levy, and M. Lipson, "High confinement micron-scale silicon nitride high Q ring resonator," Opt. Express **17**(14), 11366–11370 (2009).
20. M. C. Tien, J. F. Bauters, M. J. R. Heck, D. T. Spencer, D. J. Blumenthal, and J. E. Bowers, "Ultra-high quality factor planar Si3N4 ring resonators on Si substrates," Opt. Express **19**(14), 13551–13556 (2011).
21. S. S. Verbridge, J. M. Parpia, R. B. Reichenbach, L. M. Bellan, and H. G. Craighead, "High quality factor resonance at room temperature with nanostrings under high tensile stress," J. Appl. Phys. **99**(12), 124304 (2006).
22. Q. P. Unterreithmeier, T. Faust, and J. P. Kotthaus, "Damping of nanomechanical resonators," Phys. Rev. Lett. **105**(2), 027205 (2010).
23. D. T. H. Tan, K. Ikeda, P. C. Sun, and Y. Fainman, "Group velocity dispersion and self phase modulation in silicon nitride waveguides," Appl. Phys. Lett. **96**(6), 061101 (2010), doi:10.1063/1.3299008.
24. M. L. Gorodetsky, A. D. Pryamikov, and V. S. Ilchenko, "Rayleigh scattering in high-Q microspheres," J. Opt. Soc. Am. B **17**(6), 1051–1057 (2000).
25. G. S. Wiederhecker, L. Chen, A. Gondarenko, and M. Lipson, "Controlling photonic structures using optical forces," Nature **462**(7273), 633–636 (2009).
26. R. M. Camacho, J. Chan, M. Eichenfield, and O. Painter, "Characterization of radiation pressure and thermal effects in a nanoscale optomechanical cavity," Opt. Express **17**(18), 15726–15735 (2009).
27. V. R. Almeida and M. Lipson, "Optical bistability on a silicon chip," Opt. Lett. **29**(20), 2387–2389 (2004).
28. T. Carmon, L. Yang, and K. Vahala, "Dynamical thermal behavior and thermal self-stability of microcavities," Opt. Express **12**(20), 4742–4750 (2004).
29. J. G. E. Gardeniers, H. A. C. Tilmans, and C. C. G. Visser, "LPCVD silicon-rich silicon nitride films for applications in micromechanics, studied with statistical experimental design," J. Vac. Sci. Technol. A **14**(5), 2879–2892 (1996).
30. COMSOL material library.
31. M. Oxborrow, "How to simulate the whispering gallery modes of dielectric microresonator in FEMLAB/COMSOL," Proc. SPIE **6452**(64520J), 64520J (2007).
32. L. Ding, C. Belacel, S. Ducci, G. Leo, and I. Favero, "Ultralow loss single-mode silica tapers manufactured by a microheater," Appl. Opt. **49**(13), 2441–2445 (2010).
33. L. He, Y.-F. Xiao, C. Dong, J. Zhu, V. Gaddam, and L. Yang, "Compensation of thermal refraction effect in high-Q toroidal microresonator by polydimethylsiloxane coating," Appl. Phys. Lett. **93**(20), 201102 (2008).
34. L. W. Luo, G. S. Wiederhecker, K. Preston, and M. Lipson, "Power insensitive silicon microring resonators," Opt. Lett. **37**(4), 590–592 (2012).
35. Y. Okamura, S. Yoshinaka, and S. Yamamoto, "Measuring mode propagation losses of integrated optical waveguides: a simple method," Appl. Opt. **22**(23), 3892–3894 (1983).
36. R. Regener and W. Sohler, "Loss in low-finesse Ti: LiNbO3 optical waveguide resonators," Appl. Phys. B **36**(3), 143–147 (1985), doi:10.1007/BF00691779.
37. C. H. Henry, R. F. Kazarinov, H. J. Lee, K. J. Orlowsky, and L. E. Katz, "Low loss Si₃N₄-SiO₂ optical waveguides on Si," Appl. Opt. **26**(13), 2621–2624 (1987).
38. A. De Rossi, V. Ortiz, M. Calligaro, L. Lanco, S. Ducci, V. Berger, and I. Sagnes, "Measuring propagation loss in a multimode semiconductor waveguide," J. Appl. Phys. **97**(7), 073105 (2005).

1. Introduction

Whispering gallery mode (WGM) based optical resonators have many applications ranging from add-drop filters [1,2], biomolecule sensing [3,4], frequency comb generation [5], cavity QED [6,7] to optomechanics [8–11]. In all these applications, a high optical quality factor (Q) and a small mode volume are desirable for better performance and integration, as well as enhanced light-matter interaction. These characteristics result in high power densities that may lead to a variety of nonlinear effects. While some of these effects have practical applications in nonlinear optics [12,13], others can lead to deleterious device instabilities. An optical instability of thermal origin was reported in suspended silicon dioxide (SiO₂) microspheres [14, 15], leading to a pseudo oscillatory optical output with typical timescale in the millisecond range. In integrated photonics, silicon (Si) microdisk [16] and microring structures have been shown to exhibit a much faster and more regular oscillatory behavior

[17,18] that was assigned to an interplay between thermal and free carrier dynamics. Another platform of unique potential for integrated photonics is silicon nitride (SiN), whose good optical properties allow to obtain extremely high Q optical resonators [19,20]. The material's potential extends to nanomechanics, where its high tensile stress form provides unique mechanical Q factors [21, 22]. Moreover, SiN has a broader transparency region than silicon and benefits from the absence of two photon absorption (TPA) at telecom wavelengths [23]. In consequence, SiN optical resonators are often believed to be immune against instabilities disrupting their silicon counterparts.

Here we report on an optical instability in high-Q SiN WGM resonators. Under continuous-wave pumping, the resonators transit between chaotic-like and self-pulsing regimes for the optical output. A rich variety of timescales and amplitudes are observed depending on operating conditions. In the self-pulsing regime, unprecedentedly long periods of oscillation up to a minute are measured. The phenomenon is explained by an interaction between a fast thermo-optic and slow thermo-mechanic nonlinearity. A model is developed which reproduces experimental data and gives routes to control these instabilities.

2. Silicon nitride optical resonators

Fabrication

The fabrication starts from a commercial (HSG-IMIT) wafer composed from top to bottom of a 300 nm thick layer of high tensile stress Low Pressure Chemical Vapor Deposition (LPCVD) SiN, a 3 μm thick SiO_2 sacrificial layer and a Si substrate. The waveguides and disks are defined by e-beam lithography using a double layer PMMA positive resist. We draw straight optical waveguides 8 μm wide and 3 mm long, extending up to the sample facets (Fig. 1(a)). The central part of the waveguide is symmetrically narrowed down to a width of 900 nm using two 60 μm long linear tapering profiles (inset of Fig. 1(a)). To tune the evanescent coupling to the disk resonator, the gap distance between disk and waveguide is varied around an average value of 400nm. The 900 nm wide straight segment of the taper is 20 μm long. All disks on the sample have a nominal diameter of 20μm. A cobalt etch mask is used to protect the structure during an ICP-RIE dry etch (SF_6 and Ar chemistry) through the SiN layer. The sample facets are then cleaved. Removal of the cobalt etch mask is done in a piranha solution (3 H_2SO_4:1 H_2O_2). Finally the sample is dipped for 15 minutes in buffered oxide etchant (7 NH_4F:1 HF) which selectively etches ~1.5μm of SiO_2, freeing the tapered part of the waveguide and isolating the disk resonator on a SiO_2 pedestal (Fig. 1(b)). The disks' sidewall roughness is hardly visible in a Scanning Electron Microscope (SEM) image (Fig. 1(c)), the biggest features measuring below 10 nm (not shown here).
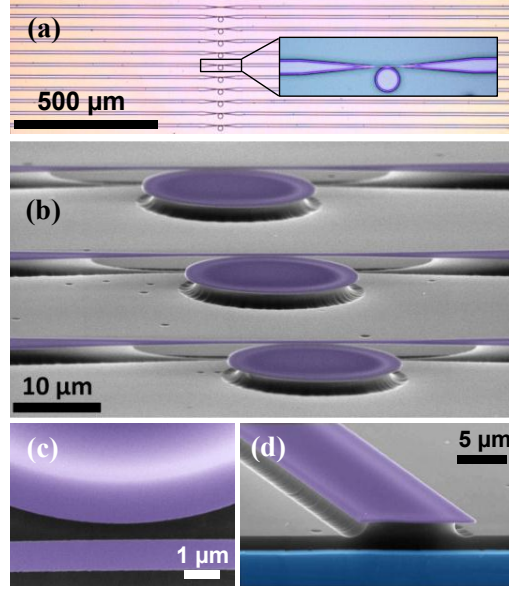
Fig. 1. (a) Optical microscope top view of a sample containing 10 waveguide/disk resonator sets. Inset: tapered part of the waveguide in the disk vicinity. (b) SEM micrograph side view of 3 SiN disk resonators and coupling waveguides. (c) SEM top view of the evanescent coupling region between tapered waveguide and disk. (d) SEM side view of the cleaved waveguide input facet. In (b), (c) and (d) SiN is colored in purple, SiO_2 in gray and Si in blue.

Optical characterization

Optical spectroscopy of each disk couple to its waveguide is performed in the 1500-1600 nm band using a tunable continuous wave external cavity diode laser. The cleaved facets of the waveguide (Fig. 1(d)) serve as optical input/output ports where laser light is injected and collected. The in-plane polarization is selected. Output light is collected by a microscope objective and sent onto a p-i-n photodetector. Figure 2(a) shows the normalized transmission of a guide evanescently coupled to a disk as a function of the laser wavelength. The normalization maintains average unity transmission over the whole wavelength range but keeps fine spectral features. Several resonances appear in this spectrum with a contrast close to unity. They correspond to WGMs with an intrinsic Q factor between 10^5 and $2 \cdot 10^5$. Finer resonances are also present, such as the one shown in Fig. 2(b) which possesses a Q-factor of 4.10^5. In our sample, these resonances tend to have a lower contrast and exhibit doublet splitting due to a symmetry breaking [24]. Because of the positive thermo-optic coefficient ($\partial n/\partial T$) of SiN [25, 26], all optical resonances present a typical bi-stable behavior [27] at high power, which translates into a triangular resonance profile Fig. 2(c) when laser-scanning the resonance.
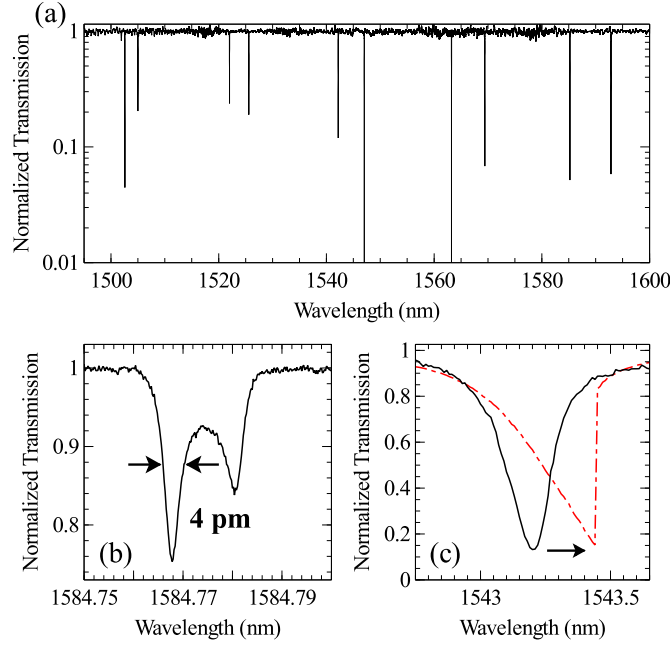
Fig. 2. (a) Optical transmission spectrum of a SiN disk resonator. (b) A fine optical resonance measured in a weakly coupled configuration far from critical coupling, showing an optical Q of 400 000, typical of the highest optical Qs in this device. (c) A broader optical resonance, measured at low power (solid black line) and high power (red dash-dot line).

3. Optical instability

Experimental observation

When the laser wavelength is tuned to the blue detuned flank of a WGM resonance, the positive thermo-optic coefficient of SiN generally provides a negative feedback on the fluctuations in the optical power circulating inside the resonator. Indeed, an increase in the circulating power leads to more heating, which leads to a red-shift of the optical resonance. For a fixed laser wavelength this produces an increased detuning which in turn leads to decreased circulating power. A drop in the optical power is compensated in similar fashion. In this situation the blue detuned flank of a WGM resonance exhibits a thermal self-stability, which is observed routinely on SiO_2 [28] or Gallium Arsenide resonators [10].

The behavior of the present device is in strong contrast with this common case. When the laser wavelength is set slightly blue-detuned to a WGM resonance (red arrow in the inset of Fig. 3(a)), the optical transmission spontaneously settles into a slow periodic oscillatory regime (Fig. 3(a)). The resonator's output alternates between an 'on state' with near unity transmission and the laser out of the WGM resonance, and an 'off state' with near zero transmission and the laser at resonance. While the optical transmission evolves slowly during the on and off states, the switching between the two is extremely sudden (Fig. 3(b)). At high power, the oscillatory behavior maintains a high level of regularity over hundreds of oscillations. The period of the oscillation is found to have an exponential dependence with the optical power circulating in the waveguide, reaching up to nearly 2 minutes for the highest power used in our experiments. The circulating power at the disk level is estimated by taking into account the linear losses in the waveguide from disk to sample facet (see appendix), the reflectivity of the guided mode at the sample facet and the losses in the collection microscope objective. At lower laser power the oscillations in the transmission are still present, however

no longer periodic but resemble a chaotic behavior, with oscillations present at multiple timescales. Characteristic times can be defined for each timescale by an average over a large number of these oscillations. Figure 3(c) shows the transition between the chaotic-like and periodic regimes as the optical power is increased, with measured characteristic times spanning over six orders of magnitude.

These experimental results indicate a complex dynamical behavior, which can be partially uncovered by laser scanning the optical resonances at high power and at different speeds. The red triangular spectrum shown in Fig. 2(c) is acquired with the laser wavelength being swept with a speed of 100 nm/s. Under these conditions and for a WGM resonance width in the 10-100 pm range, the laser wavelength is tuned to the WGM resonance only on the order of 10^{-3}-10^{-4}s. In contrast much slower sweep speeds of the order of 0.01 nm/s, where the resonance is hit during typically one second, result in shifting the resonance center position towards smaller wavelengths (not shown). These distinct behaviors call for the existence of different dynamical phenomena in the system.
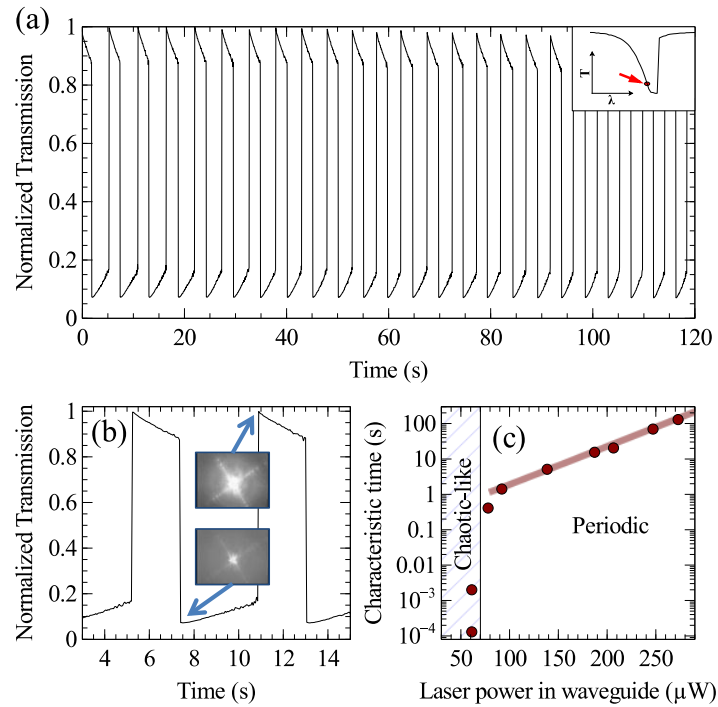
Fig. 3. (a) Normalized optical power measured as a function of time at the output of a waveguide coupled to a SiN disk resonator. The employed WGM resonance at $\lambda = 1539.31$ nm has an on-resonance normalized transmission of 7% and a FWHM of 46 pm. It is identified as a p = 1, m = 57 WGM (radial and azimuthal orders). Inset: initial position of laser wavelength λ (red arrow) with respect to the WGM resonance in the transmission T spectrum. (b) Oscillatory behavior shown with greater detail. The inset pictures are single frames from an infrared camera video of the output waveguide transmission taken during measurement (See Media 1). (c) Characteristic time of the oscillatory transmission as a function of the optical power dissipated by the disk. The line through the high power data points is an exponential fit.

Model

Based on the above experimental observation, we develop a model where the fast red-shifting thermo-optic effect competes with a blue shifting effect on a much slower time scale which will be discussed in following. Indeed the thermo-optic effect is associated with the material

temperature within the disk resonator. Given the disk's radius, the thermal conductivity of SiN and the conditions of thermal anchoring to the substrate, the disk's thermal response time is of the order of 7 μs. The much slower phenomenon associated to typical timescales approaching one second remains to be identified. A thermal response time of the substrate may be consistent with such a timescale. In order to test this hypothesis, we develop a simple model. In this model we consider two thermally coupled elements: the disk resonator and a given volume of substrate, both with a uniform temperature field. The disk's temperature T_1 influences the optical resonance position through the thermo-optic effect. In our model we consider that the substrate's temperature T_2 also changes the resonance position, but with an opposite sign effect. Equation (1) expresses the WGM's resonance wavelength λ_{res} as a function of these two parameters in the linear regime:

$$\lambda_{res}\left(T_1,T_2\right) = \lambda_{res}\left(T_0,T_0\right) + \left(\frac{\partial \lambda_{res}}{\partial T_1}\right)\left(T_1 - T_0\right) + \left(\frac{\partial \lambda_{res}}{\partial T_2}\right)\left(T_2 - T_0\right) \tag{1}$$

where T_0 is the ambient laboratory temperature. The effect on the resonance wavelength of the disk's thermal expansion is an order of magnitude smaller than the thermo-optic contribution. In this limit $(\partial \lambda_{res}/\partial T_1) = (\partial n/\partial T_1)\cdot \lambda_{res}/n$ is a function of the thermo-optic coefficient $(\partial n/\partial T)$ and the refractive index n. In our study $(\partial \lambda_{res}/\partial T_2)$ is a parameter that can be inferred experimentally or computed numerically (see next section). To relate Eq. (1) to an optically measured quantity, we express in Eq. (2) the normalized optical transmission of the resonator Λ as a function of the laser wavelength λ and of temperatures T_1 and T_2. C is the contrast of the WGM resonance (C = 1 for critical coupling and <1 otherwise) and $\delta\lambda$ its full width at half maximum.

$$\Lambda\left(\lambda,T_1,T_2\right) = 1 - \frac{C}{1 + \left(\dfrac{\lambda - \lambda_{res}\left(T_1,T_2\right)}{\delta\lambda/2}\right)^2} \tag{2}$$

This equation relates the resonator's optical transmission to the temperature evolutions. Conversely, the temperature evolutions are governed by the amount of absorbed optical power within the disk, by the thermal contact between the disk and substrate, and by the thermal coupling of the substrate to its environment. We have checked that the thermal coupling of the disk to the surrounding air can be safely neglected. These aspects are cast into the two coupled differential equations Eq. (3) and Eq. (4). Equation (3) gives the rate of change in the disk temperature:

$$\frac{dT_1}{dt} = P_{guide}\, A\, \frac{1 - \Lambda\left(\lambda,T_1,T_2\right)}{m_1\, c_1} - \frac{G_{1,2}}{m_1\, c_1}\left(T_1 - T_2\right) \tag{3}$$

where P_{guide} is the optical power in the waveguide at the disk level and A is the fraction of the laser power dissipated by the resonator which is absorbed and turned into heat within the disk. The evaluation of this fraction will be discussed below. m_1 is the mass of the SiN disk, c_1 the SiN heat capacity at constant pressure in J K^{-1} kg^{-1} and $G_{1,2}$ the thermal conductance between the disk and substrate in W K^{-1}. $G_{1,2}$ is calculated analytically by summing the thermal resistance between the pedestal and the disk's periphery where light is absorbed with the resistance of the SiO_2 pedestal. In our resonator's geometry we obtain $G_{1,2} = 2.86\cdot 10^{-5}$ W K^{-1}, in good agreement with Finite Elements Method (FEM) simulations. Equation (3) contains two terms: the first term is proportional to the optical power lost into the disk and describes the heat inflow, while the second term describes the heat outflow into the substrate.

In a similar manner, the temperature evolution of the substrate volume is written as:

$$\frac{dT_2}{dt} = \frac{G_{1,2}(T_1 - T_2)}{m_2 c_2} - \frac{G_2}{m_2 c_2}(T_2 - T_0) \qquad (4)$$

where c_2 is the Si heat capacity at constant pressure, m_2 the mass of the considered volume of substrate and G_2 its thermal conductance to the environment at T_0. The first term of the equation describes the heat inflow from the disk into the substrate, and the second term the heat outflow into the environment. Although the power flow out of the disk $G_{1,2}(T_1-T_2)$ and incoming power flow into the substrate $G_{1,2}(T_1-T_2)$ are equal, the dynamical effect on disk and bulk temperature is divided by the mass times the heat capacity of the considered element. Therefore the temperature oscillations in the bulk are significantly smaller than those of the disk.

Comparison between model and experiments

One important ingredient for the above model to explain our experimental results is the correct evaluation of the absorbed optical power Pguide.A (1-Λ). The fraction of laser power absorbed and lost as heat within the disk resonator is calculated by fitting the magnitude of the thermo-optic shift (Fig. 2(c)) on a known resonance, for a typical value of the thermo-optic coefficient ($\partial n/\partial T$) taken from the literature (see table). We find that fraction to be 80 ± 5%. Although this value is high, it is in line with optical losses measured in similarly processed straight SiN waveguides (see appendix). Surface scattering has a minor contribution to total optical losses thanks to the minimal surface roughness obtained with our fabrication process.

Other parameters entering the model are the contrast C and the resonance width $\delta\lambda$, which are directly measured at low optical power on the WGM resonance under consideration, and are independent on the temperature. The value of ($\partial\lambda_{res}/\partial T_1$) is known from the refractive index and thermo-optic coefficient of SiN. A value of ($\partial\lambda_{res}/\partial T_2$) is extracted by comparing the WGM optical shift measured at fast and slow laser-scan speeds. For the slow scan-speed, the optical resonance is blue-shifted with respect to the fast scan-speed case. The absorbed optical power is evaluated at low scan-speed and associated to a temperature increase of the substrate by means of FEM thermal simulations. This temperature rise is related to the measured blue-shift, leading to a rough estimate of ($\partial\lambda_{res}/\partial T_2$) = ~0.27 nm K^{-1}. This estimate serves as starting value for the fitting procedure where ($\partial\lambda_{res}/\partial T_2$) is then taken as an adjustable parameter. A second fit parameter is the considered volume of Si substrate. We consider a Si cylinder of equal height and radius h, positioned directly under the pedestal. The cylinder's thermal conductance G_2 is calculated as a function of h using referenced Si thermal conductivities. A summary of physical parameters employed in the model is given in Table 1.

The evolution of the optical transmission coupled dynamically to temperatures T_1 and T_2 through Eqs. (1)–(4) is obtained numerically over 10 million 1μs time steps, yielding results such as the ones shown in Fig. 4. In this figure, we compare the obtained theoretical results to experimental data. In order to recover the richness of the observed oscillatory behavior, we have selected three distinct experimental configurations, with different laser detuning and laser power. In our fitting procedure, the parameters ($\partial\lambda_{res}/\partial T_2$) and h are varied until we can fit all three sets of measurements with our model using a single set of parameters. The best fit, shown in Fig. 4, is obtained for ($\partial\lambda_{res}/\partial T_2$) = 0.227 nm K^{-1} and h = 500 μm, a height which turns out to match the Si substrate thickness. With these parameters, the disk's thermal response time $\tau_1 = (m_1 \cdot c_1)/G_{1,2}$ is 7.15 μs and the substrate volume's thermal time $\tau_2 = (m_2 \cdot c_2)/G_2$ is 0.58 s. These parameters allow obtaining a very satisfactory agreement between our experimental data and the model, with oscillatory periodic times that span from 0.4 s to 1.4 s in Fig. 4. We also checked that the correct dynamics is reproduced by the model for periodic times going from the millisecond to a few seconds. Figure 5 (a) sketches how the simple model used here reproduces the oscillatory behavior of the optical output.
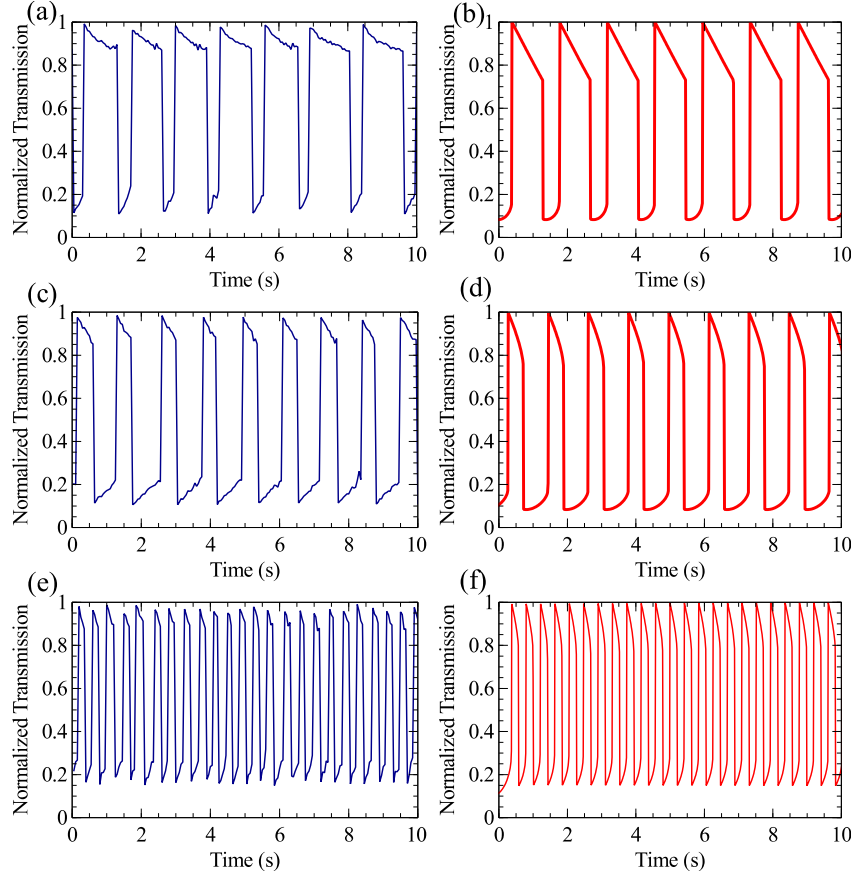
Fig. 4. Experimental (left) and model (right) results for the normalized optical transmission of a WGM resonator for three distinct pump laser configurations. (a) Experiments and (b) model for an initial blue detuned pump configuration with λ = 1539.35 nm and $A \cdot P_{guide}$ = 77 μW. (c) Experiments and (d) model for the same optical power but with initial laser blue detuning 2 pm greater. (e) Experiments and (f) model for a lower power ($A \cdot P_{guide}$ = 65 μW) and for a detuning similar to (a) and (b). In (b), (d) and (f) the temperature oscillations are on the order of a few Kelvin for T_1 and a few tens of mK for T_2.

Table 1. Physical parameters used in the models

Parameter	Name	Unit	Value	Source
SiN refractive index	n	-	2	[29]
SiN thermo-optic coefficient	$(\partial n/\partial T)$	K^{-1}	$2.44 \cdot 10^{-5}$	[25,26]
SiO_2 & Si thermal expansion coefficient		$\mu m\ m^{-1}\ K^{-1}$	0.5 & 2.6	[30]
SiN & Si heat capacity	c_1 & c_2	$J\ K^{-1}\ kg^{-1}$	700 & 700	[30]
SiN, SiO_2 & Si thermal conductivity		$W\ m^{-1}K^{-1}$	20, 1.4 & 130	[30]
SiN & Si density		$kg\ m^{-3}$	3100 & 2329	[30]
Slow blue-shift coefficient	$(\partial \lambda_{res}/\partial T_2)$	$nm\ K^{-1}$	0.227	

4. Origin of the slow thermal nonlinearity

SiO_2 and Si have different thermal expansion coefficients (see Table 1). When these materials are heated by the absorbed laser power within the resonator, this difference leads to stress and structural deformation. Figure 5 (b) shows a simplified 2D axi-symmetric FEM simulation of a SiN disk resonator atop a SiO_2 pedestal on a slab of Si substrate. A uniform increase of the temperature of the Si substrate results in an upward buckling of the whole structure. While the Si substrate expands outward, the SiN disk is bent upwards and slightly inwards, resulting in a reduction in the effective optical WGM cavity radius. This reduction translates into a blue-shift of the WGM resonance, in agreement with the experimental observations at slow time scale. In order to quantify this effect, we use a FEM simulation of the structure including a large-scale substrate slab and accounting for the stress in the SiN layer. For two distinct but close Si substrate temperatures (1K apart), we obtain the disk deformation profile and export it into to a weak-form FEM simulation of the WGM employed in the experiments [31]. This allows for calculating the WGM resonance wavelength shift associated to this differential temperature change and gives a value of $(\partial\lambda_{res}/\partial T_2)$ that agrees within a factor 5 with the value extracted from the model fit. Although these results are in the right order of magnitude, we ascribe the discrepancy to several approximations: first the exact pedestal geometry plays an important role but is not perfectly known, second the temperature profiles of the different elements were taken as uniform, when temperature gradients should influence the exact strain in the real structure. Despite these approximations, our simulations clearly point towards this thermo-mechanic deformation of the structure as being the source of the slow blue-shifting optical nonlinearity.
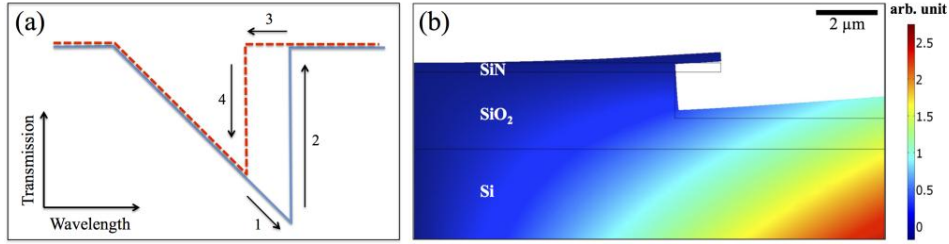
Fig. 5. (a) Schematic description of the regime of self-pulsating optical transmission. In step **1** the laser line starts on the blue-detuned flank of the WGM thermo-optically distorted resonance. The sample substrate slowly heats up, gradually blue-shifting the resonance. Once the resonance wavelength moves past the fixed laser wavelength, the laser line reaches the unstable flank of the thermo-optically distorted resonance: at this stage the WGM snaps out of laser resonance and the transmission jumps back to unity (step **2**). The WGM is out of resonance with the laser and the substrate slowly cools down, gradually red-shifting the optical resonance (step **3**). Finally when the red-shift is sufficient, the WGM snaps back into resonance with the laser in the thermo-optically distorted regime (step **4**). In the self-pulsating regime, the output optical power cycles through the hysteresis curve. (b) 2D axi-symmetric FEM simulation of the thermal strain in a SiN disk resonator structure. The surface color code shows the magnitude of the radial displacement. The deformed shape displays strongly exaggerated displacement amplitude.

Complementary simulations allow verifying that the magnitude of the blue optical shift is independent of residual stress in SiO_2 and SiN layers. Thus the type of instability reported in this article shouldn't be limited to the high-tensile stress SiN employed for our resonators. This is checked experimentally by observing similar instabilities after releasing the stress in a larger fraction of the SiN disks by deeper under-etching. Note that the magnitude of the thermal stress-induced radial displacement of the disks is very small. In the data of Fig. 4, the maximum value of the stress-induced blue shift is 14 pm. In order to account for this shift, the disk's radial displacement needs only be ~1Å, i.e. roughly the diameter of a silicon atom.

For the sake of completeness, the effect of other mechanisms influencing the dynamical behavior of the disk resonators on a slow timescale is discussed in the following. First, a possible influence of the suspended SiN coupling waveguides is ruled out by observing optical instabilities on identically processed standalone SiN disks coupled to a tapered silica fiber [32]. Second, a slow thermal expansion of the sample substrate leading to an optical misalignment at the waveguide injection facet can also safely be ignored: a 1 Kelvin temperature rise produces a displacement of the order of 1 nm.

5. Conclusion

We present chaotic and self-pulsating optical instabilities observed in SiN disk resonators. Their characteristic time spans six orders of magnitude, from hundreds of microseconds to hundreds of seconds. This phenomenon is explained by the interplay between a fast thermo-optic nonlinearity and a much slower thermo-mechanic nonlinearity. A model showing good agreement with experimental data is presented which allows proposing and supporting a credible explanation for the origin of the slow thermal nonlinearity. In this work we show that SiN resonators, despite the absence of two photon absorption, can nonetheless exhibit optical instabilities on a much longer timescale than reported in other systems. We point towards volume optical losses to be responsible for the resonator's thermal instabilities. If a reduction of optical absorption - through better control of the material and surface passivation − is an evident option to control the reported optical instabilities, a proper engineering of the resonator structures can also serve the same goal [33,34]. In our present case, modified designs for the pedestals may lead to reduced instabilities. These aspects become critical for miniature resonators operating at high optical powers.

6. Appendix: optical loss measurements in straight SiN waveguides

In this appendix, we study optical losses in SiN structures in order to support elements of the above analysis and to envision future generation of improved resonators. To this end, we fabricate several versions of straight SiN waveguides using the starting wafers described in section 2. Both fabrication and post-fabrication protocols are varied to study their impact on optical losses. An example of a straight SiN waveguide is shown in Fig. 6(a). Optical loss measurements are performed using a top-view scattering technique [35], where the light intensity scattered by the waveguide is imaged on a CCD camera positioned directly above the guide (Fig. 6(b)). This intensity image is analyzed as an exponential decay of the optical intensity along the guide propagation axis (Fig. 6(c)), and related to a linear loss coefficient α. This technique allows very straightforward monitoring of significant loss levels change, like obtained upon sample annealing (Fig. 6(d)). The top-view scattering technique can be complemented by the Fabry-Pérot interference method [36], when the upwards scattered intensity becomes too weak for a CCD measurement (Fig. 7).
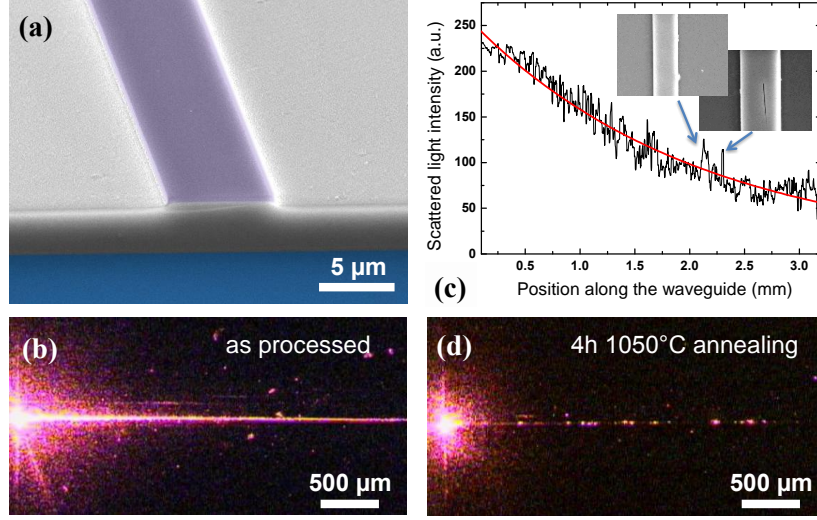
Fig. 6. (a) False color SEM micrograph of a straight SiN waveguide. (b) CCD image top view of an entire SiN waveguide fabricated using protocol 1, with 633 nm wavelength laser light injected at the left sample facet (bright spot at center left) and travelling along the waveguide (bright horizontal line with decaying intensity). (c) Corresponding upwards scattered light intensity as a function of the position along the waveguide, with an exponential decay fit (solid red line). The insets show SEM pictures featuring typical waveguide defects leading to locally increased scattering. The left inset shows an inhomogeneous waveguide width resulting from lithography errors. The right inset shows a crack in the SiN resulting from the high tensile stress. This waveguide was processed using protocol 1. (d) Same waveguide measured after 4h of annealing at 1050°C under N_2 atmosphere. The scattering is essentially caused by isolated defects like the ones shown in the inset of (c), but the output power is now higher than in (b).

Protocol 1

Samples are prepared using standard photolithography and AZ 5214E image-reversal photo resist to define an aluminum metal etch mask. The sample is then etched in a standard PP-RIE machine using CF4 chemistry. The metal etch mask is removed using a hot (80°C) potassium hydroxide (KOH) solution. Waveguides are 3.5 mm long and 2 to 10 µm wide. Waveguides 2 to 5 µm wide are consistently showing higher optical losses, which we interpret as a higher sensitivity to the residual sidewall roughness produced by the photolithography. Waveguides that are 6 to 10 µm wide all exhibit comparable loss levels, showing that sidewall roughness losses are no longer the dominant loss mechanism. For these latter guides, material and top surface losses should now be dominant. We therefore expect the measured linear losses to provide a lower bound for losses in WGM resonators fabricated in a similar fashion. The average loss level measured on 10 such wide waveguides is measured by the scattering method at wavelengths comprised between 543 and 1350 nm. The results are displayed in Table 2. Due to the relatively short length of the guides and the large amount of scattering at the injection and collection end facets, the error bar on these measurements is of the order of ±10%. The measured linear loss coefficients are quite high. The losses measured at 1350 nm would for instance correspond to optical Qs below $2 \cdot 10^4$ on a 10 µm radius SiN disk resonator, where we use the following equation to relate the optical Q and with the loss coefficient α, the free-space wavelength λ_0 and the effective index of the WGM n_{eff}.

$$Q = 2\pi \frac{1}{1 - e^{-\alpha \lambda_0 / n_{eff}}} \qquad (5)$$

Protocol 2

The second protocol is identical to the first, except the aluminum etch mask is removed using a piranha solution (3 H_2SO_4:1 H_2O_2) instead of KOH. Waveguides are 8 μm wide and 2.5 cm long. Using the top-view scattering method, losses at a wavelength of 633 nm are measured with an average value of 0.2 cm^{-1} and the smallest observed values at 0.05 ± 0.01 cm^{-1}. In the infrared, average losses were measured by the Fabry-Pérot interference method and range from 0.15 cm^{-1} at 1490 nm to 0.6 cm^{-1} at 1530 nm. In the 1490 to 1610 nm spectral window, the measured loss level as a function of wavelength shows a maximum at 1530 nm. This is in agreement with [37] which describes a similar feature as absorption induced by Si-H bonds within the material. Our measured loss values translate into optical Qs of $4 \cdot 10^5$ and $1 \cdot 10^5$ respectively, which are in good agreement with the optical Qs of disk resonators presented in this work. The use of the piranha etchant instead of KOH solution to remove the metal mask seems to consistently produce lower optical loss levels. The piranha probably improves the final surface state of the sample.
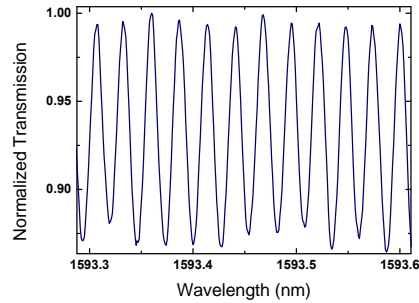
Fig. 7. Transmission spectrum of a 8 μm wide and 2.5 cm long straight waveguide fabricated using protocol 2. Due to the reflectivity of the sample facets, the transmission shows Fabry-Perot interference fringes with 26.6 pm periodicity. Linear losses can be extracted knowing the contrast of the fringes, the facet reflectivity and the sample length. The precision of this method is set by the accuracy in the evaluation of the facet reflectivity and sample length. If the waveguide is multimode, some beating in the fringes' amplitude leads to an overestimation of losses [38].

Effect of post-fabrication annealing

High temperature annealing has been shown to significantly reduce optical loss in SiN waveguides in the near infra-red [37]. Here we anneal the samples fabricated using protocol 1 for 4 hours at 1050°C under a nitrogen atmosphere. This leads to an increase of transmission levels by about an order of magnitude at a wavelength of 633 nm. After this procedure, loss measurements by the top-view scattering technique are no longer possible, as the dominant sources of upwards scattering are now localized scattering defects along the waveguide which are outshining the exponential decay (Fig. 6(d)). However, these defects do not determine optical losses in the waveguide, which remain dominated by distributed loss sources. The Fabry-Perot interference technique leads to estimated losses now below 0.3 cm^{-1} at 1550 nm. For this estimation, the reflectivity of the fundamental guided mode at the cleaved sample facet was computed using FDTD simulations, leading an intensity reflectivity of 5.9%. These losses would correspond to a SiN disk resonator optical Q above $2 \cdot 10^5$. We further found that annealing high tensile stress LPCVD SiN at 1050°C for 1h30 reduces the built in tensile stress. This might or might not be desirable depending on the application. On the waveguides fabricated using protocol 2, an annealing of one hour at 800°C did not produce any measurable change in the linear losses.

Conclusion

Table 2 summarizes the loss measurements carried-out on straight SiN waveguides. Loss levels measured on the waveguides of protocol 1 after annealing are comparable to those measured on the waveguides of protocol 2 before annealing. However, the former show a reduced amount of upwards-scattered light compared to the latter (not shown here). This points towards the interpretation that piranha impacts mostly the surface state of the waveguides, while the 1050°C annealing process would impact volume and/or surface losses.

Table 2. Optical losses measured on straight SiN waveguides at different wavelengths

Wavelength (nm)	543	633	1000	1350	1490	1530	1550
Protocol 1 loss α (cm^{-1})	13.4	7.8	2.6	3.5	-	>7	3
Protocol 1 after 1050 °C annealing	-	~0.15	-	-	<0.3	<0.3	<0.3
Protocol 2 loss α (cm^{-1})	-	0.2	-	-	0.15	0.6	0.3

Acknowledgments

5.5   Conclusion

In this chapter we first detailed the progress done during this doctoral work in the area of integrated GaAs disk resonators. Several evolutions were implemented in the design and fabrication techniques. These allowed for significant increases in the optical transmission levels as well as achieving state of the art optical quality factors and reproducible critical coupling. The origin of optical losses in current devices was investigated, and the current limitation to the optical quality factor was identified. This analysis points towards the action required for further optical improvements.

Second we described the work performed on the SiN platform. Through two generations of straight waveguides and a fine-tuning of the fabrication procedure were were able to significantly reduce optical loss levels. These developments resulted in the fabrication of on-chip integrated high Q SiN WGM resonators. The optical instabilities and self-pulsing observed in these devices was described and a model explaining this behavior was provided.

In the next chapter we move on to the optomechanical behavior of these devices.

Chapter 6

Optomechanics experiments

6.1 Introduction

In this chapter we first report chronologically our results on GaAs optomechanics, starting with earlier experiments on stand alone GaAs disk resonators probed by the fiber taper technique (sections 6.2.1 and 6.2.2). We then specifically detail the operation of the on-chip GaAs resonators in the cryostat and discuss our first results on their optomechanical behavior at low temperature (section 6.2.4). Finally we discuss the optomechanics of the silicon nitride disk+beam system and show how the two different coupling mechanisms (*dispersive* and *reactive*) occurring in these devices can interplay (see section 6.3).

6.2 GaAs disk optomechanics

6.2.1 Stand-alone GaAs disk resonators at room temperature

In this section we report experimental results on stand alone GaAs disk resonators with a disk thickness of 200 nm and disk radius varying between 3 and 6 μm. These resonators, which exhibit high optical quality factors in the 10^5 range and mechanical frequencies ranging between 300 and 900 MHz are probed with the pulled fiber taper technique described in section 1.1.1. They are fabricated using the wet etch recipe provided in section 4.1.9. The high motional sensitivity of $2 \cdot 10^{-17}$ m/$\sqrt{\text{Hz}}$ afforded by the large optomechanical coupling in these devices ($\sim$ 100 GHz/nm) allows for the detection of the Brownian motion of many of the disk's mechanical modes at room temperature. The analysis of the following results draws heavily

upon the theoretical framework detailed in chapters 1 through 3. Indeed as discussed in section 3.8.1, because of the rather large and non circular AlGaAs pedestals in these first devices, a wide variety of mechanical modes are visible close together in the experimental noise spectra. This underlines the need for an accurate mechanical description of both in-plane and out of plane mechanical modes (as provided in sections 2.3.2 and 2.3.1) in order for precise identification. Furthermore, a precise identification and description of the different WGMs in the optical transmission spectra is also required for the theoretical calculation of the g_{om} done in this work (see section 1.2). We see a certain discrepancy exists here between the simulated g_{om} and the experimentally measured g_{om}. This discrepancy can likely be explained by the non-circularity of the disk's pedestals and by the neglected of photoelastic contribution g_{om}^{pe} discussed in section 3.8.2. The following article titled 'High Frequency GaAs Nano-Optomechanical Disk Resonator' reports these first experimental results.

P H Y S I C A L   R E V I E W   L E T T E R S

High Frequency GaAs Nano-Optomechanical Disk Resonator

Lu Ding,[1] Christophe Baker,[1] Pascale Senellart,[2] Aristide Lemaitre,[2] Sara Ducci,[1] Giuseppe Leo,[1] and Ivan Favero[1,*]

[1]*Laboratoire Matériaux et Phénomènes Quantiques, Université Paris Diderot, CNRS, UMR 7162,*
10 rue Alice Domon et Léonie Duquet, 75013 Paris, France
[2]*Laboratoire de Photonique et Nanostructures, CNRS, Route de Nozay, 91460 Marcoussis, France*

Optomechanical coupling between a mechanical oscillator and light trapped in a cavity increases when the coupling takes place in a reduced volume. Here we demonstrate a GaAs semiconductor optomechanical disk system where both optical and mechanical energy can be confined in a subwavelength scale interaction volume. We observe a giant optomechanical coupling rate up to 100 GHz/nm involving picogram mass mechanical modes with a frequency between 100 MHz and 1 GHz. The mechanical modes are singled-out measuring their dispersion as a function of disk geometry. Their Brownian motion is optically resolved with a sensitivity of 10^{-17} m/$\sqrt{\text{Hz}}$ at room temperature and pressure, approaching the quantum limit imprecision.

PACS numbers: 42.55.Sa, 42.50.Wk, 62.25.−g, 63.22.−m

Optomechanical systems generally consist of a mesoscopic mechanical oscillator interacting with light trapped in a cavity. These systems have attracted a growing interest since the first experimental evidence that cavity light can be used to optically self-cool the oscillator towards its quantum regime. They are now studied in an increasing number of geometries and compositions, with the common purpose of coupling photons and phonons in a controlled way [1–3]. High-frequency nanomechanical oscillators are usually welcome in optomechanics applications, to ease the access to the quantum regime or to develop high-speed sensing systems [4]. But because the typically subwavelength size of these oscillators often implies a weak interaction with light, they need to be inserted in the core of a cavity mode to enhance the optical-mechanical interaction [5]. The typical optomechanical coupling obtained using this approach is of 50 MHz/nm for visible photons [6,7] or 50 kHz/nm in the microwave range [8]. A coupling enhancement can be obtained by further confining mechanical and optical modes in a small interaction volume, as recently achieved in nanopatterned photonic crystals [9]. However, these structures are complex to design and fabricate, and being based on silicon technology, they do not allow the insertion of an optically active medium. This precludes exploring novel situations where a (quantum) mechanical oscillator would be coupled to a (quantum) photon emitter embedded in the host material [10]. In this Letter we present a gallium arsenide (GaAs) nano-optomechanical disk resonator, a system at the crossroads with III-V semiconductor nanophotonics. This resonator combines the assets of both nanoscale mechanical systems [high frequency and low mass in the picogram (pg) range] and semiconductor optical microcavities, with optical quality factor above 10^5. The high refractive index of GaAs enables storing light in a submicron mode-volume whispering gallery mode (WGM) of the disk, where it

couples to high frequency (up to the GHz) vibrational modes of the structure. Thanks to the miniature optical-mechanical interaction volume, the coupling reaches 100 GHz/nm, providing nearly quantum-limited optical detection of vibrations. Besides offering high-frequency mechanical oscillators with an ultrasensitive optical read-out, GaAs nano-optomechanical resonators are naturally suited for integration in geometry of arrays on a chip and for interfacing with single emitters in form of InGaAs quantum dots [11].

A whispering gallery disk structure is both an optical cavity and a mechanical oscillator. The radial breathing of the structure couples naturally to photons stored in the gallery mode, by modulating the effective optical length of the cavity. The related optomechanical coupling factor $g_{\text{om}} = (d\omega/d\alpha)$ accounts for the differential dependence of the cavity angular eigenfrequency ω on the mechanical displacement α, and enters the quantum description of the system coupled through radiation pressure $H_c = \hbar g_{\text{om}}(\hat{a}^+\hat{a})\alpha$, where $\hat{a}(\hat{a}^+)$ is the optical annihilation (creation) operator and α the mechanical degree of freedom. A large value of g_{om} is required for efficiently turning mechanical information into optical information and vice versa, and is hence beneficial to most applications in optomechanics. As we will see below, a miniature disk can sustain a very large value of g_{om}.

The WGM problem can be treated solving the Helmholtz equation in a cylinder of height h and radius R [12]. Provided that h is sufficiently larger than λ/n (thick disk limit) the effective index method can be employed to separate vertical (along cylinder axis) and horizontal dependence of the electromagnetic field F ($F = E$ or H). Using the rotational invariance, F is decomposed $F = \Psi(\rho)\Theta(\theta)G(z)$ with $\Theta(\theta) = e^{\text{im}\theta}$. E.g., for the TM modes of azimuthal number m, the dispersion relation imposed by continuity of tangential E and H at the disk interface reads

$n_\zeta[\dot{J}_m(kn_\zeta R)/J_m(kn_\zeta R)] - \dot{H}_m^{(2)}(kn_\zeta R)/H_m^{(2)}(kn_\zeta R) = 0$, where n_ζ is the effective index of the slab of thickness h, J_m is the first-kind Bessel function of order m, $H^{(2)}{}_m$ is the second-kind Hankel function of order m, and $k = 2\pi/\lambda$. For a given h, this dispersion relation only depends on kR: if k_0 is a solution to this equation for a radius R_0, the solution k for radius R is given by $k = k_0 R_0/R$. Thus in the limit of a thick disk, $d\omega/dR = -\omega/R$ is the exact optomechanical coupling factor $g_{\rm om}$ for a pure radial displacement dR. Thanks to a large refractive index, GaAs disks with radius as small as 1 μm can sustain high quality factor (Q) optical WGMs in the near infrared [13–15]. According to the formula $g_{\rm om} = -\omega/R$, $g_{\rm om}$ values are expected to rise up to the THz/nm range on such disks.

Our GaAs disks are fabricated from an epitaxial wafer using e-beam lithography and wet etching [14]. The typical disk size is 5 μm in diameter and 200 nm in thickness, as seen in Fig. 1(a). Near-field experiments on a single disk are performed employing a microlooped optical fiber taper evanescent coupling technique at a wavelength of 1.55 μm [16,17], and using a balanced photodetector to remove the contribution of laser excess noise in the measurement [Fig. 1(b)]. When tuning the laser wavelength to a flank of the disk optical resonance [inset of Fig. 2(a)], the disk vibration modulates the optical transmission T of the fiber and the setup performs optical vibrational spectroscopy of the disk. At the inflection point of the flank and for a small displacement $\Delta\alpha$, we have $T(\Delta\alpha) - T(0) = (dT/d\omega)(d\omega/d\alpha)\Delta\alpha = [(3\sqrt{3})/4]\Delta T(Q/\omega)g_{\rm om}\Delta\alpha$ [18], where $\Delta T = 1 - T_{\rm on}$ is the contrast of the optical WGM resonance, $T_{\rm on}$ the on-resonance transmission, and Q the loaded optical quality factor, which is typically 10^5 in our experiments. ΔT and Q being measured quantities, the calibration of a vibrational measurement directly gives the optomechanical coupling factor $g_{\rm om}$.

Figure 2 shows vibrational optical noise spectra obtained on selected disks at room temperature and pressure. Several mechanical resonances are observed with amplitude up to 20 dB over the noise floor. A striking feature is the high frequency of these resonances, from 100 MHz to
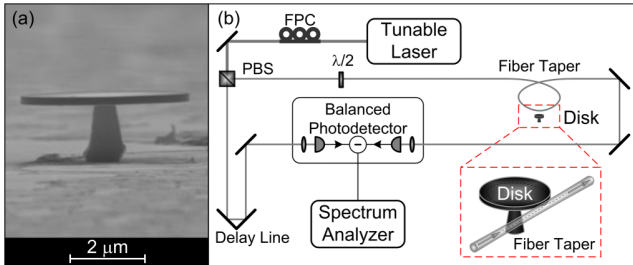
1 GHz [19]. This results from the small size of the disks, which also induces small motional masses (see also Table I). The mechanical Q factors span from a few tens to a few 10^3. Figure 2(d) shows a mechanical resonance at 858.9 MHz with $Q = 862$. This corresponds to a frequency-Q product of 0.7×10^{12}, approaching best reported values in the 10^{13} range [20] and obtained here in ambient conditions. Note that high purity crystalline GaAs mechanical oscillators should be free of mechanical losses affecting amorphous glasses at low temperature [21]. A GaAs micromechanical oscillator with Q factor above 10^5 has already been reported at low temperature [22].

Figure 2(b) displays a measurement of the disk Brownian motion at 300 K, showing a sensitivity of 2×10^{-17} m/$\sqrt{\rm Hz}$. The calibration is obtained here using equipartition of energy for the Brownian motion amplitude [18] but it can also be obtained from an independent estimation of $g_{\rm om}$, as detailed below.

The formula $g_{\rm om} = -\omega/R$ is expected to be no longer valid if the mechanical mode has a nonradial component (out-of-plane motion) or in case the effective index approach does not hold anymore. The latter occurs if the disk is too thin ($< \lambda/n$) or if it is not a perfect cylinder. With a 200 nm thickness, we expect our GaAs disk resonators to deviate from $g_{\rm om} = -\omega/R$. The general problem of how an optical resonator eigenfrequency ω depends on the deformation α of the resonator can be solved by a perturbative treatment of Maxwell's equations [23]. A convenient approach is to represent the resonator deformation by the displacement α of a chosen point of the resonator having maximum displacement amplitude. If the normalized displacement profile is known, α suffices to represent the complete resonator deformation field. With this approach $g_{\rm om}$ is expressed as the integral of

FIG. 1 (color online).   Optomechanical study of a GaAs disk. (a) Scanning electron microscope (SEM) view of a GaAs disk (4.5 μm diameter and 200 nm thickness) suspended on an AlGaAs pedestal. (b) Schematics of the near-field optomechanical spectroscopy experiment. FPC stands for fiber polarization control, PBS for polarization beam splitter.

FIG. 2 (color online).   Selected vibrational spectra of GaAs nano-optomechanical disks. (a) Optically measured motional noise spectrum of a disk of radius 5.6 μm and thickness 200 nm. (b) Calibrated displacement noise resonance of a disk of radius 4.5 μm, showing a sensitivity of 2×10^{-17} m/$\sqrt{\rm Hz}$. (c),(d) High-frequency mechanical resonances of a disk of radius 3.6 μm in the 500 MHz–1 GHz band.

an optomechanical function over the rigid resonator boundaries:

$$g_{om} = \frac{\omega}{4} \int (\mathbf{q}.\mathbf{n})[\Delta\varepsilon|\mathbf{e}_\parallel|^2 - \Delta(\varepsilon^{-1})|\mathbf{d}_\perp|^2]dA. \quad (1)$$

In this expression ω is the rigid resonator eigenfrequency, $\mathbf{q}$ is the normalized displacement profile vector such that $\max|\mathbf{q}(r)| = 1$, $\mathbf{n}$ the normal unit vector on the boundary, $\Delta\varepsilon = \varepsilon - 1$ with ε the dielectric constant of the resonator material, $\Delta(\varepsilon^{-1}) = \varepsilon^{-1} - 1$, $\mathbf{e}$ is the electric complex field vector normalized such that $\frac{1}{2}\int\varepsilon|\mathbf{e}|^2 dV = 1$, and $\mathbf{d} = \varepsilon\mathbf{e}$ [9]. Importantly Eq. (1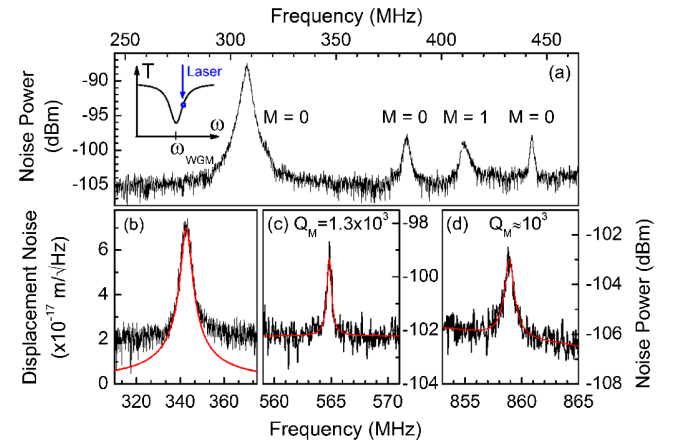) shows that g_{om} depends both on the electromagnetic and mechanical mode under consideration, which in a GaAs disk are identified as explained now.

The WGM identification is carried out performing broadband optical spectroscopy of the disk to reveal a sequence of WGM resonances of varying linewidth and wavelength spacing. This sequence is compared to that obtained from numerical simulations [24], with a generally excellent overlap that imposes a unique radial-azimuthal label (p, m) to each optical resonance [17].

The identification of mechanical modes appearing in the measurement is more involved. Indeed, their frequencies depend on the exact geometry and composition of the disk and AlGaAs pedestal, and on the possible presence of residual stress in the material after etching. Here we identify each mechanical mode by studying its dispersion line as a function of the disk size, using for that purpose disks of different size but on the same sample, hence made out of the same material and resulting from the same fabrication process. Typically, for a disk of diameter 4.5 μm, the pedestal large and small diameters are 1 and 0.6 μm [Fig. 1(a)]. The disk thickness and pedestal height are controlled during epitaxial growth. The other geometrical parameters are measured with a precision of ±50 nm in a SEM and serve as input for numerical simulations, where we treat the material as isotropic and use elastic parameters at 300 K for GaAs (Young's modulus $E = 85.9$ GPa, Poisson ratio $\sigma = 0.31$, and density 5.316 g.cm^{-3}) and for Al$_{0.8}$Ga$_{0.2}$As ($E = 83.86$ GPa, $\sigma = 0.39$, and density 4.072 g.cm^{-3}). These simulations provide us for each disk with a series of mechanical modes that can be named using radial and azimuthal numbers P and M. The displacement profile of a given mode can be factorized in the form

$q(\rho, \theta, z) = \cos(M\theta) \times f_P(\rho, z)$ as a result of the rotational symmetry of the disk.

Figure 3 shows measurements performed on disks of radius varying between 3 and 6 μm. The shadowed guides to the eyes are obtained from simulations and displayed with a thickness of ±30 MHz corresponding to the uncertainty concerning the disk geometry. Figure 3 allows identifying the prominent mechanical resonances in the spectrum as having $M = 0$ and $M = 1$ azimuthal numbers (modes A, C and D of Fig. 3 correspond to $M = 0$ and mode B to $M = 1$). This identification is further confirmed by looking at the related optomechanical coupling. As a consequence of the disk rotational symmetry, the integral of Eq. (1) contains an azimuthal prefactor of the form $\int_{\theta=0}^{2\pi}\cos(M\theta)\cos^2(m\theta)d\theta = \frac{1}{2}\delta_{M,0} + \frac{1}{4}[\delta_{M+2m,0} + \delta_{M-2m,0}]$, where m (M) is the azimuthal number of the optical (mechanical) mode under consideration. This prefactor shows that the largest optomechanical coupling g_{om} is obtained for the mechanical azimuthal number $M = 0$. This is confirmed by our measurement where dominating resonances in the spectra always correspond to $M = 0$ modes.

In case of interest $m > 1$ and $\delta_{M+2m,0} = 0$. Apart from $M = 0$, the only case of nonzero optomechanical coupling is thus expected for $M = 2m$. In WGMs investigated here, m goes from 30 to 50. Mechanical modes with $M = 2m$ are hence of very high order and practically not visible in the spectra with the current sensitivity. In contrast, we observe mechanical modes with small azimuthal numbers ($M = 1, 2...$). Even though their weight in the spectrum remains small, their presence shows that the rotational symmetry of the disk and the above selection rules are only approximate.

Once both optical and mechanical modes are singled out in the measurement, the optomechanical coupling g_{om} is computed for each optical-mechanical combination using Eq. (1). The mechanical resonance shown in Fig. 2(b) corresponds, for example, to the $M = 0$ mode labeled A in Fig. 3. The optical resonance used in Fig. 2(b) has been identified to be the WGM ($p = 3$, $m = 33$). A numerically "simulated" value $g_{om}{}^s$ of the coupling between these two modes is computed to be $g_{om}{}^s = 61$ GHz/nm. But the effective mass of the mechanical mode also leads the Brownian motion amplitude by the equipartition theorem $m_{eff}\omega^2\langle\Delta\alpha^2\rangle = k_B T$. Our measurements are performed at 300 K and the magnitude of the thermo-optic shift of the WGM resonance [25] indicates that heating induces

TABLE I. Optical-mechanical resonances of 3 GaAs disks, experimental (superscript e) and simulated (superscript s).

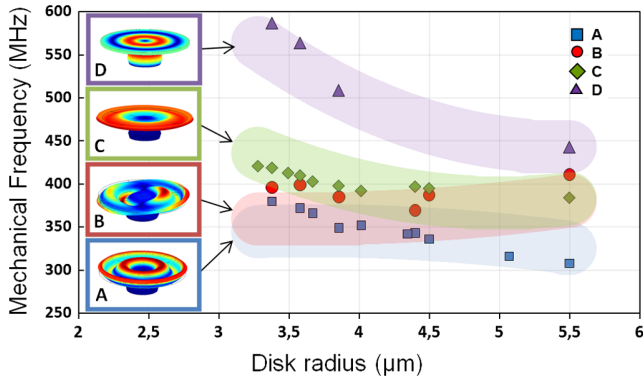| R_{disk} (μm)	λ_O (nm) (p, m)	Optical Q	$f_M{}^e$ (MHz)	$f_M{}^s$ (MHz)	$m_{eff}{}^s$ (pg)	$g_{om}{}^e$ (GHz/nm)	$g_{om}{}^s$ (GHz/nm)	Mechanical Q
4.5 ± 0.1	1551.7	1.0×10^5	343	339	21.2	71	61	66
	(3,33)		397	380	21.2	65	76	38
4.6 ± 0.1	1535.2	9.5×10^4	336	337	22.1	95	65	120
	(3,34)		395	380	20.9	60	72	66
5.6 ± 0.1	1513.9	5.9×10^4	308	326	36	132	78	73
	(3,45)		383.5	373	22.4	41	35	114

FIG. 3 (color online).   Dispersion lines of GaAs disk mechanical modes measured vs disk radius. Thickness is 200 nm. Data points were acquired on different disks of the same sample. Transparent "guide to the eyes" bands correspond to numerical simulations with an error bar represented by their thickness.

negligible modification of the thermal motion amplitude. The Brownian motion can then also be used to calibrate the measurement and extract in a second independent manner an "experimental" value g_{om}^e of the optomechanical coupling. g_{om}^e and g_{om}^s values are in reasonable agreement.

Table I contains the parameters relating to optical-mechanical resonances observed on 3 distinct disks. The effective masses are typically around 10 pg, with optomechanical coupling spanning from 30 to 150 GHz/nm. Combined with an optical Q factor in the 10^5 range, this leads to a typical displacement sensitivity of 10^{-17} m/$\sqrt{\text{Hz}}$. This is only a factor 100 above the standard quantum limit imprecision and is obtained here at room temperature and ambient pressure. This sensitivity compares favorably with other systems considering the nanoscale dimensions of the GaAs mechanical system under consideration and the high mechanical frequencies at play. Previous displacement sensitivities on MHz nano-mechanical oscillators are of 10^{-16} m/$\sqrt{\text{Hz}}$ obtained with a single electron transistor at mK temperature [26], 10^{-15} m/$\sqrt{\text{Hz}}$ using a rf stripline cavity at mK temperature [8] and 10^{-15} m/$\sqrt{\text{Hz}}$ reachable using a high finesse fiber-cavity or a silica toroid as a mechanical-optical transducer [6,7]. A sensitivity in the 10^{-17} m/$\sqrt{\text{Hz}}$ range was recently reported in optomechanical crystals [9].

This sensitivity makes semiconductor disk resonators promising candidates to study quantum limits in optomechanics. For example, a GHz mechanical mode of a GaAs disk would have a mean thermal occupation number of only 35 at 1 K. Cavity self-cooling of such disk oscillator by a factor as low as 35 would allow it to enter the quantum regime, with the peculiar advantage that it would be available on a integrable optical platform. Besides the envisioned cavity-mediated coupling [27] of this quantum

mechanical oscillator to an artificial atom (InAs quantum dot) for coherent control experiments, the GaAs-based optomechanical system presented here lends itself to the engineering of its optical and piezoelectrical properties through doping and the design of an embedded active medium. These original features should allow exploring novel architectures, at the frontier of III-V nanophotonics and optomechanics in the quantum regime.

*ivan.favero@univ-paris-diderot.fr
[1] I. Favero and K. Karrai, Nat. Photon. **3**, 201 (2009).
[2] F. Marquardt and S. Girvin, Physics **2**, 40 (2009).
[3] M. Aspelmeyer, S. Gröblacher, K. Hammerer, and N. Kiesel, J. Opt. Soc. Am. B **27**, A189 (2010).
[4] M. Li, W. H. P. Pernice, and H. X. Tang, Nature Nanotech. **4**, 377 (2009).
[5] I. Favero and K. Karrai, New J. Phys. **10**, 095006 (2008).
[6] I. Favero et al., Opt. Express **17**, 12 813 (2009).
[7] G. Anetsberger et al., Nature Phys. **5**, 909 (2009).
[8] J. D. Teufel et al., Nature Nanotech. **4**, 820 (2009).
[9] M. Eichenfield, J. Chan, R. M. Camacho, K. J. Vahala, and O. Painter, Nature (London) **462**, 78 (2009).
[10] I. Wilson-Rae, P. Zoller, and A. Imamoglu, Phys. Rev. Lett. **92**, 075507 (2004).
[11] E. Peter et al., Phys. Rev. Lett. **95**, 067401 (2005).
[12] A. Andronico et al., J. Eur. Opt. Soc. Rapid Publ. **3**, 08030 (2008).
[13] B. Gayral et al., Appl. Phys. Lett. **75**, 1908 (1999).
[14] E. Peter et al., Appl. Phys. Lett. **91**, 151103 (2007).
[15] C. P. Michael et al., Appl. Phys. Lett. **90**, 051108 (2007).
[16] L. Ding, C. Belacel, S. Ducci, G. Leo, and I. Favero, Appl. Opt. **49**, 2441 (2010).
[17] L. Ding et al., Proc. SPIE Int. Soc. Opt. Eng. **7712**, 771211 (2010).
[18] See supplementary material at http://link.aps.org/supplemental/10.1103/PhysRevLett.105.263903 for details regarding the optomechanical measurement.
[19] T. Carmon and K. J. Vahala, Phys. Rev. Lett. **98**, 123901 (2007).
[20] J. Wang, J. E. Butler, T. Feygelson, and C. T. C. Nguyen, in Proceedings of the IEEE Conference on Micro Electro Mechanical Systems (IEEE, New York, 2004), p. 641.
[21] R. O. Pohl, X. Liu, and E. Thompson, Rev. Mod. Phys. **74**, 991 (2002).
[22] I. Mahboob and H. Yamaguchi, Nature Nanotech. **3**, 275 (2008).
[23] S. G. Johnson et al., Phys. Rev. E **65**, 066611 (2002).
[24] M. Oxborrow, IEEE Trans. Microwave Theory Tech. **55**, 1209 (2007).
[25] T. Carmon, L. Yang, and K. Vahala, Opt. Express **12**, 4742 (2004).
[26] A. Naik et al., Nature (London) **443**, 193 (2006).
[27] K. Hammerer et al., Phys. Rev. Lett. **103**, 063005 (2009).

6.2.2 Gigahertz GaAs disk resonators at room temperature

Next we wished to further reduce disk dimensions beyond what was shown in the previous article in order to boost both the optomechanical coupling terms[1] and the mechanical frequencies. (High mechanical frequencies are desirable to enter the good cavity limit required to reach the quantum regime (see section 3.3) as well as for high speed sensing applications). In order to achieve GHz mechanical frequencies for the first RBM the dimensions of the GaAs disk resonators must be reduced to the extreme with a disk radius of ~ 1 μm, below the free space wavelength of the employed light ($\lambda \simeq 1.5$ μm). The size requirements are roughly twice as stringent as for silicon[2] [22]. Because of this requirement, the 1 μm radius disks shown in this work only exhibit intrinsic optical quality factors of $\sim 1 \times 10^4$, limited by radiation losses at $\lambda \simeq 1.5$ μm. (Newer designs discussed in the previous chapters use thicker 320 nm disks (giving higher n_{eff}) at a lower wavelength of $\lambda \simeq 1.3$ μm, which is why they are no longer radiation limited). Extremely small WGM disk resonators come with additional specific challenges. For instance because of the poor thermal anchoring provided by their small pedestal and the residual optical absorption (see section 5.3) these resonators are very sensitive to thermal effects. At high laser powers it is actually possible to irreversibly damage the disk by heating it up to temperatures above 700 K. Furthermore these reduced sized disks only support the p=1 family of WGMs (the higher orders are suppressed by the presence of the pedestal and bending losses) with a Free Spectral Range (FSR) of approximately 140 nm. The resonators therefore need to be fabricated to precise dimensions in order for the unique WGM resonance to fall within the $\sim$100 nm range of our tunable laser.

The miniaturization of the GaAs disk resonators boosted the g_{om} to around 500 GHz/nm and the g_0 to near 1 MHz. These results are summarized in the following article named 'Wavelength-sized GaAs optomechanical resonators with gigahertz frequency', which underscores the potential of GaAs disks as a platform to study optomechanics. (Note that since this earlier work, a better control of the pedestal geometries (see section 4.1.10) has allowed for boosting the mechanical quality factor Q_M close to tenfold in air, and even beyond that in vacuum and low temperature, reaching $Q \times f \simeq 10^{13}$).

---

[1]Since both g_{om} and x_{ZPF} are increased with reduced disk dimensions, this results in an increased $g_0 = g_{om}\, x_{\mathrm{ZPF}}$. (See chapter 3).

[2]Indeed the frequency of the first RBM scales with $\sqrt{\frac{E}{\rho}}$ (see section 2.3.2) and GaAs has roughly half the Young's modulus but twice the density of silicon (see appendix D).

Wavelength-sized GaAs optomechanical resonators with gigahertz frequency

L. Ding,[1,a] C. Baker,[1] P. Senellart,[2] A. Lemaitre,[2] S. Ducci,[1] G. Leo,[1] and I. Favero[1,b]

[1]*Laboratoire Matériaux et Phénomènes Quantiques, CNRS, UMR 7162, Université Paris Diderot, 10 rue Alice Domon et Léonie Duquet, 75013 Paris, France*
[2]*Laboratoire de Photonique et Nanostructures, CNRS, Route de Nozay, 91460 Marcoussis, France*

We report on wavelength-sized GaAs optomechanical disk resonators showing ultrastrong optomechanical interaction. We observe optical transduction of a disk mechanical breathing mode with 1.4 GHz frequency and effective mass of ~ 2 pg. The measured vacuum optomechanical coupling rate reaches $g_0 = 0.8$ MHz, with a related differential optomechanical coupling factor $g_{om} = 485$ GHz/nm. The disk Brownian motion is optically resolved with a sensitivity of 10^{-17} m/$\sqrt{Hz}$ at room temperature and pressure. © *2011 American Institute of Physics.* [doi:10.1063/1.3563711]

Optomechanical systems[1–3] combining a mechanical oscillator and an optical cavity find applications in very different fields of physics, from mesoscopic quantum physics to cold atoms[4,5] and mechanical sensing.[6] Gigahertz (GHz) mechanical oscillators can help accessing the quantum regime of optomechanics, can allow developing ultrafast sensing systems, or can match hyperfine transitions of (artificial) atoms interfaced with the mechanical system. The difficulty lies generally in coupling such GHz oscillators to photons efficiently, in order to offer optical control over the oscillator motion, together with fine optical read-out sensitivity.[7] A useful way to quantify the optomechanical coupling is to use the differential "frequency pull" parameter g_{om} defined as $g_{om} = d\omega_o/d\alpha$ expressing how the deformation of the optical resonator α modifies its optical resonance eigenfrequency ω_o. In a quantum description of the optomechanical interaction at the single photon level, another relevant parameter is the vacuum optomechanical coupling g_0 given by $g_{om}x_{ZPF}$, where $x_{ZPF} = \sqrt{\hbar/2m_{eff}\omega_m}$ is the zero-point motion of the mechanical oscillator, m_{eff} its effective motional mass and ω_m its resonance angular frequency. Large optomechanical coupling, approaching $g_{om} = \omega_o/\lambda$ with λ the wavelength of photons, was recently obtained in photonic-crystal based structures.[7–9] In this work, we scale the size of GaAs optomechanical disk resonators[10] down to λ and show that we can this way naturally couple an (over) GHz mechanical oscillator to an optical cavity of high quality factor Q and subwavelength mode volume. Thanks to the strong confinement of the optical and mechanical modes in a nanoscale disk, we approach $g_{om} = \omega_o/\lambda$ and obtain a vacuum coupling rate $g_0 = 0.8$ MHz.

Our wavelength-sized GaAs disks stand on Christmas treelike $Al_{0.8}Ga_{0.2}As$ pedestals[11] and are fabricated from an epitaxial wafer using e-beam lithography and two-steps wet etching.[12] The typical disk has a radius R=1 μm and a thickness of 200 nm, as seen in Fig. 1(a). For such a disk, two-dimensional axis-symmetry finite-element-method (FEM) simulations[13] predict in the 1500–1600 nm range one unique optical whispering gallery mode (WGM) resonance at

a wavelength of $\lambda_0 \approx 1550$ nm. The corresponding WGM is a TE (p=1, m=7) mode, where p and m are radial and azimuthal numbers, respectively.[14] The electric field intensity is localized at the periphery of the disk [Fig. 1(b)]. The free spectral range between two consecutive m numbers of this WGM is $\lambda_0^2/(2\pi n_{eff}R) \approx 140$ nm, taking R=1 μm and $n_{eff} = 2.6$ for the effective index of the 200 nm GaAs slab TE mode. The mechanical mode of the disk is simulated by three-dimensional (3D) FEM simulation. Based on our previous work,[10] we know that axis-symmetry breathing modes with azimuthal number M=0 couple maximally to WGMs photons. For the present disk, a breathing mode with M=0 is expected at a frequency around 1.5 GHz. Its 3D deformation profile is shown in Fig. 1(c).

Figure 1(d) is a schematics of near-field optomechanical experiments on a single disk,[15] where light from a mode-hope free tunable external-cavity diode laser (λ
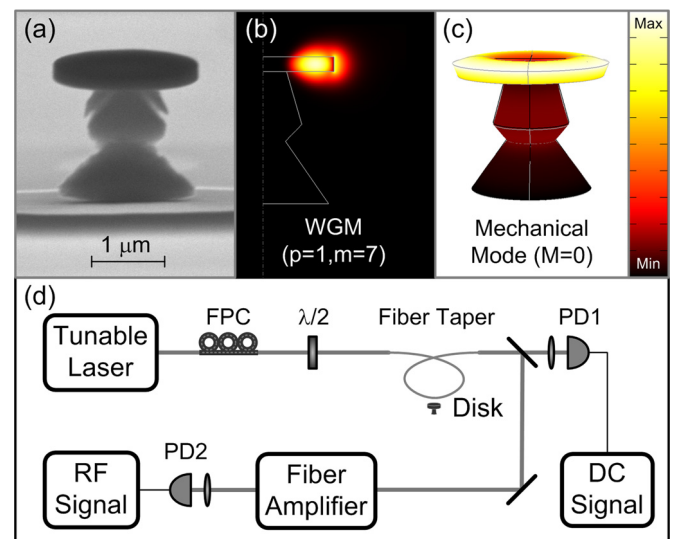
FIG. 1. (Color online) (a) SEM view of a GaAs disk (1 μm diameter and 200 nm thickness) suspended on an AlGaAs pedestal. (b) Electric field intensity $|\mathbf{E}(\mathbf{r})|^2$ of the optical mode (p=1, m=7). (c) Deformation profile of the M=0 mechanical breathing mode. (d) Schematics of the near-field optomechanical spectroscopy experiment. The linear polarization is selected by a fiber polarization controller (FPC) and a half-wave plate. PD stands for photodetector.

a)Electronic mail: lu.ding@univ-paris-diderot.fr.
b)Electronic mail: ivan.favero@univ-paris-diderot.fr.
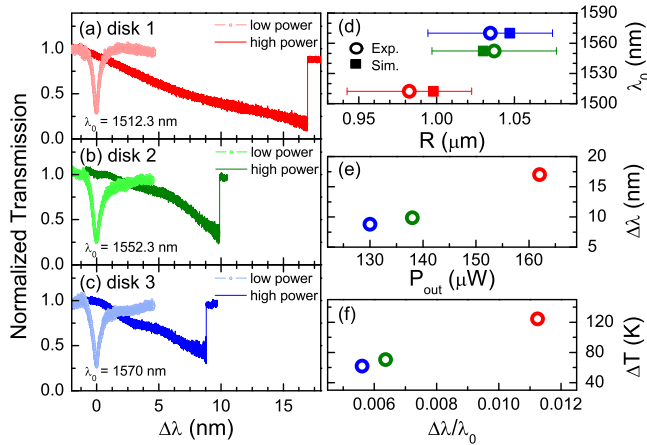
FIG. 2. (Color online) [(a)–(c)] Normalized optical transmission spectrum of optical resonance (p=1, m=7) measured at low and high optical power in three disks. (d) The WGM wavelength as a function of the disk radius. (e) Relative optical resonance shift $\Delta\lambda$ as a function of the total transmitted optical power. (f) The temperature change as a function of normalized resonance shift $\Delta\lambda/\lambda_o$ due to thermal-optic effect.

FIG. 3. (Color online) [(a)–(c)] The rf-spectrum of the M=0 breathing mechanical mode from each disk taken in ambient conditions. (d) A calibrated Brownian motion spectrum of disk 1.

=1500–1600 nm, linewidth ∼150 KHz) is evanescently coupled into the disk using a looped fiber-taper method.[15,16] All experiments and simulations are carried out at a room temperature and pressure.

The optical spectra of three GaAs disks are shown in Figs. 2(a)–2(c), at low and high optical power. They are recorded from a weak dc component of the fiber output. At low power, the symmetric optical resonance indicates linear behavior of the disk optical mode. The intrinsic optical Q reaches 1×10^4, mainly limited at this wavelength by radiation losses. In our experiments, we measure the optical resonance wavelength with an error inferior to 50 pm. Figure 2(d) shows the WGM measured wavelength λ_o as a function of the disk radius, the latter being measured in a scanning electron microscope (SEM) with an accuracy of ±50 nm. Relying on an epitaxially controlled thickness of 200 nm, the measured wavelength relates through numerical simulations to a given disk radius (solid squares), which agrees well with the measured radius (circles with error bar). In our study, the WGM has weaker dependence on the pedestal geometry.

At high optical power, we observe an important thermo-optic distortion of the optical resonance.[15,17,18] The strong confinement of optical energy in the disk combines with residual absorption and a poor thermal anchoring to produce significant heating. Figure 2(e) shows the relative optical resonance shift $\Delta\lambda$ as a function of the power transmitted by the fiber. Red, green, and blue circles represent disk 1, 2, and 3, respectively. Considering a linear thermo-optic effect n(T)=n(300 K)+(dn/dT)$\times\Delta$T and the approximate relation $2\pi Rn_{eff}=m\lambda_0$, the temperature increase corresponding to a shift of the resonance wavelength $\Delta\lambda$ [Fig. 2(f)] is ΔT
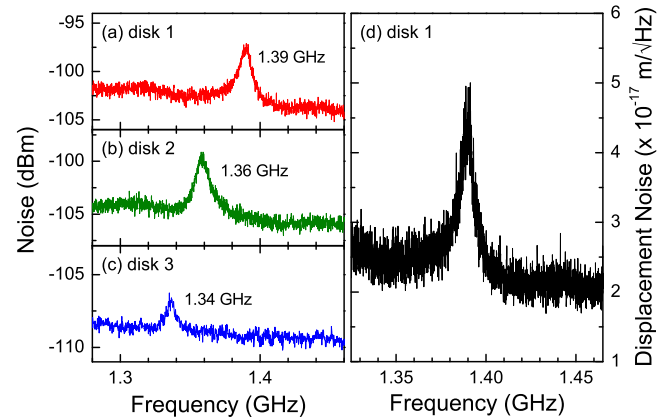
$=n_{eff}/(dn/dT)\times(\Delta\lambda/\lambda_0)$, where $dn/dT=2.35\times10^{-4}$ K^{-1} in GaAs at room temperature.[19] In extreme cases, the resonance shift reaches 100 nm corresponding to a temperature increase ΔT>700 K at which the disk is irreversibly damaged after desorption of As atoms from the GaAs surface.[20] Note that heating can also induce optical resonance shift by means of direct thermal expansion of the disk gallery, in proportion of $\alpha_L=6.05\times10^{-6}$ K^{-1}, the room temperature thermal expansion coefficient.[21] The associated shift, $\Delta\lambda=\lambda_0\alpha_L\Delta$T, is however two orders of magnitude smaller than the thermo-optical contribution. It is hence negligible and the optical resonance shift observed in our experiments is safely attributed to thermo-optical effects. In Fig. 2(e), the approximate linear scaling of the temperature increase with optical power is consistent with the fact that the three measured disks have similar geometry. However the exact optical absorption and thermal dissipation mechanisms remain to be investigated and possibly optimized in future experiments.

When the laser wavelength is tuned to a flank of the WGM resonance, the disk mechanical motion modulates the transmitted optical power, whose rf noise spectrum becomes a vibrational spectrum of the disk. Because the disk mechanical mode of interest resonates over 1 GHz, we use a high-speed PIN photodetector with 2 GHz bandwidth. We replace electronic amplification of the detector, which would limit its bandwidth, by optical amplification of the signal at the fiber output, using an erbium-doped fiber amplifier [see Fig. 1(d)]. The output of the photodetector is then analyzed by a spectrum analyzer. Figures 3(a)–3(c) show the obtained rf-spectrum of each disk. The mechanical frequency of the breathing mode is found at 1.4 GHz. Using the disk radius inferred from the optical resonance and pedestal geometry observed in the SEM, we simulate numerically the mechanical mode for each disk and obtain a correct agreement with

TABLE I. Experimental (superscript e) and simulated (superscript s) mechanical and optomechanical parameters of three miniature GaAs disks.

R_{disk} (μm)	f_M^e (GHz)	f_M^s (GHz)	m_{eff}^s (pg)	g_{om}^e (GHz/nm)	g_{om}^s (GHz/nm)	g_0^e (MHz)	g_0^s (MHz)
0.98 ± 0.05	1.39	1.39 ± 0.05	2.2	485	693	0.8	1.14
1.04 ± 0.05	1.36	1.37 ± 0.05	1.4	277	396	0.58	0.84
1.03 ± 0.05	1.34	1.34 ± 0.05	2.4	429	613	0.7	1.0

experimental frequencies. We estimate that the irregular shape of the pedestal leads to an error of ± 50 MHz in the simulated value. At high optical power, the optically induced heating barely modifies the material's elasticity so that the associated mechanical frequency shift, about 1%, is negligible.

The optomechanical coupling between the identified optical and mechanical modes is computed numerically using a perturbative treatment of Maxwell's equations,[10,22] yielding a simulated optomechanical coupling of $g_{om}^s = 690$ GHz/nm for disk 1, with a related vacuum coupling of $g_0^s = 1.1$ MHz (see Table I for values on the three disks). Note that the deformation/α is parameterized here by choosing a point of maximal displacement at the periphery of the disk. The optomechanical coupling can also be measured independently by calibrating the optical measurement knowing that the Brownian motion of the disk is transduced optically in proportion of g_{om}.[7,10] For disk 1, this second method yields an experimental optomechanical coupling of $g_0^e = 0.8$ MHz ($g_{om}^e = 485$ GHz/nm), a factor 1.4 times smaller than the simulated value. Similar discrepancies were observed in photonic crystals structures[7–9] and probably stem from an imperfect control in the geometry of the nanofabricated resonator. The associated irregularity is difficult to capture in numerical simulations. Table I lists mechanical and optomechanical parameters of the three studied disks. The calibrated Brownian motion of disk 1 is plotted in Fig. 3(d), showing a sensitivity of a few 10^{-17} m/$\sqrt{\text{Hz}}$, which is only a factor 100 above the Standard Quantum Limit imprecision.[23] The second disk in the table possesses a larger pedestal than the disk seen in Fig. 1(a). This results in a slightly less confined optical WGM and a reduced effective motional mass. The optomechanical coupling is consequently reduced with respect to the two other disks.

In summary, wavelength-sized GaAs optomechanical disk resonators with mechanical frequency over the GHz are observed. The vacuum optomechanical coupling g_o is measured to rise up to the MHz with associated g_{om} of 500 GHz/nm. This strong optomechanical interaction makes GaAs disks an interesting platform to study quantum-optomechanics phenomena at the single photon level,[24] especially since solid state single photons emitters in form of InAs quantum dots[25] are already being inserted in such disks in quantum electrodynamics experiments.[26,27]

[1] I. Favero and K. Karrai, Nat. Photonics **3**, 201 (2009).
[2] F. Marquardt and S. Girvin, Phys. **2**, 40 (2009).
[3] M. Aspelmeyer, S. Gröblacher, K. Hammerer, and N. Kiesel, J. Opt. Soc. Am. B **27**, A189 (2010).
[4] K. W. Murch, K. L. Moore, S. Gupta, and D. M. Stamper-Kurn, Nat. Phys. **4**, 561 (2008).
[5] F. Brennecke, S. Ritter, T. Donner, and T. Esslinger, Science **322**, 235 (2008).
[6] M. Li, W. H. P. Pernice, and H. X. Tang, Nat. Nanotechnol. **4**, 377 (2009).
[7] M. Eichenfield, R. Camacho, J. Chan, K. J. Vahala, and O. Painter, Nature (London) **459**, 550 (2009).
[8] Y. G. Roh, T. Tanabe, A. Shinya, H. Taniyama, E. Kuramochi, S. Matsuo, T. Sato, and M. Notomi, Phys. Rev. B **81**, 121101 (2010).
[9] A. H. Safavi-Naeini, T. P. Mayer Alegre, M. Winger, and O. Painter, Appl. Phys. Lett. **97**, 181106 (2010).
[10] L. Ding, C. Baker, P. Senellart, A. Lemaitre, S. Ducci, G. Leo, and I. Favero, Phys. Rev. Lett. **105**, 263903 (2010).
[11] The precise shape of the pedestal depends on steering of the sample in the selective etchant solution.
[12] E. Peter, A. Dousse, P. Voisin, A. Lemaitre, D. Martrou, A. Cavanna, J. Bloch, and P. Senellart, Appl. Phys. Lett. **91**, 151103 (2007).
[13] M. Oxborrow, Proc. SPIE **6452**, 64520J (2007).
[14] A. Andronico, X. Caillet, I. Favero, S. Ducci, V. Berger, and G. Leo, J. Eur. Opt. Soc. Rapid Publ. **3**, 08030 (2008).
[15] L. Ding, P. Senellart, A. Lemaitre, S. Ducci, G. Leo, and I. Favero, Proc. SPIE **7712**, 771211 (2010).
[16] L. Ding, C. Belacel, S. Ducci, G. Leo, and I. Favero, Appl. Opt. **49**, 2441 (2010).
[17] M. Vogel, C. Mooser, R. J. Warburton, and K. Karrai, Appl. Phys. Lett. **83**, 1337 (2003).
[18] T. Carmon, L. Yang, and K. J. Vahala, Opt. Express **12**, 4742 (2004).
[19] F. G. Della Corte, G. Cocorullo, M. Iodice, and I. Rendina, Appl. Phys. Lett. **77**, 1614 (2000).
[20] J. R. Arthur, Surf. Sci. **43**, 449 (1974).
[21] *Properties of Gallium Arsenide*, 2nd ed., Dataview Series (INSPEC, London, U.K., 1990), p. 18.
[22] S. G. Johnson, M. Ibanescu, M. A. Skorobogatiy, O. Weisberg, J. D. Joannopoulos, and Y. Fink, Phys. Rev. E **65**, 066611 (2002).
[23] J. D. Teufel, T. Donner, M. A. Castellanos-Beltran, J. W. Harlow, and K. W. Lehnert, Nat. Nanotechnol. **4**, 820 (2009).
[24] U. Akram, N. Kiesel, M. Aspelmeyer, and G. J. Milburn, New J. Phys. **12**, 083030 (2010).
[25] P. Michler, A. Kiraz, C. Becher, W. V. Schoenfeld, P. M. Petroff, L. Zhang, E. Hu, and A. Imamoglu, Science **290**, 2282 (2000).
[26] B. Gayral, J. M. Gerard, A. Lemaitre, C. Dupuis, L. Manin, and J. L. Pelouard, Appl. Phys. Lett. **75**, 1908 (1999).
[27] A. Kiraz, P. Michler, C. Becher, B. Gayral, A. Imamoglu, L. D. Zhang, E. Hu, W. V. Schoenfeld, and P. M. Petroff, Appl. Phys. Lett. **78**, 3932 (2001).

6.2.3   Dynamical back-action in GHz GaAs disks in air at room temperature

As known in optomechanics, the optical field confined in the disk resonator can modify a mechanical mode's effective loss rate (see section 3.2.1). Figure 6.1 (a) illustrates this phenomenon on the first RBM of an on-chip $\varnothing=2$ μm disk, with the laser tuned to the blue flank of a p=1 m=10 WGM. Increasing the power dropped in the resonator noticeably reduces the mechanical mode's FWHM. Meanwhile the mechanical mode's resonance frequency decreases by just a few MHz, mainly due to laser heating and GaAs' lower Young's modulus at higher temperature [171, 172]. A mechanical mode's intrinsic quality factor (unperturbed by the probing optical field) is inferred by taking the mode's FWHM in the limit of zero optical power (i.e. the y intercept of the red linear fit in Fig. 6.1 (a)). Figure 6.1 (b) shows the smallest mechanical linewidth attainable on the same small GaAs disk resonator. Further increasing the dropped power simply shifts the mechanical resonance towards lower frequencies because of increased heating, but does not further diminish the linewidth (the behavior is comparable at cryogenic temperatures). The ultimate limit to the mechanical linewidth needs to be further investigated. Indeed on larger ($\varnothing \simeq 10$ μm) disks the ultimate linewidth in the self-oscillation regime is significantly smaller, with effective Q_M close to one million. This difference is perhaps due to the larger contribution of TPA in small resonators, as TPA limits the optical Q at high power. Furthermore the free carriers generated by this TPA process may also be responsible for increased mechanical dissipation [11]. In summary we indeed observe dynamical back-action amplification on GHz GaAs disks, but the behavior is non standard in optomechanics with an apparent saturation.

6.2.4   On-chip GaAs disk optomechanics in vacuum and low temperature

Measuring samples in the cryostat (see Fig. 6.2) is significantly less convenient than using the simple characterization bench setup shown of Fig. 5.1. As we will see in the following, cryostat operation comes with a number of specific challenges which could only be partially resolved during this thesis work. However these difficulties should all be remedied in the future thanks to a new cryostat design discussed in section 6.2.8.
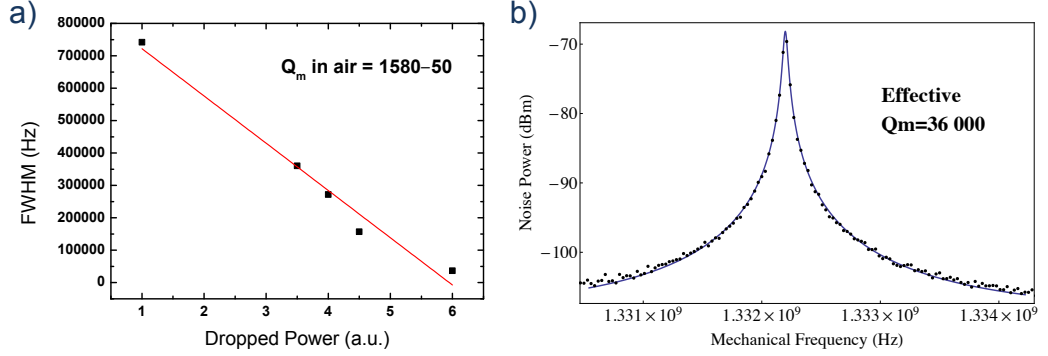
Figure 6.1: (a) Mechanical RBM FWHM as a function of dropped optical power. Red line is a linear fit through the data points. The y intercept is approximately 870 kHz, yielding an intrinsic Q_M in air of $\sim$1580. (b) At large laser powers tuning the laser to the blue side of a WGM resonance diminishes the effective mechanical damping, here boosting the mechanical Q close to 25 times to an effective Q_m of $\sim$36000.

6.2.5 Experimental setup

The experimental setup used to measure on-chip samples in the cryostat is represented in Fig. 6.3. Laser light is generated by a tunable external-cavity diode laser source (Yenista Tunics, symbol TL). The correct polarization to couple to TE WGMs is chosen with a fiber polarization controller (symbol FPC). A large beam fiber collimator (C1) then produces a large $\varnothing \simeq 7$ mm free space beam designed to use the full numerical aperture (NA) of our near-infrared long working distance microscope objective (Nachet NIR 20X 0.35 NA, Symbol μO). Beam Alignment is obtained through mirrors (M) and 3 axis positioning stages (XYZ). Light is coupled into a waveguide by focusing the laser light through the first cryostat window and onto the waveguide's cleaved input facet. The sample chip is fastened vertically on the cryostat's cold finger (see Fig. C.4 for more details). Switching from one waveguide to another is done by moving the entire cryostat vertically using the translation stages on the cryostat support structure (not represented here). Light exiting the GaAs chip is collected by an aspheric lens (AL) and focused upon an adjustable focus aspheric lens (C2). This lens injects the light into a single mode fiber. Next the collected light is amplified with an optical amplifier (OA), which depending on the laser wavelength is either an erbium doped fiber amplifier (for a wavelength λ around 1.55 μm) or a solid state booster optical amplifier (Thorlabs BOA 1132s) (for λ around 1.3 μm). The amplified optical signal is then sent on a 5 GHz bandwidth InGaAs biased photodetec-
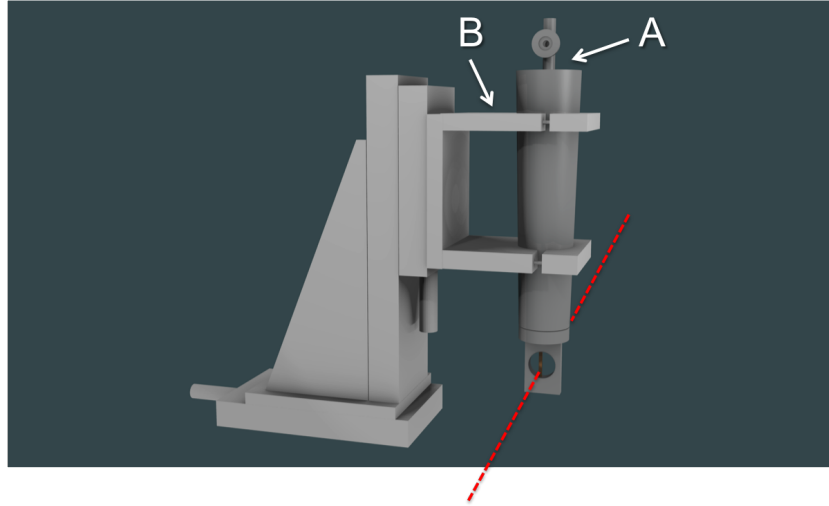
Figure 6.2: Illustration of the cryostat used in this work (Janis ST-300), with its support structure. The rough position of the optical axis is represented by the dashed red line. Letters A and B are discussed in section C.0.2.
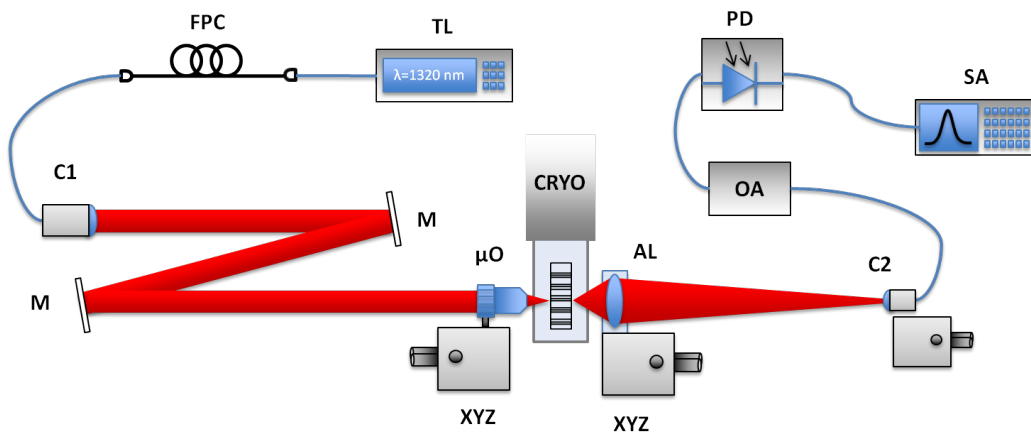
Figure 6.3: In cryostat experimental setup

tor (SIR 5 Thorlabs). The photo-current's power spectral density[3] is finally observed on a spectrum analyzer (Rhode & Schwartz FSP).

The specifics of the laser light in- and out-coupling with the chip in the cryostat, as well discussions pertaining to the thermal and mechanical stability of this coupling are presented in appendix C.0.1 and C.0.2 respectively.

6.2.6 Measurements in vacuum in the cryostat

A vacuum system composed of a scroll pump and turbo pump can pump the cryostat down to a vacuum of $\sim 10^{-6}$ mbar. Moreover, once the cryostat is cooled with liquid helium, the low temperatures cause gas molecules to condense on the cooled elements (cryopumping). Through this mechanism the pressure drops to $\sim 10^{-7}$ mbar without further need for the pumping system which can be switched off.

The contribution of air damping on the mechanical motion (see section 2.5.3) is removed at low pressures. Mechanical quality factors for the first RBM of $\varnothing = 2\mu$m GaAs resonators with a pedestal radius of 85 ± 10 nm ($>90\%$ undercut ratio) which were limited to approximately 1600 in air therefore rise in vacuum. However the mechanical Q boost is smaller than expected at room temperature, with mechanical Qs comprised between 2000 and 3000. Only at cryogenic temperatures does the Q rise to values ranging from 5000 to 7000, in excellent agreement with the FEM simulations of clamping losses discussed in section 2.5.2. In the best case, these values correspond to a quite high frequency times quality factor product $Q_M \times f = 1 \cdot 10^{13}$ Hz. This temperature dependence of Q_M seems to point towards the role of surface losses (see section 2.5.5), which are frozen out at low temperature[4]. In the future the fabrication of slightly larger test disk resonators with extremely large undercut ratios should allow to precisely determine the relative contributions of clamping losses, surface and/or bulk dissipation and thermoelastic damping to the total dissipation, thus providing a complete picture of mechanical dissipation in GaAs disks.

---

[3]The power spectral density $S_{xx}(\omega)$ of a time dependent signal x(t) is defined as the limit as the integration time T tends to infinity of the expected value E of the square modulus of the signal's Fourier transform, i.e.

$$S_{xx}(\omega) = \lim_{T \to \infty} \mathbf{E}\left[\left| \frac{1}{\sqrt{T}} \int_0^\infty x(t) e^{-i\omega t} \mathrm{dt} \right|^2 \right]$$

[4]The temperature dependent thermo-elastic damping (see section 2.5.4) should have a trivial contribution to the total Q_M at the current levels of quality factor.
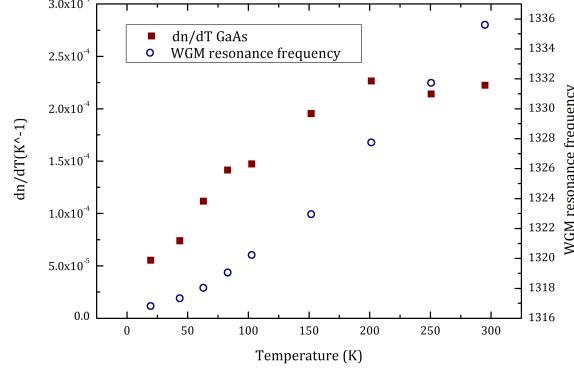
Figure 6.4: Thermo-optic coefficient (dn/dT) of GaAs as a function of temperature (red squares), obtained by following a WGM's resonance wavelength shift as a function of temperature (blue circles).

6.2.7 First measurements at cryogenic temperatures

We initially had some difficulties thermalizing our sample chip at temperatures below 20 Kelvin. After some work on the cryostat and the fabrication of a homemade radiation shield, the sample temperature can be brought down to roughly 8 K. These developments are discussed in detail in appendix C.0.3. Photographs of our current cryostat setup are provided in Fig. C.4 in the appendix. The employed laser powers produce a negligible effect on the sample's bath temperature. Indeed we experimentally verify that a 10 mW beam focused on- and absorbed by our gold sample holder only raises its temperature by only 0.02 K. Residual absorption in the disk resonator causes larger temperature increases. These are estimated by fitting changes in the mechanical mode's resonance frequency with a temperature dependent Young's modulus model [171, 172]. This method provides more accurate results than using the thermo-optic shift, which is significantly smaller at cryogenic temperatures as shown in Fig. 6.4.

In Figure 6.5, we investigate the influence of the laser power coupled in the waveguide on the GaAs disk's mechanical and optical properties and identify some interesting effects. The sample's environment is kept at 8 K throughout all these measurements. Fig. 6.5 (a) illustrates how the RBM resonance frequency decreases with increasing optical power. This frequency shift is well explained by the previously mentioned temperature dependent Young's modulus model and serves to accurately estimate the mechanical resonator's actual temperature.

Fig. 6.5 (b) shows the dependence of the GaAs disk RBM effective me-

177

Figure 6.5: This figure shows the dependency of the RBM mechanical resonance frequency (a), the effective mechanical quality factor (b) and the WGM resonance contrast and derived normalized loss rate (c) with the optical power in the coupling waveguide. Measurements are done on a 1 μm radius GaAs disk at 8 K.

chanical quality factor with the optical power. At low laser power the mechanical Q is close to 6000. With increasing laser power the disk heats up due to optical absorption and the effective mechanical Q initially decreases, reflecting the mechanical Q's temperature dependence previously discussed in section 6.2.6. Then with further laser power increase (here above 70 μW coupled in the waveguide) the effective mechanical Q starts rising, due to the effect of dynamical back-action (the laser is tuned to the blue flank of the WGM in these measurements).

Fig. 6.5 (c) plots the contrast[5] of the under-coupled p=1 m=10 WGM as a function of optical power in the waveguide (red squares). We can see the WGM contrast noticeably decreases with increasing laser power, from 0.85 to just above 0.55. We explain these changes with Eq. 1.25 from chapter 1, which relates the WGM contrast to both the intrinsic and extrinsic loss rates γ_{int} and γ_{ext}. Since these measurements are all taken on a same disk and the coupling conditions to the waveguide do not change, γ_{ext} can be considered essentially unchanged. This means the intrinsic loss rate γ_{int} increases with rising laser power, rendering the WGM more and more under-coupled. Using Eq. 1.25 we plot the normalized intrinsic loss rate, normalized such that it equals 1 at low laser power (blue circles). The loss rate is multiplied by a factor of $\sim$2.2 at the highest optical power. This is in good agreement with the estimated effect of TPA, discussed in section 5.3.2. This phenomenon is also seen to a lesser extent on large stand-alone GaAs disks probed by pulled fiber taper. Furthermore we observe how the rising intrinsic loss rate decreases the contrast of under-coupled WGMs, while simultaneously increasing the contrast of over-coupled WGMs of the same disk, in agreement with coupled mode theory.

Figure 6.6 investigates the dependency of the same three mechanical and optical parameters, this time with the cryostat temperature. (All measurements are performed in a vacuum $\leq 10^{-6}$ mbar). Fig. 6.6 (a) illustrates the temperature dependency of the GaAs disk RBM resonance frequency. Fig. 6.6 (b) shows how the RBM mechanical quality factor is roughly three times higher at 8 K than at room temperature. Next, Fig. 6.6 (c) investigates how the WGM contrast and loss rate are modified by the sample temperature. While the effect is not as strong as in Fig. 6.5 (c), there nonetheless appears to be a noticeable ($\sim$60%) gain in optical Q when going from 40 K to 8 K.

Finally in Fig. 6.7 we show a low power measurement of the Brownian motion of the RBM of a GaAs disk resonator at 8 K. At the level of optical power employed, the heating of the disk due to residual optical absorption is

---

[5]A contrast of 0 means there is no optical transmission dip at resonance, while a contrast of 1 corresponds to critical coupling, (see section 1.3.1).
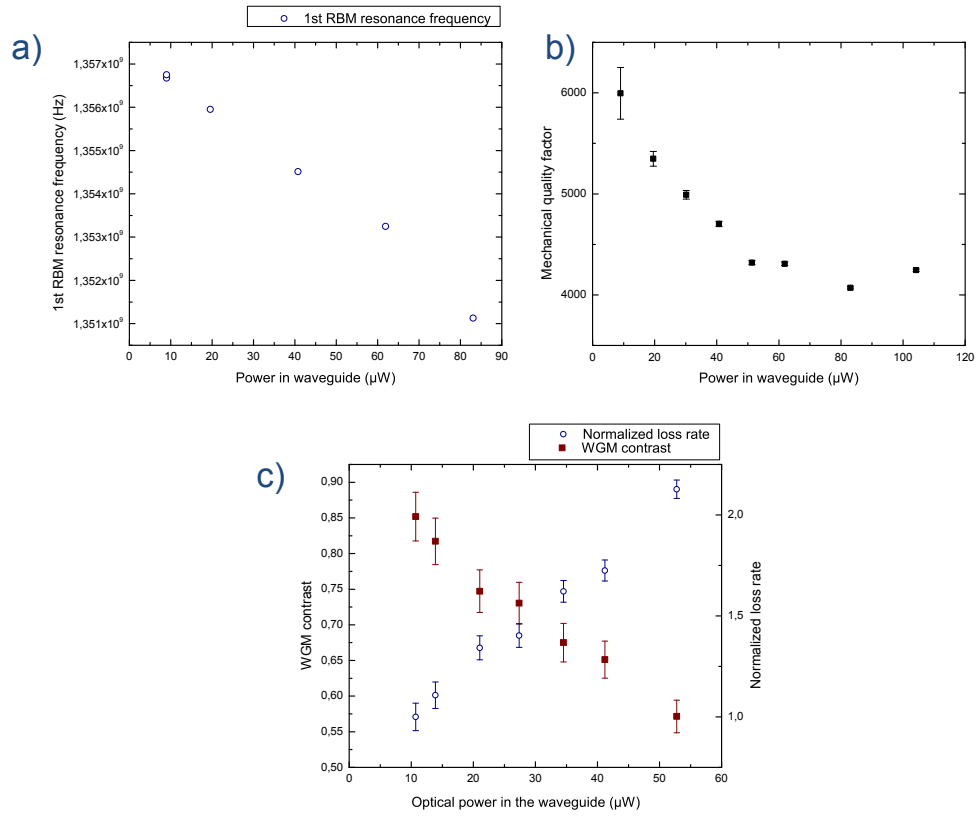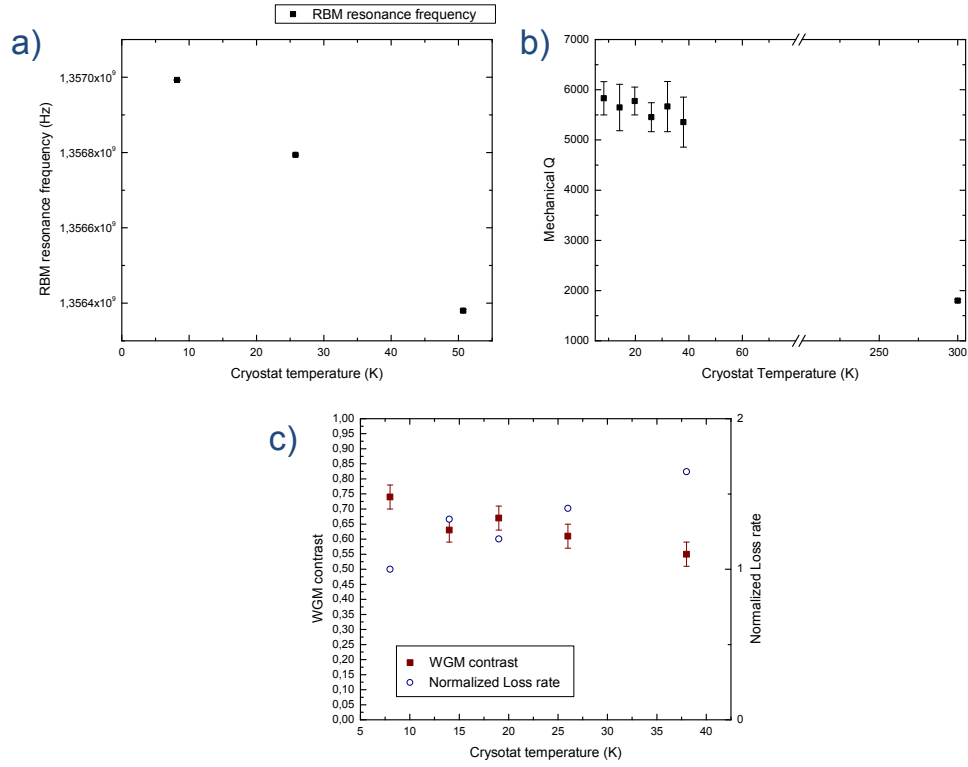
Figure 6.6: This figure shows the dependency of the RBM mechanical resonance frequency (a), the effective mechanical quality factor (b) and the WGM resonance contrast and derived normalized loss rate (c) with the cryostat temperature. Measurements are done on the same 1 μm radius GaAs disk as in Fig. 6.5.
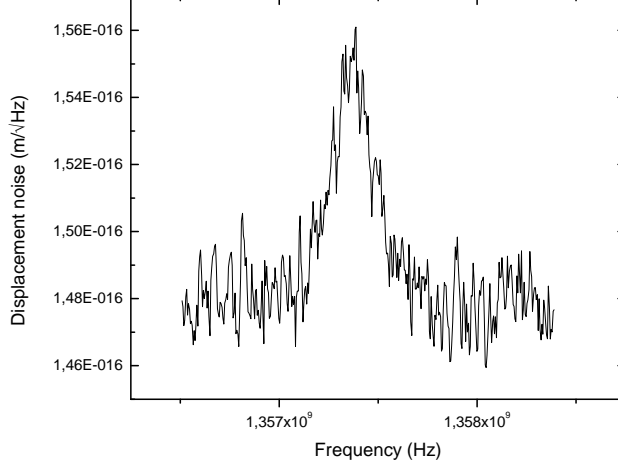
Figure 6.7: Calibrated noise spectrum

of the order of 5 K. This therefore corresponds to the detection of the Brownian motion of a mechanical mode cryogenically cooled down to roughly 13 K with a phonon occupancy on the order of 200. The calibrated displacement noise reveals a displacement sensitivity of the order of 10^{-16} m/$\sqrt{\text{Hz}}$. This value is less good than what we observed on our previous experiments in air at room temperature (see sections 6.2.1 and 6.2.2) and is roughly a factor 50 above the standard quantum limit imprecision. We ascribe the lower sensitivity of these first measurements in the cryostat to the ∼10 dB noise figure of our solid state optical booster[6], combined with the notable optical losses in our current setup (see section C.0.1).

6.2.8 Future developments

Even though it has already allowed us to learn a lot, the current cryostat setup is not perfectly optimized yet for the extremely stringent experimental requirements needed to detect mechanical occupancies at the level of a single phonon. While this first cryostat already allows important advances in the low temperature optomechanics, the team will soon acquire a new cryostat, designed from the start with thermal and mechanical stability in mind. It will provide access for high efficiency light in- and out coupling with micro-lensed fibers and will reach lower temperatures close to 4 K with dry cryogenics. Since both the GaAs chip and the coupling fibers will be mounted together

---

[6]This means the noise floor is 10 dB higher than with an ideal amplifier.

inside a single enclosure it will be dramatically less sensitive to mechanical vibrations and thermal drift. Furthermore the combination of reduced optical losses in the entire optical chain, the replacement of the noisy optical booster with an ultra-low noise narrow bandwidth electrical amplifier centered around the mechanical frequency and boosted RBM mechanical quality factors through pedestal engineering[7] should provide substantial gains in detection sensitivity.

---

[7]The team is currently developing a design in which a phonon shield incorporated in the disk's pedestal considerably raises the RBM's mechanical quality factor.
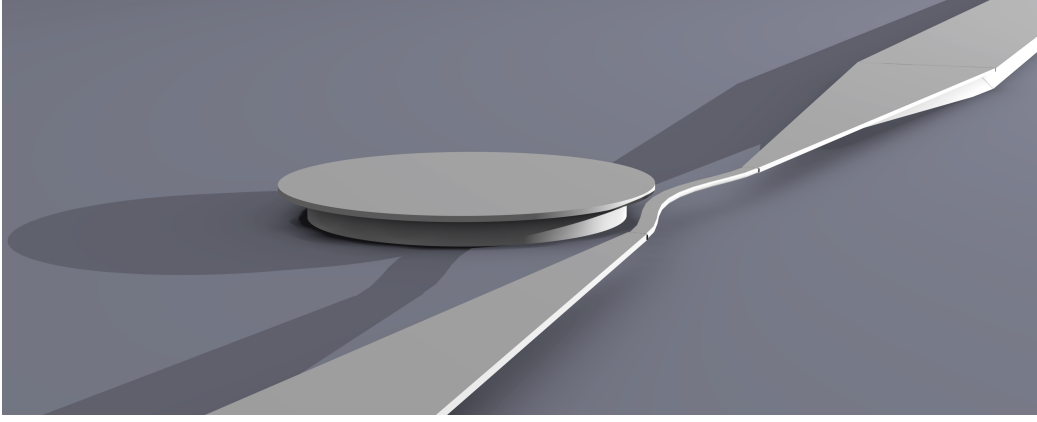
Figure 6.8: Oscillations in the suspended SiN coupling waveguide, responsible for both reactive and dispersive optomechanical coupling.

6.3   SiN optomechanics on the chip

Here we report some results on optomechanical coupling in integrated SiN resonators. Less time was available to pursue this subject as the thesis mainly focused on GaAs disk resonators. The studied system consists of a nanomechanical SiN beam resonator -which also serves as an optical coupling waveguide- placed in the evanescent field of an adjacent WGM resonator (see Fig. 6.8). This type of system has been studied in [31] which reported the observation of reactive[8] force on a silicon waveguide similar to what is shown here. Reference [31] however did not look at the resonator's Brownian motion or show any dynamical back-action due to the coupling.

6.3.1   Detection of the Brownian motion of the SiN beam

The first step was to see whether we could detect the Brownian motion of the beam in such a device, by monitoring the noise of the optical transmission. Using the same setup as shown in Fig. 6.3, we identify one mechanical mode clearly above the others in the mechanical spectrum, located between 10 and 14 MHz depending on the waveguide geometry and the SiO_2 under-etch depth[9], see Fig. 6.9. As expected it is the fundamental *in-plane* bending mode of the suspended waveguide which couples best to the WGM optical resonator, as it is the mechanical mode which best modulates the gap distance

---

[8]These different coupling mechanisms are defined in the following section 6.3.2.

[9]The RBM of the disk itself is visible as well, but of poor Q_M as the disk is only underetched on ~ 15 % of its radius.

Figure 6.9: Fundamental in-plane bending mechanical mode of a suspended SiN waveguide at 13.6 MHz. The FEM obtained resonance frequency is in relatively good agreement with the value obtained through the analytical formula of Eq. 2.19.

between disk and waveguide. An illustration of this mode's profile is shown in Fig. 6.10.

Mechanical quality factor

High tensile stress LPCVD SiN is a material which has garnered a lot of interest for its ability to provide very high mechanical Qs. The $Q_M \times$ f product in SiN nanobeams reaches around 10^{12} in the good cases, with typical values of Q_M of one million at 1 MHz or 100 000 at 10 MHz [168, 105]. Here we measure a mechanical Q of $\sim$20 in air and $\sim$1.3·10^4 in vacuum at room temperature, which corresponds to a $Q_M \times$ f product only in the low 10^{11}. We ascribe this lower value to the tapering profile of the waveguide, which is necessary to adiabatically guide the photons from the large portion of the waveguide to the suspended section (see Fig. 6.10). This tapering unfortunately also works as a funnel which adiabatically guides phonons in and out of the resonator and contributes to a lower overall mechanical Q. On the contrary, in the previous references the SiN beams make a right angle with the support structure at the anchoring points, providing a better impedance mismatch[10].

Detection sensitivity

In the low optical power limit, we notice that the detection sensitivity depends in some cases on which flank of the WGM the laser is tuned to. This is

---

[10]Recently the energy flow occurring at the anchoring points of suspended SiN string resonators has been investigated using a spatially resolved AFM probe technique. This approach is detailed in J. Rieger's thesis [173].
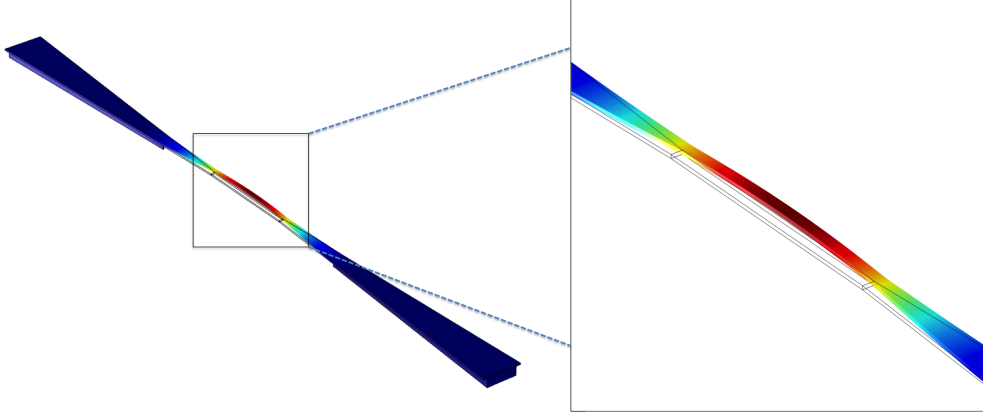
Figure 6.10: FEM simulation of the fundamental in-plane bending mode of a suspended SiN beam under tensile stress. The color code represents the total displacement amplitude. The inset shows a blow-up of the 20 μm long central portion of the guide. Agreement between FEM simulated and experimentally measured frequencies is very good. The σ_{SiN}=830 MPa tensile stress in the silicon nitride layer is responsible for roughly doubling the resonance frequency from 6.9 MHz in the stress-free case to 13.6 MHz here. The SiN material parameters used for the simulation are listed in appendix D.

unlike what is observed in the usual dispersive optomechanical coupling case. This behavior can be explained by the contribution of two distinct types of optomechanical coupling, which we will detail in the following section.

6.3.2 Dispersive and reactive coupling in SiN optomechanical resonators

When the SiN waveguide oscillates in the vicinity of the disk resonator, two types of coupling occur:

- As the beam moves towards and away from the disk, the evanescent field of the disk's WGM senses a changing environment, which leads to a shift in the WGM's effective index and resonance wavelength. This is the typical *dispersive* coupling of optomechanics, encountered for instance in a Fabry-Perot cavity with free end mirrors.

- In the particular case considered here, the beam/waveguide also plays the role of an input-output bus for the energy to and from the disk resonator. Therefore as the beam moves towards and away from the disk, the coupling strength between the WGM and the optical mode in the
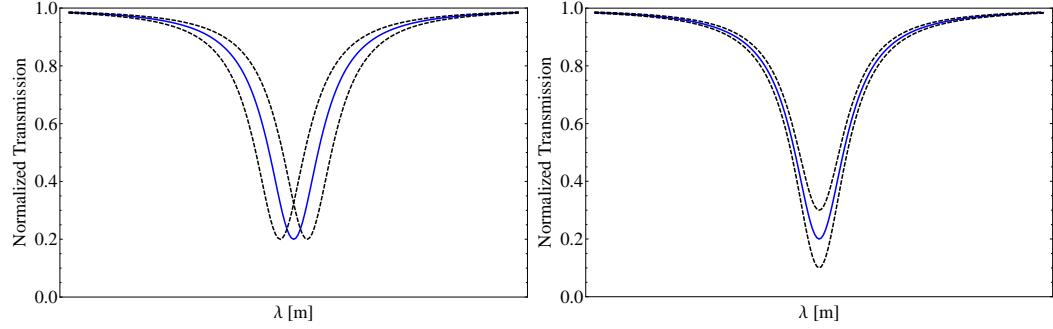
Figure 6.11: Optical resonance with beam at equilibrium (solid blue line) and with beam displaced towards and away from disk (dashed black lines) in the case of pure dispersive coupling (left) and pure reactive coupling (right). In the pure dispersive case the resonance wavelength shifts while maintaining constant contrast. In the case of pure reactive coupling the resonance contrast is modified at constant resonance wavelength.

waveguide is modulated. This coupling which modifies the cavities' extrinsic loss rate γ_{ext} is named the *reactive* or *dissipative* optomechanical coupling[11].

For clarity Fig. 6.11 visually sums up the effect of pure dispersive versus pure reactive coupling on the lorentzian profile of a WGM resonance.

The detection sensitivity to the mechanical motion of the beam depends on how strongly the transmitted optical power T through the waveguide is modified by an elementary displacement of the beam's position dx , *i.e.* $\frac{dT}{dx}$. (See figure 6.12). Both dispersive and reactive coupling will modify the optical transmission. In the following subsections, we will treat the dispersive and reactive coupling independently before summing their contributions. (This treatment is mathematically accurate, see C.0.6). We will see that both contributions may add up either constructively or destructively, depending on the experimental parameters.

6.3.3 Dispersive optomechanical coupling

When a small dielectric element is introduced inside a resonant cavity (or inside its evanescent field), the resonance frequency is changed by a small

---

[11]Note that whether the approached beam couples light into the cavity (as in our case and in [31]), or is simply a passive beam approached in the resonator's near field (as in [126]) is relevant. In terms of the coupled-mode formalism discussed in chapter 1, the first case amounts to increasing γ_{ext} while the second amounts to increasing the intrinsic loss rate γ_{int}. While the effect on the cavity linewidth is identical, only γ_{ext} serves as a source term to drive the cavity $\left(|\kappa|^2 = \gamma_{\text{ext}} \right)$.
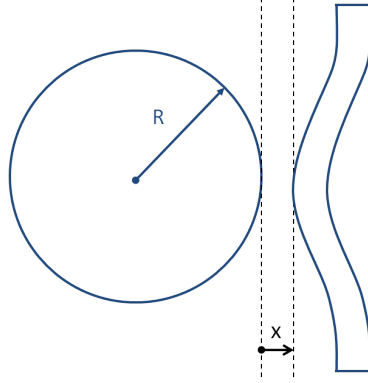
Figure 6.12: SiN coupling waveguide's fundamental in plane bending mode, in the vicinity of the disk resonator. 'x' is defined as the distance between disk and waveguide.

amount. Perturbation theory analysis [174] provides the shift in resonance frequency $\Delta\omega_0$:

$$\frac{\Delta\omega_0}{\omega_0} = -\frac{1}{2}\frac{\int_{V_{\text{beam}}}\left(\varepsilon\left(r\right)-1\right)|\vec{E}(\vec{r})^2|d^3(\vec{r})}{\int_{V_{\text{np}}}\varepsilon(r)|\vec{E}(\vec{r})^2|d^3(\vec{r})} \tag{6.1}$$

Here V_{beam} is the volume of the perturbative element (the waveguide), V_{np} and ω_0 denote respectively the volume and resonance frequency of the unperturbed optical mode (*i.e.* in the absence of the waveguide). $\vec{E}(\vec{r})$ is the electric field of the WGM and $\varepsilon(r)$ is the relative permittivity. The dispersive shift $\frac{d\omega_0}{dx}$ depends on the x coordinate. Indeed, as the WGM optical field decays exponentially outside the disk, a same beam displacement dx will induce a greater optical frequency shift close to the disk than further away. The dispersive shift $\frac{d\omega_0}{dx}$ is also going to depend on the considered whispering gallery optical mode. Since different radial order p modes extend for varying distances outside the disk resonator, they will experience varying frequency shifts due to the movement of the beam.

Each WGM in the optical spectrum can be precisely identified by its radial order p and its azimuthal order m. Once identified, a WGM's field inside the disk (Bessel function) and outside (Hankel function) is analytically known and Eq. 6.1 can be calculated for a given gap distance x. The function $\frac{\Delta\omega_0}{\omega_0} = f(x)$ is then reconstructed by varying the distance x between the waveguide and the disk resonator. For a given WGM and waveguide geometry (length, width and thickness) such a function is plotted in Fig. 6.13. We can now estimate the wavelength and position dependent variation in the output
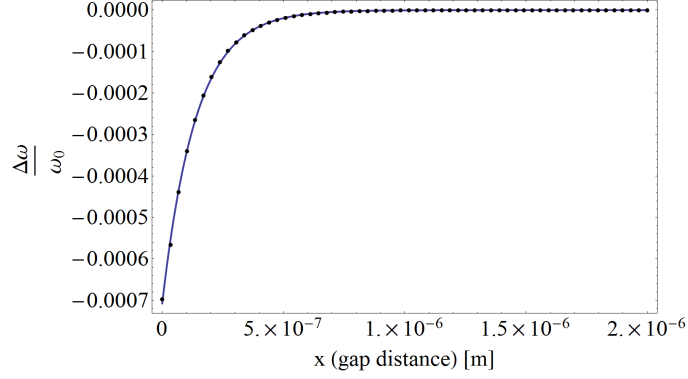
Figure 6.13: Relative frequency shift as a function of gap distance x between disk and waveguide. Beam dimensions are 20 μm length $\times$ 900 nm width $\times$ 300 nm thickness; the WGM is a (p=1 m=57). The frequency shift depends on the WGM but is independent of the WGM's optical Q. Black dots correspond to discrete calculations of Eq. 6.1 while the blue line is a fit of the form $-\alpha\,e^{-\beta\,x}$.

power for a small beam displacement dx due to the dispersive coupling:

$$\left(\frac{dT}{dx}\right)_{\text{disp}}(\lambda, x) = \left(\frac{dT}{d\omega_0}\right)\left(\frac{d\omega_0}{dx}\right) \tag{6.2}$$

The first term on the right hand of Eq. 6.2, $\left(\frac{dT}{d\omega_0}\right)$ is proportional to the slope of the WGM at the operating laser wavelength λ. It is calculated using Eq. 6.3 which gives the optical transmission of a WGM resonance as a function of λ:

$$T(\lambda) = 1 - \frac{1 - T_{\text{on}}}{1 + \left(\frac{\lambda - \lambda_0}{\delta\lambda/2}\right)^2} \tag{6.3}$$

T_{on} is the normalized transmission at resonance (which is equal to 1 minus the WGM contrast), λ_0 the resonance wavelength and $\delta\lambda$ the WGM FWHM. The second term $\left(\frac{d\omega_0}{dx}\right)$ is simply equal to ω_0 times the slope of the function plotted in Fig. 6.13. Figure 6.14 plots $\left(\frac{dT}{dx}\right)_{\text{disp}}$ as a function of the laser wavelength for a small displacement dx around a beam equilibrium position[12] of x=400 nm, for an over-coupled p=1 WGM resonance with loaded optical Q of $1.2 \cdot 10^4$.

---

[12]The position x=400 nm is the gap distance between disk and waveguide measured under the SEM for the experimental data shown in section 6.3.5 .

Figure 6.14: Purely dispersive transmission change for an elementary displacement dx around a gap distance $x = 400$ nm, as a function of λ (solid blue line). The WGM resonance is added for reference (dashed purple line). The dispersive sensitivity to mechanical displacement $\left| \left(\frac{dT}{dx} \right)_{\text{disp}} \right|$ is maximum along the flanks of the optical resonance, and zero at resonance. As the beam moves away from the disk (positive dx), the WGM effective index decreases and λ_0 is blue shifted. Therefore for a blue detuned probe laser the transmission dips $\left(\left(\frac{dT}{dx} \right)_{\text{disp}} < 0 \right)$. In the case of dispersive coupling, the sign of the transmission change depends on which flank of the WGM resonance the laser sits on.

6.3.4 Reactive coupling

In the case of reactive coupling, the optical cavity extrinsic loss rate γ_{ext} is modulated by the position of the moving coupling waveguide. As a consequence, the contrast of the optical resonance is modulated, through the relationship shown in Eq. 6.4:

$$T_{\text{on}} = \left(\frac{1 - \gamma_{\text{ext}}/\gamma_{\text{int}}}{1 + \gamma_{\text{ext}}/\gamma_{\text{int}}} \right)^2 \tag{6.4}$$

Therefore, the optical transmission modulation through purely reactive coupling can be expressed as Eq. 6.5):

$$\left(\frac{dT}{dx} \right)_{\text{reac}} = \left(\frac{dT}{dT_{\text{on}}} \right) \left(\frac{dT_{\text{on}}}{dx} \right) \tag{6.5}$$

The first term on the right hand side of Eq. 6.5 is calculated using Eq. 6.3:

$$\left(\frac{dT}{dT_{\text{on}}} \right) = \frac{1}{1 + \left(\frac{\lambda - \lambda_0}{\delta\lambda/2} \right)^2}$$

In order to know the value of the second term $\left(\frac{dT_{\text{on}}}{dx} \right)$, one must reconstruct the function $T_{\text{on}} = f(x)$ in the vicinity of the operating gap distance x.

189
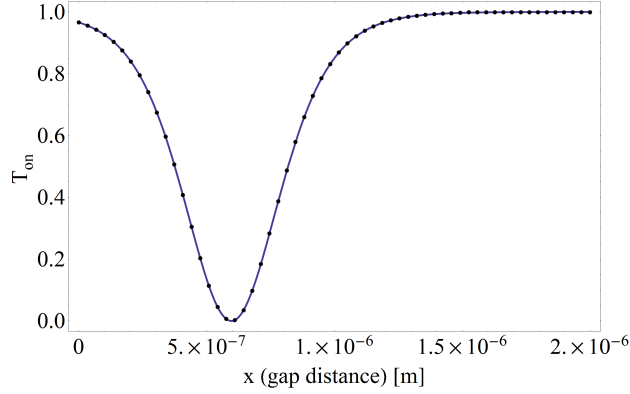
Figure 6.15: T_{on} as a function of gap distance x between disk and waveguide for a (p=1 m=57) WGM with intrinsic optical Q $\simeq 4 \cdot 10^4$. Black dots correspond to individual calculations of T_{on} by the overlap integral method described in chapter 1. The blue line is a fit using Eq. 6.4. Remarkably both are in very good agreement, even though they are derived by entirely different methods. For this WGM the critical coupling regime occurs around x=600 nm.

Using the method described in section 1.3.1, we calculate the overlap integral between the considered WGM and the optical mode in the waveguide for discrete values of x. This provides the coupling strength κ between disk and waveguide and the extrinsic loss rate γ_{ext}. The intrinsic loss rate γ_{int} is obtained through experimental spectroscopy of the disk's WGM. Plotted in Fig. 6.15 is the function $T_{\mathrm{on}} = f(x)$ thus obtained for the same p=1 WGM as previously. Finally Fig.6.16 plots $\left(\frac{dT}{dx}\right)_{\mathrm{reac}}$ as a function of wavelength for this WGM. Note that the from Eq. 6.5 it appears that in order for the reactive coupling to be maximal the laser should be at resonance with the WGM. However the critical coupling regime should be avoided as at this point $\left(\frac{dT_{\mathrm{on}}}{dx}\right) \simeq 0$ (see Fig. 6.15); the WGM should be either under- or over-coupled.

6.3.5   Experimental results

The total sensitivity due to the dispersive and reactive contributions is given by Eq. 6.6:

$$\left|\left(\frac{dT}{dx}\right)_{\mathrm{total}}\right| = \left|\left(\frac{dT}{dx}\right)_{\mathrm{disp}} + \left(\frac{dT}{dx}\right)_{\mathrm{reac}}\right| \tag{6.6}$$

Thus when $\left(\frac{dT}{dx}\right)_{\mathrm{disp}}$ and $\left(\frac{dT}{dx}\right)_{\mathrm{reac}}$ are of identical sign, both contributions will add constructively to provide enhanced measurement sensitivity; when they are of opposite sign, their contributions will add destructively resulting in diminished sensitivity. This modeling satisfactorily explains the different
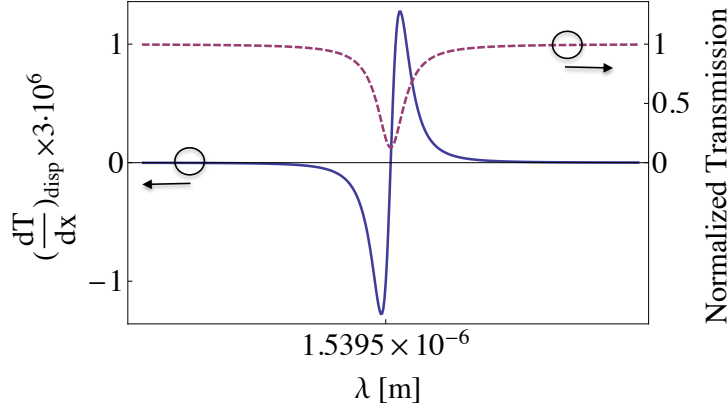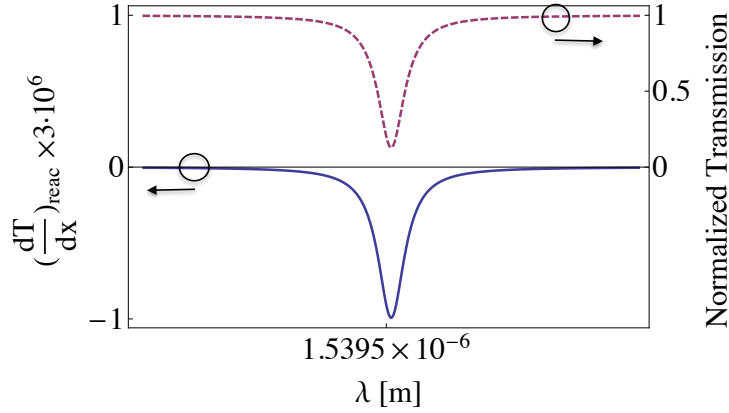
Figure 6.16: Purely reactive transmission change for an elementary displacement dx around x=400 nm, as a function of λ (solid blue line). The WGM position is added for reference (dashed purple line). The reactive sensitivity to mechanical displacement $|(\frac{dT}{dx})_{\text{reac}}|$ is maximum at resonance. In the case of reactive coupling, the sign of the transmission change is independent of which flank of the resonance the laser sits on. However, the sign depends on whether the optical mode is over-coupled ($(\frac{dT}{dx})_{\text{reac}} < 0$), or under-coupled ($(\frac{dT}{dx})_{\text{reac}} > 0$).

behavior observed between an over-coupled p=1 and an undercoupled p=3 WGM. This can be seen in Fig. 6.17, which plots the mechanical signal amplitude obtained at various points along the WGM resonance.

After this study of the displacement sensitivity variations due to contributions of both dispersive and reactive coupling mechanisms, we see the physics of this interaction is well understood. The next step will be to investigate reactive dynamical back-action.

6.4 Conclusion

In this chapter we discussed our first optomechanical measurements on standalone GaAs disk resonators. The detection of mechanical modes of WGM disk resonators above the GHz was reported for the first time. Next we showed the first measurements of the integrated disk resonators under vacuum and at low temperature. Regarding the SiN resonators we showed some results of Brownian motion detection as well as a model and some first results on the dispersive and reactive optomechanical coupling at play in these resonators.
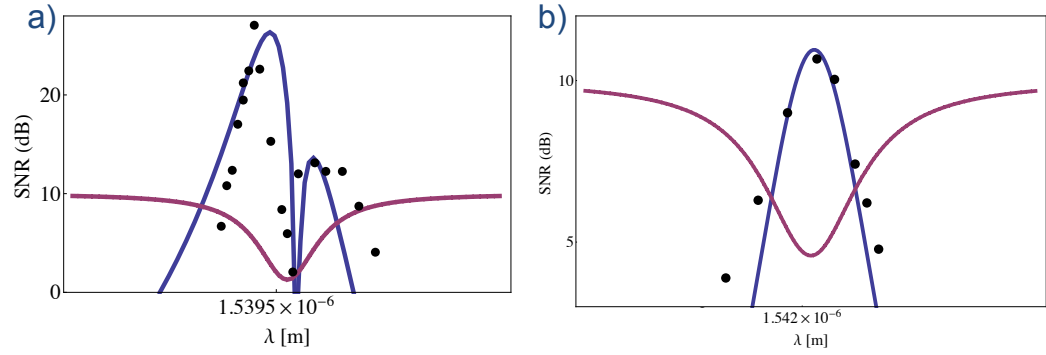
Figure 6.17: (a) Signal to noise ratio (dB) for the mechanical resonance (blue line theoretical fit, black dots experimental points), as a function of laser position along the optical resonance (p=1 WGM. at constant laser power . The optical resonance position has been plotted (purple line) for reference. The optical resonance being over-coupled, the reactive and dispersive contributions are constructive on the blue detuned flank and destructive on the red detuned flank of the optical resonance. Indeed the mechanical Brownian motion signal is 14 dB stronger on the blue flank, when it should be identical were the coupling purely dispersive. Note that the poor agreement wavelength-wise between experimental and theoretical points is due to the thermo-mechanical shifting of the WGM resonance wavelength during the measurement discussed in section 5.4.2. (b) In the case of an under-coupled, bending loss limited (Q_{int}=5000) p=3, m=47 WGM the coupling is essentially reactive in nature: there is no dispersive coupling related sensitivity dip at resonance.

Conclusion and perspectives

During this thesis, we were able to design and fabricate on-chip GaAs disk optomechanical resonators with monolithic integrated coupling waveguides boasting state of the art optical quality factors, and achieve precise control over the evanescent coupling conditions. We presented an analytical description of both the out-of-plane and in-plane mechanical modes of GaAs disk resonators and investigated the main loss mechanisms limiting the mechanical Q of the disk resonators. Next, the various mechanisms responsible for the optomechanical interaction were presented and their relative magnitude calculated, underscoring the strength of GaAs disk resonators for optomechanical applications. After providing an account of the nanofabrication of these samples, the origin of optical losses in current devices was identified. Finally, we discussed our initial optomechanical measurements on standalone GaAs disk resonators and showed the first measurements of the integrated samples under vacuum and at low temperature.

Our work on the SiN platform resulted in the fabrication of on-chip integrated high Q SiN WGM resonators, which displayed optical instabilities and self-pulsing. We also presented some results of Brownian motion detection, as well as a model and some first results on the dispersive and reactive optomechanical coupling at play in these resonators.

In the relatively near future, the improvements provided by the new cryostat setup and the developments outlined in section 6.2.8 should allow William Hease, the new PhD candidate, to bring the mechanical mode of a GaAs disk resonator into the quantum ground state and accurately measure its occupancy.

In the field of optomechanics, progress is often limited not for want of ideas or theoretical framework, but by simple limitations in device performance. In this spirit two new members of the team, Biswarup Guha and Dac-Trung NGuyen, are seeking to boost the optical and mechanical properties of the GaAs resonators through better understanding and control of the surface chemistries, as well as through the development of novel fabrica-
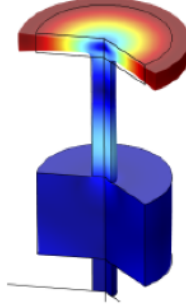
Figure 6.1: This novel disk resonator design, with an acoustic shield integrated in the pedestal, dramatically reduces mechanical dissipation. From DT NGuyen et al. "Ultrahigh Q frequency product for optomechanical disk resonators with a mechanical shield", *in preparation*.

tion designs such as shown in Figure 6.1. The on-chip resonators developed during this thesis also function as a multipurpose tool with applications in force sensing and optomechanical experiments in liquids, which Eduardo Gil-Santos is currently investigating. We can also envision novel designs better suited to take advantage of the photoelastic optomechanical coupling discussed in section 3.8.2.

Finally the GaAs/AlGaAs platform lends itself to the inclusion of quantum dots or quantum wells [45], opening the perspective of hybrid cavity QED-optomechanics setups [175]. The team has started to explore these concepts theoretically in collaboration with the theory group of MPQ and experimentally in collaboration with the LPN.

Since the beginning of this work, the field of optomechanics has experienced explosive growth and is now being researched by several dozen teams worldwide. During this time, the important milestone of measuring a macroscopic mechanical resonator in its quantum ground state has been achieved by three groups [13, 12, 11]. The field is however still quite young and bustling with activity, and a lot of exciting physics lies ahead.

Bibliography

[1] D. de Mairan, *Traité physique et historique de l'aurore boréale*, vol. 4. De l'Imprimerie royale, 1754.

[2] "Virgo interferometer." `http://www.ego-gw.it/virgodescription/index.html`.

[3] "Nasa solar sail." `http://science.nasa.gov/science-news/science-at-nasa/2011/24jan_solarsail/`.

[4] P. Lebedew, "Untersuchungen über die druckkräfte des lichtes," *Annalen der Physik*, vol. 311, no. 11, pp. 433–458, 1901.

[5] E. F. Nichols and G. F. Hull, "The pressure due to radiation," *Proceedings of the American Academy of Arts and Sciences*, vol. 38, no. 20, pp. pp. 559–599, 1903.

[6] V. Braginski and A. Manukin, "Ponderomotive effects of electromagnetic radiation," *Sov. Phys.JETP*, vol. 25, p. 653, 1967.

[7] C. M. Caves, "Quantum-mechanical noise in an interferometer," *Physical Review D*, vol. 23, no. 8, p. 1693, 1981.

[8] F. Marquardt and S. Girvin, "Optomechanics (a brief review)," *Physics*, vol. 2, p. 40, 2009.

[9] I. Favero and K. Karrai, "Optomechanics of deformable optical cavities," *Nature Photonics*, vol. 3, no. 4, pp. 201–205, 2009.

[10] M. Aspelmeyer, T. J. Kippenberg, and F. Marquardt, "Cavity optomechanics," *arXiv preprint arXiv:1303.0733*, 2013.

[11] J. Chan, T. M. Alegre, A. H. Safavi-Naeini, J. T. Hill, A. Krause, S. Gröblacher, M. Aspelmeyer, and O. Painter, "Laser cooling of a nanomechanical oscillator into its quantum ground state," *Nature*, vol. 478, no. 7367, pp. 89–92, 2011.

Bibliography

[12] J. Teufel, T. Donner, D. Li, J. Harlow, M. Allman, K. Cicak, A. Sirois, J. Whittaker, K. Lehnert, and R. Simmonds, "Sideband cooling of micromechanical motion to the quantum ground state," *Nature*, vol. 475, no. 7356, pp. 359–363, 2011.

[13] A. D. OConnell, M. Hofheinz, M. Ansmann, R. C. Bialczak, M. Lenander, E. Lucero, M. Neeley, D. Sank, H. Wang, M. Weides, *et al.*, "Quantum ground state and single-phonon control of a mechanical resonator," *Nature*, vol. 464, no. 7289, pp. 697–703, 2010.

[14] E. Verhagen, S. Deléglise, S. Weis, A. Schliesser, and T. J. Kippenberg, "Quantum-coherent coupling of a mechanical oscillator to an optical cavity mode," *Nature*, vol. 482, no. 7383, pp. 63–67, 2012.

[15] D. Armani, T. Kippenberg, S. Spillane, K. Vahala, *et al.*, "Ultra-high-q toroid microcavity on a chip," *Nature*, vol. 421, no. 6926, pp. 925–928, 2003.

[16] K. H. Lee, T. G. McRae, G. I. Harris, J. Knittel, and W. P. Bowen, "Cooling and control of a cavity optoelectromechanical system," *Physical review letters*, vol. 104, no. 12, p. 123604, 2010.

[17] C. H. Metzger and K. Karrai, "Cavity cooling of a microlever," *Nature*, vol. 432, no. 7020, pp. 1002–1005, 2004.

[18] T. Corbitt, Y. Chen, E. Innerhofer, H. Müller-Ebhardt, D. Ottaway, H. Rehbein, D. Sigg, S. Whitcomb, C. Wipf, and N. Mavalvala, "An all-optical trap for a gram-scale mirror," *Physical review letters*, vol. 98, no. 15, p. 150802, 2007.

[19] A. Kuhn, M. Bahriz, O. Ducloux, C. Chartier, O. Le Traon, T. Briant, P.-F. Cohadon, A. Heidmann, C. Michel, L. Pinard, *et al.*, "A micropillar for cavity optomechanics," *Applied Physics Letters*, vol. 99, no. 12, pp. 121103–121103, 2011.

[20] L. Ding, C. Baker, P. Senellart, A. Lemaitre, S. Ducci, G. Leo, and I. Favero, "High frequency gaas nano-optomechanical disk resonator," *Physical review letters*, vol. 105, no. 26, p. 263903, 2010.

[21] C. Baker, C. Belacel, A. Andronico, P. Senellart, A. Lemaitre, E. Galopin, S. Ducci, G. Leo, and I. Favero, "Critical optical coupling between a gaas disk and a nanowaveguide suspended on the chip," *Applied Physics Letters*, vol. 99, no. 15, pp. 151117–151117, 2011.

[22] X. Sun, X. Zhang, and H. X. Tang, "High-q silicon optomechanical microdisk resonators at gigahertz frequencies," *Applied Physics Letters*, vol. 100, no. 17, pp. 173116–173116, 2012.

[23] W. C. Jiang, X. Lu, J. Zhang, and Q. Lin, "High-frequency silicon optomechanical oscillator with an ultralow threshold," *Opt. Express*, vol. 20, pp. 15991–15996, Jul 2012.

[24] J. Thompson, B. Zwickl, A. Jayich, F. Marquardt, S. Girvin, and J. Harris, "Strong dispersive coupling of a high-finesse cavity to a micromechanical membrane," *Nature*, vol. 452, no. 7183, pp. 72–75, 2008.

[25] T. Purdy, R. Peterson, and C. Regal, "Observation of radiation pressure shot noise on a macroscopic object," *Science*, vol. 339, no. 6121, pp. 801–804, 2013.

[26] K. Usami, A. Naesby, T. Bagci, B. M. Nielsen, J. Liu, S. Stobbe, P. Lodahl, and E. S. Polzik, "Optical cavity cooling of mechanical modes of a semiconductor nanomembrane," *Nature Physics*, vol. 8, no. 2, pp. 168–172, 2012.

[27] I. Mahboob and H. Yamaguchi, "Bit storage and bit flip operations in an electromechanical oscillator," *Nature nanotechnology*, vol. 3, no. 5, pp. 275–279, 2008.

[28] H. Okamoto, D. Ito, K. Onomitsu, H. Sanada, H. Gotoh, T. Sogawa, and H. Yamaguchi, "Vibration amplification, damping, and self-oscillations in micromechanical resonators induced by optomechanical coupling through carrier excitation," *Physical Review Letters*, vol. 106, no. 3, p. 036801, 2011.

[29] I. Favero, S. Stapfner, D. Hunger, P. Paulitschke, J. Reichel, H. Lorenz, E. M. Weig, and K. Karrai, "Fluctuating nanomechanical system in a high finesse optical microcavity," *Opt. Express*, vol. 17, pp. 12813–12820, Jul 2009.

[30] S. Stapfner, L. Ost, D. Hunger, J. Reichel, I. Favero, and E. M. Weig, "Cavity-enhanced optical detection of carbon nanotube brownian motion," *Applied Physics Letters*, vol. 102, no. 15, p. 151910, 2013.

[31] M. Li, W. H. Pernice, and H. X. Tang, "Reactive cavity optical force on microdisk-coupled nanomechanical beam waveguides," *Physical review letters*, vol. 103, no. 22, p. 223901, 2009.

[32] G. Wiederhecker, L. Chen, A. Gondarenko, and M. Lipson, "Controlling photonic structures using optical forces," *Nature*, vol. 462, no. 7273, pp. 633–636, 2009.

[33] S. Gröblacher, J. B. Hertzberg, M. R. Vanner, G. D. Cole, S. Gigan, K. Schwab, and M. Aspelmeyer, "Demonstration of an ultracold micro-optomechanical oscillator in a cryogenic cavity," *Nature Physics*, vol. 5, no. 7, pp. 485–488, 2009.

[34] O. Arcizet, P.-F. Cohadon, T. Briant, M. Pinard, and A. Heidmann, "Radiation-pressure cooling and optomechanical instability of a micromirror," *Nature*, vol. 444, no. 7115, pp. 71–74, 2006.

[35] I. Favero, C. Metzger, S. Camerer, D. Konig, H. Lorenz, J. Kotthaus, and K. Karrai, "Optical cooling of a micromirror of wavelength size," *Applied Physics Letters*, vol. 90, no. 10, pp. 104101–104101, 2007.

[36] Y.-S. Park and H. Wang, "Resolved-sideband and cryogenic cooling of an optomechanical resonator," *Nature physics*, vol. 5, no. 7, pp. 489–493, 2009.

[37] T. Carmon and K. J. Vahala, "Modal spectroscopy of optoexcited vibrations of a micron-scale on-chip resonator at greater than 1 ghz frequency," *Physical review letters*, vol. 98, no. 12, p. 123901, 2007.

[38] T. Purdy, D. Brooks, T. Botter, N. Brahms, Z.-Y. Ma, and D. Stamper-Kurn, "Tunable cavity optomechanics with ultracold atoms," *Physical review letters*, vol. 105, no. 13, p. 133602, 2010.

[39] S. Camerer, M. Korppi, A. Jöckel, D. Hunger, T. W. Hänsch, and P. Treutlein, "Realization of an optomechanical interface between ultracold atoms and a membrane," *Physical Review Letters*, vol. 107, no. 22, p. 223001, 2011.

[40] M. Notomi, H. Taniyama, S. Mitsugi, and E. Kuramochi, "Optomechanical wavelength and energy conversion in high-q double-layer cavities of photonic crystal slabs," *Physical review letters*, vol. 97, no. 2, p. 023903, 2006.

[41] E. Gavartin, R. Braive, I. Sagnes, O. Arcizet, A. Beveratos, T. J. Kippenberg, and I. Robert-Philip, "Optomechanical coupling in a two-dimensional photonic crystal defect cavity," *Physical Review Letters*, vol. 106, no. 20, p. 203902, 2011.

[42] D. Rafizadeh, J. Zhang, S. Hagness, A. Taflove, K. Stair, S. Ho, and R. Tiberio, "Waveguide-coupled algaas/gaas microcavity ring and disk resonators with high f inesse and 21.6-nm f ree spectral range," *Optics Letters*, vol. 22, no. 16, pp. 1244–1246, 1997.

[43] B. Gayral, J. Gérard, A. Lemaitre, C. Dupuis, L. Manin, and J. Pelouard, "High-q wet-etched gaas microdisks containing inas quantum boxes," *Applied physics letters*, vol. 75, no. 13, pp. 1908–1910, 1999.

[44] B. J. W. S. Rayleigh, *The theory of sound*, vol. 2. Macmillan, 1896.

[45] E. Peter, P. Senellart, D. Martrou, A. Lemaître, J. Hours, J. Gérard, and J. Bloch, "Exciton-photon strong-coupling regime for a single quantum dot embedded in a microcavity," *Physical Review Letters*, vol. 95, no. 6, p. 67401, 2005.

[46] K. Srinivasan, M. Borselli, T. J. Johnson, P. E. Barclay, O. Painter, A. Stintz, and S. Krishna, "Optical loss and lasing characteristics of high-quality-factor algaas microdisk resonators with embedded quantum dots," *Applied Physics Letters*, vol. 86, no. 15, pp. 151106–151106, 2005.

[47] T. A. Birks and Y. W. Li, "The shape of fiber tapers," *Lightwave Technology, Journal of*, vol. 10, no. 4, pp. 432–438, 1992.

[48] T. Kippenberg, H. Rokhsari, T. Carmon, A. Scherer, and K. Vahala, "Analysis of radiation-pressure induced mechanical oscillation of an optical microcavity," *Physical Review Letters*, vol. 95, no. 3, p. 033901, 2005.

[49] L. Bobb and P. Shankar, "Tapered optical fiber components and sensors," *Microwave Journal*, vol. 35, p. 218, 1992.

[50] G. Heinrich, M. Ludwig, J. Qian, B. Kubala, and F. Marquardt, "Collective dynamics in optomechanical arrays," *Physical Review Letters*, vol. 107, no. 4, p. 043603, 2011.

[51] L. Ding, C. Belacel, S. Ducci, G. Leo, and I. Favero, "Ultralow loss single-mode silica tapers manufactured by a microheater," *Applied Optics*, vol. 49, no. 13, pp. 2441–2445, 2010.

[52] A. Andronico, *Etude Électromagnétique D'émetteurs Intégrés Infrarouges Et Thz en AlGaAs*. PhD thesis, 2008.

Bibliography

[53] E. Rosencher and B. Vinter, *Optoélectronique: cours et exercices corrigés.* Dunod, 2002.

[54] J. Love, W. Henry, W. Stewart, R. Black, S. Lacroix, and F. Gonthier, "Tapered single-mode fibres and devices. i. adiabaticity criteria," in *Optoelectronics, IEE Proceedings J*, vol. 138, pp. 343–354, IET, 1991.

[55] L. Ding, C. Baker, P. Senellart, A. Lemaitre, S. Ducci, G. Leo, and I. Favero, "Wavelength-sized gaas optomechanical resonators with gigahertz frequency," *Applied Physics Letters*, vol. 98, no. 11, pp. 113108–113108, 2011.

[56] C. Baker, S. Stapfner, D. Parrain, S. Ducci, G. Leo, E. M. Weig, and I. Favero, "Optical instability and self-pulsing in silicon nitride whispering gallery resonators," *Optics express*, vol. 20, no. 27, pp. 29076–29089, 2012.

[57] M. Dakss, L. Kuhn, P. Heidrich, and B. Scott, "Grating coupler for efficient excitation of optical guided waves in thin films," *Applied physics letters*, vol. 16, no. 12, pp. 523–525, 1970.

[58] D. Taillaert, W. Bogaerts, P. Bienstman, T. F. Krauss, P. Van Daele, I. Moerman, S. Verstuyft, K. De Mesel, and R. Baets, "An out-of-plane grating coupler for efficient butt-coupling between compact planar waveguides and single-mode fibers," *Quantum Electronics, IEEE Journal of*, vol. 38, no. 7, pp. 949–955, 2002.

[59] V. R. Almeida, R. R. Panepucci, and M. Lipson, "Nanotaper for compact mode conversion," *Optics Letters*, vol. 28, no. 15, pp. 1302–1304, 2003.

[60] Q. V. Tran, S. Combrié, P. Colman, and A. De Rossi, "Photonic crystal membrane waveguides with low insertion losses," *Applied Physics Letters*, vol. 95, no. 6, pp. 061105–061105, 2009.

[61] Z. Han, X. Checoury, D. Néel, S. David, M. El Kurdi, and P. Boucaud, "Optimized design for 2×10^6 ultra-high q silicon photonic crystal cavities," *Optics Communications*, vol. 283, no. 21, pp. 4387–4391, 2010.

[62] E. Peter, *Couplage fort exciton-photon pour une boîte quantique de GaAs en microdisque.* PhD thesis, Université Paris Sud-Paris XI, 2006.

[63] A. B. Matsko and V. S. Ilchenko, "Optical resonators with whispering-gallery modes-part i: basics," *Selected Topics in Quantum Electronics, IEEE Journal of*, vol. 12, no. 1, pp. 3–14, 2006.

[64] G. C. Righini, Y. Dumeige, P. Féron, M. Ferrari, G. Nunzi Conti, D. Ristic, and S. Soria, "Whispering gallery mode microresonators: fundamentals and applications," *Rivista del Nuovo Cimento*, vol. 34, no. 7, pp. 435–488, 2011.

[65] A. Baca, C. Ashby, A. Baca, and C. Ashby, "Fabrication of gaas devices," Institution of Electrical Engineers, 2005.

[66] A. Andronico, I. Favero, and G. Leo, "Difference frequency generation in gaas microdisks," *Optics letters*, vol. 33, no. 18, pp. 2026–2028, 2008.

[67] M. Oxborrow, "How to simulate the whispering-gallery modes of dielectric microresonators in femlab/comsol," in *Lasers and Applications in Science and Engineering*, pp. 64520J–64520J, International Society for Optics and Photonics, 2007.

[68] M. I. Cheema and A. G. Kirk, "Implementation of the perfectly matched layer to determine the quality factor of axisymmetric resonators in comsol," in *COMSOL conference, Boston, Oct*, 2010.

[69] M. Soltani, Q. Li, S. Yegnanarayanan, and A. Adibi, "Toward ultimate miniaturization of high q silicon traveling-wave microresonators," *Optics express*, vol. 18, p. 19, 2010.

[70] A. Yariv, "Coupled-mode theory for guided-wave optics," *Quantum Electronics, IEEE Journal of*, vol. 9, no. 9, pp. 919–933, 1973.

[71] H. A. Haus and W. Huang, "Coupled-mode theory," *Proceedings of the IEEE*, vol. 79, no. 10, pp. 1505–1518, 1991.

[72] G. I. Stegeman and C. T. Seaton, "Nonlinear integrated optics," *Journal of applied physics*, vol. 58, no. 12, pp. R57–R78, 1985.

[73] H. A. Haus, *Waves and fields in optoelectronics*, vol. 1. Prentice-Hall Englewood Cliffs, NJ, 1984.

[74] C. Manolatou, M. Khan, S. Fan, P. R. Villeneuve, H. Haus, and J. Joannopoulos, "Coupling of modes analysis of resonant channel add-drop filters," *Quantum Electronics, IEEE Journal of*, vol. 35, no. 9, pp. 1322–1331, 1999.

[75] T. Kamalakis and T. Sphicopoulos, "Frequency dependence of the coupling coefficients and resonant frequency detuning in a nanophotonic waveguide-cavity system," *Quantum Electronics, IEEE Journal of*, vol. 42, no. 8, pp. 827–837, 2006.

Bibliography

[76] E. S. Hosseini, S. Yegnanarayanan, A. H. Atabaki, M. Soltani, and A. Adibi, "Systematic design and fabrication of high-q single-mode pulley-coupled planar silicon nitride microdisk resonators at visible wavelengths," *Optics express*, vol. 18, no. 3, pp. 2127–2136, 2010.

[77] S. Spillane, T. Kippenberg, O. Painter, and K. Vahala, "Ideality in a fiber-taper-coupled microresonator system for application to cavity quantum electrodynamics," *Physical Review Letters*, vol. 91, no. 4, p. 043902, 2003.

[78] A. W. Leissa, "Vibration of plates," tech. rep., DTIC Document, 1969.

[79] D. Sarid, *Scanning force microscopy: with applications to electric, magnetic, and atomic forces*, vol. 5. Oxford University Press on Demand, 1994.

[80] M. Onoe, "Contour vibrations of isotropic circular plates," *the Journal of the Acoustical Society of America*, vol. 28, p. 1158, 1956.

[81] M. A. Abdelmoneum, M. U. Demirci, and C.-C. Nguyen, "Stemless wine-glass-mode disk micromechanical resonators," in *Micro Electro Mechanical Systems, 2003. MEMS-03 Kyoto. IEEE The Sixteenth Annual International Conference on*, pp. 698–701, IEEE, 2003.

[82] A. E. H. Love, *A treatise on the mathematical theory of elasticity*. Cambridge University Press, 2013.

[83] S. Bashmal, R. Bhat, and S. Rakheja, "Frequency equations for the in-plane vibration of circular annular disks," *Advances in Acoustics and Vibration*, vol. 2010, 2010.

[84] J. Blakemore, "Semiconducting and other major properties of gallium arsenide," *Journal of Applied Physics*, vol. 53, no. 10, pp. R123–R181, 1982.

[85] Z. Hao and F. Ayazi, "Support loss in the radial bulk-mode vibrations of center-supported micromechanical disk resonators," *Sensors and Actuators A: Physical*, vol. 134, no. 2, pp. 582–593, 2007.

[86] M. Eichenfield, J. Chan, A. H. Safavi-Naeini, K. J. Vahala, and O. Painter, "Modeling dispersive coupling and losses of localized optical and mechanical modes in optomechanical crystals," *Optics Express*, vol. 17, no. 22, pp. 20078–20098, 2009.

[87] F.-C. Hsu, J.-C. Hsu, T.-C. Huang, C.-H. Wang, and P. Chang, "Reducing support loss in micromechanical ring resonators using phononic band-gap structures," *Journal of Physics D: Applied Physics*, vol. 44, no. 37, p. 375101, 2011.

[88] H. Hosaka, K. Itao, and S. Kuroda, "Damping characteristics of beam-shaped micro-oscillators," *Sensors and Actuators A: Physical*, vol. 49, no. 1, pp. 87–95, 1995.

[89] F. Blom, S. Bouwstra, M. Elwenspoek, and J. Fluitman, "Dependence of the quality factor of micromachined silicon beam resonators on pressure and geometry," *Journal of Vacuum Science & Technology B: Microelectronics and Nanometer Structures*, vol. 10, no. 1, pp. 19–26, 1992.

[90] L. Landau and E. Lifshitz, "Fluid mechanics, vol. 6," *Course of Theoretical Physics*, pp. 227–229, 1987.

[91] D. Parrain, C. Baker, T. Verdier, P. Senellart, A. Lemaitre, S. Ducci, G. Leo, and I. Favero, "Damping of optomechanical disks resonators vibrating in air," *Applied Physics Letters*, vol. 100, no. 24, pp. 242105–242105, 2012.

[92] V. Yakhot and C. Colosqui, "Stokes' second flow problem in a high-frequency limit: application to nanomechanical resonators," *Journal of Fluid Mechanics*, vol. 586, no. 1, pp. 249–258, 2007.

[93] M. Bao and H. Yang, "Squeeze film air damping in mems," *Sensors and Actuators A: Physical*, vol. 136, no. 1, pp. 3–27, 2007.

[94] W. E. Newell *et al.*, "Miniaturization of tuning forks," *Science*, vol. 161, no. 3848, pp. 1320–1326, 1968.

[95] K. Y. Yasumura, T. D. Stowe, E. M. Chow, T. Pfafman, T. W. Kenny, B. C. Stipe, and D. Rugar, "Quality factors in micron-and submicron-thick cantilevers," *Microelectromechanical Systems, Journal of*, vol. 9, no. 1, pp. 117–125, 2000.

[96] W. Zhang and K. L. Turner, "Thermoelastic damping in the longitudinal vibration: analysis and simulation," in *Proc. of IMECE04 2004 ASME International Mechanical Engineering Congress and Exposition*, pp. 1–5, 2004.

Bibliography

[97] Z. Hao, "Thermoelastic damping in the contour-mode vibrations of micro-and nano-electromechanical circular thin-plate resonators," *Journal of Sound and Vibration*, vol. 313, no. 1, pp. 77–96, 2008.

[98] "Comsol material library,"

[99] H. Okamoto, D. Ito, K. Onomitsu, and H. Yamaguchi, "Thermoelastic damping in gaas micromechanical resonators," *physica status solidi (c)*, vol. 5, no. 9, pp. 2920–2922, 2008.

[100] B. Houston, D. Photiadis, M. Marcus, J. Bucaro, X. Liu, and J. Vignola, "Thermoelastic loss in microscale oscillators," *Applied Physics Letters*, vol. 80, no. 7, pp. 1300–1302, 2002.

[101] J. Yang, T. Ono, and M. Esashi, "Energy dissipation in submicrometer thick single-crystal silicon cantilevers," *Microelectromechanical Systems, Journal of*, vol. 11, no. 6, pp. 775–783, 2002.

[102] Y. Wang, J. A. Henry, A. T. Zehnder, and M. A. Hines, "Surface chemical control of mechanical energy losses in micromachined silicon structures," *The Journal of Physical Chemistry B*, vol. 107, no. 51, pp. 14270–14277, 2003.

[103] A. M. Richter, D. Sengupta, and M. A. Hines, "Effect of surface chemistry on mechanical energy dissipation: Silicon oxidation does not inherently decrease the quality factor," *The Journal of Physical Chemistry C*, vol. 112, no. 5, pp. 1473–1478, 2008.

[104] S. Timoshenko, "Vibration problems in engineering," 1974.

[105] S. S. Verbridge, J. M. Parpia, R. B. Reichenbach, L. M. Bellan, and H. Craighead, "High quality factor resonance at room temperature with nanostrings under high tensile stress," *Journal of Applied Physics*, vol. 99, no. 12, pp. 124304–124304, 2006.

[106] Q. Unterreithmeier, T. Faust, and J. Kotthaus, "Damping of nanomechanical resonators," *Physical review letters*, vol. 105, no. 2, p. 27205, 2010.

[107] C. Metzger, I. Favero, A. Ortlieb, and K. Karrai, "Optical self cooling of a deformable fabry-perot cavity in the classical limit," *Physical Review B*, vol. 78, no. 3, p. 035309, 2008.

[108] T. J. Kippenberg and K. J. Vahala, "Cavity opto-mechanics," *Optics Express*, vol. 15, no. 25, pp. 17172–17205, 2007.

[109] F. Marquardt, "Quantum optomechanics. les houches lecture notes 2011, school on quantum machines.," *Annalen der Physik*, 2011.

[110] F. Marquardt, J. P. Chen, A. Clerk, and S. Girvin, "Quantum theory of cavity-assisted sideband cooling of mechanical motion," *Physical review letters*, vol. 99, no. 9, p. 093902, 2007.

[111] S. M. Barnett, "Resolution of the abraham-minkowski dilemma," *Physical review letters*, vol. 104, no. 7, p. 070401, 2010.

[112] J. Jackson, *Classical Electrodynamics.* John Wiley & Sons: New York, 1998.

[113] P. T. Rakich, P. Davids, and Z. Wang, "Tailoring optical forces in waveguides through radiation pressure and electrostrictive forces," *Optics express*, vol. 18, no. 14, pp. 14439–14453, 2010.

[114] P. T. Rakich, C. Reinke, R. Camacho, P. Davids, and Z. Wang, "Giant enhancement of stimulated brillouin scattering in the subwavelength limit," *Physical Review X*, vol. 2, no. 1, p. 011008, 2012.

[115] A. Feldman, "Relations between electrostriction and the stress-optical effect," *Physical Review B*, vol. 11, pp. 5112–5114, 1975.

[116] P. Etchegoin, J. Kircher, M. Cardona, C. Grein, and E. Bustarret, "Piezo-optics of gaas," *Physical Review B*, vol. 46, no. 23, p. 15139, 1992.

[117] Z. Popovic, J. Spitzer, T. Ruf, M. Cardona, R. Nötzel, and K. Ploog, "Folded acoustic phonons in gaas/alas corrugated superlattices grown along the [311] direction," *Physical Review B*, vol. 48, no. 3, p. 1659, 1993.

[118] R. E. Newnham, *Properties of Materials: Anisotropy, Symmetry, Structure: Anisotropy, Symmetry, Structure.* OUP Oxford, 2004.

[119] D. R. Lide and T. J. Bruno, *CRC handbook of chemistry and physics.* CRC PressI Llc, 2012.

[120] D. K. Biegelsen, "Photoelastic tensor of silicon and the volume dependence of the average gap," *Physical Review Letters*, vol. 32, no. 21, pp. 1196–1199, 1974.

Bibliography

[121] C. Metzger, M. Ludwig, C. Neuenhahn, A. Ortlieb, I. Favero, K. Karrai, and F. Marquardt, "Self-induced oscillations in an optomechanical system driven by bolometric backaction," *Physical review letters*, vol. 101, no. 13, p. 133903, 2008.

[122] J. Restrepo, J. Gabelli, C. Ciuti, and I. Favero, "Classical and quantum theory of photothermal cavity cooling of a mechanical oscillator," *Comptes Rendus Physique*, vol. 12, no. 9, pp. 860–870, 2011.

[123] S. G. Johnson, M. Ibanescu, M. Skorobogatiy, O. Weisberg, J. Joannopoulos, and Y. Fink, "Perturbation theory for maxwells equations with shifting material boundaries," *Physical review E*, vol. 65, no. 6, p. 066611, 2002.

[124] A. Schliesser, P. DelHaye, N. Nooshi, K. Vahala, and T. Kippenberg, "Radiation pressure cooling of a micromechanical oscillator using dynamical backaction," *Physical Review Letters*, vol. 97, no. 24, p. 243905, 2006.

[125] S. Grblacher, K. Hammerer, M. R. Vanner, and M. Aspelmeyer, "Observation of strong coupling between a micromechanical resonator and an optical cavity field," *Nature*, vol. 406, pp. 724–727, 2009.

[126] G. Anetsberger, O. Arcizet, Q. Unterreithmeier, R. Riviere, A. Schliesser, E. Weig, J. Kotthaus, and T. Kippenberg, "Near-field cavity optomechanics with nanomechanical oscillators," *Nature Physics*, vol. 5, no. 12, pp. 909–914, 2009.

[127] A. Fainstein, N. Lanzillotti-Kimura, B. Jusserand, and B. Perrin, "Strong optical-mechanical coupling in a vertical gaas/alas microcavity for subterahertz phonons and near-infrared light," *Physical review letters*, vol. 110, no. 3, p. 037403, 2013.

[128] H. Elsner, H. Meyer, A. Voigt, and G. Grützner, "Evaluation of ma-n 2400 series duv photoresist for electron beam exposure," *Microelectronic engineering*, vol. 46, no. 1, pp. 389–392, 1999.

[129] A. Ivanisevic and C. A. Mirkin, "dip-pen nanolithography on semiconductor surfaces," *Journal of the American Chemical Society*, vol. 123, no. 32, pp. 7887–7889, 2001.

[130] A. Griñe, J. Clevenger, M. Martinez, F. Austin, P. Vigil, K. Romero, R. Timon, G. Patrizi, and C. Sullivan, "Pre-photolithographic gaas surface treatment for improved photoresist adhesion during wet chemical etching and improved wet etch profiles,"

[131] M. Kirchner and M. Kahl, "Raith-electron beam lithography for research," in *Proceedings of the III National Conference on Nanotechnology NANO*, 2009.

[132] D. Kyser and N. Viswanathan, "Monte carlo simulation of spatially distributed beams in electron-beam lithography," *Journal of Vacuum Science and Technology*, vol. 12, no. 6, pp. 1305–1308, 1975.

[133] P. Rai-Choudhury, *Handbook of microlithography, micromachining, and microfabrication*, vol. 1. Inspec/Iee, 1997.

[134] M. Borselli, T. J. Johnson, and O. Painter, "Beyond the rayleigh scattering limit in high-q silicon microdisks: theory and experiment," *Optics Express*, vol. 13, no. 5, pp. 1515–1530, 2005.

[135] A. Gondarenko, J. S. Levy, and M. Lipson, "High confinement micronscale silicon nitride high q ring resonator," *Opt. Express*, vol. 17, no. 14, pp. 11366–11370, 2009.

[136] L. Collot, V. Lefevre-Seguin, M. Brune, J. Raimond, and S. Haroche, "Very high-q whispering-gallery mode resonances observed on fused silica microspheres," *EPL (Europhysics Letters)*, vol. 23, no. 5, p. 327, 1993.

[137] S. Bouchoule, S. Azouigui, S. Guilet, G. Patriarche, L. Largeau, A. Martinez, L. Le Gratiet, A. Lemaitre, and F. Lelarge, "Anisotropic and smooth inductively coupled plasma etching of iii-v laser waveguides using hbr-o2 chemistry," *Journal of The Electrochemical Society*, vol. 155, no. 10, pp. H778–H785, 2008.

[138] S. Adachi, "Chemical etching of inp and ingaasp/inp," *Journal of The Electrochemical Society*, vol. 129, no. 3, pp. 609–613, 1982.

[139] M. Gad-el Hak, *The MEMS handbook*, vol. 17. CRC PressI Llc, 2002.

[140] H. Kuiken, J. Kelly, and P. Notten, "Etching profiles at resist edges i. mathematical models for diffusion-controlled cases," *Journal of The Electrochemical Society*, vol. 133, no. 6, pp. 1217–1226, 1986.

[141] K. Hjort, "Sacrificial etching of iii-v compounds for micromechanical devices," *Journal of Micromechanics and Microengineering*, vol. 6, no. 4, p. 370, 1999.

Bibliography

[142] E. Yablonovitch, T. Gmitter, J. Harbison, and R. Bhat, "Extreme selectivity in the lift-off of epitaxial gaas films," *Applied Physics Letters*, vol. 51, no. 26, pp. 2222–2224, 1987.

[143] S. Koseki, *Monolithic Waveguide Coupled Gallium Arsenide Microdisk Microcavity Containing Indium Gallium Arsenide Quantum Dots*. ProQuest, 2008.

[144] U. Khankhoje, S. Kim, B. Richards, J. Hendrickson, J. Sweet, J. Olitzky, G. Khitrova, H. Gibbs, and A. Scherer, "Modelling and fabrication of gaas photonic-crystal cavities for cavity quantum electrodynamics," *Nanotechnology*, vol. 21, no. 6, p. 065202, 2010.

[145] J. Sweet, B. Richards, J. Olitzky, J. Hendrickson, G. Khitrova, H. Gibbs, D. Litvinov, D. Gerthsen, D. Hu, D. Schaadt, *et al.*, "Gaas photonic crystal slab nanocavities: Growth, fabrication, and quality factor," *Photonics and Nanostructures-Fundamentals and Applications*, vol. 8, no. 1, pp. 1–6, 2010.

[146] B. Guan, X. Guo, T. Liang, X. Gu, J. Deng, J. Guo, H. Yang, Q. Lin, and G. Shen, "Sacrificial algaas etching for microstructures in integrated optoelectronic devices," *Journal of applied physics*, vol. 100, p. 113508, 2006.

[147] X. Sun, L. Hu, H. Song, Z. Li, D. Li, H. Jiang, and G. Miao, "Selective wet etching of $al_{0.7}ga_{0.3}$as layer in concentrated hcl solution for peeling off gaas microtips," *Solid-State Electronics*, vol. 53, no. 9, pp. 1032–1035, 2009.

[148] M. Borselli, *High-Q microresonators as lasing elements for silicon photonics*. PhD thesis, California Institute of Technology, 2006.

[149] M. Soltani, "Novel integrated silicon nanophotonic structures using ultra-high q resonators," 2009.

[150] S. Combrié, A. De Rossi, Q. V. Tran, and H. Benisty, "Gaas photonic crystal cavity with ultrahigh¡ i¿ q¡/i¿: microwatt nonlinearity at 1.55 μm," *Optics letters*, vol. 33, no. 16, pp. 1908–1910, 2008.

[151] Y. Okamura, S. Yoshinaka, and S. Yamamoto, "Measuring mode propagation losses of integrated optical waveguides: a simple method," *Applied Optics*, vol. 22, no. 23, pp. 3892–3894, 1983.

[152] V. R. Almeida and M. Lipson, "Optical bistability on a silicon chip," *Optics letters*, vol. 29, no. 20, pp. 2387–2389, 2004.

[153] R. Kamikawachi, I. Abe, A. Paterno, H. Kalinowski, M. Muller, J. Pinto, and J. Fabris, "Determination of thermo-optic coefficient in liquids with fiber bragg grating refractometer," *Optics Communications*, vol. 281, no. 4, pp. 621–625, 2008.

[154] E. McLaughlin, "The thermal conductivity of liquids and dense gases," *Chemical Reviews*, vol. 64, no. 4, pp. 389–428, 1964.

[155] G. M. Hale and M. R. Querry, "Optical constants of water in the 200-nm to 200-μm wavelength region," *Applied optics*, vol. 12, no. 3, pp. 555–563, 1973.

[156] W. C. Hurlbut, Y.-S. Lee, K. Vodopyanov, P. Kuo, and M. Fejer, "Multiphoton absorption and nonlinear refraction of gaas in the mid-infrared," *Optics letters*, vol. 32, no. 6, pp. 668–670, 2007.

[157] S. Krishnamurthy, Z. G. Yu, L. P. Gonzalez, and S. Guha, "Temperature-and wavelength-dependent two-photon and free-carrier absorption in gaas, inp, gainas, and inasp," *Journal of Applied Physics*, vol. 109, no. 3, pp. 033102–033102, 2011.

[158] D. Kleinman, R. C. Miller, and W. Nordland, "Two-photon absorption of nd laser radiation in gaas," *Applied Physics Letters*, vol. 23, no. 5, pp. 243–244, 1973.

[159] T. J. Johnson, M. Borselli, and O. Painter, "Self-induced optical modulation of the transmission through a high-q silicon microdisk resonator," *Optics express*, vol. 14, no. 2, pp. 817–831, 2006.

[160] M. Soltani, S. Yegnanarayanan, Q. Li, A. A. Eftekhar, and A. Adibi, "Self-sustained gigahertz electronic oscillations in ultrahigh-q photonic microresonators," *Physical Review A*, vol. 85, no. 5, p. 053819, 2012.

[161] N. Cazier, X. Checoury, L.-D. Haret, and P. Boucaud, "High-frequency self-induced oscillations in a silicon nanocavity.," *Optics express*, vol. 21, no. 11, pp. 13626–13638, 2013.

[162] E. Yablonovitch, C. Sandroff, R. Bhat, and T. Gmitter, "Nearly ideal electronic properties of sulfide coated gaas surfaces," *Applied physics letters*, vol. 51, no. 6, pp. 439–441, 1987.

Bibliography

[163] C. I. Ashby, K. R. Zavadil, A. G. Baca, P.-C. Chang, B. Hammons, and M. Hafich, "Metal-sulfur-based air-stable passivation of gaas with very low surface-state densities," *Applied Physics Letters*, vol. 76, no. 3, pp. 327–329, 2000.

[164] H. Oigavva, J.-F. Fan, Y. Nannichi, H. Sugahara, and M. Oshima, "Universal passivation effect of (nh4) 2sx treatment on the surface of iii-v compound semiconductors," 1991.

[165] G. Mariani, R. B. Laghumavarapu, B. Tremolet de Villers, J. Shapiro, P. Senanayake, A. Lin, B. J. Schwartz, and D. L. Huffaker, "Hybrid conjugated polymer solar cells using patterned gaas nanopillars," *Applied Physics Letters*, vol. 97, no. 1, pp. 013107–013107, 2010.

[166] S. Offsey, J. Woodall, A. Warren, P. Kirchner, T. Chappell, and G. Pettit, "Unpinned (100) gaas surfaces in air using photochemistry," *Applied physics letters*, vol. 48, no. 7, pp. 475–477, 1986.

[167] D. K. Sparacin, S. J. Spector, and L. C. Kimerling, "Silicon waveguide sidewall smoothing by wet chemical oxidation," *Journal of Lightwave Technology*, vol. 23, no. 8, p. 2455, 2005.

[168] Q. P. Unterreithmeier, E. M. Weig, and J. P. Kotthaus, "Universal transduction scheme for nanomechanical systems based on dielectric forces," *Nature*, vol. 458, no. 7241, pp. 1001–1004, 2009.

[169] R. Regener and W. Sohler, "Loss in low-finesse ti: Linbo3 optical waveguide resonators," *Applied Physics B*, vol. 36, no. 3, pp. 143–147, 1985.

[170] Y. Deng, F. Liu, Z. C. Leseman, and M. Hossein-Zadeh, "Thermo-optomechanical oscillator for sensing applications," *Optics express*, vol. 21, no. 4, pp. 4653–4664, 2013.

[171] Y. M. B. S. Y. D. Burenkov, Yu. A. and S. P. Nikanorov, "Temperature dependence of the elastic constants of gaas," *Sov. Phys. Solid State*, vol. 15, no. 6, pp. 1175–1177, 1973.

[172] R. t. Cottam and G. Saunders, "The elastic constants of gaas from 2 k to 320 k," *Journal of Physics C: Solid State Physics*, vol. 6, no. 13, p. 2105, 1973.

[173] J. Rieger, *AFM manipulation of damping in nanomechanical resonators.* PhD thesis, Juli 2013.

[174] R.A.Waldron, "Perturbation theory of resonant cavities," 1960.

[175] J. Restrepo, C. Ciuti, and I. Favero, "Single polariton optomechanics," *arXiv preprint arXiv:1307.4282*, 2013.

[176] D. Weiss, V. Sandoghdar, J. Hare, V. Lefevre-Seguin, J.-M. Raimond, and S. Haroche, "Splitting of high-¡ i¿ q¡/i¿ mie modes induced by light backscattering in silica microspheres," *Optics letters*, vol. 20, no. 18, pp. 1835–1837, 1995.

[177] N. W. McLachlan, *Bessel functions for engineers.* Clarendon Press Oxford, 1955.

[178] "The engineering toolbox," *http://www.engineeringtoolbox.com/emissivity-coefficients-d_447.html.*

[179] E. Gmelin, M. Asen-Palmer, M. Reuther, and R. Villar, "Thermal boundary resistance of mechanical contacts between solids at sub-ambient temperatures," *Journal of Physics D: Applied Physics*, vol. 32, no. 6, p. R19, 1999.

[180] E. Palik, *Handbook of optical constants of solids*, vol. 3. Academic press, 1998.

[181] F. Della Corte, G. Cocorullo, M. Iodice, and I. Rendina, "Temperature dependence of the thermo-optic coefficient of inp, gaas, and sic from room temperature to 600 k at the wavelength of 1.5 μm," *Applied Physics Letters*, vol. 77, no. 11, pp. 1614–1616, 2000.

[182] S. Adachi, "Gaas, alas, and $al_x ga_{1-x}$ as material parameters for use in research and device applications," *Journal of Applied Physics*, vol. 58, no. 3, pp. R1–R29, 1985.

[183] S. Adachi, *Properties of aluminium gallium arsenide*, vol. 7. Inspec/Iee, 1993.

[184] S. Gehrsitz, F. Reinhart, C. Gourgon, N. Herres, A. Vonlanthen, and H. Sigg, "The refractive index of algaas below the band gap: Accurate determination and empirical modeling," *Journal of Applied Physics*, vol. 87, p. 7825, 2000.

[185] J. Gardeniers, H. Tilmans, and C. Visser, "Lpcvd silicon-rich silicon nitride films for applications in micromechanics, studied with statistical experimental design*," *Journal of Vacuum Science & Technology A: Vacuum, Surfaces, and Films*, vol. 14, no. 5, pp. 2879–2892, 1996.

Bibliography

[186] R. Camacho, J. Chan, M. Eichenfield, and O. Painter, "Characterization of radiation pressure and thermal effects in a nanoscale optomechanical cavity," *Optics express*, vol. 17, no. 18, pp. 15726–15735, 2009.

Appendix A

Optics

A.0.1 Whispering gallery modes

The description of the eigenmodes of an optical disk resonator starts with Maxwell's equations in the absence of free charges and currents in the material (Eq. A.1):

$$
\begin{cases}
\vec{\nabla} \cdot \vec{D} = 0 & \vec{\nabla} \times \vec{E} = -\dfrac{\partial \vec{B}}{\partial t} \\
\vec{\nabla} \cdot \vec{B} = 0 & \vec{\nabla} \times \vec{H} = \dfrac{\partial \vec{D}}{\partial t}
\end{cases}
\text{with}
\begin{cases}
\vec{D} = \varepsilon_0 \, \varepsilon_r \, \vec{E} \\
\vec{B} = \mu_0 \, \mu_r \, \vec{H}
\end{cases}
\tag{A.1}
$$

This leads to the following eigenvalue equation for the field $\vec{F}$, which represents either the electric or magnetic field:

$$
\nabla^2 \vec{F} + n^2 \frac{\omega^2}{c^2} \, \vec{F} = 0
\tag{A.2}
$$

Here $c = 1/\sqrt{\varepsilon_0 \, \mu_0}$ and $n = 1/\sqrt{\varepsilon_r \, \mu_r}$ are respectively the speed of light and the disk material's bulk refractive index. (We limit our discussion to dielectric materials that have isotropic and homogeneous ε_r and μ_r, with little dispersion in the frequency range of interest[1]). The solution to Equation A.2 in spherical coordinates (r, ϕ, x) can be computed analytically under two specific assumptions. First we assume that there are two sets of uncoupled optical modes with orthogonal polarizations, labeled TM and TE modes. For a TM mode, the electric field is polarized perpendicularly to the disk plane and the magnetic field lies in the plane of the cavity (H^r, H^ϕ, E^x)$\neq$0, whereas for a TE mode, the non-vanishing mode components are (E^r, E^ϕ, H^x). This

---

[1]The case of an inhomogeneous and anisotropic relative permitivity ε_r caused by strain in the disk is solved numerically in section 3.8.2.

assumption is reminiscent of the usual effective index approach for treating optical slab waveguides (see section 1.1.2): it holds reasonably well as long as the disk thickness h is greater than the wavelength in the dielectric ($h > \lambda/n$). For thinner disks, TE and TM modes start to hybridize and the distinction between TE and TM no longer holds. Second we assume that we can separate the variables in the field's spatial dependence, i.e. $F^x(r, \phi, x) = \Psi(r)\Phi(\phi)X(x)$. These assumptions lead to a set of three equations, describing the axial, azimuthal and radial properties of the WGM. The axial characteristics are defined by the axial number l, which describes the number of maxima in the electric field along the x direction (we always have $l = 1$ throughout this thesis), while the azimuthal properties are defined by the azimuthal number m, which defines the WGM's $e^{im\phi}$ spatial dependency. Below we focus on the radial profile $\Psi(r)$ of the WGM, given by Eq. A.3:

$$\Psi(r) = \begin{cases} N J_m\left(\tilde{k}n_\xi r\right) & r \leq R \\ \dfrac{N J_m\left(\tilde{k}n_\xi R\right)}{H_m^{(1)}\left(\tilde{k}R\right)} H_m^{(1)}\left(\tilde{k}r\right) & r \geq R \end{cases} \tag{A.3}$$

Here N is a normalization constant, $\tilde{k}$ the WGM wavenumber and R the disk radius. The resonance eigenfrequencies can be found by enforcing the continuity of the field's tangential components E^x and H^ϕ (E^ϕ and H^x) for TM (TE) mode at the dielectric/air boundary (r = R):

$$\begin{cases} n_\xi \dfrac{\dot{J}_m\left(\tilde{k}n_\xi R\right)}{J_m\left(\tilde{k}n_\xi R\right)} - \dfrac{\dot{H}_m^{(1)}\left(\tilde{k}R\right)}{H_m^{(1)}\left(\tilde{k}R\right)} = 0 & \text{TM modes} \\[4mm] \dfrac{\dot{J}_m\left(\tilde{k}n_\xi R\right)}{J_m\left(\tilde{k}n_\xi R\right)} - n_\xi \dfrac{\dot{H}_m^{(1)}\left(\tilde{k}R\right)}{H_m^{(1)}\left(\tilde{k}R\right)} = 0 & \text{TE modes} \end{cases} \tag{A.4}$$

By solving these equations for the wave vector $\tilde{k}$, we obtain the complex WGM eigenfrequency $\tilde{\omega} = c\tilde{k}$. Note that the imaginary part of the resonance frequency stems from the curved geometry of the disk and causes the WGM to have a finite radiative quality factor Q_{rad}. Also notice that, if m is fixed, multiple solutions of Eq. A.4 exist. These solutions can be labeled with the radial number p (p = 1, 2,...). Once F^x is known, the other mode
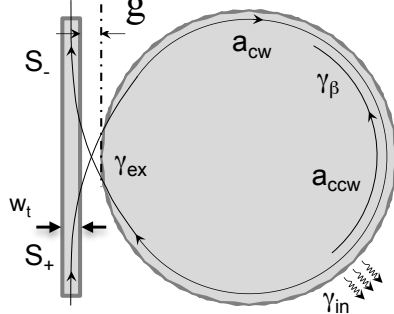
Figure A.1: Schematic illustrating the parameters used for the WGM doublet splitting description, where rough resonator sidewalls scatter energy between clockwise and counterclockwise propagating modes.

components can be obtained by using Eq. A.1:

$$
\begin{cases}
H^r = -\dfrac{m}{\mu_0 r \tilde{\omega}} E^x \\[2mm]
H^\phi = \dfrac{i}{\mu_0 \tilde{\omega}} \dfrac{\partial E^x}{\partial r}
\end{cases}
\text{(TM modes)} \quad \text{and} \quad
\begin{cases}
E^r = \dfrac{m}{\varepsilon_0 \varepsilon_r r \tilde{\omega}} H^x \\[2mm]
E^\phi = \dfrac{-i}{\varepsilon_0 \varepsilon_r \tilde{\omega}} \dfrac{\partial H^x}{\partial r}
\end{cases}
\text{(TE modes)}
\tag{A.5}
$$

Doublet splitting

For each chosen radial and azimuthal numbers (p,m), a perfectly symmetric rotationally invariant disk supports two frequency degenerate (p,m) WGMs: the clockwise (cw) and counterclockwise (ccw) propagating modes. In reality, small fabrication imperfections, or even the non-isotropic nature of the underlying crystal lattice, can break the symmetry and lift this degeneracy, resulting in a splitting of the WGM resonance into a doublet [176], as visible in section 5.4.2. In the case where the optical input power is injected in the cw mode (see Figure A.1), the coupling between the two modes leads to:

$$
\begin{aligned}
\frac{da_{ccw}}{dt} &= -i\omega_0 a_{ccw} - \left(\frac{\gamma_{\text{int}}}{2} + \frac{\gamma_{\text{ext}}}{2} \right) a_{ccw} + i\frac{\gamma_\beta}{2} a_{cw} \\
\frac{da_{cw}}{dt} &= -i\omega_0 a_{cw} - \left(\frac{\gamma_{\text{int}}}{2} + \frac{\gamma_{\text{ext}}}{2} \right) a_{cw} + i\frac{\gamma_\beta}{2} a_{ccw} + i\sqrt{\gamma_{\text{ext}}} s_+ \\
s_- &= s_+ + i\sqrt{\gamma_{\text{ext}}} a_{cw}
\end{aligned}
\tag{A.6}
$$

Here γ_β is the energy exchange rate due to photons scattering between the cw and ccw modes and ω_0 the WGM resonance frequency. We introduce the
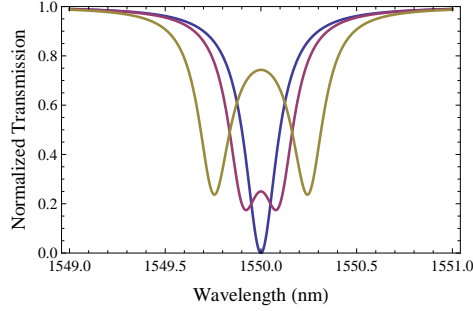
Figure A.2: Normalized optical transmission in the critical coupling coupling regime (with $\gamma_{\text{int}} = \gamma_{\text{ext}} = 0.1$), and γ_β worth respectively 0, 2 and 5 times γ_{int} (blue, red and yellow curves).

.

standing wave basis:

$$
\begin{aligned}
a_1 &= \frac{1}{\sqrt{2}} \left(a_{ccw} + a_{cw} \right) \leftrightarrow a_{ccw} = \frac{1}{\sqrt{2}} \left(a_1 + a_2 \right) \\
a_2 &= \frac{1}{\sqrt{2}} \left(a_{ccw} - a_{cw} \right) \leftrightarrow a_{cw} = \frac{1}{\sqrt{2}} \left(a_1 - a_2 \right)
\end{aligned}
\tag{A.7}
$$

The steady-state solution for the standing wave mode amplitudes is given by Eq. A.8:

$$
a_{1,2} = \frac{i\sqrt{\gamma_{\text{ext}}/2}}{\mp \left(i\Delta\omega - \left(\frac{\gamma_{\text{int}}}{2} + \frac{\gamma_{\text{ext}}}{2} \right) \right) - i\frac{\gamma_\beta}{2}} s_+
\tag{A.8}
$$

The optical transmission is then given by:

$$
\frac{|s_-|^2}{|s_+|^2} = \left| 1 + i\sqrt{\frac{\gamma_{\text{ext}}}{2}} \left(\frac{a_1}{s_+} - \frac{a_2}{s_+} \right) \right|^2
\tag{A.9}
$$

Two transmission minima occur at $\omega = \omega_0 \pm \gamma_\beta/2$. In the measurement, the backscattering effect can hence be quantified by the spectral distance γ_β between the two minima, and translated into the quantity $Q_\beta \equiv \omega_0/\gamma_\beta$. If $Q_\beta \gg Q_{\text{int}}$, the degeneracy of the ccw and cw WGMs still holds (meaning that the coupling between the cw and ccw modes is weaker than the coupling of each of them to its environment). When $Q_\beta \ll Q_{\text{int}}$, the converse situation occurs: the cw-ccw degeneracy is lifted and a doublet is resolved in the measured transmission spectrum. The two standing-wave modes are well resolved spectrally. Figure A.2 plots the doublet resonance spectrum in case of $\gamma_{\text{int}} = \gamma_{\text{ext}} = 0.1$ and γ_β worth 0, 0.2 and 0.5. Note that the magnitude of the doublet splitting of a WGM resonance can provide an estimation of the disk resonator's surface roughness [134].

216

Appendix B

Mechanics

B.1   bending of the suspended waveguide

The Euler-Bernoulli equation gives the relation ship between the beam deflection $\delta(z)$ and the load q:

$$EI\frac{d^4\delta}{dz^4} = -q \tag{B.1}$$

Integrating Eq. B.1 four times gives the deflection as function of the position along the beam:

$$\delta(z) = -\frac{q}{EI}\frac{z^4}{24} + c_1\frac{z^3}{6} + c_2\frac{z^2}{2} + c_3 z + c_4 \tag{B.2}$$

The beam is clamped at both ends in z=0 and z=L. These boundary conditions imply $\delta(0) = \delta'(0) = 0$ and $\delta(L) = \delta'(L) = 0$. Solving for these boundary conditions provides $c_3 = c_4 = 0$; $c_1 = \frac{qL}{2EI}$ and $c_2 = \frac{-qL^2}{12EI}$. Thus $\delta(z)$ equals:

$$\delta(z) = -\frac{qz^4}{24EI} + \frac{qLz^3}{12EI} - \frac{qL^2z^2}{24EI} = -\frac{qz^2}{24EI}(z-L)^2 \tag{B.3}$$

The sag is maximal at the middle of the beam, so $\delta_{\max} = |\delta(L/2)| = \frac{qL^4}{384EI}$

B.2   Out of plane modes

Equation B.4 provides the equation of motion for the transverse displacement w of a plate :

$$D\nabla^4 w + \rho_s\frac{\partial^2 w}{\partial t^2} = 0 \tag{B.4}$$

where D is the flexural rigidity defined as:

$$D = \frac{Eh^3}{12\left(1 - \sigma^2\right)} \tag{B.5}$$

Here E, h, σ, and ρ_s are respectively the plate's Young's modulus, thickness, Poisson ratio and mass per unit surface. For free plate vibrations, the displacement as a function of time t reads:

$$w = W\cos\omega t \tag{B.6}$$

with ω the angular frequency and W a function of the coordinates r and θ which represents the deformation amplitude. By inserting Eq.B.6 in Eq.B.4, we get:

$$\left(\nabla^4 - k^4\right)W = 0 \tag{B.7}$$

with:

$$k^4 = \frac{\rho_s\omega^2}{D} \tag{B.8}$$

Equation B.7 can be factored as:

$$\left(\nabla^2 + k^2\right)\left(\nabla^2 - k^2\right)W = 0 \tag{B.9}$$

A solution to the differential equation (B.7) can therefore be expressed as a linear combination of the solutions W_1 and W_2 to equations (B.10):

$$\begin{cases} \nabla^2 W_1 + k^2 W_1 = 0 \\ \nabla^2 W_2 - k^2 W_2 = 0 \end{cases} \tag{B.10}$$

Assuming W is continuous and periodic in θ, it is expressed as its Fourier series:

$$W\left(r, \theta\right) = \sum_{M=0}^{\infty} W_M\left(r\right)\,\cos M\theta\,+\,\sum_{M=1}^{\infty} W_M^*\left(r\right)\,\sin M\theta \tag{B.11}$$

Subsituting (B.11) into (B.10) provides the set of equations (B.12) for W_M, as well as identical set of equations for W_M^* :

$$\begin{cases} \frac{d^2 W_{M1}}{dr^2} + \frac{1}{r}\frac{dW_{M1}}{dr} - \left(\frac{M^2}{r^2} - k^2\right)W_{M1} = 0 \\ \frac{d^2 W_{M2}}{dr^2} + \frac{1}{r}\frac{dW_{M2}}{dr} - \left(\frac{M^2}{r^2} - k^2\right)W_{M2} = 0 \end{cases} \tag{B.12}$$

Equations (B.12) are forms of Bessel's equations, whose solutions are [177]:

$$\begin{cases} W_{M1} = A_M J_M\left(kr\right) + B_M\,Y_M\left(kr\right) \\ W_{M2} = C_M\,I_M\left(kr\right) + D_M\,K_M\left(kr\right) \end{cases} \tag{B.13}$$

Here J_M and Y_M are respectively the Bessel functions of first and second kind, while I_M and K_M are the modified Bessel functions of first and second kind respectively. Therefore the general solution to Equation B.7 giving the deformation amplitude due to the free transverse oscillations of a plate reads:

$$W(r,\theta) = \sum_{n=0}^{\infty} [\, A_M J_M(kr) + B_M Y_M(kr) + C_M I_M(kr) + D_M K_M(kr)] \cos M\theta$$

$$+ \sum_{n=1}^{\infty} [\, A_M^* J_M(kr) + B_M^* Y_M(kr) + C_M^* I_M(kr) + D_M^* K_M(kr)] \sin M\theta$$

$$\text{(B.14)}$$

In the case of a plate with rotationally invariant boundary conditions, the $\sin M\theta$ terms can be discarded. Furthermore if the plate does not have a hole in the center (e.g. a simple circular plate) the coefficients B_M and D_M must be zero, as the terms $Y_M(kr)$ and $K_M(kr)$ diverge for r=0. The deformation amplitude of the M_{th} mode then reads:

$$W_M(r,\theta) = [A_M J_M(kr) + C_M I_M(kr)] \cos(M\theta) \qquad \text{(B.15)}$$

Appendix C

Cryostat operation

C.0.1   In-out coupling

The coupling of light in- and out of a waveguide is the main weakness of the current setup, both in terms of efficiency and stability (see section C.0.2).

Injection

Light injection efficiency is strongly dependent on the focused laser spot size produced by the long working distance microscope objective. (Small spots yield better coupling - this is confirmed through BPM simulations not shown here). Equation C.1 relates a Gaussian beam's waist radius to its angular divergence θ (see Fig. C.1, a). According to this approximate formula, the smallest waist diameter attainable at $\lambda \simeq 1.3$ μm with a 0.35 NA objective is 2.3 μm.

$$\theta = \frac{\lambda}{\pi w_0} \tag{C.1}$$

Using the knife edge method we experimentally measure our focused spot diameter to be 2.9$\pm$0.1 μm, without the cryostat window[1]. The spot size is very sensitive to any error in beam tilt, centering or collimation. While the obtained spot size is relatively small, it is still $\sim$50 % larger than what can be achieved with a micro-lensed fiber, resulting in a less efficient coupling. On a practical note, since the chip cannot be seen inside the cryostat, a waveguide is identified by counting the number of waveguides between it and the sample edge.

---

[1]We verify with ray tracing software that the thin cryostat windows do not negatively impact the spot size, provided they are orthogonal to the optical axis.
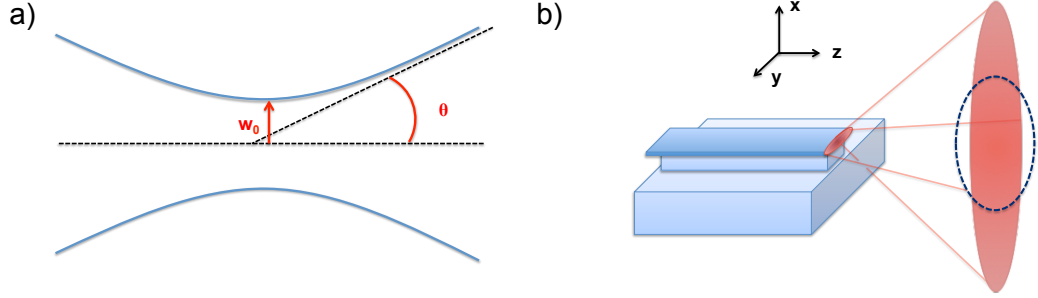
Figure C.1: (a) Illustration of a gaussian beam's waist radius w_0 and divergence angle θ which are linked through Eq. C.1. The blue lines outline the position at which the field intensity drops to $1/e^2 \simeq 0.14$ of the axial value. The numerical aperture is defined as $\sin(\theta)$ in air. (b) Inefficient light collection with the aspheric lens because of the large optical divergence along the x direction. The dashed black line marks the outer edges of the aspheric lens.

Collection - Fiber coupling

Light exiting the GaAs chip is collected with a 0.54 NA aspheric lens positioned behind the second cryostat window. This collection is non-optimal due to the strong divergence of the output beam along the chip growth direction x (see Figure C.1, b). Indeed as the elliptic guided mode in the waveguide is strongly (resp. weakly) confined in the x (y) direction, the output beam has a large (small) divergence along the x (y) direction, as expected through Eq. C.1. Far field simulations of the guided mode reveal the divergence θ along x is close to 70 degrees (see Fig. 1.14), meaning only about half the optical power is actually collected by the aspheric lens. (A 0.5 NA lens only accepts rays with an angular divergence below 30 degrees).

The collected light is then sent upon a fiber collimator (C2) to be coupled into a single mode fiber. Because of the beam's anisotropic divergence and aberrations brought on by the aspheric lens[2] this coupling is also only about 40 % efficient, close to the value predicted by ray tracing software. Because of these combined inefficiencies over three quarters of the power leaving the waveguide is lost before reaching the optical amplifier. This shortcoming could be solved by employing an inverted taper design at the output facet to reduce angular divergence, or better yet by collecting light directly inside the cryostat, as detailed in section 6.2.8. Furthermore both input and output are extremely sensitive to mechanical and thermal fluctuations which negatively affect the coupling stability. These are discussed in the following section.

---

[2]Aspheric lenses are designed to be diffraction limited for a specific wavelength. Their performance rapidly degrades when the operation wavelength is removed from the design wavelength. We could not find large NA aspheres designed for λ=1300 nm.

C.0.2 Coupling stability

Coupling light into a sub-micrometer thick waveguide from a one centimeter distance with a microscope objective requires the same level of angular precision as aiming at a one meter target from 10 km. (The precision requirements are similar for the collected light which must be focused inside the $\sim$10 μm core of a single mode fiber). Because of this any fluctuations in the position of the chip with respect to the optical axis severely compromise the coupling efficiency.

Mechanical stability

Great care is taken to minimize all mechanical vibrations: the setup is mounted on an optical table with air damping, vibrations from the pumping system are damped using a concrete block and the pumps are switched off a low temperature, the liquid helium bottle is positioned on inflated tires to shield it from the building's vibrations and the helium transfer rod is fixed upon the ceiling with an elastic cord and mechanically supported by the optical table, so that it does not weigh upon the cryostat and transfer its vibrations to it. With these measures and in the absence of cryogenic cooling the *average* optical transmission measured after C2 is very stable over the course of several hours. Nevertheless transmission fluctuations of $\pm$ 10 to 15 % of total amplitude at frequencies of 10-100 Hz is still present. This is likely due to vibrations in the overhanging cryostat support structure and the setup's non ideal location on the 6th floor of the building.

Thermal stability thermal drift

The light input coupling into the chip is also extremely sensitive to thermal drift when the cryostat is cooled down. The drift is due to fast (timescale of minutes) temperature fluctuations due to variations in the helium flow affecting the top of the cryostat where the cold inner tube is anchored to the outer vacuum shroud (see Fig. 6.2, letter A). An additional long term drift is due to gradual cooling of the cryostat support structure over the course of several hours (Fig. 6.2, letter B). Indeed the $\sim 22 \cdot 10^{-6}$ K^{-1} thermal expansion coefficient of duralumin (material the support structure is made of) means a 1°C change in a 10 cm long element is enough to displace the chip sample by 2 microns and disalign the input light coupling. We measured that exposure to the cold helium fumes cooled element B by over 10°C over the course of several hours. (On the contrary the temperature measured at the level of the sample chip varies by less than 0.02 K throughout the whole experiment). Because of these two sources of drift the optimal light input
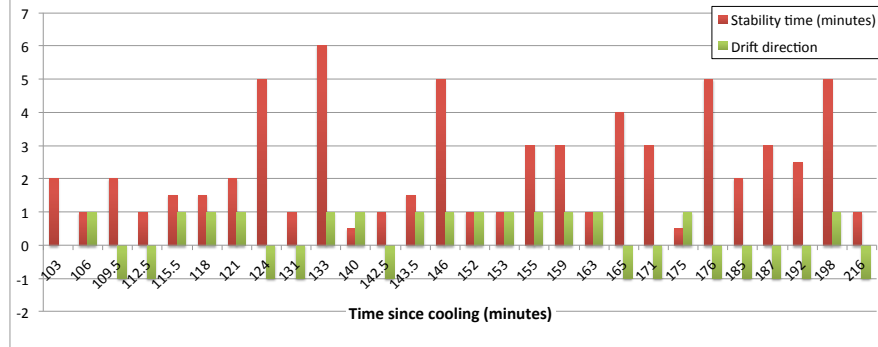
Figure C.2: This diagram illustrates the un-optimized setup's coupling stability measured over the course of a three and a half hour period, underscoring the problem of thermal drift. The average time the setup stays coupled is under two and a half minutes. The green bar (which takes the value ± 1) indicates the drift direction and illustrates the seemingly random nature of the process.

coupling could not be maintained for more than a few minutes (see Fig. C.2). Isolating the support structure with foam, releasing the cold helium exhaust further from the cryostat and adding at temperature feedback controller with heating coils to maintain a constant temperature at the top of the cryostat (point A) is sufficient to remove most but not all of the thermal drift. These efforts have enabled us to obtain a decent stability of the light input coupling at low temperature during 15-30 minutes.

C.0.3   Cryogenic operation

Cryogenic operation comes with two requirements. The first is to cryogenically reach the lowest possible chip temperature before relying on optomechanical cooling in order to facilitate access to the quantum regime (see Eq. 3.20). The second is the need to very accurately measure the temperature close to the chip in order to make sure the sample appropriately thermalizes. (These temperature measurements will serve to calibrate mechanical spectra). To this end we added a second temperature sensor (Si diode) on the cold finger holding the chip in addition to the first sensor already present on the sample mount (see Fig. C.3, a and Fig. C.4, a). While the temperature of the first sensor went down to 4.3 K as expected, the temperature at the level of the second sensor could initially not be brought below 20 K. This is in part due to the problematic contribution of black body radiation emitted by the surrounding cryostat walls and glass windows, which is discussed in the following.

Material	Emissivity ϵ
Glass	0.92-0.94
Copper (heavily oxidized)	0.78
Copper (polished)	0.02-0.05
Aluminum (polished)	0.03

Table C.1: Emissivity of various materials used in the cryostat setup. Data taken from [178].

Influence of black body radiation

All bodies at non-zero temperature emit electromagnetic radiation which is peaked around a wavelength corresponding to the body's outer temperature[3]. A black body is an idealized physical body that absorbs all incoming electromagnetic radiation. The power per unit surface j radiated by a black body is given by Stefan-Boltzmann's law (Eq. C.2):

$$j = \sigma \, T^4 \tag{C.2}$$

Here $\sigma = 5.67 \cdot 10^{-8}$ W·m^{-2}·K^{-4} is the Stephan-Boltzmann constant and T is the temperature of the black body. Real materials (also called grey bodies) emit only a fraction of the energy of a black body at the same temperature. This fraction is called the *emissivity* ϵ, with $0 \leq \epsilon \leq 1$. The emissivity of various materials used in our cryostat setup are listed in Table C.1. The power P emitted by a grey body of surface A is therefore given by

$$P = \epsilon \, A \, \sigma \, T^4 \tag{C.3}$$

In our setup the GaAs sample with the disk resonators is fixed with silver lacquer on a gold sample holder, itself fixed with silver lacquer on a 100 mm long × 5 mm wide × 7 mm thick copper cold finger (see Fig C.3). Two large ⌀= 2.5 cm glass windows are positioned on either side of the cold finger at the sample level to allow for optical in- and out-coupling (see Fig. 6.2). The windows and cryostat walls are $\sim$ 3 mm away from the cold finger without any kind of radiation shielding. As shown in Table C.1, glass behaves almost like a black body : a glass surface emits a large $\sim$ 420 W/m^{-2} at 300 K. In order to get an idea of the influence of thermal radiation on the lowest attainable operating temperature we performed a simple thermal FEM simulation with these three assumptions:

- All outer surfaces of the sample, sample holder and cold finger receive 420 W m^{-2} of radiation.

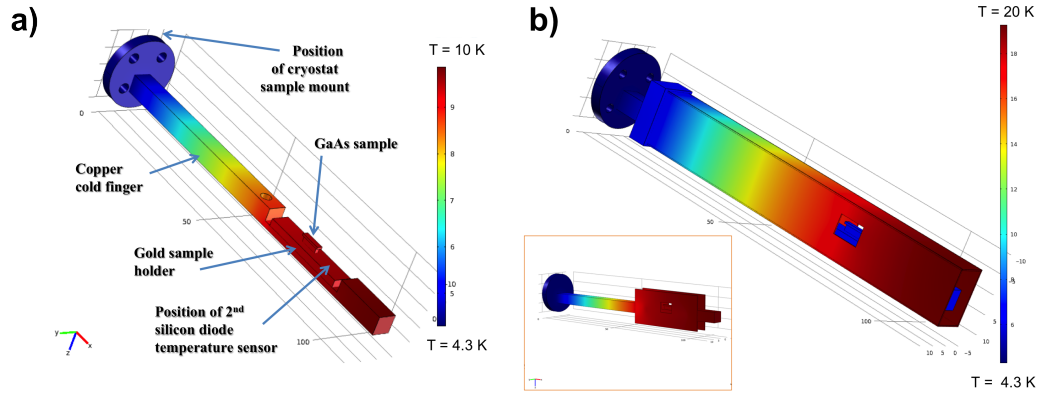[3]e.g. the sun's emission is centered around 500 nm, and that of humans around 10 μm.

225

Figure C.3: (a) Copper cold finger with gold sample mount and GaAs sample. All elements are exposed to uniform radiation of intensity 420 W/m². The circular extremity kept in contact with the cryostat sample mount is kept at a constant 4.3 K in the simulation. The surface color represents the equilibrium temperature. (b) Copper cold finger surrounded by the radiation shield. Note how the radiation shield undergoes significant heating but the cold finger and sample remain cold. Simply having a shield temperature 10 times lower than the cryostat walls and windows divides the emitted power ∼10 000 times to less than 0.04 W/m² (see Eq. C.2). Poor shield design which does not bypass the cold finger shown in inset.

- Thermal contact between all elements is ideal.
- The top of the cold finger is maintained at a constant 4.3 K.

Results of this simulation are shown in Fig. C.3 (a). This shows blackbody radiation can indeed increase the lowest achievable temperature by close to 6 K under the previous assumptions.

C.0.4   Radiation shield design

Here we describe some changes made to the setup in light of the previous observations. The cold finger is surrounded over its whole length by a 0.3 mm thick homemade radiation shield, in which two small windows are cut out in order to maintain optical access (see Fig. C.3, b and Fig. C.4, b). The shield is polished to minimize thermal absorption (see Table C.1) and does not touch the cold finger on any side. Care is also taken to minimize the low-temperature thermal boundary resistances of the mechanical contacts between the different elements [179]. For instance the cold finger is dipped in acid and polished to remove its surface oxide and a sheet of indium foil is added between it and the sample mount (see Fig. C.4, a). The silicon diode temperature sensor is mechanically clamped into contact with the sample holder and high thermal conductivity Apiezon N cryogenic vacuum grease
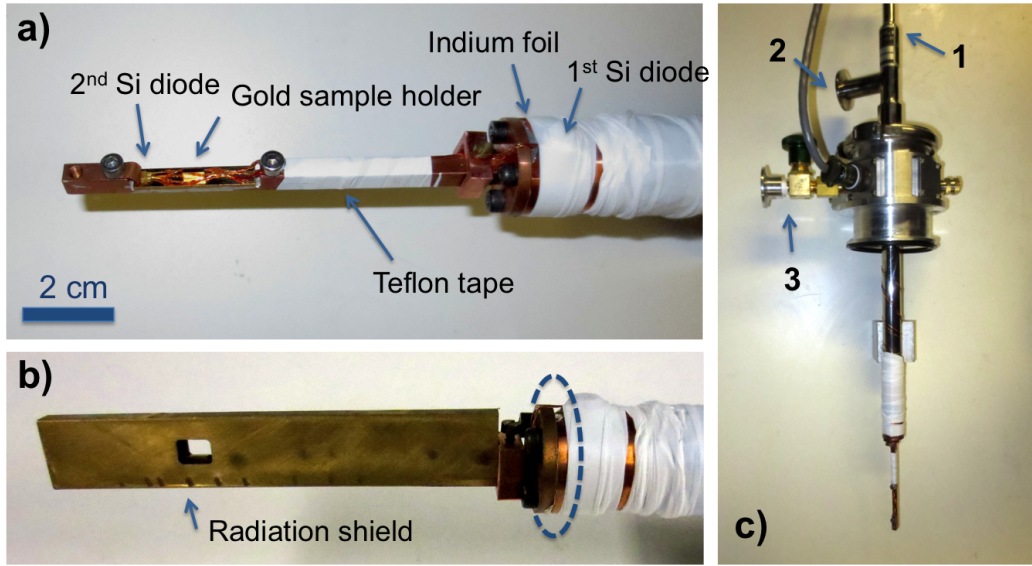
Figure C.4: (a) Top view of the cold finger connected to the cryostat. (b) Same cold finger now protected by the fabricated radiation shield. The dashed circle represents the position of the extremity of the cryostat's default aluminum radiation shield which is removed in these pictures. (c) Side-view of the opened cryostat. **1**) Access for liquid helium transfer rod. **2**) Helium exhaust vent. **3**) Vent connecting the vacuum shroud to the exterior pumping system. The valve can be closed to operate under static vacuum.

is added between these two elements. Finally the electrical leads to the Si sensor are tightly wound around the cryostat tubing with teflon tape in order to minimize thermal contamination of the measurement from the outside. Figure C.3 (b) shows the beneficial influence of the radiation shield on the sample temperature. Note that it is not sufficient to simply shield the GaAs sample alone from thermal radiation: the shield design in the inset of Fig. C.3 (b) just increases the amount of absorbed radiation and raises the sample temperature by 2 K.

C.0.5 Sample temperature - first measurements

With these improvements the sample holder temperature is divided by more than a factor two to just below 8 K. This is slightly above the ∼6 K predicted by the FEM simulation. This discrepancy could be due to both the neglected thermal resistances between the different elements and residual thermal contamination from the diode leads (we used small diameter copper wiring instead of the optimal low thermal conductivity phosphor bronze wiring).

C.0.6 Mathematical accuracy of separating the treatment of reactive and dispersive coupling

$$T(\omega_{laser}, x) = \frac{\Delta\omega^2 + \left(\frac{\gamma_{in}}{2} - \frac{\gamma_{ex}}{2}\right)^2}{\Delta\omega^2 + \left(\frac{\gamma_{in}}{2} + \frac{\gamma_{ex}}{2}\right)^2} \tag{C.4}$$

with $\Delta\omega = \omega_{laser} - \omega_c(x)$. Here ω_{laser} is fixed in the experiment. The terms $\omega_c(x)$ and $\gamma_{ex}(x)$ depend on x. Let us call f and g the functions corresponding respectively to the numerator and the denominator of Eq. C.4, so that $f(x) = \Delta\omega^2 + \left(\frac{\gamma_{in}}{2} - \frac{\gamma_{ex}}{2}\right)^2$ and $g(x) = \Delta\omega^2 + \left(\frac{\gamma_{in}}{2} + \frac{\gamma_{ex}}{2}\right)^2$. Therefore :

$$\begin{aligned}
f'_{total}(x) &= \frac{d}{dx}(\Delta\omega^2) + \frac{d}{dx}\left(\frac{\gamma_{in}}{2} - \frac{\gamma_{ex}}{2}\right)^2 \\
&= f'_{\text{disp}} + f'_{\text{reac}}
\end{aligned} \tag{C.5}$$

and

$$\begin{aligned}
g'_{total}(x) &= \frac{d}{dx}(\Delta\omega^2) + \frac{d}{dx}\left(\frac{\gamma_{in}}{2} + \frac{\gamma_{ex}}{2}\right)^2 \\
&= g'_{\text{disp}} + g'_{\text{reac}}
\end{aligned} \tag{C.6}$$

We thus have:

$$\begin{aligned}
\left(\frac{f}{g}\right)' = \frac{f'_{total}\, g - f\, g'_{total}}{g^2} &= \frac{(f'_{\text{disp}} + f'_{\text{reac}})\, g - f(g'_{\text{disp}} + g'_{\text{reac}})}{g^2} \\
&= \frac{f'_{\text{disp}}\, g - f\, g'_{\text{disp}}}{g^2} + \frac{f'_{\text{reac}}\, g - f\, g'_{\text{reac}}}{g^2} \\
&= \left(\frac{f}{g}\right)'_{\text{disp}} + \left(\frac{f}{g}\right)'_{\text{reac}}
\end{aligned} \tag{C.7}$$

Where each term is derived only with respect to the *dispersive* or *reactive* component.

Appendix D

Material properties

Parameter	Name	Unit	Value	Source
Mechanical parameters				
Young's modulus [100] axis	E	GPa	85.9	[98]
Density	ρ	kg·m^{-3}	5317	[98]
Poisson ratio	σ	-	0.31	[98]
Thermal parameters				
Specific heat at 300 K	c	J·K^{-1}·kg^{-1}	327	[84]
Thermal conductivity	κ	W·K^{-1}·m^{-1}	55	[84]
Linear thermal expansion coefficient at 300K	α_{th}	K^{-1}	5.7·10^{-6}	[84]
Optical parameters				
Refractive index at $\lambda =$ 1550 nm and room temperature	n	-	3.374	[180]
Refractive index at $\lambda =$ 1330 nm and room temperature	n	-	3.40	[180]
Thermo-optic coefficient at 298 K and λ=1.5μm	$\frac{\partial n}{\partial T}$	K^{-1}	2.34·10^{-4}	[181]
			$\sim$2.3·10^{-4}	our work

Table D.1: Gallium Arsenide parameters

Parameter	Name	Unit	Value	Source
Mechanical parameters				
Young's modulus [100] axis	E	GPa	83.86	[182]
Density at 300 K (formula for $Al_xGa_{1-x}As$: 5320-1560x)	ρ	kg·m^{-3}	4072	[182]
Poisson ratio at 300 K (111) plane (formula: 0.31+0.01x)	σ	-	~ 0.32	[183]
Thermal parameters				
Specific heat at 300 K	c	J·K^{-1}·kg^{-1}	426	[183]
Thermal conductivity at 300 K	κ	W·K^{-1}·m^{-1}	14	[183]
Linear thermal expansion coefficient at 300 K (formula: $\alpha_{th,x} = 5.97 - 1.76x$)	α_{th}	10^{-6}K^{-1}	~ 4.6	[183]
Optical parameters				
Refractive index at 1550 nm and T=298 K	n	-	2.977	[184]
Refractive index at 1330 nm and T=298 K	n	-	2.99	[184]

Table D.2: Aluminum Gallium Arsenide ($Al_{0.8}Ga_{0.2}As$) parameters

Parameter	Name	Unit	Value	Source
Mechanical parameters				
Young's modulus	E	GPa	250	[98]
			270	our fit
Density	ρ	kg·m^{-3}	3100	[98]
Poisson's ratio	σ	-	0.23	[98]
Tensile Stress (measured on 100 nm thick SiN)	σ_{SiN}	MPa	830	[106]
Thermal parameters				
Specific heat at 300 K	c	J·K^{-1}·kg^{-1}	700	[98]
Thermal conductivity at 300 K	κ	W·K^{-1}·m^{-1}	20	[98]
Linear thermal expansion coefficient at 300 K	α_{th}	10^{-6}K^{-1}	2.3	[98]
Optical parameters				
Refractive index at 1550 nm and 300 K	n	-	~ 2	[185]
Thermo-optic coefficient at room	$\frac{\partial n}{\partial T}$	K^{-1}	4·10^{-5}	[32]
temperature			1.9·10^{-5}	[186]
			2.44·10^{-5}	our fit

Table D.3: LPCVD Silicon Nitride parameters

Parameter	Name	Unit	Value	Source
Mechanical parameters				
Young's modulus	E	GPa	70	[98]
Density	ρ	kg·m^{-3}	2200	[98]
Poisson's ratio	σ	-	0.17	[98]
Thermal parameters				
Specific heat at 300 K	c	J·K^{-1}·kg^{-1}	730	[98]
Thermal conductivity at 300 K	κ	W·K^{-1}·m^{-1}	1.4	[98]
Linear thermal expansion coefficient at 300 K	α_{th}	10^{-6}K^{-1}	0.5	[98]
Optical parameters				
Refractive index at 1550 nm and room temperature	n	-	1.44	[180]
Refractive index at 1330 nm and room temperature	n	-	1.44	[180]

Table D.4: Silicon Dioxide (SiO$_2$) parameters

Parameter	Name	Unit	Value	Source
Mechanical parameters				
Young's modulus	E	GPa	170	[98]
Density	ρ	kg·m^{-3}	2329	[98]
Poisson's ratio	σ	-	0.28	[98]
Thermal parameters				
Specific heat at 300 K	c	J·K^{-1}·kg^{-1}	700	[98]
Thermal conductivity at 300 K	κ	W·K^{-1}·m^{-1}	130	[98]
Linear thermal expansion coefficient at 300 K	α_{th}	10^{-6}K^{-1}	2.6	[98]
Optical parameters				
Refractive index at 1550 nm and 300 K	n	-	3.48	[180]
Refractive index at 1330 nm and 300 K	n	-	3.5	[180]

Table D.5: Silicon parameters

Appendix E

ICP recipes

Ar (sccm)	SiCl$_4$ (sccm)	ICP Power (W)	RF Power (W)	Temperature (°C)	Pressure (Pa)
3	3	20	10	10	0.1

Table E.1: Recipe 1. Self Bias = -60 V. Very slow etch 4 nm/min.

Ar (sccm)	SiCl$_4$ (sccm)	ICP Power (W)	RF Power (W)	Temperature (°C)	Pressure (Pa)
6	6	40	20	10	0.2

Table E.2: Recipe 2. Self Bias = -107 V. Etch speed 55 nm/min. Some roughness.

Ar (sccm)	SiCl$_4$ (sccm)	ICP Power (W)	RF Power (W)	Temperature (°C)	Pressure (Pa)
3	3	40	20	10	0.1

Table E.3: Recipe 3. Self Bias = -118 V. Etch speed ∼50 nm/min. Smoother sidewalls than with recipe 2.

H$_2$ (sccm)	SiCl$_4$ (sccm)	ICP Power (W)	RF Power (W)	Temperature (°C)	Pressure (Pa)
5	15	400	15	90	0.14

Table E.4: Recipe 4. Self Bias = -30 V. Etch speed ∼650 to 800 nm/min. Very poor results with significant sidewall erosion (see results in Fig. 4.11, c).

Ar (sccm)	SiCl$_4$ (sccm)	ICP Power (W)	RF Power (W)	Temperature (°C)	Pressure (Pa)
3	3	45	15	10	0.1

Table E.5: Recipe 5. Self Bias = -84 V. Etch speed ∼55 nm/min. Somewhat rough with sidewall erosion and mask undercut (see results in Fig. 4.11, b).

Ar (sccm)	SiCl$_4$ (sccm)	ICP Power (W)	RF Power (W)	Temperature (°C)	Pressure (Pa)
3	3	25	17	10	0.1

Table E.6: Recipe 6. Quite good results, somewhat inferior to recipe 7 (less vertical sidewalls).

Ar (sccm)	SiCl$_4$ (sccm)	ICP Power (W)	RF Power (W)	Temperature (°C)	Pressure (Pa)
9	3	25	17	10	0.1

Table E.7: Recipe 7. Self Bias under 100 V. Etch speed $\leq$ 40 nm/min. This recipe provided the best results obtained during the course of this work. Further improvements are nevertheless likely achievable, for instance maintaining the same level of smoothness while increasing the etch speed. (See results in Fig. 4.12).

Appendix F

List of publications

F.1   Publications

- L. Ding, C. Baker, P. Senellart, A. Lemaitre, S. Ducci, G. Leo, and I. Favero. High frequency GaAs nano-optomechanical disk resonator. *Physical Review Letters*, 105(26):263903, 2010.

- L. Ding, C. Baker, P. Senellart, A. Lemaitre, S. Ducci, G. Leo, and I. Favero.   Wavelength-sized GaAs optomechanical resonators with gigahertz frequency. *Applied Physics Letters*, 98:113108, 2011.

- C. Baker, C. Belacel, A. Andronico, P. Senellart, A. Lemaitre, E. Galopin, S. Ducci, G. Leo, and I. Favero. Critical optical coupling between a GaAs disk and a nanowaveguide suspended on the chip.   *Applied Physics Letters*, 99:151117, 2011.

- C. Baker, S. Stapfner, D. Parrain, S. Ducci, G. Leo, E.M. Weig, and I. Favero. Optical instability and self-pulsing in silicon nitride whispering gallery resonators. *Optics Express*, 20(27):29076–29089, 2012.

- D. Parrain, C. Baker, T. Verdier, P. Senellart, A. Lemaitre, S. Ducci, G. Leo, and I. Favero. Damping of optomechanical disks resonators vibrating in air. *Applied Physics Letters*, 100(24):242105–242105, 2012.

- C. Baker, W. Hease, DT. NGuyen, S. Ducci, G. Leo, and I. Favero. Photoelastic coupling in GaAs semiconductor optomechanical disk resonators. *In preparation*, 2013.

- DT. NGuyen, C. Baker, W. Hease, S. Sejil, P. Senellart, A. Lemaitre, S. Ducci, G. Leo and I. Favero. Ultrahigh Q frequency product for op-

tomechanical disk resonators with a mechanical shield. arXiv preprint arXiv:1309.4971., 2013.

F.2 Book Chapter

- *Gallium Arsenide Disk Optomechanical Resonators.* Lu Ding, Christophe Baker, Alessio Andronico, David Parrain, Pascale Senellart, Aristide Lemaitre, Sara Ducci, Giuseppe Leo, Ivan Favero.

F.3 Conference Presentations

- **Dispositif Nano-optomécanique intégré**. Christophe Baker, Lu Ding, Pascale Senellart, Aristide Lemaitre, Sara Ducci, Giuseppe Leo, and Ivan Favero. JNOG - Société Française d'Optique, Besançon, France, October, (2010) - (Talk)

- **Nanoscale GaAs disk/waveguide system for integrated optomechanics applications**. Christophe Baker, Cherif Belacel, Alessio Andronico, Pascale Senellart, Aristide Lemaitre, Sara Ducci, Giuseppe Leo, Ivan Favero ; NEMS2011 Seminar Toulouse, France, 4-5 July, (2011) - (Poster)

- **GaAs Disk Optomechanics**. Christophe Baker, Lu Ding, David Parrain, Sara Ducci, Giuseppe Leo, Ivan Favero. Frontiers in Optics/Laser science XXVII, San Jose, Californie, USA, 16-20 October, (2011) - (Talk)

- **GaAs Disk Optomechanics**. Christophe Baker, Lu Ding, David Parrain, Sara Ducci, Giuseppe Leo, Ivan Favero. WE-Heraeus-Seminar on Micro & macro-cavities in classical and non-classical light. Bad Honnef, Germany, 30 Octobre 04 November, (2011) - (Talk)

- **Miniature GaAs Disk Optomechanical Resonators**. Christophe Baker, David Parrain, Pascale Senellart, Aristide Lemaitre, Sara Ducci, Giuseppe Leo, Ivan Favero. Gordon Research Conference Mechanical Systems in the Quantum Regime Galveston, Texas, USA, 4-9 March, (2012) - (Poster)

- **Strongly coupled GaAs nano-optomechanical systems**. Christopher Baker, David Parrain, Pascale Senellart, Aristide Lemaitre, Sara Ducci, Giuseppe Leo, Ivan Favero. 13th International Conference on

Physics of Light-Matter Coupling in Nanostructure (PLMCN 2012), Hangzhou, China , 19-23 June, (2012) - (Talk)

- **GaAs disk quantum optomechanical resonators in a cryogenic environment**. Christopher Baker, William Hease, Dac-Trung Nguyen, Pascale Senellart, Aristide Lemaitre, Sara Ducci, Giuseppe Leo, Ivan Favero. Quantum Nano- and Micromechanics (QNM 2013), Monte Verita, Switzerland, 21-25 July, (2013) - (Poster)